UNIVERSITY OF SOUTHAMPTON

FACULTY OF PHYSICAL AND APPLIED SCIENCES

School of Electronics and Computer Science

DESIGN, MODELLING AND CHARACTERISATION OF IMPACT BASED AND NON-CONTACT PIEZOELECTRIC HARVESTERS FOR ROTATING OBJECTS

By

Ghaithaa Manla

Thesis for the degree of Doctor of Philosophy

November 2010

UNIVERSITY OF SOUTHAMPTON

ABSTRACT

FACULTY OF PHYSICAL AND APPLIED SCIENCES
SCHOOL OF ELECTRONICS AND COMPUTER SCIENCE

Doctor of Philosophy

DESIGN, MODELLING AND CHARACTERISATION OF IMPACT BASED AND NON-CONTACT PIEZOELECTRIC HARVESTERS FOR ROTATING OBJECTS

by Ghaithaa Manla

This thesis highlights two different methods of extracting electrical energy from rotational forces using impact based and non-contact based piezoelectric harvesters. In this work, the centripetal force is used as the main acting force that causes the piezoelectric harvesters to produce output power. In order to achieve this, the harvesters are mounted in a horizontal position while the rotational forces are applied. The impact based piezoelectric harvester consists of a tube with one piezoelectric pre-stressed beam mounted at each end of the tube. A ball bearing that has the freedom of movement between the two ends of the tube generates an impact force on the piezoelectric structures due to the effect of the centripetal force. The impact based piezoelectric harvester is modelled and its behaviour is analysed and verified experimentally. For the non-contact piezoelectric harvester, the applied force on the piezoelectric element is produced by a magnetic levitation system without the need for a direct physical contact. The impact of the magnet size and shape is studied and the results become a guideline that is used to design and optimize the piezoelectric harvester. The model of the non-contact piezoelectric harvester is derived and verified experimentally in order to analyse its behaviour at different boundary conditions. A comparison between the two harvesters is carried out. This includes highlighting the advantages and the limitations of each of them.

Contents

List of Figures

List of Tables

Declaration of Authorship

I, Ghaithaa Manla declare that the thesis entitled ‘design, modelling and characterisation of impact based and non-contact piezoelectric harvesters for rotating objects’ and the work presented in the thesis are my own. I confirm that:

- This work was done wholly or mainly while in candidature for a research degree at the University;
- Where any part of this thesis has previously been submitted for a degree or any other qualification at this University or any other institution, this has been clearly stated;
- Where I have consulted the published work of others, this is always clearly attributed;
- Where I have quoted from the work of others, the source is always given. With the exception of such quotation, this thesis is entirely my own work;
- I have acknowledge all main sources of help;
- Where the thesis is based on work done by myself jointly with others, I have made clear exactly what was done by others and what I have contributed myself;
- Parts of this work have been published as listed in section 1.4 of this thesis.

Signed: …….

Date: ……

Acknowledgements

My thanks to Prof. Neil White for his supervision over the course of my PhD and for the times of encouragement and motivation when they were needed most. I am also indebted to Prof. Neil White for the opportunity afforded to me to do my PhD here in Southampton University.

A special thanks to Dr John Tudor for his guidance and helpful ideas which direct me throughout my academic study. Also a special thanks to Eric Webb for his help designing and building the rotating wheel.

I would like to thank all my friends who I have met during my time in Southampton. I have been blessed with a friendly and cheerful group of fellow colleagues and friends. You have all made the office such an enjoyable place to work in.

Finally, I would like to thank my parents for their encouragement and support, both emotionally and financially, throughout all my studies and life. I also wish to thank my siblings and grandparents who are far away in distance, but close to my heart. Without you I could not have gone this far in my academic study. I would like to thank Dr David Angland for making my life more meaningful.

Nomenclature

A	Area, m^2
$\mathbf{a}$	Acceleration vector
a_{cp}	Centripetal acceleration, m/s^2
a_t	Tangential acceleration, m/s^2
α	Thermal expansion coefficient, $/^oC$
C	Capacitance, F
c	Elastic compliance constant, m/N^2
c_e	Electrical damping coefficient, N.s/m
c_m	Mechanical damping coefficient, N.s/m
c_T	Total damping coefficient, N.s/m
D	Electric displacement
d	Distance between capacitance plate, m
d_{ij}	Piezoelectric charge constant C/N
δ	Deflection, m
E	Electric field, V/m
$E_{rotation}$	Kinetic energy, J
$\mathbf{e_r}$	Radial unit vector
$\mathbf{e_\theta}$	Tangential unit vector
e^*	Energetic coefficient of restitution
ε	Dielectric constant
$\mathbf{F}$	Force, N
f_r	Natural frequency, Hz
g_{ij}	Piezoelectric voltage constant, Vm/N
h	Thickness, m
I	Area moment of inertia, m^4
I_m	Mass moment of inertia, $kg.m^2$
K	Stiffness (spring constant), N/m
k	Electromechanical coupling coefficient
L	Length, m
l	Length of the capacitor plate, m
λ_r	Wavelength, m

M	Mass of the rotating disk, kg
m	Mass, kg
μ	Efficiency
n	Modular ratio
$\mathbf{P}$	Momentum, kg.m/s
P	Power, W
$\overline{p}$	Mean applied pressure, N/m^2
ϕ	Transformer ratio, V/N
Q	Quality factor
q	Charge, C
$\mathbf{R}$	Position vector
R	Radius, m
R_L	Load resistance, Ω
RC	Time constant, s
r_n	Radius of neutral axis, m
ρ	Density, $kg.m^{-3}$
S	Strain
σ	Stress, N/m^2
T	Temperature, ^oC
T_o	Incident kinetic energy of colliding bodies
T_f	Final kinetic energy of system at termination of period of restitution
t	Time, s
$\tan\delta$	Dielectric loss
θ	Angle, rad
τ	Torque, N.m
υ	Poisson's ratio
V	Voltage, V
$\mathbf{v}$	Velocity vector
v	Velocity magnitude, m/s
W	Work, N.m
w	Width of the capacitor plate, m
ω	Angular velocity, rad/s
ω_o	Resonant angular frequency, rad/s
Y	Young's modulus, N/m^2
ξ_e	Electrical damping ratio

ξ_m	Mechanical damping rate
ζ	Damping ratio

Glossary of Terms

ABS	Anti-Lock Braking System
AR	Aspect Ratio
CAD	Computer Aided Design
CF	Effect of the Centripetal Force
DC	Direct Current
ECS	Electronics and Computer Science
ECF	Effect of Centripetal Force
EGF	Effect of Gravitational Force
FEM	Finite Element Method
GF	Effect of the Gravitational Force
LCR	Inductance (L), Capacitance (C) and Resistance (R)
MEMS	Micro-Electro-Mechanical Systems
NA	Neutral Axis
NASA	National Aeronautics and Space Administration
PC	Personal Computer
PLC	Programmable Logic Controller
PSD	Power Spectral Density
PVDF	Polyvinylidene Fluoride
PZT	Lead Zirconate Titanate
RF	Radio Frequency
RMS	Root Mean Squared
TPMS	Tyre Pressure Monitoring System

Chapter 1

Introduction

1.1 Research objectives

The aim of this research is to investigate and develop a harvester that has the ability to power sensors that are mounted on rotating objects. Therefore, this research is focused on understanding power generation mechanisms associated with rotation and the method by which this energy is extracted. The focus of this research is directed towards powering sensors that are located in unreachable areas within rotating systems such as the tyre pressure monitoring system located inside the vehicle tyre. Moreover, this research will focus on designing a harvester that has the ability to generate the required amount of power over a range of rotating speed and withstand the high acceleration amplitude caused by centripetal force at high rotating speed. For such applications, different types of resonant vibration based micro harvesters including piezoelectric, electromagnetic or electrostatic transducer have been designed to convert the available vibration within a rotating object into electrical energy [1]. The performance of these harvesters depends on the frequency of the ambient vibration. Using vibration based micro harvester inside the vehicle tyre as an example of rotating object, leads to the fact that the maximum generated output power is achieved when the natural frequency of the harvester matches the vibration frequency produced at a specific rotating speed. Therefore, if the resonant frequency of the harvester does not mach that of the ambient, the level of the output power decreases dramatically.

In order to overcome this problem, two types of piezoelectric harvester are designed, analysed, tested and their results compared with each other. The first approach is based on using impact force to extract electrical power. The second

approach is based on a non-contact system. No existing studies reported the use of the previous two systems to extract electrical energy from centripetal force in particular. Therefore, the main objective of this work is to develop a harvester that uses centripetal force to extract output power using impact based piezoelectric harvester as well as non-contact based piezoelectric harvester.

This present work employs a variety of experimental and theoretical techniques to analyse the effect of rotational forces produced by the rotating object on the piezoelectric harvester. The method by which the harvester is mounted on the rotating object will be investigated and its effect on the amount of the generated power will be analysed. As part of the experimental investigation, an impact based piezoelectric harvester will be designed, analysed numerically and tested. The same approach will be used with a non-contact piezoelectric harvester. For both harvesters, the numerical results from the developed models will be compared to the experimental results by which the model will be tested and verified. Both harvesters will be optimized and their output power will be compared with each other and the limitations of each harvester will be addressed.

After understanding the behaviour of the developed piezoelectric harvester under rotational forces and analysing its performance, the focus of the research will be directed towards implementing the method in a practical application such as tyre pressure monitoring sensors. In this case, tyre pressure sensors are mounted directly inside each tyre. In an effort to generate power from a vehicle wheel, researchers have focused on vibration, since this is one of the main sources of energy in the tyre [2]. As mentioned before, the aim of this research is focused on extracting power from the rotational forces, particularly the centripetal force.

1.2 Document structure

This thesis describes the work that was carried out to investigate the ability of generating output power from rotational forces in general and from the centripetal force in particular. A commercial type of pre-stressed beam called Thunder™ is used in this investigation. The report is divided into nine main chapters.

Chapter 2 introduces the background of the field, a review of the relevant literature and a discussion of the previous work performed in this area. This chapter addresses the issues of the different designs of the energy harvesting generators. A discussion about different methods that can be used to convert kinetic energy into

electrical energy is presented. A discussion about the suitability of the each method with the surrounding environment is analysed and followed by analysis about piezoelectric harvesters and the ability of using rotation as a source to generate an output power. Applications by which the harvester can be used are introduced with a focus on the possibility of using the harvester inside a vehicle tyre. This is followed by a discussion about the advantages of using piezoelectric pre-stressed beam (Thunder™) for this type of application.

Chapter 3 presents a theoretical analysis of the Thunder™ pre-stressed beam and addresses the influence of beam curvature on the amount of stress developed in the piezoelectric structure. The dependency of the structure characteristics on the applied compression forces is addressed and measured.

Chapter 4 presents a numerical analysis of the impact based piezoelectric harvester. The principle by which this harvester operates is detailed. Numerical methods are used in order to analyse the behaviour of the impact based harvester in general and the Thunder™ beam in particular under impact force. The simulated results of the finite element analysis using the ANSYS software are used to analyse the developed stress in the Thunder™ beam due to the effect of an impulse force. Moreover, ANSYS is used to analyse the amount of generated stress in the clamped area due to the clamping method. An optimization of the output power in geometries perspectives is carried out in this chapter.

In Chapter 5 a testing wheel with the ability of mounting the developed harvester in different method is designed. The different methods of mounting are presented to analyse the effect of the different types of rotational forces on the harvester. The method that is used to monitor the effect of the rotational forces in general and the centripetal force in particular on the impact based piezoelectric harvester is detailed in this chapter. The generated experimental results are presented, discussed and compared with the theoretical results presented in Chapter 4.

In Chapter 6, the principle of the non-contact piezoelectric based harvester is introduced. Simulation and optimization of the non-contact piezoelectric harvester is presented.

An experimental method that is used to testify the theory is then introduced in Chapter 7. This is followed by experimental characterization of the non-contact piezoelectric harvester. In this chapter, the experimental results are presented and compared to the numerical ones.

The two prototypes of the piezoelectric based harvester that have been designed and tested are compared to each other and discussed in Chapter 8. The comparison focused on the amount of the generated power and the limitation of each prototype. This chapter presents a discussion about the possibility of mounting the designed harvesters inside the vehicle tyre to power the tyre pressure monitoring system.

Chapter 9 concludes both experimental and theoretical conclusions along with suggestions for future development in this area.

1.3 Statement of novelty

The outcome of this research presented these novelties:

- Experimental and theoretical proof of the feasibility of using rotational forces to generate output power from piezoelectric pre-stressed beam (Thunder™).
- Theoretical analysis of the Thunder™ beam and establishment of a model and an experimental method that presents the effect of applying force on its stiffness and damping.
- Design and build of a piezoelectric harvester to generate output power from impact force due to the effect of the centripetal force.
- Modelling the behaviour of the piezoelectric harvester that uses Thunder™ beam under impact.
- Experimental verification of the impact based harvester model.
- Design and build of a non-contact based piezoelectric harvester to generate output power from magnetic force due to the effect of the centripetal force.
- Model the behaviour of the non-contact piezoelectric harvester that uses Thunder™ beam under the effect of the magnetic forces.
- Experimental verification of the model of the non-contact harvester.

1.4 Publications

1. G. Manla, N. M. White, J. Tudor. Harvesting energy from vehicle wheels for tyre pressure sensors. Presented at 22nd International Conference *Eurosensors*, Dresden, Germany. September 7-10, 2008.

2. G. Manla, N. M. White, J. Tudor. Harvesting energy from vehicle wheels. Presented at *the 15th International conference on Solid State Sensors, Actuators and Microsystems, Transducer2009*, Denver, Colorado, USA. June 21-25, 2009.

Chapter 2

Background and literature review

2.1 Introduction

Wireless system networks are attractive because they facilitate the placement of sensors in inaccessible locations. Moreover, embedded wireless microsensors have potential applications in areas such as continuous monitoring of structure and machine functionality without the expense and the inconvenience of wiring failure. This includes monitoring temperature, the location and movement of persons and acceleration and pressure in automobile tyres [3]. At present, these electronics rely on the use of batteries to provide electrical energy to the wireless sensor nodes. This is due to the fact that batteries are an easy power solution and they provide a stable voltage, which means electronic devices can be run directly without any intervening power electronics. In the past few decades, the performance of computing systems has grown steadily, which has led to a large area of research based on wireless sensor networks. Long transmission distances can be replaced with low-cost, low-power wireless devices which operate in a multi-hop fashion, i.e. the transmitting data to the final destination port should be routed via at least one intermediate port [4]. This results in dense networks which comprise thousands of small wireless nodes. However, the reduction of the nodes' size and the increase in their number within the network, make the use and the replacement of batteries impractical. As the electronics of a wireless sensor node decrease in size, the size of the battery must also be reduced, otherwise it will dominate the system volume. On the other hand, reducing the batteries' size limits their lifetime.

This creates a problem in powering a large number of nodes that make up a network due to the cost of replacing the batteries. Although battery technology provides enough energy for applications that require high and constant power consumption in the range of one year or less, the need to develop other methods, which provide sustainable energy throughout the lifetime of the device, is desired. In order to achieve this, researchers have focused on three methods [5]:

- Improving the energy density of storage systems.
- Developing technologies that enable a node to scavenge power available in the surrounding environment.
- Developing a suitable method to distribute power to the nodes.

Among these different methods of powering a wireless network, power scavenging has the advantage that the lifetime of the node depends only on the reliability of its parts. However, each environment has different forms and characterizations of the available ambient energy. This makes designing one type of harvester that is suitable to harvest energy from different environments and at different conditions impossible. The focus of this research is directed towards designing a harvester that uses rotational energy as a source to provide an electrical energy.

This Chapter is divided into five main sections. Section 2.2 presents the principle behind generating electrical energy from mechanical energy. A comparison between resonant and non-resonant systems in terms of its generated output power is presented in this section. Three different mechanisms that have been used to convert the kinetic energy into useful power are illustrated and compared. Section 2.3 presents the possibility of using rotation as a main source of electrical energy. Section 2.4 outlines the previous efforts that have been described in the literature in order to achieve that. Suitable applications that can use the developed harvesters detailed in this work are discussed in Section 2.5 with the focus on extracting energy from the vehicle tyre environment. The reason for choosing this application as the main one is explained in this chapter. Section 2.6 focuses on using a piezoelectric transducer as a method to convert kinetic energy into electrical energy. Different types of piezoelectric harvesters that are developed in the literature are discussed in this section.

2.2 Electromechanical harvesters

In order to generate electrical energy from kinetic energy or mechanical forces, a suitable harvester is required. The three main methods to convert mechanical motion into an electrical signal, based on their damping mechanisms, are:

- Electromagnetic, which depends on changing the flux linkage of a coil with a magnetic field. This method depends on damping velocity.
- Electrostatic, which depends on moving the plates of a capacitor apart against the attractive electrostatic force. This method depends on damping Coulomb force.
- Piezoelectric, which depends on straining the piezoelectric material to create an electric charge. This method depends on damping the material deformation.

The principle by which these harvesters convert mechanical energy into electrical energy can be explained as follows. The input kinetic energy causes the harvester frame to accelerate. The inertia of the harvester mass causes relative motion between the frame and the mass. The work done on the damper is the product of the force and the relative movement between the mass and the frame. The integral of the work over a cycle represents the converted energy. The amount of output power depends on the chosen method which depends on the type of application. Moreover, the material type, aspect ratio and the dimensions of the different parts of the harvester are factors that affect the amount of output power. These three methods of energy conversion from mechanical into electrical energy can be divided into resonant and non-resonant systems based on the spring-mass motion.

2.2.1 Resonant and non-resonant systems

Resonant harvesters can be modelled as second-order, spring-mass-damper system as shown in Figure 2.1. In a resonant system the work can be stored in the spring and then released to the damper at a different part of the motion cycle. A mass (m) is significantly smaller than the mass of the vibration source and thus it will not be affected by its presence. The mass is suspended from a spring of stiffness (K). The total damping coefficient of the system (c_T) is the sum of the mechanical damping coefficient (c_m) and the electrical damping coefficient (c_e). c_m represents the loss in the system due to air resistance and support damping. c_e represents the useful extracted

energy from the converter. The spring mass system, located within the inertial frame, is being excited by an external harmonic excitation giving by $y(t) = Y_0 \sin(\omega t)$, where Y_0 is the source motion amplitude. The absolute motion of the frame and the mass are *y(t)* and *x(t)* respectively. The displacement of the mass from its rest position relative to the frame is presented as *z(t)*. Z_l is the maximum amplitude of the mass-frame displacement. The differential equation of motion is described as:

$$m\ddot{z}(t) + c_T \dot{z}(t) + Kz(t) = -mY_0 \sin(\omega t) \qquad 2.1$$

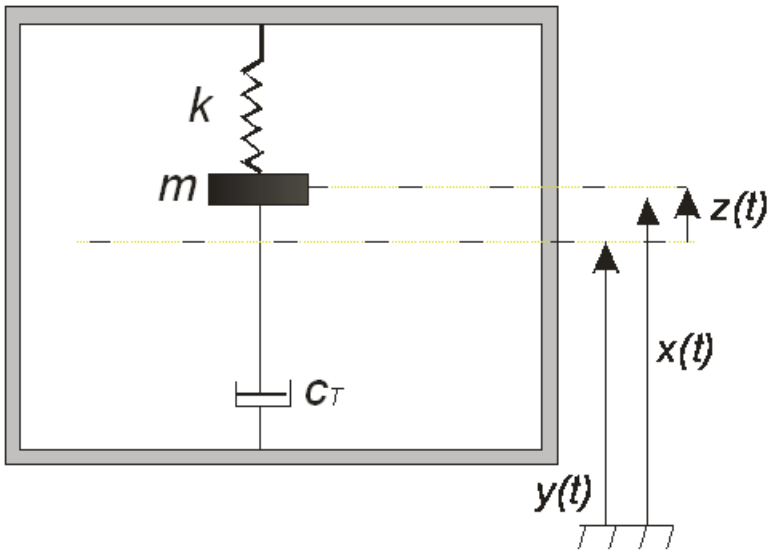

Figure 2.1 Schematic of a generic mechanical-to-electricity converter

The useful electrical power is equal to the power removed from the mechanical system by c_e. Equation 2.2 shows the power dissipated within the damper [6].

$$P = \frac{m\xi_T Y_0^{\,2} \left(\frac{\omega}{\omega_o}\right)^3 \omega^3}{\left[1 - \left(\frac{\omega}{\omega_o}\right)^2\right]^2 + \left[2\xi_T \left(\frac{\omega}{\omega_o}\right)\right]^2} \qquad 2.2$$

The damping coefficients c_T is replaced with the damping ratio ξ_T according to the following equation:

$$\xi_T = \frac{c_T}{2m\omega_o} \qquad 2.3$$

ω is the frequency of the driving vibration and ω_o, which is equal to $\sqrt{K/m}$, is the resonant frequency of the mass spring system. Maximum power can be extracted when the input frequency matches the resonant frequency of the system. Therefore, the system must be designed to resonate at the excitation frequency and in this case P can be given by the following equations:

$$P = \frac{m\xi_e \omega_o{}^3 Y_0^2}{4\xi_T{}^2} \tag{2.4}$$

$$P = \frac{m\xi_e a^2}{4\omega_o(\xi_m + \xi_e)^2} \tag{2.5}$$

Equation 2.5 used the excitation acceleration (a) in the expression of P which is derived from $a = \omega_o^2 Y_0$. For a given acceleration, the output power is inversely proportional to the resonant frequency. Therefore, the harvester should be designed to be resonant at the lowest fundamental frequency. Equation 2.5 shows that the output power can be increased by increasing the mass within the given space constraints. The mechanical damping ratio (ξ_m), that represents the designed harvester, is constant. The output power is maximized when the value of the electrical damping ratio (ξ_e) matches the value of the mechanical damping ratio (ξ_m).

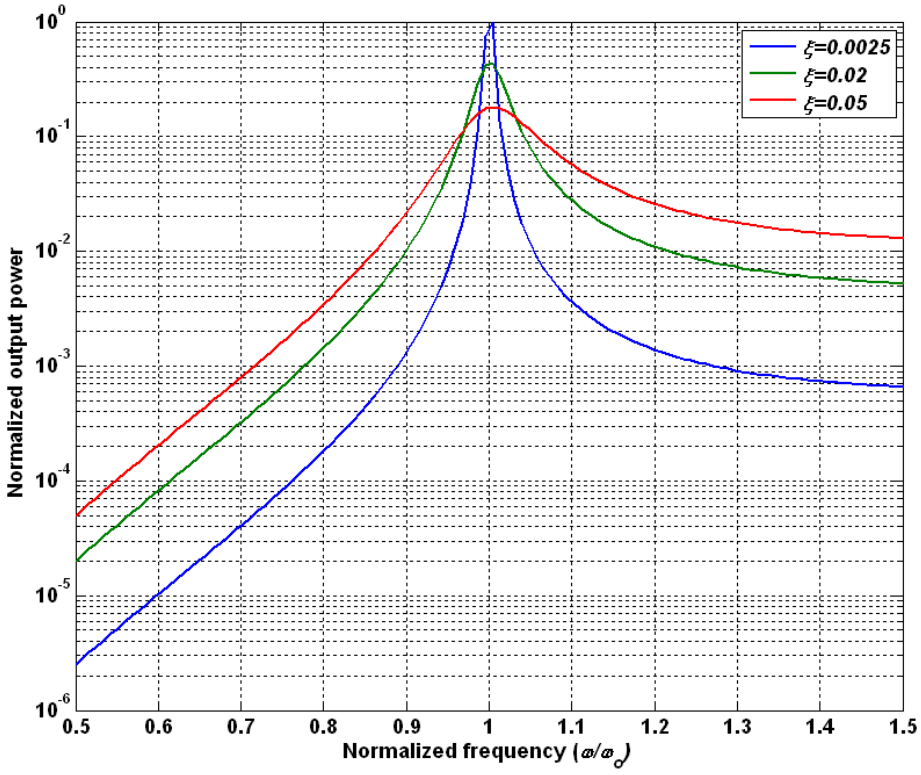

Figure 2.2 Power output vs. frequency in resonant harvesters

Figure 2.2 shows the output power versus frequency for different values of the damping ratio. The natural frequency of the harvester is 100 Hz and the frequency of the exciting frequency is varied from 10 to 200 Hz. In order to extract the maximum power, this figure assumes that $\xi_e = \xi_m$. Systems with a low damping ratio (around 0.01) have the potential for higher output power. However, this power drops off quickly when the frequency of the driving vibration moves away from the natural frequency. On the other hand, increasing the damping results in a broader bandwidth response.

The previous model of the harvester does not specify the mechanism by which the conversion takes place (electrostatic, electromagnetic or piezoelectric). For a real harvester, the model will be more complicated due to the transduction damping coefficient being dependant on the conversion method.

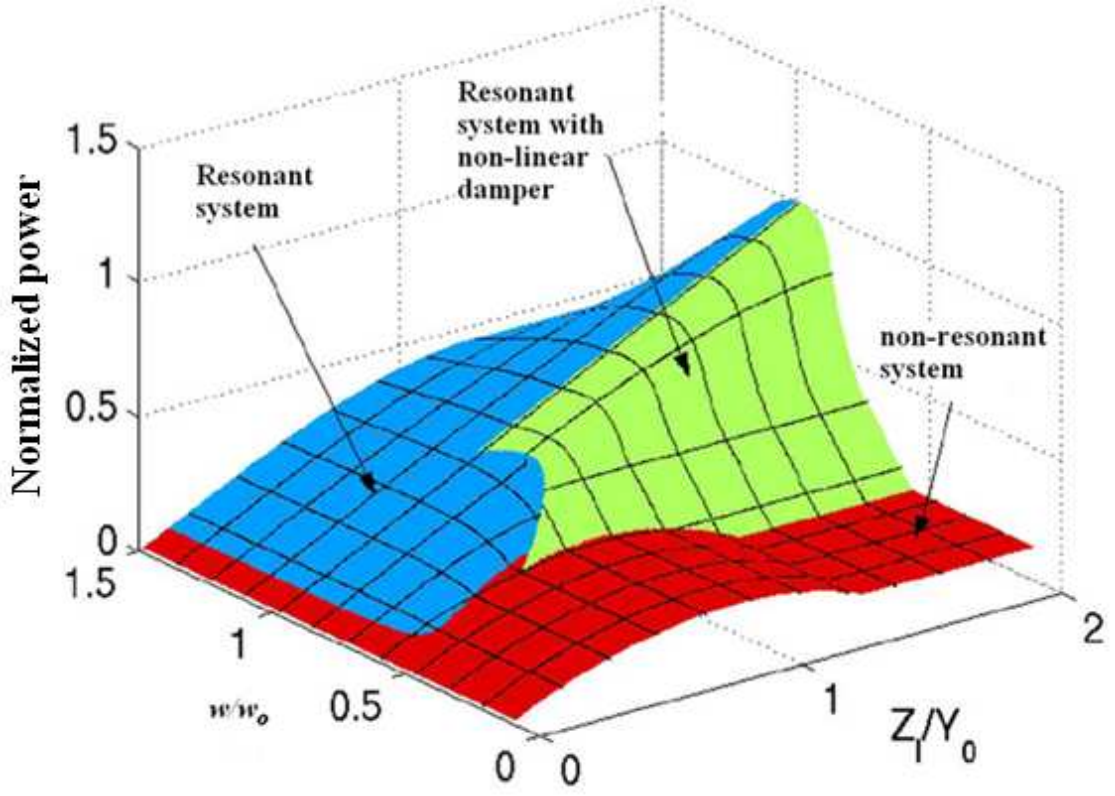

Figure 2.3 Performance of different type of transducer under varying operating conditions [7]

The work in a non-resonant system, on the other hand, is only done on the damper, where the spring constant (K) is zero. The output power is proportional to the damping force and the displacement of the mass (Z_l). In order to increase the output power, the damping force should be as high as possible. However, this force must be below the maximum frame acceleration which can be given by $Y_o\omega^2$. In case the damping force is more than the frame acceleration the mass moves with the frame.

Therefore, no relative motion between the mass and the frame is created and thus no work will be done on the damper. The conversion will start when the acceleration of the frame is just above the damping force. Thus the mass will break away from the frame and move from one end of the frame to the other during the peak of acceleration [8]. Figure 2.3 shows the relationship between the normalized output power to ($mY_o^2\omega^3$) and the normalized frequency (ω/ω_o) [7]. In addition Figure 2.3 shows the relationship between the normalized power and the ratio between the maximum available displacement of the mass and the acceleration amplitude (Z_l/Y_0).

Figure 2.3 is divided into three main areas. The blue area represents a resonant system with linear damping such as electromagnetic and piezoelectric transducers. The green area represents resonant system with non-linear damping such as an electrostatic transducer. The red area represents non-resonant systems. As can be seen, resonant systems generate more power when the ratio between the applied frequency and the harvester resonant frequency (ω/ω_o) is 1. This means the resonant frequency of the harvester matches the applied frequency. Resonant systems with linear damping are more suitable when the normalized frequency is between 1 and 1.5. Resonant systems with non-linear damping are more suitable when the normalized frequency is between 0.5 and 1. However, when the resonant frequency of the harvester is twice the applied frequency or more, non-resonant systems produce more output power than resonant systems. Figure 2.3 shows that resonances are useful when (Z_l/Y_0) is large around 1 or more for resonance with non-linear damping and 0.25 or more for resonance with linear damping. If the amplitude of the frame-mass displacement is a quarter of the acceleration amplitude or less, then a non-resonant system is preferable [7].

In conclusion, resonant electromechanical harvesters generate the maximum output power when the resonant frequency of the harvester matches the input frequency. This is a drawback of the resonant system, especially when the value of the input frequency changes over time. Therefore, an alternative conversion mechanism based on a non-resonant system, which works without a spring and thus does not have a resonant behaviour, is used in this situation. In case of generating power from rotating objects both (Z_l/Y_0) and (ω/ω_o) are small making the non-resonant system more suitable for this application.

2.2.2 Types of electromechanical harvesters

There are three main methods to convert mechanical motion into electrical signal. These are electromagnetic, electrostatic and piezoelectric transduction. In this section these techniques are covered and their basic concepts and operating principles are outlined. Different designs are described and analysed. In addition, these three methods are evaluated as potential transduction mechanisms for harvesting energy from rotation.

2.2.2.1 Electromagnetic harvesters

Electromagnetic power conversion results from the relative motion of a conductor in a magnetic field. Typically the conductor takes the form of a coil. The amount of electricity generated depends on the velocity of the relative motion, the strength of the magnetic field and the number of turns of the coil. Increasing the strength of the magnetic field and the other two factors results in an increase in the current flow in the coil [9].

Different configurations of resonant electromagnetic harvesters have been designed based on the use of relative movement between magnets and coils in a mass-spring system to generate electrical energy from mechanical movement. Generating power by means of a coil, cantilever beam and a permanent magnet is one of the most attractive methods for energy harvesting from low frequency vibration sources. In this configuration a cantilever is used as a resonant element and either the coil or the magnet can be mounted on the beam while the other is fixed. The magnet will act as the inertial mass if it has been attached to the beam and vice versa if the coil is mounted to the beam.

Two devices with different combinations of magnets and coils have been developed at Southampton University [6, 10, 11]. Both structures are based on a cantilever structure. The first device was based on moving coil between two fixed magnets. However, the second device, which was based on moving 4 magnets with fixed coil, generated an output power up to 180 μW for 0.85 mm displacement. The second harvester generated more than twice the output voltage (1V) and more than four times the power for the same input. This harvester is presented in Figure 2.4. Therefore, using the coil as a mass is less effective than using the magnet as a mass especially if the harvester dimension is in the range of a few cm^3. This is due to the flux density, as reducing the size of the magnet leads to a reduction in flux.

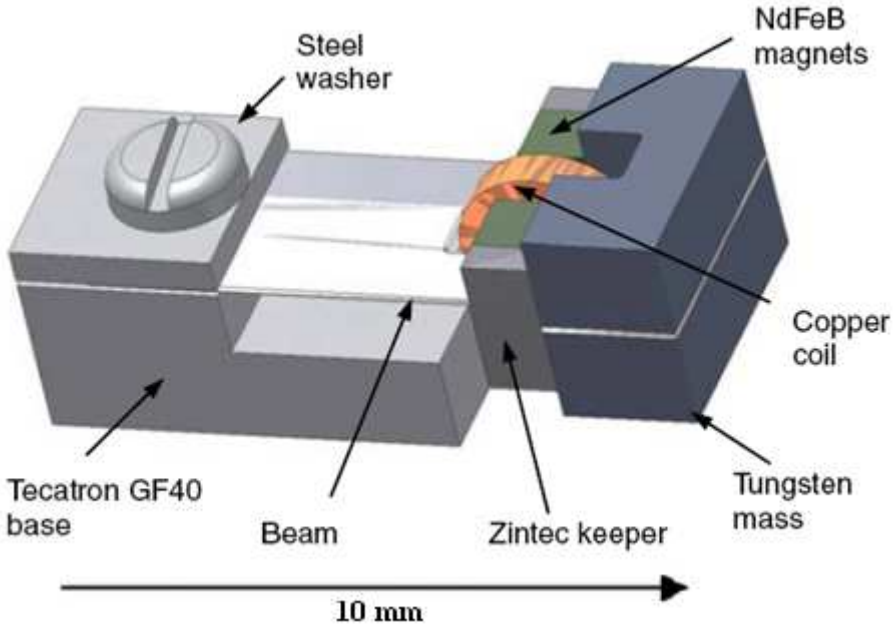

Figure 2.4 Micro-cantilever harvester with a moving magnet [10]

Figure 2.4 shows an example of electromagnetic resonant harvester that can be used to extract electrical power from vibration. In this type of harvester, the maximum output power is achieved when the resonant frequency of the harvester matches the input frequency. If the input frequency is outside the range of the harvester, the output power will drop significantly. This makes this type of harvester not useful when the input frequency changes over time. An alternative to the resonant system is the non-resonant harvester.

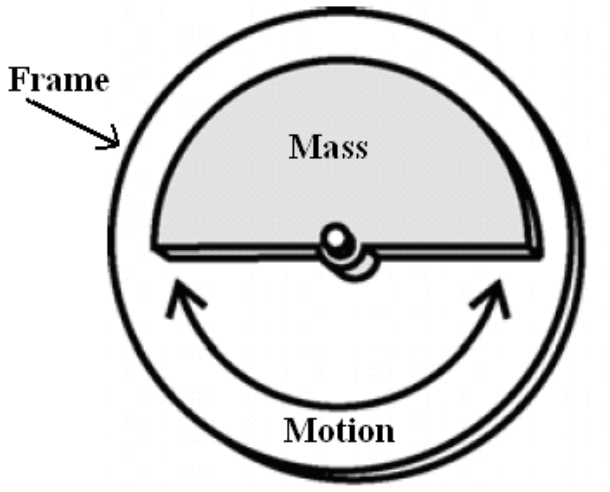

Figure 2.5 A schematic of the basic structure of a non-resonant rotating harvester [12].

In a non-resonant electromagnetic harvester the spring, that connects the mass to the frame, is omitted. As discussed before, the output power in a linear inertial scavenger is proportional to the internal travel of the mass. Therefore, Yeatman [12]

tried to overcome this limit by eliminating the range constraint on the internal motion by using rotating proof mass motion. In this case, the mass can rotate in either case without a mechanical limit. He reported that the rotating mass could be powered by linear or rotational host motion. A schematic of non-resonant rotating harvester, where a semicircular mass rotates freely on a bearing, is shown in Figure 2.5.

The energy extracting mechanism in this transducer is denoted by a torque applying coupling between the frame and the rotating mass. The maximum power can be achieved when the damping torque equals the product of the mass moment of inertia and the frequency of the source motion. The damping torque, on the other hand, is proportional to the relative rotational velocity between the mass and the frame. The author noted that for low damped cases, the mass motion is small and thus the relative motion between the mass and the frame. However, for a strongly damped case, the relative motion between the frame and the mass equals zero. In both cases, the power approaches zero.

Yeatman [12] compared the output power of his harvester with the one that has a mass with linear internal motion. Both types of harvesters were based on electromagnetic transduction, as the only existing rotating devices use electromagnetic conversion. Moreover, both devices were driven by harmonic linear excitation. The author concluded that for a given mass and linear travel range, the extracted power from the transducer will be the same whether the mass movement is linear or rotating. The choice between these techniques depends on the application reliability and cost. Moreover, both systems can be used over a wide range of input frequencies.

The transducer developed by Yeatman can extract power from rotational excitation when an eccentric mass is used in the system. In this case, the frame rotates and the extracted power depends on the relative velocity between the frame and the mass. Two types of torque will be generated; damping torque and gravitational torque. The maximum power will be extracted when these torques are equal because the mass remains static. In this case, the output power is proportional to the rotation speed. The author describes the motion of the mass as highly nonlinear if the damping and the gravitational torques are not equal. This is due to the fact that gravitational torque depends on the rotational position of the mass. For this analysis, the semi-circular mass rotates freely on a bearing located in the centre of the rotating frame. However, because the rotational mass depends on the gravitational torque rather than the inertial mass, the performance of the transducers is dependent on their orientation. Two different

configurations based on electromagnetic transduction that were developed based on the concept of a rotating mass are presented in the following paragraphs. The ability of using them to extract power from rotating object is addressed.

The harvester, designed by Spreemann et al [13] was aimed at converting linear vibration into rotary motion using a non-resonant electromagnetic harvester. For this harvester the output power depended on the vibration amplitude, the harvester geometry and the initial conditions. This harvester, which is shown in Figure 2.6, converted the linear vibration into a rotary motion. The harvester was designed to operate under small vibration amplitudes, i.e. 100 μm. This harvester was modelled as a damped mechanical pendulum where the effect of initial conditions and the harvester geometry were analysed. It was found that if the length of the pendulum was one order of magnitude greater than the vibration amplitude or more, an initial angular velocity was required to start the rotation motion. This initial rotary frequency should be the same order of magnitude as the vibration frequency. Once the initial rotary frequency was applied, the pendulum performed a rotation driven by the applied vibration. At this point the rotation frequency followed the vibration frequency and its value changes proportionally to the rotary frequency.

If the vibration amplitude was in the same order of magnitude as the pendulum length, the energy from vibration was enough to start the rotation without the initial rotary frequency. In this situation the system showed undetermined chaotic behaviour. The advantage of this harvester is that, the output power is proportional to the square of the rotating angular velocity. This means the output power increases by increasing the input vibration. Moreover, the maximum output power is generated when the output load resistance equals the coil resistance (20 Ω). A harvester with a volume of 1.5 cm^3, a mass of 2.85 grams, a pendulum length of 5.62 mm and frequency amplitude of 100 μm at vibration frequencies ranging from 30 to 80 Hz generated an output power ranging from 0.4 mW to 3 mW. The authors did not present the effect of applying a vibration amplitude that is one order of magnitude higher than the pendulum length or more. The disadvantage of this design is that its behaviour starts to get chaotic when the pendulum length is less than the vibration amplitude. Therefore, this system is not suitable to be used when the input vibration amplitude is higher than the pendulum length.

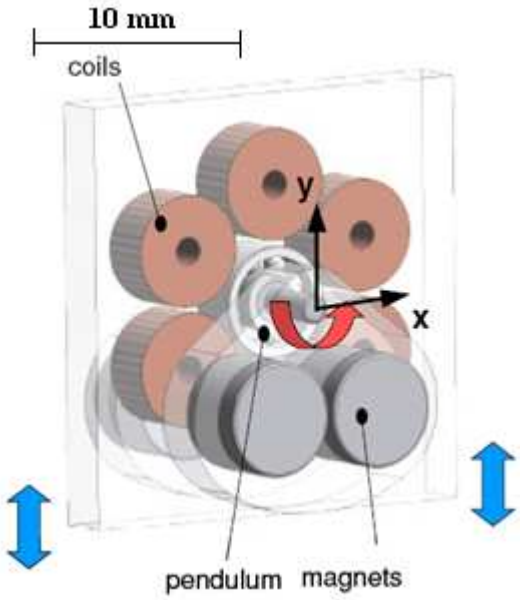

Figure 2.6 Converting the linear vibration into rotary motion, non-resonant electromagnetic harvester [13]

The authors did not simulate the effect of rotation on the movement of the pendulum. Therefore, in the next paragraph a discussion about the possibility of using this type of harvester to harvest energy from rotating objects is presented. For this application, the energy harvester device shown in Figure 2.6 is positioned at a specific distance from the centre of rotation. The simulation software Working Model is used to predict the behaviour of the pendulum movement. The behaviour of the pendulum movement when its length is an order of magnitude less than the radius of rotation can be summarised in the following paragraph. Using the rotating object as a frame of reference, at low rotating speeds the pendulum movement can be described as pure rotation (below 3 rps). Increasing the rotating speed any further causes the pendulum to oscillate. The amplitude of the oscillation movement reduces as the rotating speed increases. Therefore, this harvester is suitable to be used when the rotating object operates at low rotating speed.

Another electromagnetic transducer configuration based on a non-resonant system is analysed and tested by Tzern et al [14]. This harvester is based on generating output power from rotation. The generic rotating harvester consisted of stator and a rotor. The relative movement between these two components converted the mechanical energy into electrical energy. The group who developed this harvester proposed that such a harvester can be used to power a tyre pressure monitoring sensors located inside the vehicle tyre. For this experiment, a DC motor is used as a harvester as show in Figure 2.7. The rotor of the harvester is coupled to the rotating source. To prevent the

outer housing of the harvester (stator) from rotating along with the rotor, an offset mass from the axis of rotation is added to the stator. In order for the host to act as a stator the magnetic torque should be equal to the gravitational torque. The flip-over speed by which the stator starts to rotate with the rotor is calculated. As the output power equals the rotational angular velocity squared, the team added a gearbox between the rotating source and the harvester in order to increase the angular speed and thus the output power. This harvester, which uses a 20 gram mass, produced an output power of 8 mW at 477 rpm. Tzern at al [14] discuss the possibility of mounting the harvester off-axis. In this situation the centripetal force tended to throw the mass attached to the harvester host outwards and affect the gravitational force. Therefore, increasing the offset position of the harvester will result in reduced output power. For a 10 cm offset position, it has been found that the stator starts to flip over and when the rotating speed reaches 280 rpm the motion of the stator is almost synchronized with the rotor motion. This means no output power is generated.

This harvester is more suitable for application where there are no size or weight restrictions on the harvester. In addition, this harvester is more suitable to be used when the centre of rotation is aligned with the harvester's centre of rotation. Moreover, it is more preferable to design a harvester that has the ability to produce an output power at any value of the offset position from the centre of rotation.

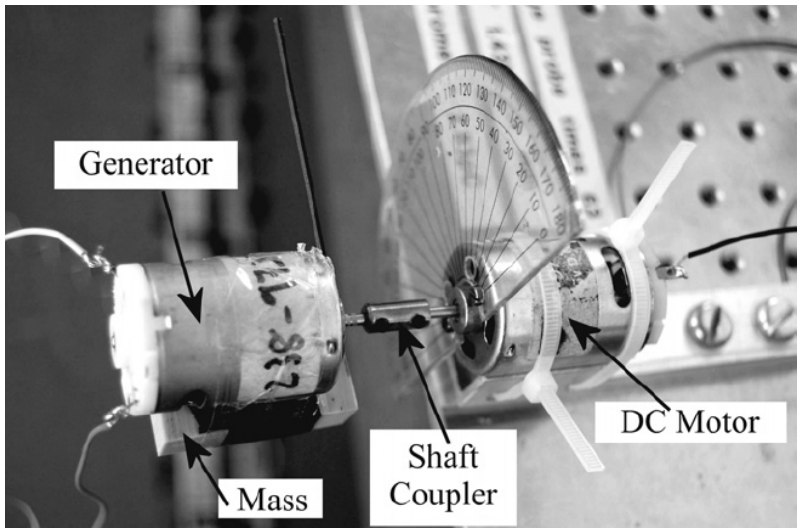

Figure 2.7 Setup to generate power from rotation using electromagnetic harvester [14]

Holmes et al [15] designed, simulated, fabricated and tested an axial-flux permanent magnet electromagnetic harvester based on a rotating harvester. The idea of this device is that it generates power from an externally generated gas flow. The harvester comprises of a polymer rotor with embedded permanent magnets sandwiched

between two silicon stators with electroplated planar coils. This harvester is shown in Figure 2.8. The device has a volume of 0.5 cm^3 and it has the capability of generating up to 1 mW at a pressure drop of 8 mbar, a flow rate of 35 litres per minute and rotation speed of 30000 rpm. This type of transducer is more suitable if there is a gas flow in the surrounding environment. Moreover, this device is expensive to fabricate because it involves many manual assembly and bonding operations due to the design of this device. The reliability of using this device over high cycle of operation was not presented in this paper.

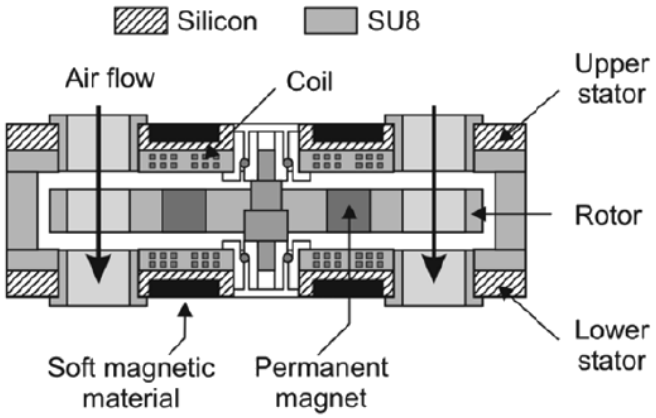

Figure 2.8 Schematic cross section of axial-flow turbine with integrated axial-flux electromagnetic harvester [15]

2.2.2.2 Electrostatic harvesters

Electrostatic harvesters consist of two conductors (plates) separated by a dielectric such as air. This type of converter needs to be charged up to an initial voltage for the conversion process to start. This can be done by using a separate voltage source, which means electrostatic energy harvester can hardly become a separate power supply. This voltage creates an equal but opposite charge q on the plates, leading to the storage of a charge when the voltage source is disconnected. The variable capacitor is the basis of the power conversion. As the conductors move relative to each other, the energy stored in the capacitor changes, thus providing the mechanism for mechanical to electrical conversion. The voltage across a simple rectangular parallel plate capacitor is given by the following equation:

$$V = \frac{q}{C} \qquad 2.6$$

where q is the charge on the capacitor and C is the capacitance, which is given by the following equation:

$$C = \frac{\varepsilon L w}{d} \qquad 2.7$$

where d is the distance between the plates, w is the width of the plates, L is the length of the plates and ε is the permittivity of the material between the plates. The energy stored in a capacitor is given by:

$$E = \frac{1}{2} qV = \frac{1}{2} CV^2 = \frac{q^2}{2C} \qquad 2.8$$

This equation demonstrates that the energy can be increased by increasing either q or V. If the charge is held constant, the voltage can be increased by either reducing the area of the plates or increasing the gap between the plates. However, if the voltage is held constant, the charge can be increased by either increasing the area of the plates or reducing the gap between the plates. The work done against the electrostatic force acts between the plates provides the harvested energy. Therefore, the inertia electrostatic transducer can be operated under constant charge or constant voltage. Electrostatic transducers can be divided into two groups depending on the movement of the mass as described by Roundy et al [16]. In the first group, the movement of the mass is out of the wafer plane as shown in Figure 2.9.

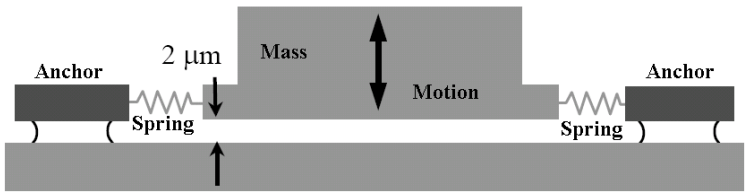

Figure 2.9 Out-of-plane electrostatic transducer (after [16]).

For this group the input force changes the gap between the capacitor plates (out-of-plane gap closing). However, in the second group, the movement of the mass occur in the plane of the wafer. For this group the input force changes either the gap between the capacitor plates (in-plane gap closing) Figure 2.10 or the overall area (in-plane overlap) Figure 2.11.

The change in the capacitance in the in-plane overlap is linear with the mass displacement, whereas this relationship is non-linear in the in-plane gap closing. However, the in-plane gap closing is easier to fabricate than the in-plane overlap transducer. Moreover, Roundy concluded that the in-plane gap closing produces more

power than in-plane overlap because it does not suffer from excessive parasitic damping. The value of parasitic air damping in out-of-plane gap closing operating under constant charge is higher than the in-plane types. This is based on the assumption that the gap between the plates must be as small as possible to produce high output power, as the output power is proportional to the damping force and this force is proportional to $1/d^3$. Reducing the gap between the plates reduces both the parasitic capacitances and priming voltage. However, as a MEMS device, the out-of-plane gap closing is harder to fabricate than the in-plane types.

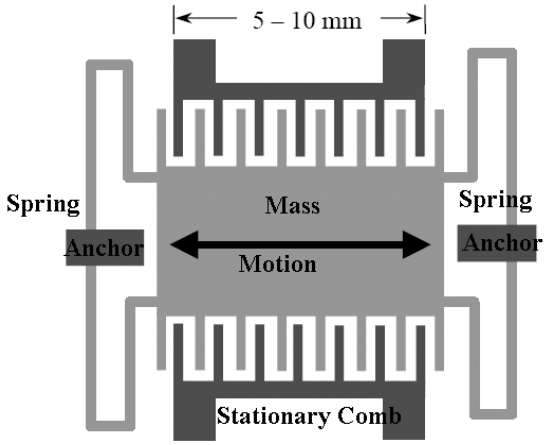

Figure 2.10 In-plane gap closing electrostatic transducer (after [16]).

In constant charge electrostatic transducers, the generated energy is proportional to the ratio between the initial capacitance C_1 and final capacitance C_2 [17]. By setting the holding force to be as high as possible, it has been found that the constant charge device has higher initial capacitance than the constant voltage one. Having higher initial capacitance reduces the voltage required to obtain the holding force and thus reduces the pre-charge voltage. Moreover, it has been found that it is easier to get higher values for the initial capacitance in the gap-closing electrostatic transducer than in the overlap one. This is due to the fact that a small gap can be set between the plates of the capacitance by using a mechanical stop for the initial and final separation between the two plates. In the overlap electrostatic transducer, suspension is used to maintain the separation between the plates over the whole range of travel.

Despesse [18] presented an in-plane gap closing structure that produced a scavenging power of 1mW for a vibration amplitude of 90 μm at 50 Hz (acceleration of 8.8 ms^{-2}). The size of the device was 18 cm^2 with 104 g inertial mass. This design used a piezoelectric spring to prime the electrostatic transduction. A honeycomb structure

was described by Tashiro et al [19]. This structure has a variable capacitance between 110 and 32 nF. After charging the capacitor to 45 V from a battery, the harvester was put on a shaker. A power of 36 μW was harvested form acceleration amplitude of 1 ms^{-2} at 6 Hz, which is the resonant frequency of the device.

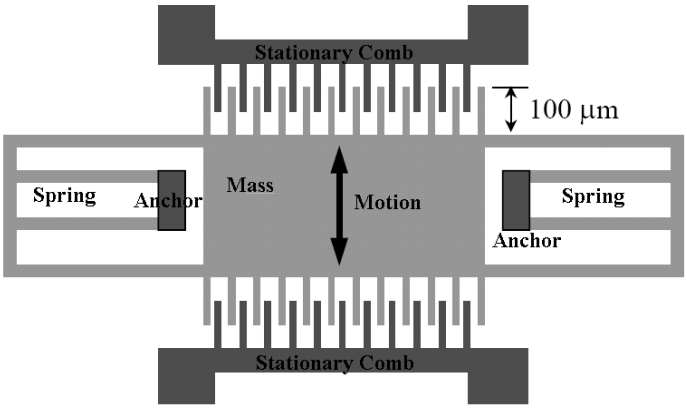

Figure 2.11 In-plane overlap electrostatic transducer (after [16]).

Mitcheson et al [20] described the benefit of using a non-resonant electrostatic transducer. This research group carried both simulation and experimental work. For non-resonant electrostatic transducer the spring constant was set to zero. Therefore, the device is not tuned to a specific resonant frequency. The mass forms one of the capacitor's plates. A holding force or electrostatic force is created due to pre-charging the capacitor which operates under constant charge or constant voltage. The conversion of energy starts when the frame acceleration is greater than the holding force. This forces the mass to move relative to the frame. If the damping force is at its maximum value, the mass moves from one end of the frame to the other at the peak of the frame acceleration and thus produces the maximum output power.

For an application where it is necessarily to operate across a wide range of excitation frequencies Yeatman [21] proposed a non-resonant electrostatic harvester (Figure 2.12). In this harvester, the mass is held in place by pre-charging it using a separate power supply. The generated electrostatic force between the two plates of the capacitor keeps them at certain distance from each other. When the applied force is high enough to overcome the electrostatic force, the mass accelerates to the other side of the frame and discharges its energy. The suspensions are made from polyimide to give low suspension stiffness to avoid resonant effects. These suspensions work as electrical contact and mechanical stop. This device can be used for wide range of input motion. The output voltage waveform is in the form of pulses. Therefore, a circuit is required to convert the output to a DC signal.

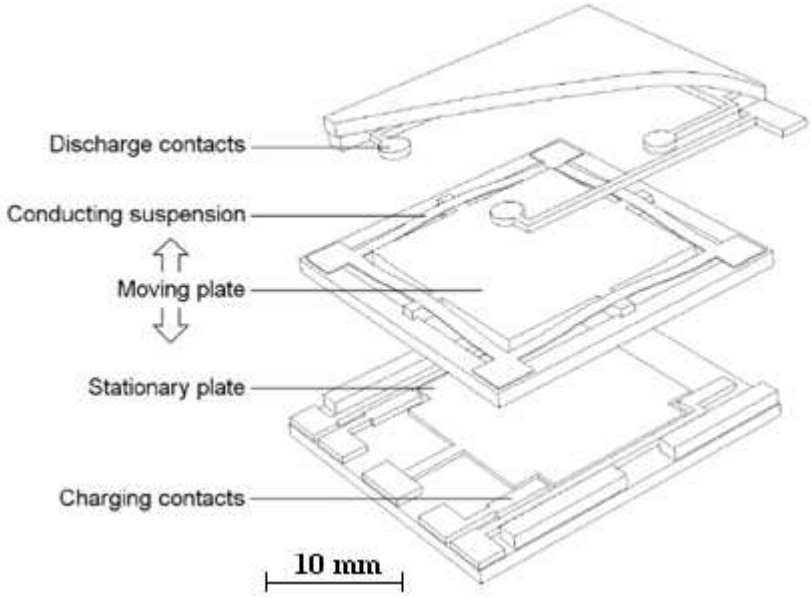

Figure 2.12 Non-resonant electrostatic harvester [21].

2.2.2.3 Piezoelectric harvesters

The piezoelectric effect was discovered by Jacques and Pierre Curie in the 1880's. They found that if certain crystals were subjected to a mechanical strain, the crystalline structure would generate a voltage proportional to the applied pressure. Conversely, these materials would deform when they were exposed to an electric field.

Motion driven piezoelectric transducers can be divided into two main groups: resonant and non-resonant systems. In the case of resonant system the piezoelectric material can take a shape of a beam rigidly supported at one end with an attached mass to the free end of the beam. The mass inertia results in a relative displacement when the frame accelerates due to the input force. In the case of non-resonant system, the spring constant is zero leading to direct force on the damper. This means a mechanical contact occurs between the two objects that move relative to each other which are the mass and the piezoelectric material. A detailed description of some of the developed prototypes of the piezoelectric harvesters are presented and discussed in Section 2.6.4 and Section 2.6.5. This includes resonant and non-resonant piezoelectric harvesters. Piezoelectric harvesters have the simplest structure among the three different types of electromechanical harvesters presented in this chapter. However, the properties of the piezoelectric material decay and change over time. This limits the overall performance of the harvester.

2.2.3 Comparison of transduction method

For a resonant electromagnetic transducer, the output power is proportional to the damping force. This force is proportional to the mass internal velocity. This means this harvester is more suited for higher frequency applications and the maximum power can be achieved when the harvester is tuned to operate at the applied frequency. Moreover, the optimal damping is the one that allows the mass to use all the internal available displacement and thus maximum power can be extracted. The optimal damping factor is given by the following equation [22], where Z_l is the mass displacement and Y_o is the input acceleration amplitude:

$$\xi = 0.5\frac{y_o}{Z_l} \qquad 2.9$$

As it has been explained in Section 2.2.1 the lower the value of the damping ration (ξ), the more power will be extracted at the resonant frequency. Therefore, for this type of harvester, the available mass displacement must be higher than the acceleration amplitude.

For non-resonant electromagnetic transducers, especially at low frequencies, the damping force must be maximized to increase the output power. Increasing the damping force requires rapid flux changes. A slow moving mass requires a larger number of coil turns, which increases both the coil resistance and the required magnetic flux. This is difficult to achieve in small geometries. In general electromechanical harvesters that are designed to power sensors node produce output voltages of less than 1 V. Therefore, this value should be stepped up to be used in standard electronics circuit. This can be achieved either by designing an electronic circuit to improve the output voltage [22, 23] or by increasing the effective length of the harvester's conductor. As the output voltage increases proportionally to the effective length of the conductor, this length can be improved by increasing the coil turns. By increasing the length of the coil it will become more difficult to fabricate and more expensive. Moreover, increasing the coil turns requires a larger volume of magnets to increase the flux present in the air gap between the two poles of the magnet.

Electrostatic harvesters provide high output voltage that might reach a few hundred volts. This value must be reduced in order to be used in suitable for powering low-power systems. Moreover, electrostatic harvesters suffer from parasitic capacitance in parallel with the harvester, which reduces the output power. Therefore, the designed

circuit that connects between the load and the harvester has two challenges: reducing the output voltage and minimizing the parasitic capacitance [24]. The holding force in the electrostatic transducer depends on both the applied voltage and on the rate of change of the capacitance. Dealing with high voltage in the range of tens of volts is undesirable in low-power circuits. Moreover, electrostatic transducers require a pre-charge or priming voltage to start the conversion between mechanical and electrical energy. However, electrostatic harvesters are easy to integrate into electronic circuits.

For resonant piezoelectric transducers, harvesters based on beam theory are available commercially [25]. For non-resonant harvesters, especially at low frequencies, increasing the damping is the main factor to improve the output power. The output impedance of a piezoelectric transducer is dominated by the device capacitance, which is in the range of nF. Therefore, to maximize the output power the optimum load must match the magnitude of the capacitance impedance $1/\omega C$. Piezoelectric harvesters are attractive because the generated output voltage is in the range which is suitable to be used directly in a rectifying circuit. Moreover, different types, shapes and properties of piezoelectric harvesters are available commercially. The piezoelectric structures that are used to generate an output power are simple in comparison with the electrostatic and the electromagnetic harvesters. Moreover, the piezoelectric harvesters do not require an external voltage source as is the case with the electrostatic one. Piezoelectric harvesters need to be strained to generate power. Therefore, their mechanical properties limit their performance and the lifetime of the harvesters.

Beside the ultimate power limit, practical consideration must be taken into account when the suitable type of electromechanical harvester is chosen. As discussed in Section 2.2.1, a non-resonant electromechanical harvester is more suitable to generate power from a rotating object in comparison with resonant systems. The chosen type should obey some criteria such as ease to manufacture, low cost and high reliability. Non-resonant electromagnetic harvesters are more expensive to fabricate than the other two technologies. Non-resonant electrostatic transducers require separate pre-charge or priming voltage to start the conversion. Parasitic capacitance is one of the problems in this type of devices. Another problem is the leakage of the capacitor or the battery that will be used to pre-charge the harvester. Moreover, this type of harvester requires a mechanical constraint to stop the two plates from coming in contact with each other under the applied force.

The non-resonant piezoelectric harvester has the simplest structure in comparison with the electrostatic or the electromechanical harvesters. Therefore, a non-resonant piezoelectric transducer is chosen in this work. For a non-resonant device the conversion of energy happens when the piezoelectric element deforms due to the applied force. The external force can be applied on the piezoelectric structure directly (impact force) or indirectly. This creates some challenges including choosing the right type of the piezoelectric material and the right shape of the piezoelectric structure in order to produce the maximum power as well as provide high mechanical stability. Understanding the behaviour of the harvester under the applied force and its reliability are challenges that will be addressed in the future work.

2.3 Extracting energy from rotation

This section highlights the fundamental knowledge about rotation and demonstrates its ability to be used as a source of energy. In an effort to generate power from a rotating object, its rotational motion is analysed. Due to the rotational motion, two types of acceleration are generated; radial and tangential. The aim of the study is to understand the effect of these accelerations on a harvester mounted on the rotating object at a certain distance from the centre of rotation. The polar coordinate system is the most intuitive way to describe circular motion, where the position of the particle along the path is described by two quantities; R and θ. R is the radial distance of the object from the origin O. The angle θ is defined as the angle which the vector makes relative to an arbitrary direction. Two units vectors can be defined $\mathbf{e_r}$ and $\mathbf{e_\theta}$. The radial unit vector $\mathbf{e_r}$ always points radially outwards. Moreover, the tangential $\mathbf{e_\theta}$ unit vector is always normal to $\mathbf{e_r}$ in the direction of increasing θ as shown in Figure 2.13.

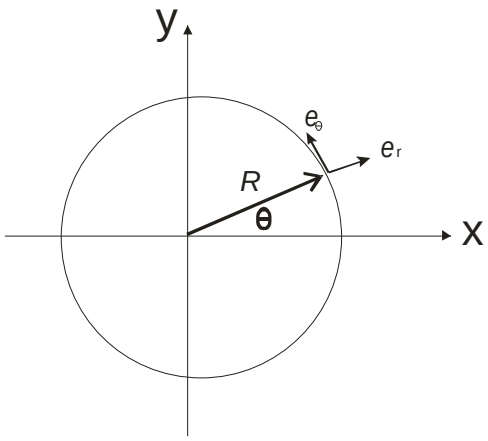

Figure 2.13 Polar coordinates

These unit vectors can be described in a Cartesian coordinate as following

$$\boldsymbol{e_r} = \cos(\theta)\mathbf{i} + \sin(\theta)\mathbf{j} \qquad 2.10$$

$$\mathbf{e_\theta} = -\sin(\theta)\mathbf{i} + \cos(\theta)\mathbf{j} \qquad 2.11$$

where **i** and **j** are unit vectors that points in the same direction as the x and y axes. The position vector **R**, which designates the location of an object moving in a circular motion around an axis, can be represented as:

$$\mathbf{R} = R\cos(\theta)\,\mathbf{i} + R\sin(\theta)\,\mathbf{j} \qquad 2.12$$

The velocity of the object can be given by the following equations:

$$\mathbf{v} = \frac{d}{dt}\mathbf{R} = -R\frac{d\theta}{dt}\sin(\theta)\,\mathbf{i} + R\frac{d\theta}{dt}\cos(\theta)\,\mathbf{j} \qquad 2.13$$

$$\mathbf{v} = \underbrace{R\frac{d\theta}{dt}}_{v}\underbrace{(-\sin(\theta)\mathrm{i} + \cos(\theta)\mathrm{j})}_{e_\theta} \qquad 2.14$$

The velocity vector is defined by speed and also by the direction of motion. The first term represents the magnitude (v). The second term represents the direction of the velocity vector, which is the same direction as $\mathbf{e_\theta}$. This means the velocity vector is always perpendicular to the position vector as shown in Figure 2.14.

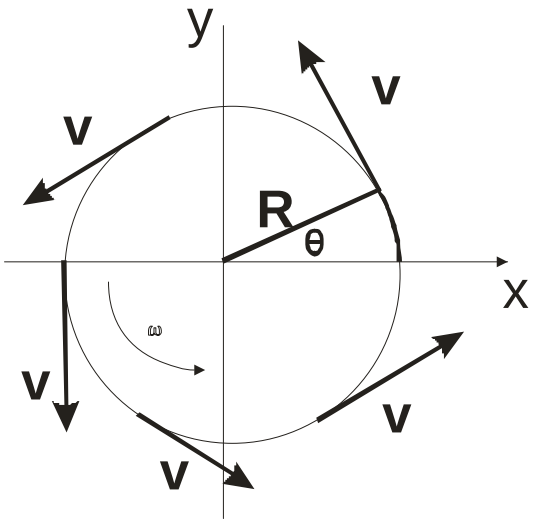

Figure 2.14 The direction of the velocity vector

This vector may change in magnitude by speeding up or slowing down. However, it always changes its direction as shown in Figure 2.14. The result is two different types of motion non-uniform and uniform circular motion. Non-uniform circular motion is a case in which both the magnitude and direction of **v** are changing, because an object

moves in a circular path has a varying speed. However, in uniform circular motion, where an object moves with constant speed along a circular path, the direction of **v** is constantly changing and its magnitude remains constant.

Acceleration is the rate change in velocity and can be obtained by differentiation of the velocity vector and can be given by the following equation:

$$\mathbf{a} = -R\frac{d^2\theta}{dt^2}\sin(\theta)\mathrm{i} + R\frac{d^2\theta}{dt^2}\cos(\theta)\mathrm{j} - R\left[\frac{d\theta}{dt}\right]^2\cos(\theta)\mathrm{i} - R\left[\frac{d\theta}{dt}\right]^2\sin(\theta)\mathrm{j} \qquad 2.15$$

$$\mathbf{a} = -R\left[\frac{d\theta}{dt}\right]^2\underbrace{\{\cos(\theta)\mathrm{i} + \sin(\theta)\mathrm{j}\}}_{\mathrm{e_r}} + R\left[\frac{d^2\theta}{dt^2}\right]\underbrace{\{-\sin(\theta)\mathrm{i} + \cos(\theta)\mathrm{j}\}}_{\mathrm{e}_\theta} \qquad 2.16$$

As the angular velocity (ω) equals to $\frac{d\theta}{dt}$ and $\frac{v}{R}$; therefore, the above equation becomes:

$$\mathbf{a} = \underbrace{-\frac{v^2}{R}}_{\substack{\textit{Radially}\\ \textit{inward}}}\mathbf{e_r} + \underbrace{\frac{dv}{dt}}_{\textit{Tangential}}\mathbf{e_\theta} \qquad 2.17$$

The first term is the centripetal acceleration a_{cp}. This acceleration is always perpendicular to the direction of motion. The negative sign indicates that the direction of this acceleration is towards the centre of the circle, opposite to the direction of $\mathbf{e_r}$. The second term is the tangential acceleration $a_t = \frac{dv}{dt}$ in the $\mathbf{e_\theta}$ direction. This acceleration is caused by a change of speed. If the object speeds up, a_t is in the direction of motion $+\frac{dv}{dt}$. If the object slows down, a_t is opposite to the direction of motion $-\frac{dv}{dt}$. In addition, if the speed is constant a_t is zero. Although the object has a constant speed, its direction always changes due to the centripetal acceleration. In this case the centripetal acceleration has constant magnitude. However, its direction is always changing. For non-uniform circular motion, the total acceleration has a magnitude of $a = \sqrt{a_t^2 + a_{cp}^2}$ and its direction can be seen in Figure 2.15

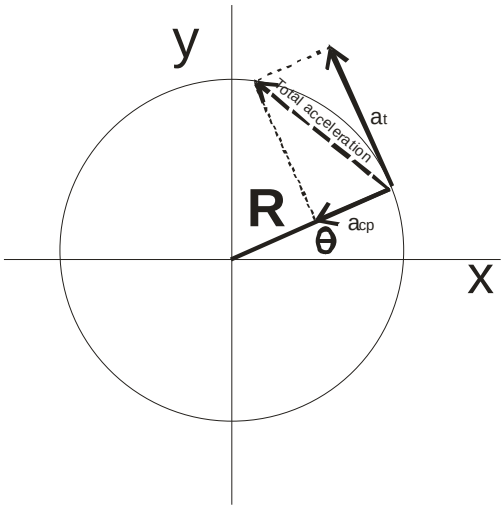

Figure 2.15 Total acceleration for non-uniform motion

The momentum **P** of a particle at any time (t) is a vector, which is defined as the product of the mass (m) of the particle and its velocity:

$$\mathbf{P} = m\mathbf{v} \tag{2.18}$$

Newton's second law of motion states that the rate of change in momentum of a moving object equals the resultant force and it is in the direction of that force.

$$\sum \mathbf{F} = \frac{d}{dt}\mathbf{P} = m\frac{d}{dt}\mathbf{v} \tag{2.19}$$

For the derivative of the product $m\mathbf{v}$, the Newton's second law can be written as following, where m is constant:

$$\sum \mathbf{F} = m\frac{d}{dt}\mathbf{v} = m\mathbf{a} = = \underbrace{-\frac{mv^2}{R}}_{\substack{Radially \\ inward}} \mathbf{e_r} + \underbrace{\frac{mdv}{dt}}_{Tangential} \mathbf{e_\theta} \tag{2.20}$$

Where m is the mass, and **a** is the net acceleration of the object. An object moving in a non-uniform circular motion has two acceleration components tangential and radial. The result is two force components acting in the same direction as the tangential and radial acceleration directions. The total force acting is the vector sum of the radial and the tangential components. In uniform circular motion, the velocity is constant. Therefore, $\frac{dv}{dt} = \frac{d\omega}{dt}$ equals to zero. Thus, in uniform circular motion, the magnitude of the tangential acceleration is always zero and the only force is acting on the rotating object is the centripetal force, which can be expressed as:

$$\sum \mathbf{F} = m\mathbf{a} = = \underbrace{-\frac{mv^2}{R}}_{\substack{Radially \\ inward}} \mathbf{e_r} = -m\omega^2 R\,\mathbf{e_r} \qquad 2.21$$

This force is constant in magnitude and it always acts opposite to the direction of the radius vector unit. The maximum work on the harvester is achieved when the direction of the applied force is in the same direction as the free movement of the harvester. In this situation maximum power will be extracted. Therefore, the method by which the harvester is mounted at the rotating object affects the amount of the generated output power as explained in Section 4.3.

An object moving in a non-uniform circular motion has two force components acting in the same direction as the tangential and radial acceleration directions. However, in uniform circular motion the only force is acting on a rotating object is the centripetal force. Therefore an object located at a distance *R* from the centre of rotation is always under a centripetal force. Therefore, this force has a potential to be the main source of generating electrical power.

The number of revolution per seconds (f) that a rotating object is doing can be calculated using the following equation:

$$f = \frac{\omega}{2\pi} \qquad 2.22$$

On the other hand, the angular velocity (ω) is given by the following equation, where *v* is the linear velocity:

$$\omega = \frac{v}{R} \qquad 2.23$$

The magnitude of the centripetal force is given by the following equation:

$$|F| = \frac{mv^2}{R} \qquad 2.24$$

Substituting equation 2.22 and equation 2.23 into equation 2.24 and rearranging terms yields the following equation:

$$|F| = 4\pi^2 mRf^2 \qquad 2.25$$

Equation 2.25 shows that the applied force on the object is directly proportional to the object mass and the distance between the object and centre of rotation when *f* is constant. Therefore, the further the object is mounted from the centre of rotation, the

more force that the object will be subjected to. Therefore, if a harvester is using the centripetal force to generate power, it should be mounted as far as possible from the centre of rotation. However, this applied force is proportional to the square of *f* when both *R* and *m* are kept constant.

2.4 Harvesters that generates power from rotation

All the harvesters that extract energy from rotation and presented in the literature are electromagnetic as mentioned in Section 2.2.2.1. The output power from these harvesters reduces when the rotating speed reaches a certain value due to the effect of the centripetal force. At high rotating speed this force reduces the relative velocity between the coil and the magnet causing a reduction in the output power. The aim of this research is to develop a piezoelectric harvester that generates a predictable amount of energy using centripetal force.

2.5 Applications by which rotation is a source of energy

The type of harvester that extracts power from rotation can be the source to power sensors that are mounted on a rotating object at a certain distance from the centre of rotation. Tyre pressure sensors are one of these examples which is discussed in Section 2.5.1.

2.5.1 Vehicle tyre pressure

Over the last few years, the safety and the reliability of different parts of a vehicle have improved due to the growth of the vehicle market. Tyres perform multiple tasks including carrying the vehicle load, transmitting mechanical input, rolling smoothly and providing grip for braking, steering and acceleration. Therefore, they must be kept in good condition and their pressure must be regularly checked.

If the tyre pressure is less than the recommended one, the vehicle wheel rolling resistance increases causing more fuel consumption and accelerating the wear of the tyre's tread. Moreover, under-inflated tyres reduce the vehicle's handling stability, affect the braking performance by increasing the stopping distance and produce excessive heat that damages the tyre [26]. In addition, an under-inflated tyre increases the fuel consumption and hence creates more air pollution. Moreover, if the tyre is 30

% under-inflated, the tyre life will be reduced by 50 % [27]. Over-inflated tyres, on the other hand, cause poor grip and reduce the vehicle stability when braking and cornering. In summary, correct tyre pressure not only increases the lifetime of the tyre, but also reduces the fuel consumption. According to Tyre Industry Council, 90 % of all vehicles on the road have at least one tyre at the wrong pressure [28]. This is due to the fact that tyres can be more than 20 % under-inflated before the drivers realises it. Therefore, drivers should perform regular tyre checks at least once every week and especially before long journeys.

Different types of gauge can be used to check the tyre pressure manually including a pencil gauge [29]. Another method of checking the tyre pressure is using Tyre Pressure Monitoring System (TPMS) [30, 31]. This device, which is mounted inside the vehicle tyre, provides an automatic method of informing the driver with the pressure status of each tyre. The measured data from TPMS sensors located inside the tyres is sent using RF signals to a receiver on the vehicle's dashboard [32]. The receiver decodes and presents the pressure within each wheel to the driver. Mounting the pressure sensor directly inside each tyre is achieved by either fitting it to the inside end of the tyre valve (Figure 2.16 (a)) or on the bed rim using a stainless steel clamp (Figure 2.16 (b)). Each of these sensors needs a power source. At present, most of them are powered by a 3V lithium battery. Because of the finite battery life, different approaches have been used to reduce the power consumption. This can be achieved by using extra hardware to detect the mechanical situation of the vehicle and thus turn the system off when the vehicle is stationary or if both the pressure and temperature measurements have not changed significantly [33]. Designing low power wireless sensors is another method to reduce the power consumption. In current systems on the market, both the sensor and the transmitter are powered by batteries while the receiver, fixed on the dashboard, is powered by the vehicle power supply (Figure 2.17).

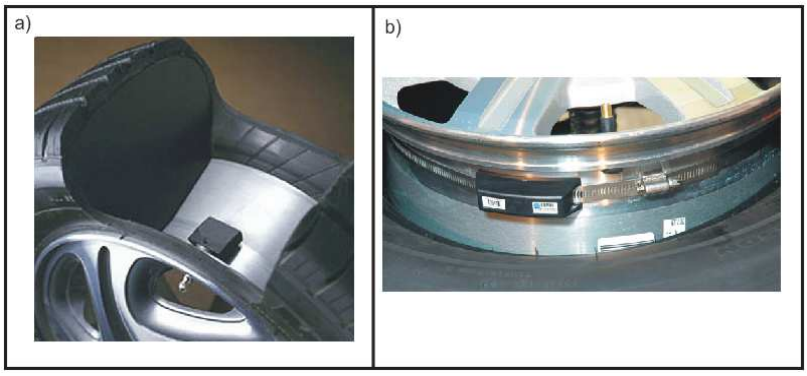

Figure 2.16 a) Transmitter by Schrader Electronics b) Transmitter by SmarTyre [30, 31].

The aim of this research is to generate power from rotation. The harvester will be mounted on the rim. This means the developed harvester in this work has the potential to power TPMS which is fixed on the rim of the vehicle wheel. Both impact based and non-contact piezoelectric harvesters will be developed in this research and their suitability for this application will be discussed in Section 8.3.

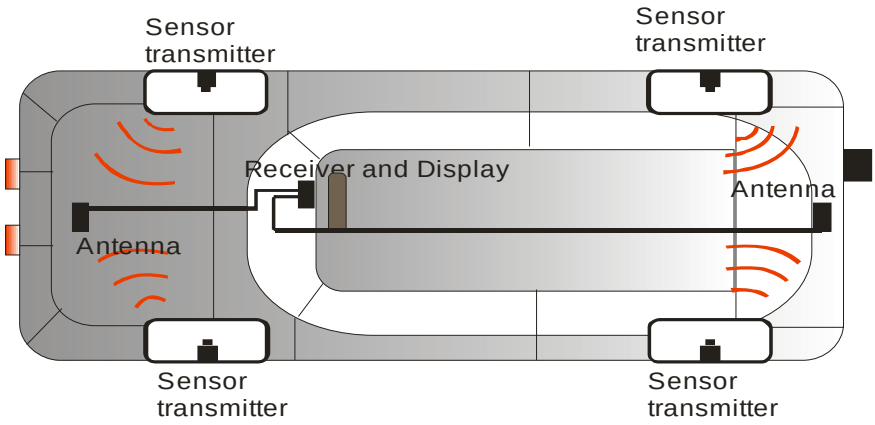

Figure 2.17 Pressure monitoring system

2.5.2 Generating power from the vehicle wheel

Périsse [2] investigated the tyre-road interaction and radial vibration of a vehicle tyre rolling on a smooth and rough surface. Experimental measurements were performed on a rolling smooth tyre with test laboratory facilities. The tyre axis was fixed in space and the tyre belt was in contact with a rotating drum. Two types of drum surfaces were used; a smooth and rough surface. Radial vibrations were measured through a piezoelectric accelerometer mounted on the interior surface of the tyre. The author determined that compression forces and shearing forces were the two excitation mechanisms in the contact zone. Compression forces are produced by the roughness of the road surface and the tread patterns. However, the existence of shearing forces was due to the contact friction. The radial accelerations of a loaded tyre rolling on a rough surface were divided into stationary and non-stationary radial accelerations. It was found that, at low frequencies, stationary accelerations dominated over the non-stationary vibrations. In the middle frequencies range the non-stationary vibrations were dominant. Stationary radial accelerations were generated due to the tyre surface deformation in the contact zone. In the time domain the signal from stationary acceleration was periodic and its magnitude and frequency depended only on the velocity and did not depend on the tread or road surface. Theoretically, for a smooth

tyre rotating on a smooth road, the shape of the acceleration signal for one revolution is shown in Figure 2.18. It was found that, by increasing the velocity, the length of the positive and negative peaks would increase. However, the width of the negative peak would reduce by increasing the speed due to the reduction in the contact length.

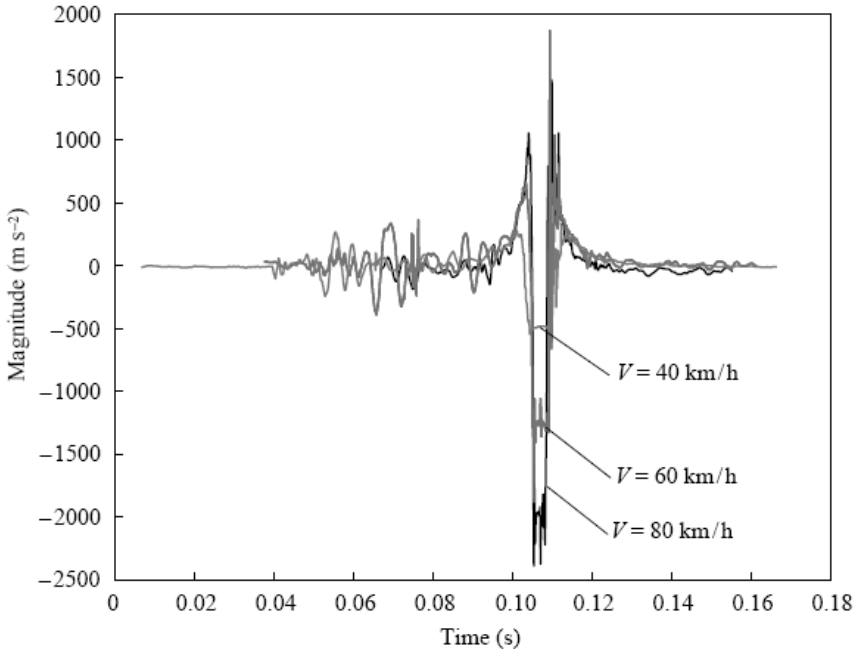

Figure 2.18 Radial stationary acceleration due to the tyre-road connection [2]

Unlike the stationary accelerations, non-stationary vibrations depended on the velocity and both the road and the tyre tread surfaces. For a tyre rolling on a rough surface, stationary accelerations were superposed with the non-stationary vibrations as shown in Figure 2.19.

Analysing the measurements in the frequency domain showed that the energy spectrum due to radial accelerations is mainly contained in the frequency range < 500 Hz. This frequency range is extended with increasing speed. An important observation was that the magnitude of the tread acceleration response is bigger than that of the sidewall for frequencies above 500 Hz due to high material damping. Because vibration energy is concentrated in the contact area, Périsse suggested that the contact zone between the tyre and the road surface is the best place for mounting an energy harvesting device. Périsse concluded that vibration level increased with velocity.

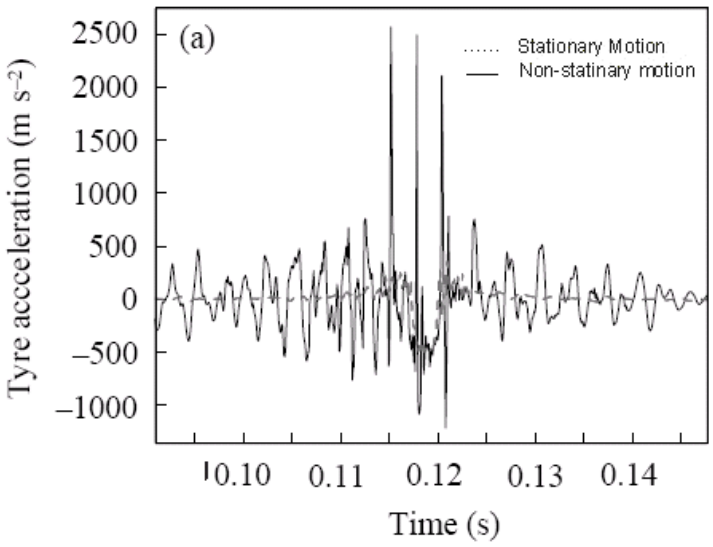

Figure 2.19 Tread vibrations due to rolling on a rough surface [2]

Allison [34] performed an experiment to understand the vibration developed in a rolling tyre. The model of the tyre was presented as a belt, a rigid rim and a hub. The hub was mounted on a suspension system and had the freedom to rotate. Experimental results showed that, damped vibrations due to the direct contact between the tyre and the road were transferred to the rim. This result agreed with the results presented by Périsse [2]. Recent research is trying to develop a new self powered tyre pressure sensor that can be molded with the tyre [35, 36].

The mechanical energy available in the vehicle wheel and presented by both vibration and rotation can be converted into electrical energy. It has been found that the vibration in the vehicle wheel depends on the car type, driving conditions, the vehicle tyre tread, vehicle speed and the road condition. Therefore, the electromechanical harvester should be designed to operate under a wide range of applied frequencies. Moreover, it has been found that the vibration is available only in the contact zone between the road and the tyre. Therefore, the inner side of the tyre is the best place to mount the harvester. However, the available TPMS are mounted on the vehicle wheel rim. Therefore, in order to replace the TPMS battery, the harvester must be designed to be mounted on the wheel rim and withstand the centripetal acceleration amplitude.

Using rotation to generate power is an alternative method, where the output power will depends only on the speed of the vehicle. As it has been explained tangential force is only available when there is a change in the vehicle's speed. Centripetal force, on the other hand, is always available and its magnitude depends on the vehicle speed. Moreover, this force is proportional to the square of the vehicle

velocity. This makes centripetal force a promising solution to convert the wheels energy due to rotation into useful electrical energy.

2.5.3 Self powered tyre pressure sensors

Löhndorf et al [35] used in-plane electrostatic transducers to generate power from vibration available in a vehicle tyre. The power spectral density (PSD) of an acceleration signal measured at the inner liner of a vehicle tyre driven at 50 km/h showed that the acceleration signal was affected by the surface roughness of the road, fluctuations in driving speed, dynamics of the tyres and road conditions. According to Löhndorf et al, the harvester was designed to be sensitive to a wide range of frequencies between 1 Hz and 1 kHz. They noted that a harvester mounted parallel to the inner liner of a tyre was subjected to a radial acceleration and a tangential acceleration. The simulated results of the harvester showed that 10 μW of average power was generated at 80 km/h. The authors noted that the relationship between the output power and the vehicle velocity was linear. They suggested that maximum acceleration peaks of 40000-50000 m/s^2 must be taken into account when designing a harvester.

Keck's [36] experimental and theoretical studies were aimed at measuring the extracted energy from vibration available in a vehicle tyre. The harvester shown in Figure 2.20 was mounted in the inner tread area of the tyre. The metal substrate beam with a piezoelectric layer on top enhanced the robustness of the system and allowed compressive stress to be developed in the piezoelectric structure. The added mass increased the stress around the centre of the beam and it was used to change the stiffness of the harvester. A harvester mounted at the inner liner of the tyre was exposed to gravity in the contact patch region between the road and the tyre surface and it was exposed to centripetal force during the residual revolution. Additionally, the harvester was exposed to random vibrations resulting from tyre-road interaction. According to Keck's simulation results, the spring-mass harvester was designed to be resonant between a frequency range of 550 Hz and 600 Hz. This corresponded to a speed range between 80 km/h and 100 km/h. The experimental result showed that up to 80 μW was generated at 80 km/h. However, reducing or increasing the speed by 20 km/h resulted in half the output power. This highlighted the problem of using a resonant system to generate power from the tyre as explained previously by Löhndorf et al [35].

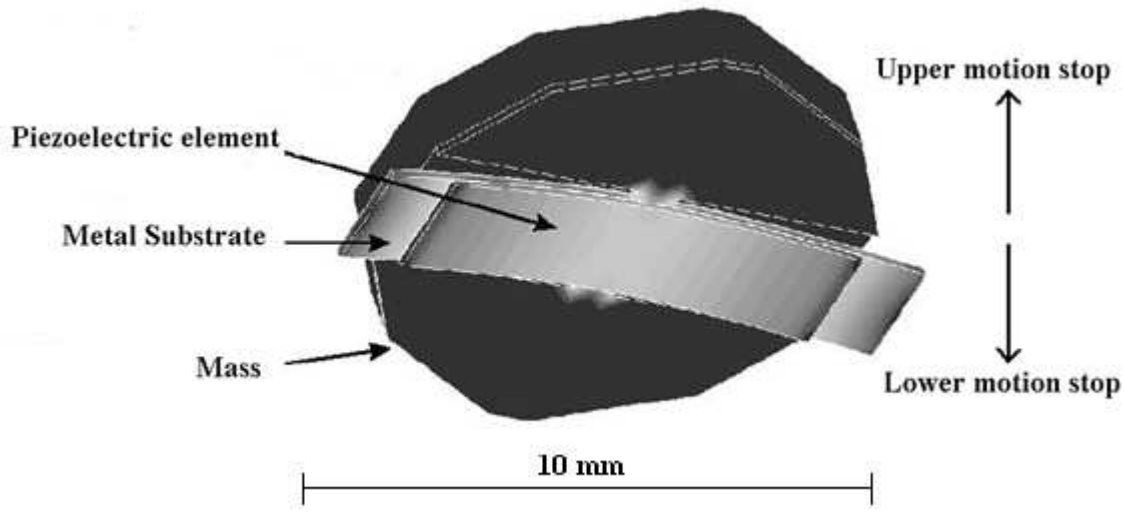

Figure 2.20 Finite element structure of Keck's harvester [36]

The behaviour of Keck's harvester was described as moving from a lower motion stop to an upper motion stop. The lower motion stop was caused by the centripetal force. It was found that, during the tyre-road contact the centripetal acceleration was ramped up. This caused deflection of the mass and thus forcing the harvester to spring back to its upper motion stop. Keck noted that the output energy can be mainly generated during the tyre-road contact. However, at a speed up to 100 km/h a free oscillation contributed toward generating energy. Keck summarised the problems of the harvester as follows. The harvester produced maximum power when its natural frequency matched the applied frequency at a certain speed. Under this speed the stiffness of the device was enough to reduce the deflection of the upper motion stop. Increasing the speed, on the other hand, created a problem with the mechanical stability of the harvester. For this case the stiffness was not enough to withstand the force applied by the centripetal acceleration, which can reach 50000 m/s^2.

EoPlex developed a new process to manufacture piezoelectric harvesters for tyre pressure sensors [1]. The work aimed at using a bimorph piezoelectric structure, which was well studied in the literature, to convert some of the available vibration of the tyre into electricity. As shown in Figure 2.21, the harvester had a bimorph beam structure. The beam was fixed at one end while the other end was vibrating freely. A mass was built into the free end to tune the device to a certain available vibration in the tyre. EoPlex used printing pastes to build blocks in layers to create a 3D structure. The paste was a mixture of inorganic powder (e.g. glass and PZT), which created the final structure, and an organic portion, which allowed the paste to be printed. Another printing paste called 'fugitive' was used to build complex open areas within the

structure, such as channels. A CAD model was used in this technology to print masks which produced positive and negative images. Positive images were printed with the normal paste while the negative images were printed with the fugitive paste. The number of masks depended on the number of layers and the number of materials in each layer.

The paper focused on the fabrication side rather than the practicality of using piezoelectric beam as a harvester inside the vehicle tyre. Resonant systems are not suitable to be used to extract useful power from the vehicle tyre due to the nature of the vibration and the high acceleration amplitude generated by the centripetal acceleration.

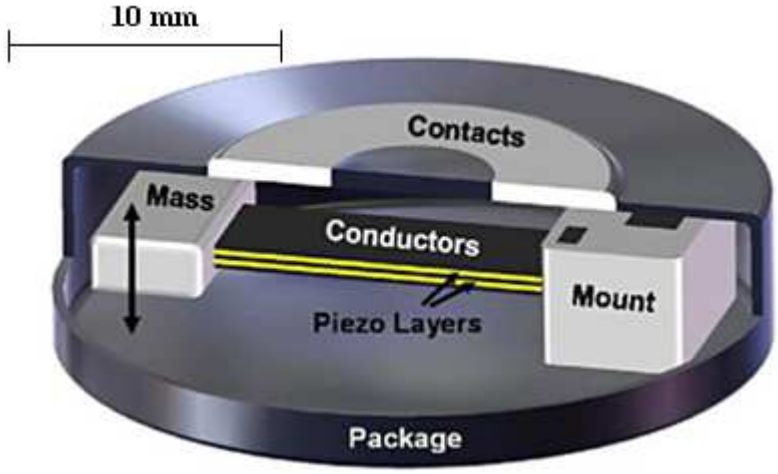

Figure 2.21 An EoPlex energy harvester design for tyre pressure sensors [1]

2.6 Piezoelectricity

Piezoelectricity is the ability of certain crystals to generate an output voltage when they are mechanically deformed. Moreover, these types of crystals deform when an input voltage is applied. Piezoelectric crystals such as quartz rely on the presence of a spontaneous electric moment or dipole in their structure to exhibit the piezoelectric effect. Ceramics, on the other hand, are isotropic polycrystalline materials, where the direction of the spontaneous polarisation through the materials is randomly orientated. This leads to zero net polarisation in the material and thus no overall piezoelectric effect. These materials require a process called polarisation before they exhibit piezoelectric behaviour. The poling process involves exposing the ceramics to a strong electric field (10^6-10^7 V/m) at a temperature slightly below the Curie point. This process orients the polar domains in the direction of the external electrical field [37].

When the poling field is removed, the dipoles remain locked in approximate alignment, giving the ceramic material remnant polarisation and making it anisotropic.

After the poling procedure the piezoelectric properties decay with time. The speed at which this happens depends on the environment in which the material operates. There are three mechanisms that lead to depolarisation and thus the loss of their piezoelectric properties; electrical, mechanical and thermal.

The performance of piezoelectric materials decreases, as the operating temperature increases. Once the Curie point is reached the piezoelectric material will lose its piezoelectric properties and become depolarized. This is due to the fact that the structure of the material becomes centrosymmetric with both negative and positive charge sites coinciding, so there are no dipoles present in the material. Therefore, the operating temperature should be below this point. Applying a strong electric field with polarity opposite to the original poling field affects the performance of the piezoelectric material. The limit of the strength of this field depends on the operating temperature, the time and the type of the piezoelectric material. Applying this field for a short time at a temperature below the Curie point will depolarize the material. Reverse poling can occur when the material is subjected to this field for a long time at a temperature near to its Curie point. Applying high mechanical stress can depolarize a piezoelectric material and lower the Curie temperature of the piezoelectric material [38]. The level of stress required depends on the type of the material and duration of the applied stress. Ageing rate is defined as the change in the properties of the piezoelectric material with time. When these materials are used in sensors and harvesters, the ageing will decrease the efficiency, sensitivity or accuracy of the devices. The ageing process depends on the operating conditions, structure of the piezoelectric devices and the type of the materials.

2.6.1 Piezoelectric notation

Piezoelectric materials are anisotropic, meaning their properties are dependant on the direction in which the properties are evaluated such as the direction of stress, polarisation, electrodes and applied electric field. Therefore, piezoelectric physical constants are defined by a system of symbols with superscript and subscript notations. The superscripts refer to quantities that are kept constant under boundary conditions. Subscripts describe the direction of action and the direction of response. The directions are denoted using numbers as shown in Figure 2.22. The positive direction of the z-axis

refers to the direction of the polarisation. The positive directions of *x*, *y* and *z* are represented by 1, 2 and 3 respectively, and the shear of these axes by 4, 5 and 6 respectively.

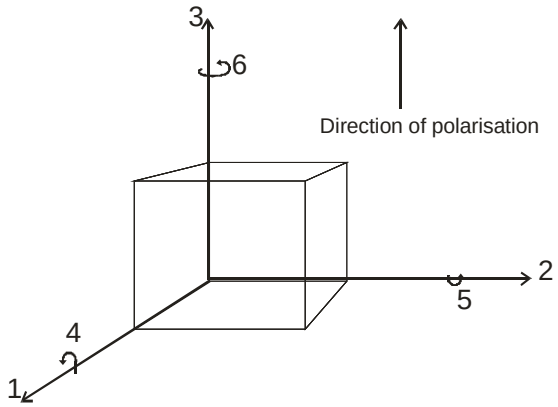

Figure 2.22 Notation of axes

The piezoelectric charge constant (d_{ij}) is defined as the mechanical strain experienced by the material per unit electric field applied to it (m/V). Alternatively, it is the electric polarisation generated in the material per unit mechanical stress applied (C/N). In case of using piezoelectric materials as a harvester, the first subscript indicates the direction of the polarisation and the second subscript indicates the direction of the applied stress. Figure 2.23 illustrates two different modes in which piezoelectric materials are used as a harvester. Using a piezoelectric in the 33 mode means that both the voltage and the stress are acting in the 3 direction. This means the applied mechanical stress is perpendicular to the electrodes. This exploits the d_{33} coefficient of the material. However, in the 31 mode the voltage acts in the 3 direction and the mechanical stress acts in the 1 direction. In this case the applied mechanical stress is parallel to the electrodes. This exploits the d_{31} coefficient of the material.

Piezoelectric voltage constant (g_{ij}) is defined as the electric field generated per unit mechanical stress applied, or the mechanical strain developed in the material per unit electric displacement applied. As with the piezoelectric charge constant, the first subscript indicates the direction of the electric field generated and the second subscript indicates the direction of the applied stress.

The permittivity or the dielectric constant of the material (ε) is defined as the dielectric displacement per unit electric field. Elastic compliance constant (c) is defined as the strain produced per unit of stress applied to the material. Thus Young's modulus (Y) is given by the following equation:

$$Y = \frac{1}{c} = \frac{stress}{strain} \qquad 2.26$$

Another important constant is the electromechanical coupling coefficient (*k*), which indicates the material's ability to convert mechanical energy into electrical energy or vice versa.

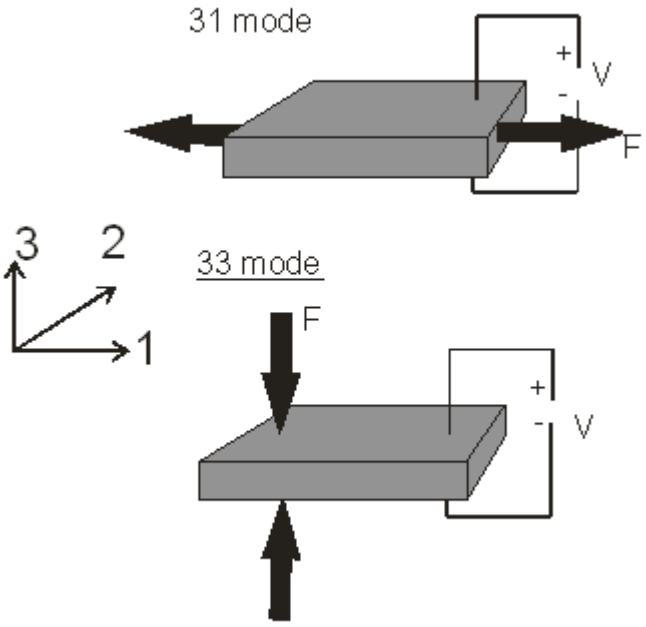

Figure 2.23 Two different modes in which piezoelectric material can be used

Piezoelectricity is a combined effect of the mechanical and electrical behaviour. The mechanical behaviour defines the relationship between the stress (σ) and strain (*S*) through Hooke's Law:

$$[\sigma_\alpha]_{\alpha=1,6} = [Y_{\alpha\beta}]_{\alpha,\beta=1,6} \cdot [S_\alpha]_{\alpha=1,6} \qquad 2.27$$

The stress is given as the ratio of the acting force on the element surface to the area of the element. This tensor has six components. The strain is defined as a relative deformation of the original length and this tensor has 6 components.

The electrical behaviour defines the relationship between the electric field *E* and the electric displacement *D* and is given by the following equation:

$$[D_i]_{i=1,3} = [\varepsilon_{ij}]_{i,j=1,3} \cdot [E_i]_{\alpha=1,3} \qquad 2.28$$

The vectors *E* and *D* are each defined by three components. These equations can be coupled using the piezoelectric constant matrix to give the piezoelectric equations:

$$S_\alpha = c^E{}_{\alpha\beta} \cdot \sigma_\beta + d_{i\alpha} \cdot E_i \quad 2.29$$

$$D_i = d_{i\alpha} \cdot \sigma_\alpha + \varepsilon^T{}_{ij} \cdot E_i \quad 2.30$$

Where α, β = 1, 6 and *i*, *j* = 1, 3.

2.6.2 Piezoelectric materials

Piezoelectric materials can be used as harvesters, sensors, ultrasonic transducers and actuators. For this research these materials are used as harvesters where mechanical energy is converted into electrical energy. Piezoelectric materials can be categorized into three groups:

- Crystals such as quartz
- Piezoelectric ceramics such as barium titanate ($BaTiO_3$) and lead zirconate titanate (PZT)
- Piezoelectric polymers such as polyvinylidene fluoride (PVDF).

The earliest piezoelectric materials were crystalline materials that exhibited natural polarisation. These crystals can only be cut along certain crystallographic directions. This limits the possible shapes and sizes for harvester designs. The piezoelectric properties of lead zirconate titanate (PZT) were discovered in the 1950's. PZT with various additives has since become the dominant piezoelectric ceramic due to its high stability. Different types of PZT have been developed and tailored for different applications. These materials can be divided into hard and soft materials. Hard materials such as PZT 4 and PZT 8 have a high mechanical quality factor (*Q*), low dielectric constant, and low mechanical and dielectric losses. Therefore, this type of ceramic has been used in applications where a high level of mechanical stress and electrical excitation are applied, e.g. sonar. On the other hand, soft materials such as PZT 5H offer better sensitivity and permittivity, at the cost of more losses, and a lower *Q*. This type of ceramic has been used in applications such as low power harvesters and sensors.

The type of piezoelectric material selected for power harvesting applications has a major influence on both the performance and the functionality of the harvester. Comparing between different types of piezoelectric materials means comparing their properties. Materials with higher strain and coupling coefficients have a higher potential for energy conversion. Piezoelectric materials have high impedance resulting in a higher voltage and a lower current output in comparison to the electromagnetic

harvesters. However, materials with a high dielectric constant are preferable for some applications because it lowers the source impedance of the harvester.

Although PZT is widely used as a power harvesting material, it is brittle [39]. This causes limitations in the strain level that can be applied. In order to eliminate the disadvantages of piezoelectric ceramic materials, other more flexible piezoelectric materials are developed and used in certain applications, where flexible materials are required. PVDF has the ability to withstand large amount of strain leading to more mechanical energy available for conversion into electrical energy [40]. Although, this material has a low electromechanical coupling coefficient (k) it is ideal for many applications because of its higher tensile strength, lower stiffness and its ease of manufacture.

2.6.3 Piezoelectric pre-stressed devices

The type of piezoelectric material, the design of the harvester and its size affect the amount of the output power that the harvester provides under the same conditions of the input force. All these parameters depend on the type of application and the nature of the input force. In order to generate power from a rotating object using a non-resonant piezoelectric harvester mounted at a certain distance from the centre of rotation, the design, shape, type of the piezoelectric materials and the method by which the harvester will be mounted on the rotating object will be studied and addressed in this research. The basic requirements for the piezoelectric harvester will be:

- The ability to convert most of the applied mechanical energy into electrical energy. This can be achieved by choosing the right design and materials. This means piezoelectric material should have high value of k. Another factor that must be taken into account during the design of the structure of the piezoelectric harvester is the value of the product of the effective piezoelectric charge constant (d_{eff}) and the piezoelectric voltage constant (g_{eff}). The output power is proportional to this value [41].
- Low value of the total mass of the harvester, in a range of few grams, in order not to influence the rotating object performance.
- The ability to generate an output power at any rotating speed ranging from 15 km/h to 150 km/h when the harvester is mounted on the rim of the vehicle wheel that has a radius of 25.25 cm. The harvester should have the ability to generate enough power for the first transmission after

100 tyre revolutions at low driving speed [42]. Moreover, the harvester should survive without damage 300 km/h.

- The ability to withstand and operate in an environment where the temperature might vary from -20 ^{o}C to 200 ^{o}C. The temperature values are evaluated by Continental Automotive Gmbh. Therefore, PVDF piezoelectric material is not suitable for this application as its melting point is around 170 ^{o}C.
- High mechanical stability.

Pre-stressed piezoelectric harvesters are an attractive design for mechanical to electrical energy conversion. Examples of pre-stressed devices include Rainbow and Thunder™ [43]. Induced stress in the piezoelectric structure in a form of a curvature is formed in Thunder™ during the cooling procedure due to the different thermal shrinkage of the piezoelectric and the passive material (electrodes). However, the curvature in the Rainbow device is formed due to the mismatch in sintering shrinkage. The piezoelectric coefficients are a function of the stress bias in the material which can be used to enhance the properties of the piezoelectric transducer. Moreover, by adding mechanical pre-stress to the piezoelectric harvesters, their behaviour and shape will change [44]. It is found that the induced stress in the pre-stressed devices enhance the value of the piezoelectric charge constant (d_{31}) by a factor (A). According to Kim [41] the effective piezoelectric charge constant (d_{eff}) for pre-stressed harvesters is given by the following equation:

$$d_{eff} = A|d_{31}| + d_{33} \qquad 2.31$$

This enhances the strain developed in the piezoelectric harvester leading to an increase in the output power. It is reported that for PZT 5H its d_{31} increased from -190 pm/V to -994 pm/V by making the structure pre-stressed [45]. Moreover, a pre-stressed harvester has higher electromechanical coupling factor and higher mechanical strength under the same value of the compressive stress than the same harvester without the pre-stressed characteristics. Therefore, pre-stressed Thunder™ transducer with Curie point of 350 ^{o}C is used in this project.

2.6.3.1 Thunder™ technology

Thunder™ is a NASA invention and is only available through Face International Corporation. Thunder™ is a ferroelectric device made of multiple layers bonded on top of each other to form a sandwich. The bottom layer is a stainless steel substrate

followed by an adhesive, thin layer unimorph PZT, another adhesive layer and aluminium on top. Both top and bottom layers are used as electrodes. The bottom layer has a tab on both ends with slots for mounting as can be seen in Figure 2.24.

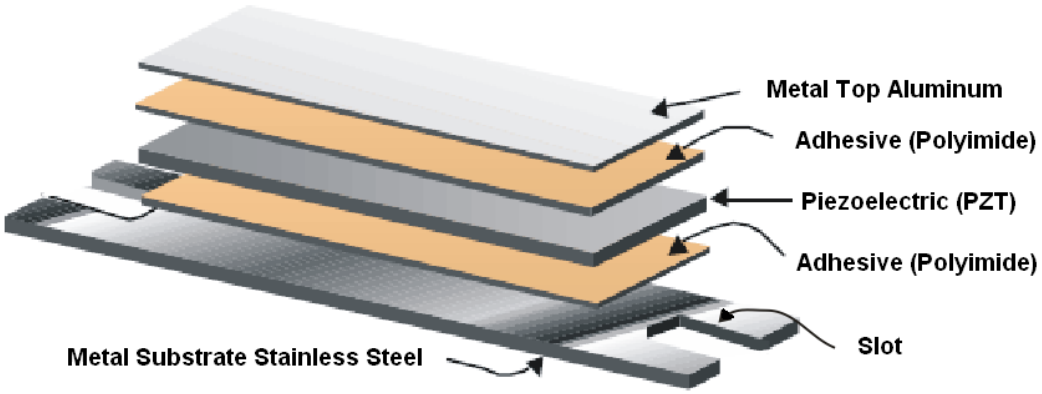

Figure 2.24 Thunder™ construction [46]

The manufacturing process involves heating the entire assembly at a high temperature (320 ^{o}C) and cooling it down to room temperature [47]. The strength of the adhesive bond holds the different layers together. During the cooling procedure, the mismatch in the thermal expansion coefficients causes the metal and the ceramic layers to contract at different rates. The result is internal pre-stresses that are developed in different layers. The pre-stress keeps the stainless steal substrate in tension and the PZT in compression and creates a domed shape as shown in Figure 2.25. This allows Thunder™ to be deflected more than standard piezoceramics without cracking. These devices can be used both as actuators and sensors.

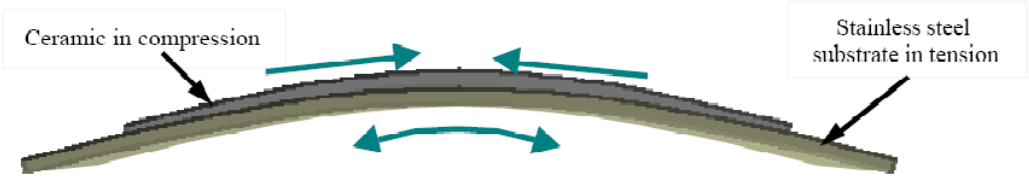

Figure 2.25 Internal pre-stresses [46]

As a harvester, the mechanical deformation within the PZT layers produces electrical energy. These deformations are accomplished by using the Thunder™ as a cantilever or a simple beam. Thunder™ are clamped firmly at one end when they are used as cantilevers as shown in Figure 2.26 (a). Using Thunder™ as a simple beam means one end should be completely fixed, while the other end is simply supported [48] as shown in Figure 2.26 (b). Rigidly fixing both ends prevents the Thunder™ from moving and thus reduces the output power.

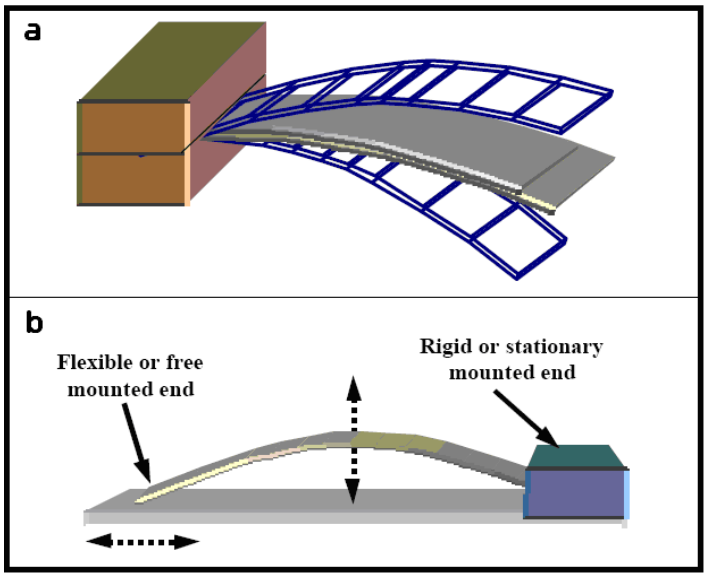

Figure 2.26 a) Cantilever [46]. b) Simply supported Thunder™ [46]

2.6.4 Piezoelectric harvesters based on resonant system

Since piezoelectric materials were first used as harvesters, numerous theoretical and experimental studies were performed to improve their efficiency and power generation capabilities. In general, this can be achieved by choosing a suitable type of material, operating at a suitable mode, tuning the resonant frequency of the harvester and adding pre-stress to maximize the coupling and the applied strain of the material [32, 39]. The type of piezoelectric material selected for power harvesting applications has an important influence on the output power.

The two practical coupling modes in which piezoelectric material can be used are the 31 mode, i.e. cantilever configuration, and the 33 mode, i.e. stack configuration. Other modes are not considered due to their relatively small coupling coefficients compared with 31 and 33 modes. Although the coupling coefficient for 31 mode is lower than the 33 mode, the 31 mode has been the most commonly used coupling mode. This is due to the fact that a harvester operating in 31 mode develops more strain and has a lower resonant frequency than one that operates in 33 mode. These results were discussed by Roundy et al [25].

Baker et al [49] compared the output power of a piezoelectric stack operating in 33 mode to the output power of a cantilever beam operating in 31 mode of equal volumes. It was found that although the stack had a higher coupling coefficient, the cantilever produced two orders of magnitude more power when subjected to the same force. This result is due to the fact that the mechanical stiffness in the stack

configuration is higher than the one in the cantilever configuration which makes straining of the material difficult. It was concluded that a stack configuration had more mechanical stiffness and was more suitable for high forces. Baker et al concluded that using a cantilever configuration was more efficient in an environment with small acceleration amplitude (~10 m/s^2). In this case because the applied force is small the stack mechanism would be unable to generate significant energy.

Therefore, generating power from a rotating object using a non-resonant piezoelectric harvester requires the piezoelectric element to operate on the 33 mode. This is because mode 33 has higher coupling coefficient and thus higher efficiency than 31 mode. Moreover mode 33 is more robust under impact force especially if the force has been generated by the centripetal force where the acceleration amplitude can reach a value that is 3 orders of magnitude greater than the gravitational acceleration [42].

Yang et al [50] has shown that the output power of a piezoelectric plate operating in the 33 mode was proportional to the coupling coefficient. Their analytical calculations showed that, when the harvester operated at resonance, the output power increased significantly. The authors concluded that higher displacements and strains were observed in the material when the driving frequency was close to the resonant frequency of the system.

A cantilever configuration which consisted of one single piezoelectric material mounted on a metallic cantilever beam was described by Glynne-Jones et al [51]. This unimorph configuration provided a low resonant frequency and resulted in high average strains for a given input force. The work included a method to reduce the harvester resonant frequency by placing a mass on the free end of the beam. This made the system more likely to be driven at resonance in the natural environment, thus providing more power. The results showed that the resonant frequency of the cantilever was reduced by increasing the mass on the end of the beam. The same conclusion is observed and drawn by Gurav et al [52]

Ng and Liao [53] work was focused on using a bimorph configuration. Their study was aimed at improving the power harvesting capability of a unimorph beam by using two piezoelectric sheets with a metallic layer between them. As the beam deformed, the top layer of the element was in tension and the bottom one was in compression or vice versa. In parallel poling the current produced by each layer will be superposed. In this case, the poling of the two layers is in the same direction. However, in series poling, where the two layers are poled in opposite directions, the voltage was

added. The experimental study showed that the unimorph beam was more suitable for lower frequencies and load resistance. The bimorph configuration with piezoelectric layers electrically in parallel had the highest power output, under medium frequencies and load resistance. The series configuration, on the other hand, under high load resistance and frequencies produced the greatest power.

The cymbal transducer was developed by Kim et al [54]. It had two dome-shaped metal end-caps which were bonded on both sides of a piezoelectric circular plate. A 29 mm diameter, 1.8 mm thickness piezoelectric plate and 0.4 mm thick steel end-caps produced 52 mW of power into a load of 400 kΩ. The applied force was 70 N at a frequency of 100 Hz. The structure of the device can be seen in Figure 2.27.

The authors argued that cymbal transducer provides higher output power than other transducer structures such as multilayer stacks and bimorphs. This result is due to the fact that the effective piezoelectric electrical coefficient of the cymbal device is amplified several times. As the output power is proportional to both the effective value of charge constant (d_{eff}) and voltage constant (g_{eff}), increasing these values resulted in an improvement in the output power. The value of the effective charge constant can be given as following:

$$d_{eff} = A\left|d_{31} + d_{33}\right| \qquad 2.32$$

where A is amplification factor. The amplification factor can be in the range of 10–100 depending on the design of the caps. The value of g_{eff} is proportional to the effective value of d_{eff}. The increase in the values of the piezoelectric electrical coefficient is due to the presence of a cavity which allows the steel end-caps to serve as a mechanical transformer for transforming and amplifying a portion of the incident axial stress in the radial stresses of opposite sign.

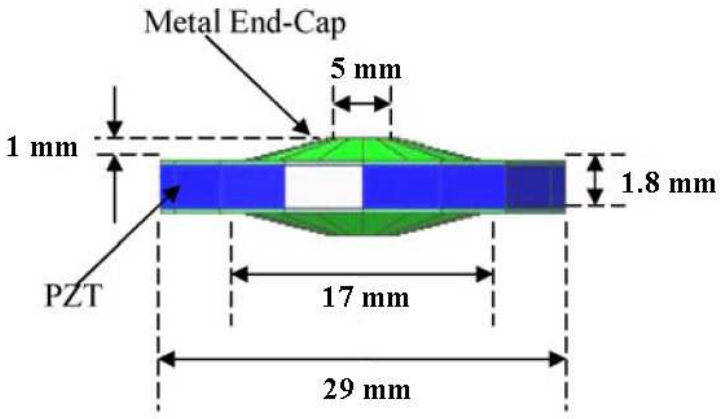

Figure 2.27 The cymbal transducer developed by Kim [54]

A novel configuration was developed by Baker et al [49], in which a piezoelectric beam was compressed, fixed at both ends with pins and a 22 gram mass was attached to the centre of the beam (Figure 2.28). The device generated power by snapping from one stable mode to another (bi-stable). The group found that, the bi-stable device required an acceleration amplitude four times higher that the gravity acceleration to snap the beam between its two modes. Both compressed and uncompressed beams were tested by changing the frequency between 20 and 100 Hz. This range of frequencies was chosen by the authors because it covered the resonant frequencies for both designs. It has been found that bi-stable device generate around 30 % to 100 % more power than the uncompressed device. It was concluded that a bi-stable configuration is required when the excitation frequency keeps changing and thus the device has more available power than the uncompressed beam.

Another example of bi-stable devices is a piezoelectric ultrasonic transducer [55]. The thermal expansion coefficient was mismatched between the silicon membrane and the PZT layer deposited on its surface. This resulted in a build-in stress within the structure. The membrane was found to snap from one position to another by rotating the device in the earth's gravitational field due to the deflection of the centre of the membrane.

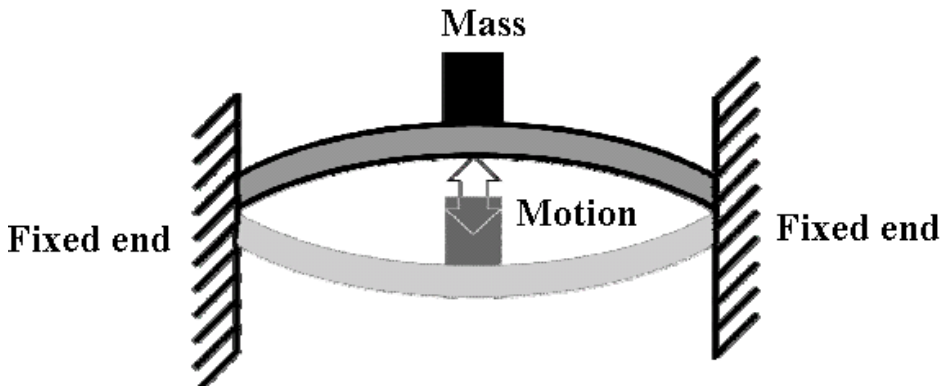

Figure 2.28 Schematic of bi-stable mechanism (after [49])

For a bi-stable device the maximum power will be extracted when the device resonant frequency matches the applied frequency. The output value reduces when the applied frequency drops either side of the resonant frequency. However, this drop is lower that the one provided by the standard beam. Therefore, the output power generated by a compressed beam device is higher than an uncompressed one. Moreover, the beam starts to snap from one side to another when the input acceleration amplitude reaches its critical value. Below this value the snap will not happen.

However, above this value the stress developed, where the beam has been rigidly fixed, increases. This affects the mechanical stability of the device. This structure is not suitable to convert the rotational energy into electrical energy because the centripetal acceleration changes over a wide range of amplitude depending on the rotating speed.

2.6.5 Impact coupled piezoelectric harvesters

Harvesters based on resonant piezoelectric transducers delivering sufficient power for sensors located in different environments are developed. However, when the sensors are located in an environment where the applied acceleration amplitude is greater than the internal displacement of the harvester's mass, using resonant systems to power these sensors is not sufficient. For this reason, this section discusses and analyses an alternative way to generate power using non-resonant piezoelectric transducers. In this system a direct contact between the mass and the piezoelectric bending structure creates an impact force on the piezoelectric material. The deformation of this material generates an output power.

Umeda et al [56] performed an experiment to illustrate a new mechanism of electric power generation in which mechanical impact energy is transformed into electrical energy using a piezoelectric transducer. They introduced an electrical equivalent model to simulate the generation mechanism and analyse the transformation efficiency as functions of the coupling coefficient (k), the dielectric loss ($\tan\delta$) and the quality factor (Q) of the transducer. Umeda et al studied the collision between a steel ball and a piezoelectric disk fixed to the holder at its edge as shown in Figure 2.29. The output of the transducer was connected to a load resistance (R_L). The ball had a mass of 5.5 grams and was at a height h from the centre of centre of the disk. Numerical calculations showed that 76 % of the impact energy was transferred back to the ball as kinetic energy.

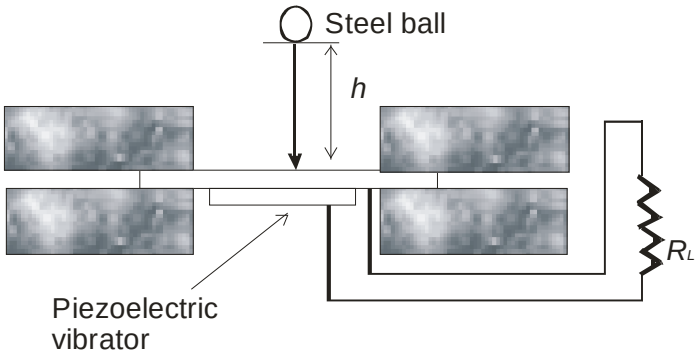

Figure 2.29 Principle of Umeda et al generation (after [56])

Umeda et al noted that the output energy increased when the transducer was left to vibrate at its resonant frequency after the collision without the ball bouncing off with the transducer. No physical explanation of the dynamic behaviour of the impact was given in Umeda's work. They concluded that the transducer efficiency increased by increasing Q and k and reducing $\tan\delta$. The simulation results carried out by Umeda et al showed that the resonant frequency of the piezoelectric disk vibrating on its own, without the ball, is around three times higher than when the ball is in contact with the disk while its vibrating. Moreover, Umeda [57] investigated the characteristics of energy storage using a bridge rectifier and a capacitor. This energy storage is essential to convert the generated pulses into a DC signal that can be used to power sensors.

Renaud et al [58] tried to explain the impact dynamics of their harvester which had the same characteristics as the one developed by Umeda et al. The piezoelectric harvester designed by Renaud et al was aimed at transforming mechanical power from human limb motion into electrical energy. They argued that using a non-resonant harvester was more suitable for their application than a resonant system. In this system, the kinetic energy of a sliding mass was transformed into useful energy using piezoelectric cantilevers as shown in Figure 2.30. The equations of motion were integrated numerically to calculate the output energy. The assumptions made were that the collisions were perfectly inelastic and the mass of the cantilevers were smaller than the free mass. This created a highly damped situation, where the mass stuck to the cantilever until the frame acceleration changed direction. The level of the output power was increased by introducing a holding force. This was achieved by placing magnets on both sides of the frame and using ferromagnetic mass. This holding force allowed the mass to move when the frame reached its maximum acceleration. After the separation, the cantilever did not vibrate. The theoretical results showed that the harvester was capable of generating 40 $\mu W/cm^2$ when it was mounted on the wrist of a walking person. However, in practice the collision was elastic and high frequency vibrations of the cantilever were observed after the separation of two bodies.

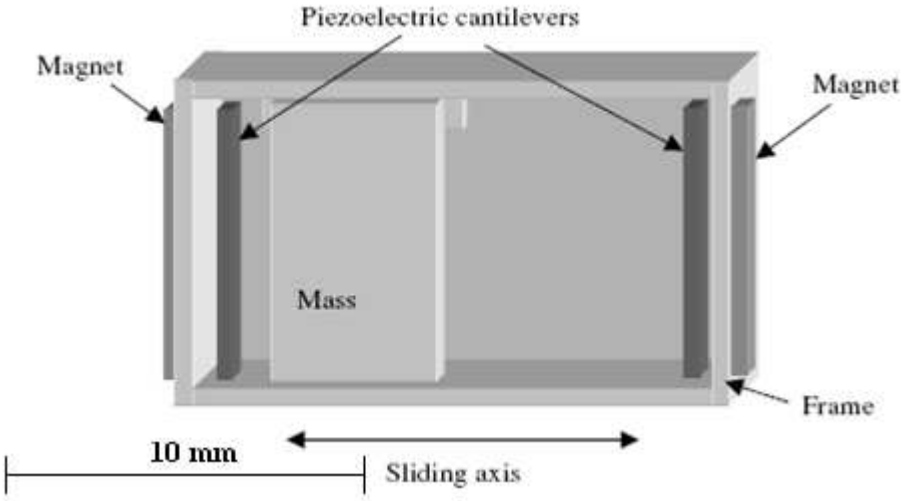

Figure 2.30 Piezoelectric harvester designed for human application (after [58])

A later theoretical study by Renaud et al [59] explained the dynamic behaviour of the piezoelectric transducer under an impact excitation. The non-resonant piezoelectric harvester developed by Renaud has the same concept of extracting electrical energy from kinetic energy as the one proposed in this thesis. The difference between the two harvesters is that the one proposed in this thesis (Chapter 4) has a ball bearing as a mass. This means the impact area is small and the friction between the moving mass and the frame is negligible. In the harvester that has been developed by Renaud, there is more contact surface between the sliding mass and the frame and thus more friction will be generated between them. For modelling, Renaud used a piezoelectric cantilever where the impact force is located at the tip of the cantilever. However, for the design proposed in this thesis the piezoelectric beam is pre-stressed and the applied force is located at the middle of the pre-stressed beam. This means not only the amount of the output power will be different, but also the behaviour of the piezoelectric structure under impact will differ. As the dynamic behaviour of the pre-stressed beam under impact force has not been exploited before, the work of this thesis will focus on analysing this behaviour. The mechanical stability of the proposed harvester is reflected and studied in this work at the maximum applied rotating speed. This can be achieved by optimizing the harvester geometry such as the mass weight, the tube length and the stiffness of the beam that the pre-stressed beam is mounted on.

The design and the modelling of a piezoelectric pulse harvester is presented and discussed by Keawboonchuay et al [60, 61]. This investigation presented a theoretical description of the harvester under impact force. Keawboonchuay et al performed experiments on a piezoelectric harvester to compare the results with a computer model.

The piezoelectric element produced a voltage pulse when it was mechanically compressed. This harvester consisted of the piezoelectric material located between two steel masses, i.e. 70 grams compression mass and 30 grams front-end mass as shown in Figure 2.31. The dimensions of the compression mass, piezoelectric and front-end mass were 0.3 m, 0.0127 m and 0.1 m respectively. Force was applied to the compression mass which compressed the piezoelectric material and generated the output voltage. The impact force was introduced by either decelerating a projectile containing the piezoelectric harvester into a target or dropping a mass into the harvester. The experiment gave results that agreed with the model in the second experiment when a mass was dropped into the harvester. The experimental peak output power was found to be 15.6 kW when 9 kg of mass was dropped from 1 m height into the harvester. This generated 7 kN impact force. From the first experiment, both experimental and simulation results gave the same shape and signal width. However, the magnitude of the peak power of the simulation results is around four times higher than the experimental one due to a diagnostic problem. The experimental peak power was 28.4 kW. The speed by which the projectile was launched to the ground was 300 m/s. The simulated model gave the displacement of the piezoelectric material caused by the impact force. The piezoelectric displacement was found to be proportional to the impact force according to Hooke's law and it has been used to calculate the mechanical energy.

A later study was conducted by Keawboonchuay et al [62] on the behaviour of the piezoelectric transducers under quasi-static and dynamic stress conditions. The electromechanical model was presented and used to explain the effects of different stress conditions on the harvester. For quasi-static stress, the rising and falling time of the applied force pulse were more than the time constant (*RC*) of the piezoelectric transducer. Therefore, the output voltage had two peaks; a positive peak during the rising edge of the applied force pulse and a negative peak during the falling edge of the applied pulse. Under dynamic stress, the length of the applied force pulse is less than *RC*. This produced a positive peak only with higher output voltage amplitude. The authors concluded that when equal stresses were applied to the harvester, the dynamic stress generated 10 times more output voltage than the quasi- static stress. The simulation results agreed with the experimental results.

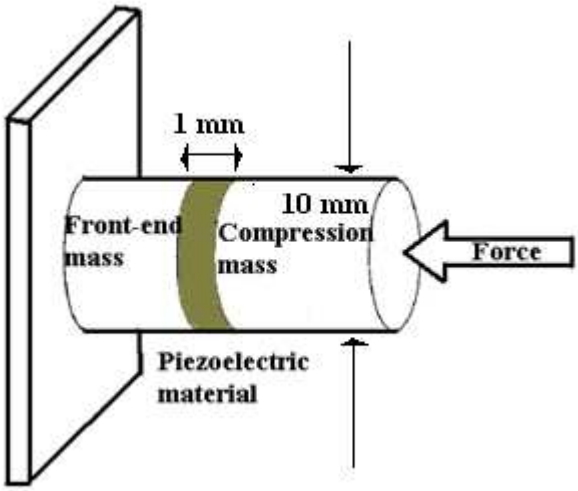

Figure 2.31 Mechanical configuration of piezoelectric disk under impact force (after [60])

The study performed by Cavallier et al [63] was aimed at improving the energy harvesting capability by introducing a vibrating structure excited by an impact force. They claimed that using a vibrating structure as a storage element for mechanical energy improved the quality factor (Q) of the harvester. In their design the ball bearing introduced the shock load. The energy from the shock load was stored in the beryllium brass frame and the Si beam as shown in Figure 2.32. Cavallier et al's experimental results showed that using a Si beam as an energy storage element did not improve the output energy because this layer introduced clamping and interface losses to the design. This study did not explain the difference in the output energy between applying the shock directly into a PZT harvester or through the beryllium brass frame. The authors did not explain the effect of using an energy storage element on Q as they predicted. Moreover, no theoretical calculations were introduced to explain the experimental results.

The beryllium brass works as a frame that extracts some of the kinetic energy provided by the impact force of the ball bearing. Some of this extracted energy will be transferred to the piezoelectric beam. In this case, the beryllium brass acts as an intermediate layer to protect the piezoelectric beam and thus increases the reliability and its lifetime. However, adding an intermediate layer increases the mechanical loss and thus less power will be generated.

Kymissis et al [64] performed an experiment to extract energy from human weight transfer during walking. Nike running shoes were used to carry out the experiment. For this experiment an average man's shoe size has been used. Two types of piezoelectric materials were used; a thin flexible foil of PVDF and PZT Thunder™.

The PVDF foil was moulded into the shoe sole, while the Thunder™ was mounted in the shoe heel. The results showed that a maximum peak voltage of 60 V and 150 V generated by PVDF foil and PZT respectively. The peak power approached 20 mW for the PVDF foil and 80 mW for a Thunder™ per step.

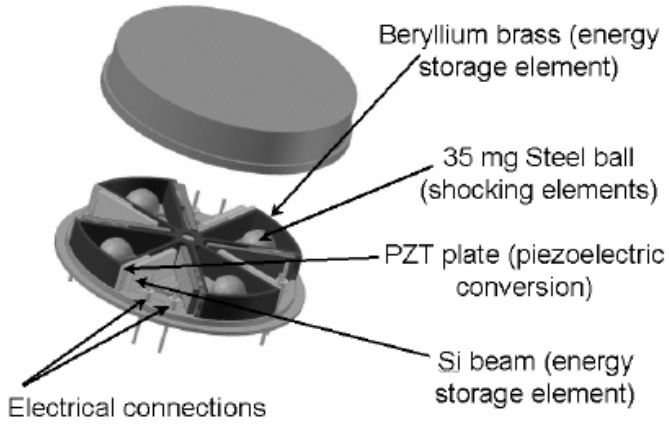

Figure 2.32 PZT/Si/PZT harvester designed by Cavallier et al [63]

2.7 Conclusion

There are three techniques to convert the kinetic energy into electrical energy electromagnetic, electrostatic and piezoelectric transduction. These techniques can be used as resonant and non-resonant systems based on the value of the spring constant. Non-resonant systems can be achieved by omitting the spring constant. Resonant converters are more effective if the excitation vibration provides a single frequency that matches the harvester's resonant frequency. However, this system is not suitable for harvesting energy when the frequency of the excitation vibration is not matching the resonant frequency of the harvester or if this frequency is irregular and has a large amplitude compared to the frame-mass displacement amplitude. It was found that in order to extract power from rotational motion, a non-resonant harvester is preferable.

A comparison between the three different transduction techniques showed that piezoelectric transducers are the most suitable candidate for this application. Piezoelectric transducers provided high output voltages and low electrical current in comparison with the electromagnetic harvester. Moreover, their output impedance was greater than the electromagnetic harvesters. However, this can be reduced by introducing a suitable design. Unlike the electrostatic convertors, separate voltage sources or mechanical stops were not required for this type of harvester. A pre-stressed curved piezoelectric cantilever was shown to be effective in increasing both the general

developed strain in the piezoelectric material and thus the output power of the harvester and the mechanical stability of the piezoelectric structure.

Various piezoelectric configurations based on converting mechanical energy into electrical power were discussed in the literature. Some of these were based on resonant system such as the beam configuration. Others were based on non-resonant systems, where direct contact between the mass and the piezoelectric material will occur due to the applied force. Using impact force to generate power from piezoelectric transducer was identified in the literature as an important method of energy harvesting. The combination of experimental and theoretical work was used in an attempt to achieve better understanding of the behaviour of the piezoelectric harvester under impact forces.

A concept of an energy harvester that converts the rotational motion into linear one when it is mounted on a rotating object was discussed. It was concluded that piezoelectric harvester based on non-resonant system was the most suitable one for this application. In this system a direct force will be applied between the mass and the piezoelectric structure. The contact between the mass and the piezoelectric structure occurs due to the effect of the rotational forces. Other methods that generated output power from rotation using electromagnetic harvesters were presented and discussed. Their suitability for extracting power by being mounted at a certain distance from the centre of the rotating object was analysed and their limitations were highlighted. It was concluded that these harvesters had the ability to generate power from a rotating object when the rotating speed was low. At high rotating speeds, the behaviour of these harvesters became chaotic and their output power reduced due to the effect of the centripetal force.

The aim of this thesis is to design a harvester that can be mounted on a rotating object and extract electrical power from the rotational forces in general and the centripetal force in particular. Generating power from the vehicle tyre is one of the applications for which the harvester can be used. Two different methods can be used to extract the kinetic energy presented in the vehicle tyre including vibration and rotation. Previous works have identified the contact zone between the tyre and the road surface to be a promising area for generating power as vibration decays rapidly outside this zone. In this case, the harvester should be mounted in the inner side of the tyre. Moreover tyre vibration depends on the vehicle type, road conditions, driving conditions, tyre tread surface and the vehicle speed. Some of the harvesters presented in

this chapter were designed to convert the vibration due to the tyre deflection in the contact zone into electrical energy. Although the vibration range was found to be between 10 Hz and 1 kHz, all the harvesters that were mentioned in the literature were based on a resonant system. This means they can provide maximum power only when the applied vibration matched their natural frequencies. As these harvesters were mounted on the inner side of the tyre, overload protection became an essential consideration. Using rotational forces is another method that can be used to generate power from the vehicle tyre. Tangential force as one of the rotational forces is available only when there is a change in the vehicle speed, whereas centripetal force is always available and its amplitude depends only on the vehicle speed. Therefore centripetal force can be considered to be a promising source of electrical power. In this case, the harvester can be mounted on the rim of the vehicle wheel instead of the inner side of the tyre.

Chapter 3

A general model and performance of a piezoelectric pre-stressed beam

3.1 Introduction

In this chapter, an analytical model of the composite beam that uses piezoelectric materials as a source of harvesting energy is developed and discussed. The model development is divided into two main sections. Firstly, a static model that relates the stress developed in the composite structure to the developed curvature is analysed. The composite beam consists of different materials that have different values of thermal expansion coefficient. Therefore, during the manufacturing process, different stresses develop in each layer which causes a bending moment to be induced within the structure. When the composite beam is released from its flat configuration, the developed stresses are relieved causing the beam to have a curvature. Secondly, a dynamic energy based model beside the fully coupled electro-mechanical harvester is developed to calculate the resonant frequency of the structure and predict the output power. Thunder™, model TH 10-R is used in this analysis as an example of a curved pre-stressed beam. The effect of the boundary conditions of the Thunder™ beam on its stiffness damping and resonant frequency is analysed analytically and experimentally.

3.2 Theoretical analysis of piezoelectric pre-stressed beam

A Thunder™ beam is a composite beam because it consists of three thin layers; a stainless steel base, a piezoelectric layer and an aluminium top cover. These layers are bonded together using LaRC SI polyimide adhesive layers. The top and bottom layers work as an electrode, while the piezoelectric material converts mechanical energy into electrical energy. At this stage the beam is flat as shown in Figure 3.1, where h_a, h_b, h_c refer to the thickness of stainless steel, piezoelectric and aluminium layer, respectively. y_a, y_b, y_c refer to the coordinate of the centrelines of stainless steel, piezoelectric and aluminium layer, respectively. L_{steel} and L_{PZT} refer to the length of the stainless steel and the piezoelectric layer, respectively. During fabrication, the structure is heated up to 325 ^{o}C and left to cool down to the room temperature 25 ^{o}C. The difference in the materials thermal expansion coefficients cause a stress to be generated within the structure. These stresses generate a bending moment that causes the beam to bend creating a curved beam. During the cooling period the stainless steel layer shrinks more than the piezoelectric layer as its thermal expansion coefficient is higher than the piezoelectric layer. Therefore, the PZT layer is put under compression while the stainless steel layer is put under tension. Moreover, each layer has a different elastic modulus. Therefore, different stresses will be developed in each layer.

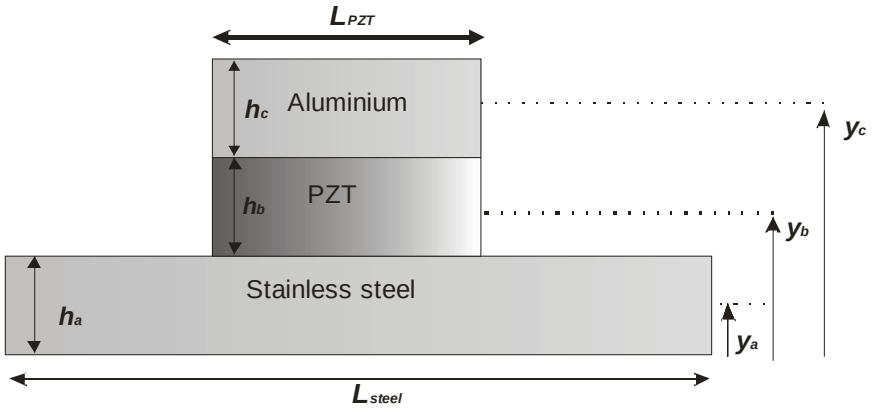

Figure 3.1 The three layers of the flat Thunder™ beam.

The first step in modelling Thunder™ under an input force is to find the relationship between the applied force and the displacement. In order to do that an analysis of the stress developed within the structure, due to the mismatch in the thermal expansion coefficient between the three layers, is carried out. This is followed by calculating the beam curvature due to the thermal effect as well as the maximum

applied force required to return the beam to a flat state. Finally, the resonant frequency of the structure is calculated.

3.2.1 Location of the neutral axis

In order to calculate the beam curvature that results from the thermal stress, bending theory must be applied. This requires a constant value of Young's modulus across the structure. As a composite beam, different values of Young's modulus are presented across the section of the structure. This can be solved by transforming the cross section of the composed beam (Figure 3.1) into an equivalent cross section that consists of only one material. The new cross section is called the transformed section. For this calculation, stainless steel is chosen to replace the other materials. As the aluminium layer of the fabricated Thunder™ is thin in comparison with the other two layers, its effect will be ignored. However, the piezoelectric section will be replaced with an equivalent section of stainless steel material. The width of the equivalent stainless steel section is proportional to the modular ratio (*n*) which is given by equation 3.1 , where Y_{PZT} and Y_{steel} are the young modulus of the PZT and the stainless steel materials, respectively as given in Table 3.1 [65].

$$n = \frac{Y_{PZT}}{Y_{steel}} \tag{3.1}$$

Therefore, the equivalent stainless steel length (L') is given by the following equation, where (L_{PZT}) is length of the piezoelectric layer [65]:

$$L' = nL_{PZT} \tag{3.2}$$

Figure 3.2 shows the transformed section, which consists of one material. As can be seen, the part of the beam that is made originally from stainless steel will not change. However, the part which is made of piezoelectric material changes into an equivalent section of stainless steel.

In order to determine the bending caused by the thermal effect, the position of the neutral axis (*NA*) must be found. As the thermal effect causes the beam to bend, one surface of the beam is subjected to tension and the other surface of the beam to compression. This creates a region in the beam structure where the stress is zero. The equivalent structure can be used to determine the position of the neutral axis. The

position of *NA* can be calculated by taking the moment of area about the base of the structure using the following equation [65]:

$$NA = \frac{\sum y_i A_i}{\sum A_i} = \frac{y_a L_{steel} h_a + y_b n L_{PZT} h_b}{L_{steel} h_a + n L_{PZT} h_b} \qquad 3.3$$

where y_i , A_i are the coordinates of the centrelines and the cross section of each layer, respectively as shown in Figure 3.2.

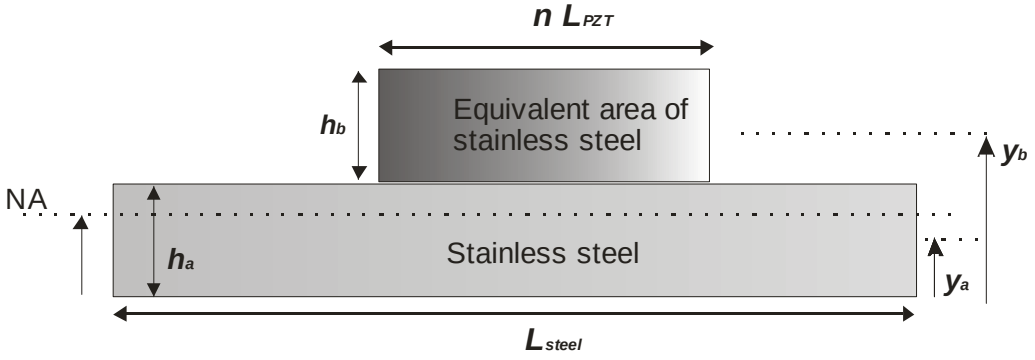

Figure 3.2 Transformed cross-section of a composite beam with the position of neutral axis.

3.2.2 Thermal stress in piezoelectric pre-stressed beam

When a flat composite beam is subjected to a change in temperature (ΔT) during the fabrication procedure, each layer expands at a different rate depending on its thermal expansion coefficient (α). During the cooling process, when the temperature dropped from 325 ^{o}C to 25 ^{o}C, the composite beam is left to bend. As the thermal coefficient of the stainless steel material is higher than the one for the piezoelectric material, the stainless steel will be under tension and the piezoelectric layer will be under compression. The thermal expansion coefficient of the stainless steel material (α_{steel}) is (17.3 × 10^{-6}/^{o}C), while the thermal expansion coefficient for the PZT material (α_{PZT}) is (3 × 10^{-6}/^{o}C). In order to calculate the amount of stress generated in the structure, two rules will be applied.

1. The sum of the expansion of the stainless steel and the compression of the PZT layer equals the difference in the free length [65].

$$\frac{\sigma_{steel} L_{steel}}{Y_{steel}} + \frac{\sigma_{PZT} L_{PZT}}{Y_{PZT}} = (\alpha_{PZT} L_{PZT} - \alpha_{steel} L_{steel}) \Delta T \qquad 3.4$$

Where σ_{steel} and σ_{PZT} refer to the stress developed in the stainless steel and the piezoelectric layer, respectively.

2. The tensile force applied to the piezoelectric layer by the stainless steel layer is equal in magnitude to the compression force applied by the piezoelectric layer to the stainless steel layer [65].

$$\sigma_{PZT} A_{PZT} = -\sigma_{steel} A_{steel} \quad 3.5$$

By assuming that the area of the piezoelectric layer (A_{PZT}) equals to the area of the stainless steel layer (A_{steel}) multiplied by a factor *m*, the stress developed in the PZT layer can be found using the following equation:

$$\sigma_{PZT} = \frac{\sigma_{steel}}{m} \quad 3.6$$

By substituting equation 3.6 into equation 3.4, the stress developed in the stainless steel layer can be calculated using equation 3.7.

$$\sigma_{steel} = \frac{(\alpha_{PZT} L_{PZT} - \alpha_{steel} L_{steel})\Delta T}{(\frac{L_{steel}}{Y_{steel}} + \frac{L_{PZT}}{mY_{PZT}})} \quad 3.7$$

The magnitude and the direction of the generated stresses in the structure within each layer are illustrated in Figure 3.5. These stresses are presented as uniform distributed loads as shown in Figure 3.5 (a). As a result of the developed stresses, the beam will bend. The deflection of the beam is described and calculated in the next paragraph.

3.2.3 Maximum allowed deflection in the piezoelectric pre-stressed beam

In order to calculate the deflection of the composite beam caused by thermal effects, the bending moment across the beam must be found. This requires calculating the area moment of inertia. For a simple structure shown in Figure 3.3, the area moment of inertia (*I*) about the neutral axis (*NA*), where the axis passes through the edge of the section, can be found using the following equation [65]:

$$I = \frac{Ly^3}{3} \quad 3.8$$

where *L* and *y* are the length and the thickness of the beam, respectively.

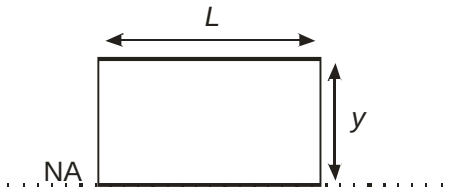

Figure 3.3 Rectangular beam cross section.

For built-up sections, the area moment of inertia (I) can be calculated by dividing the section into convenient rectangles that have the neutral axis as one of their edges. This rule can be applied to the flat equivalent section of the composite beam shown in Figure 3.4. The area moment of inertia for this beam can be calculated using the following equation:

$$I = I_1 + I_2 + I_3 + I_4 \tag{3.9}$$

$$I = \frac{L_{steel} h_{NA}^3}{3} + \frac{nL_p \left(h_b + h_a - h_{NA}\right)^3}{3} + \frac{\left(L_{steel} - nL_{PZT}\right)\left(h_a - h_{NA}\right)^3}{3}$$

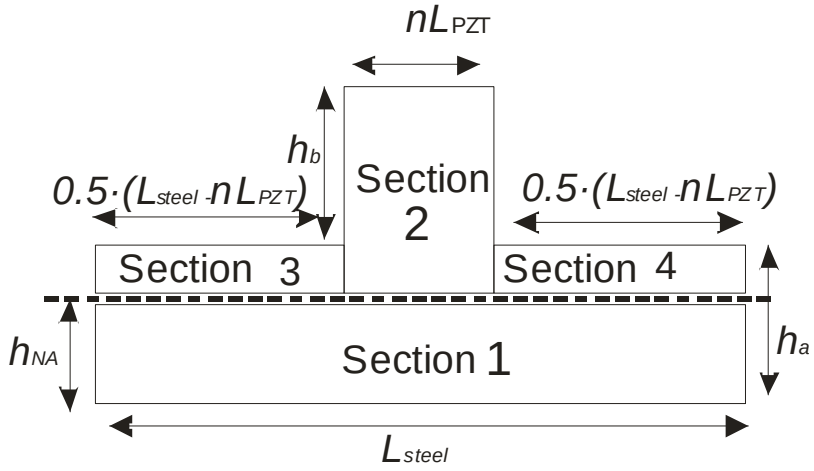

Figure 3.4 (I) total is the sum of (I) of area 1, (I) of area 2 and double (I) of area 3.

The deflection of the beam due to the thermal effect is calculated numerically using the following equation:

$$M = Y_{steel} I \frac{d^2 y}{dx^2} \tag{3.10}$$

The second order differential term in equation 3.10 can be replaced by its finite difference approximation as shown in equation 3.11, where M is the bending moment, h is the length of the beam divided by the number of segments and y is the vertical deflection at the selected point across the length of the beam x.

$$\frac{d^2y}{dx^2} = \frac{1}{h^2}\left(y_{i+1} - 2y_i + y_{i-1}\right) \qquad 3.11$$

The deflection equations of the beam are obtained in terms of moments at various points along the beam and by solving these equations simultaneously, the deflection across the beam is obtained. In order to calculate the moments at different points of the beam, the load generated by the thermal stress must be known. The load presented due to the thermal stress is shown in Figure 3.5 (a). The load developed on the surface of the stainless steel layer and the piezoelectric layer equals the thermal stress times the area. According to equation 3.5 the generated forces in both layers have the same magnitude with opposite directions. The load will be compression in the PZT layer (w_1) and tensile in the stainless steel layer (w_2).

The equilibrium of moments about each end produces reactions of R_A and R_B. To calculate R_A, a bending moment at the other end will be calculated and then it will be divided by the length of the beam (L_{PZT}). In order to do that the load must be redistributed using Macaulay's method [65] as shown in Figure 3.5 (b).

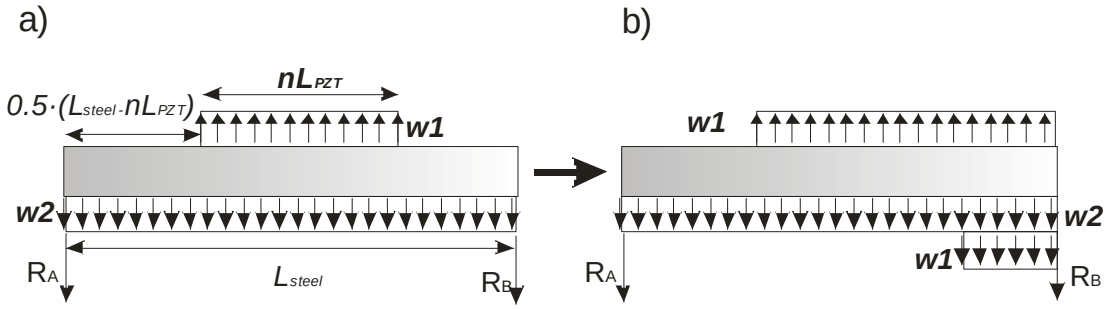

Figure 3.5 a) Distributed loads caused by the thermal effect. b) Equivalent load system using Macaulay method for distributed load.

As the structure has a symmetric shape, the maximum deflection (δ_1) is expected to be in the middle of the beam. This presents the dome height of the beam. By applying a concentrated load in the middle point of the curved beam, the beam moves downwards by δ_2. The total deflection of the beam is given by the following equation, where h is the height of the beam:

$$\delta_{total} = \left(\delta_1 - h\right) - \delta_2 = \delta' - \delta_2 \qquad 3.12$$

For simply supported curved beam, the maximum beam displacement due to concentrated static load (P) is given by the following equation [65]:

$$\delta' = \frac{3PL^3}{256YI} \qquad 3.13$$

Therefore, the maximum applied load (in Newton) is the one that causes the beam to be flat and it is given by equation 3.14:

$$P_{\max} = \frac{\delta' 256YI}{3L^3} \tag{3.14}$$

3.2.4 Radius of curvature of piezoelectric pre-stressed beam

The thermal effect produces a configuration depicted in Figure 3.6. In this figure R is the radius of curvature, δ presents the beam deflection and L is the beam length. It is thus necessary to quantify the relation between the radius of curvature R, the calculated maximum beam deflection (δ_1) and the length of the beam (L).

Given the radius of curvature (R) and the beam length (L), the angle (θ) is given by the following equation:

$$\theta = \frac{L}{2R} \tag{3.15}$$

Furthermore, the radius (R) and height (r) are related by the following expressions:

$$\cos(\theta) = \frac{r}{R} \tag{3.16}$$

Since $R = \delta_1 + r$, it follows that

$$R\cos(\frac{L}{2R}) = R - \delta_1 \tag{3.17}$$

Given the value of L and δ_1 , equation 3.17 provides the value of radius (R).

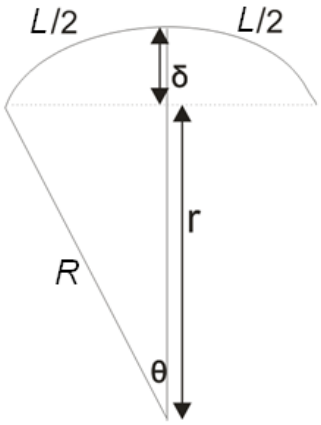

Figure 3.6 Radius of curvature of a composite beam due to the thermal effect.

As the curvature is introduced to the composite beam due to the thermal stress, the location of the neutral axis calculated in Section 3.2.1 will change. It is expected to move further away from the centreline of the equivalent area of the stainless steel material as shown in Figure 3.7. The radius of neutral axis can be calculated using the following equation:

$$r_n = \frac{A}{\int_A \left(\frac{dA}{r}\right)} = \frac{\left(L_{steel} h_a\right) + \left(nL_{PZT} h_b\right)}{L_{steel} \ln\left[\left(r_1 + h_a\right)/r_1\right] + nL_{PZT}\left[r_2/\left(r_2 - h_b\right)\right]} \qquad 3.18$$

Where, r_2 is the radius of curvature which can be obtained using equation 3.17. By knowing the total thickness of the beam, the value of r_1 equals to $r_2 - \left(h_a + h_b\right)$.

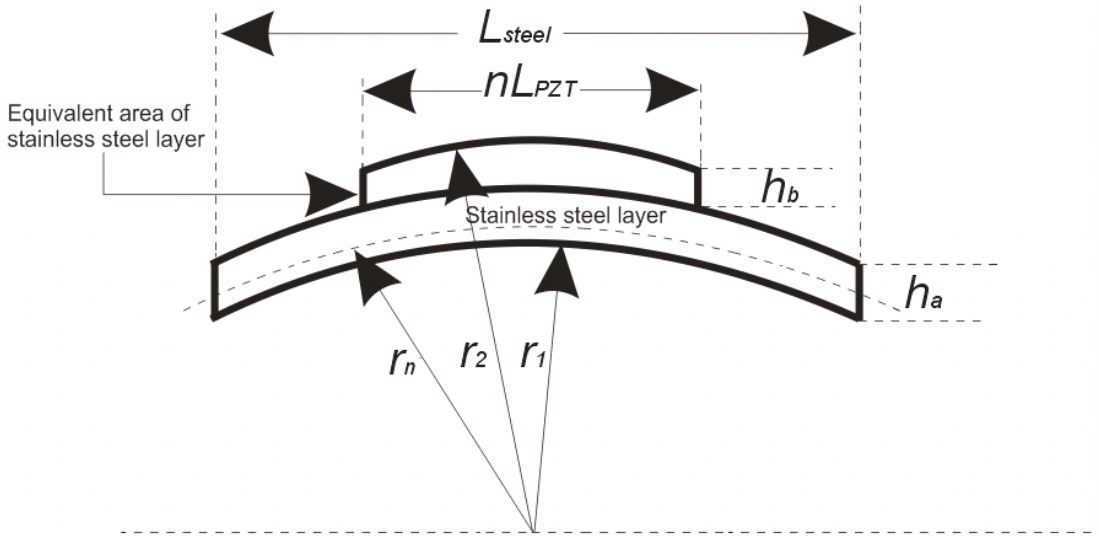

Figure 3.7 Neutral axis for cross section of a curved composite beam

3.2.5 Stress developed in the composite structure due to an input force

The stress obtained in any cross section of the composite beam is given by equation 3.19, where *I* is the area moment of inertia, *M* is the bending moment, *L* is the length of the layer and *y* is the distance from the neutral axis.

$$\sigma = \frac{1}{L}\int_0^L \frac{M(l)y}{I} dl \qquad 3.19$$

As can be seen, the developed stress along the neutral axis (*NA*) is zero and it increases proportionally by moving away from the *NA*. Therefore, the maximum stress

values are located on the surface of the upper and lower surfaces of the composite beam. The moment as a function of the beam length of a vector $\vec{B}$ calculated about a point *A* is given by the following equation, where $\vec{r}_{AB}$ is a vector from point *A* to the position where quantity $\vec{B}$ is applied:

$$M(l) = \vec{r}_{AB} \times \vec{B} \tag{3.20}$$

When a force is applied to a composite beam with radius of curvature, internal forces are generated within the structure. As the beam consists of 5 layers bonded together, the generated forces and stresses prevent the sliding between the layers when bending takes place. The prevention of sliding is achieved by generating shear stresses within the structure. Therefore applying a force on the surface of the pre-stressed beam not only generates direct stresses, but it also generates shear stresses. Theoretically, for the top and the bottom surface of the beam, the shear stress is zero as the surface is free to unload. However, the maximum shear stress is located at the surface where different materials are bonded together. The shear stress across the beam section is calculated using the following equation [65, 66]:

$$\tau = \frac{QAy}{IL} \tag{3.21}$$

where *Q* is the shear force at the point where the shear stress is calculated, *A* is the area of the section, *L* is the length of the cross section area and *I* is the moment of inertia. The value of *y* can be calculated using equation 3.22, where *h* is the height of the section [65].

$$y = NA - \frac{h}{2} \tag{3.22}$$

The value of the shear stress depends on the developed shear force in the materials. This depends on the location of the cross section, boundary conditions and the type of the applied force. Equation 3.21 can be used if the applied force is static. In the case of applying a dynamic force, the developed shear force and thus the shear stress is more complicated to calculate. Therefore, numerical calculation using ANSYS is used.

3.2.6 Natural frequency of curved composite beam

The resonant frequency of the composite beam in terms of bending modulus is derived using the Bernoulli-Euler equation as presented in equation 3.23. Where, *D* is the bending modulus per unit width, *m* is the mass per unit area and *v* is a coefficient that is related to the boundary conditions. The value of *v* equals 10.9 in case of simply supported beam and 4.4 for the cantilever beam.

$$f_o = \frac{v}{2\pi L_{steel}^2}\sqrt{\frac{D}{m}} \qquad 3.23$$

The mass per unit area (*m*) is given by the following equation:

$$m = \rho_{steel} h_a + \rho_{PZT} h_b + \rho_{Al} h_c \qquad 3.24$$

where, ρ_{steel}, ρ_{PZT}, ρ_{Al} present the density of stainless steel, PZT and Aluminium layer, respectively. h_a, h_b, h_c refer to the thickness of stainless steel, PZT and Aluminium layer, respectively (Figure 3.1). The bending modulus per unit width of a flat composite beam (*D*) is given by the following equation:

$$D = \sum_{i=1}^{n} Y_i \int (h - h_{NA})^2 \, dh \qquad 3.25$$

Where, Y_i represent the Young's modulus of the *i* layer of the composite beam, *h* is the thickness of the layer measured from the reference point and h_{NA} is the height of the neutral axis measured from the reference line as shown in Figure 3.4.

As shown in equation 3.23, the resonant frequency of the composite beam is inversely proportional to the square of the beam length. This means that the resonant frequency of the structure can be reduced by increasing the length of the beam. The resonant frequency of the beam depends on the mounting method. Mounting the beam as a cantilever lowers the resonant frequency by 2.8 times compared to a simply supported beam. The resonant frequency is proportional to the square root of the bending modulus. Therefore, any increase in its value results in a higher resonant frequency. Several factors can affect the value of the bending modulus and thus the resonant frequency. These parameters include the types of materials, thickness of the layers and the curvature of the fabricated beam. Increasing the thermal stress developed in the structure, by choosing materials that have higher differences in their thermal expansion coefficient, causes the composite beam to bend more. As illustrated in

Section 3.2.4, increasing the curvature of the composite beam causes the neutral axis to move away from the centreline of the piezoelectric material. This increases the value of the bending modulus and thus provides higher resonant frequency.

3.2.7 Analysis and discussion on using Thunder™ TH-10R

The pre-stressed composite beam that will be analysed is Thunder™, model TH 10-R, which is provided by Face International Corporation. The dimensions of the device are presented in Table 3.1 as well as some of the physical and mechanical properties of the materials of the beam. A diagram of the device structure is presented in Figure 3.8. This model is chosen because of its size as it has the smallest dimensions in comparison with other models.

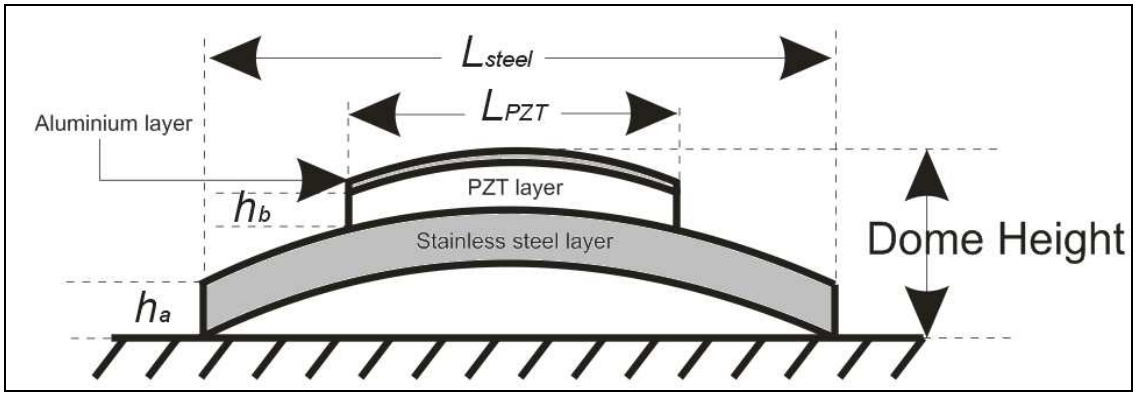

Figure 3.8 Cross section of Thunder™ pre-stressed beam provided by Face International Corporation

The aim of this section is to calculate the deflection of the Thunder™ beam due to thermal effects and thus the radius of curvature of the beam. Moreover, the maximum force that causes the beam to be flat is calculated and compared to the recommended value provided by the device data sheet. The resonant frequencies of the beam mounted as a cantilever and simply supported are calculated.

The position of the neutral axis (*NA*) is calculated by taking the moment of area about the base of the structure using equation 3.3. The height of the *NA* from the base of the structure is 0.13 mm. This means the location of the neutral axis is in the stainless steel layer. Therefore, the resultant stress in the PZT layer is not zero. The distance from the centroid of the PZT layer to the natural axis is 0.17 mm. In order to calculate the location of the *NA*, the calculated values of modular ratio (*n*) and the equivalent length of the stainless steel layer are 0.34 and 3.4 mm, respectively. The

area moment of inertia for the equivalent structure using equation 3.9 equals to 5.48×10^{-14} m^4.

Material	Stainless steel	Aluminium	PZT(5A)
Length *L*, mm	25	12.5	12.5
Width *w*, mm	12.7	12.5	12.5
Thickness *h*, mm	0.2	-	0.2
Young's modulus *Y*, N/m^2	200×10^9	69×10^9	68×10^9
Density ρ, kg/m^3	7800	2700	7800
Poisson's ratio υ	0.31	0.33	0.31
Tensile yield strength *Y*, N/m^2	520×10^6	90×10^6	20×10^6
Shear strength, N/m^2	186×10^6	30	-
Thermal expansion coefficient α, $^oC^{-1}$	17.3×10^{-6}	23×10^{-6}	3×10^{-6}

Table 3.1 Physical and mechanical properties for aluminium, stainless steel and PZT (5A) [67-70].

As the area of the piezoelectric layer is half the area of the stainless steel layer, the stress developed in the PZT layer is twice the stress generated in the stainless steel layer. Using equation 3.7, the stress developed in the stainless steel layer due to the mismatch in the thermal expansion coefficient between the layers of the composite beam is found to be 192.5 MPa. As the stress generated in the PZT layer is twice the stress generated in the stainless steel layer, the stress in the PZT layer equals 384.97 MPa. As the area of the stainless steel layer is twice the one of the PZT layer, the generated forces in both layers have the same magnitude, but have opposite directions. The magnitude of the compression load generated in the piezoelectric layer (w_1) and thus the magnitude of the tensile load in the stainless steel layer (w_2) equals to 66.9 kN. The load at each end of the beam R_A and R_B (Figure 3.5) is found by calculating the bending moment at the other end and then dividing it by the length of the beam. The value of R_A equals to -426.3 N. The negative value indicates that the direction of force is downwards (compression).

After analysing the effect of the thermal stress on the composite beam, the beam deflection can be calculated. This is achieved by dividing the beam into sections and calculating the generated moment due to the thermal stress at both ends of each section. Then by using equation 3.10 and equation 3.11, multiple equations can be generated and solved simultaneously to demonstrate the deflection of the composite beam. For a Thunder™ beam, the total length of the beam is divided into four sections. A new section is taken into account every time a change in the load due to the thermal effect is presented in the structure. Moreover, this number of sections covers the middle of the beam where the maximum deflection is expected. The maximum deflection (δ_1) is found to be in the middle of the Thunder™ beam and the dome height is found to be 0.6 mm. Therefore, the maximum applied load that causes the beam to be flat is 35.9 N. The calculated value of the maximum applied force agrees with the one provided by the device data sheet (36 N). Given the value of the beam's length and its deflection δ_1, the radius of the beam equals to 0.135 m (equation 3.17). As the thermal stress causes the beam to bend, the location of the neutral axis is recalculated using equation 3.18. It is found that the neutral axis moved by 6 μm further down away from the centreline of the piezoelectric layer. Therefore, the location of the neutral axis is approximately 0.124 mm above the bottom layer of the stainless steel layer (reference point).

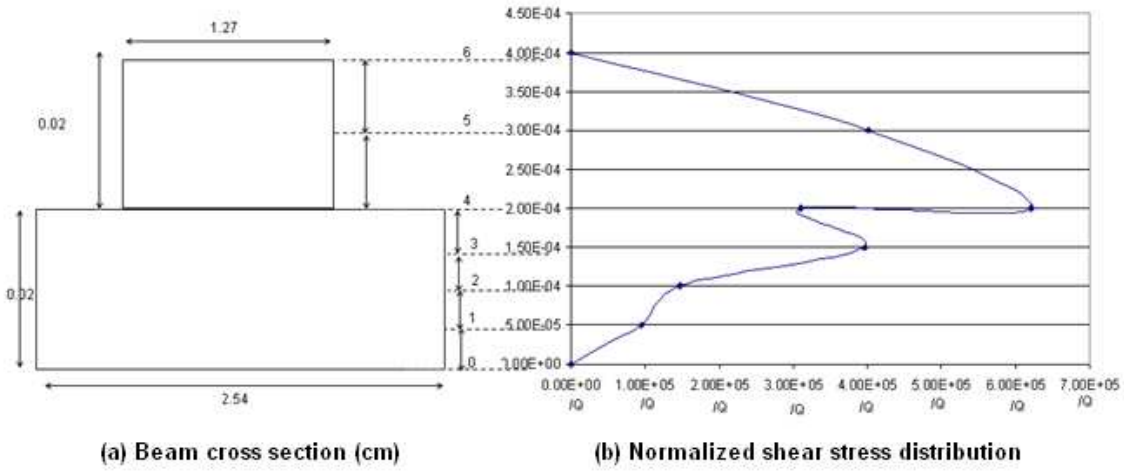

Figure 3.9 Developed shear stress across the thickness of the Thunder™ beam.

Figure 3.9 shows the cross section of the beam and the normalized shear stress distribution in the middle across the thickness of the beam under static applied force (10 N). As can be seen, the maximum calculated shear stress is located at the surface where different materials are bonded together. Equation 3.23 is used to calculate the resonant frequency for the composite pre-stressed beam shown in Figure 3.8 with dimensions and physical properties presented in Table 3.1. Taking into account the

effect of curvature on the resonant frequency, the bending modulus per unit width and the mass per unit area are 0.857 and 3.22, respectively and thus the calculated resonant frequency is 1432 Hz. For a cantilever configuration, the resonant frequency is 578 Hz.

3.3 Analytical model of piezoelectric pre-stressed composite beam

An analytical model is needed to predict the response of the pre-stressed piezoelectric composite beam under different input conditions. The piezoelectric material converts energy between mechanical and electrical domains. A common approach for describing coupled electromechanical systems is to use lumped parameter models. Thunder™ pre-stressed beam is a device that consists of a piezoelectric material coupled to a mechanical structure. The mechanical properties of the device can be modelled as a spring, mass, damper and a piezoelectric element as shown in Figure 3.10 [71]. An applied force excites the system and energy can be extracted across a load connected to the electrodes of the piezoelectric element.

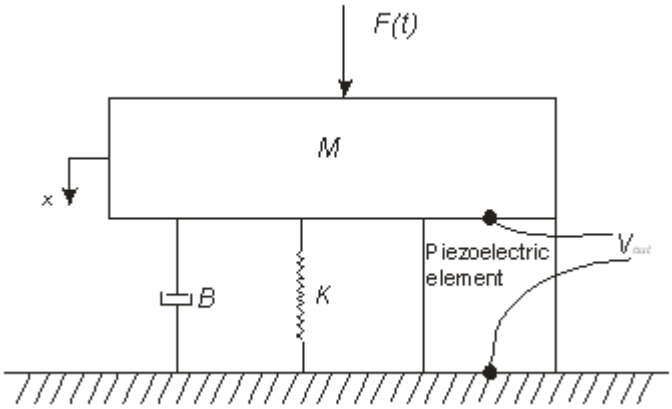

Figure 3.10 Equivalent model of the piezoelectric structure

The equation of motion for this system is given by the following equation:

$$F_m = M_m \ddot{x}_m + B\dot{x}_m + Kx_m + F_i \qquad 3.26$$

Where F_{m} is the external force, F_i is the force generated by the piezoelectric material, M_{m} is the mass of the structure, B is the damping, which represents the mechanical loss of the structure, and K is the stiffness of the mechanical structure. $\ddot{x}_m$, $\dot{x}_m$, x_m are the acceleration, velocity and the displacement of the mass, respectively. An equivalent electrical circuit for the system can be found by taking a Laplace transform of equation 3.26 which gives:

$$F_m = s^2 X(s) M_m + sBX(s) + X(s)K + F_i \tag{3.27}$$

The force generated by the piezoelectric material can be calculated using the following equation [72]:

$$F_i = \left(\frac{c^D A - h^2 C_p' t}{t} \right) X(s) + \frac{V_{out}}{\phi} \tag{3.28}$$

where, A, t, C_p', h, Y^D are the cross section area, thickness, piezoelectric capacitance, piezoelectric constant and the Young's modulus under constant electric displacement of the piezoelectric material, respectively. ϕ is the transformer ratio, which represents the ratio of electrical output to the mechanical input. Therefore, equation 3.26 can be written as following:

$$F_m = s^2 X(s) M_m + sBX(s) + \underbrace{\left(K + \frac{c^D A - h^2 C_p' t}{t} \right)}_{K_m} X(s) + \frac{V_{out}}{\phi} \tag{3.29}$$

K_m is the total stiffness of the composite pre-stressed beam. The calculated value of the resonant frequency of the simply supported Thunder™ beam, model TH equals to 1432 Hz (Section 3.2.7). The resonant frequency relates to the beam stiffness as follows:

$$f_o = \frac{1}{2\pi} \sqrt{\frac{K_m}{M_m}} \tag{3.30}$$

Such a harvester can be presented using the piezoelectric circuit model shown in Figure 3.11 (a). The capacitance of the piezoelectric beam is given by the following equation, where ε_o is the vacuum permittivity (8.854×10^{-12} F/m):

$$C_p^{'} = \left(1 - \frac{d^2}{s^E \varepsilon_o \varepsilon^T} \right) \frac{\varepsilon^T \varepsilon_o A}{t} \tag{3.31}$$

where d is the strain coefficient, s^E is the elastic compliance in a constant electric field and ε^T is the dielectric constant under constant stress. An equivalent electrical circuit of the system with resistive load is presented in Figure 3.11 (b). Equation 3.29 can be written as follows:

$$\phi F_m = \frac{sX(s)}{\phi} \left(s\phi^2 M_m + \phi^2 B + \frac{\phi^2 K_m}{s} \right) + V_{out} \tag{3.32}$$

The electrical transduction constants are given as follows [73]:

$$\begin{aligned} R_{em} &= B_m \phi^2 \\ L_{em} &= M_m \phi^2 \\ \frac{1}{C_{em}} &= K_m \phi^2 \\ V_{in} &= \phi F_{in} \end{aligned} \qquad 3.33$$

Moreover the total current is given by the following equation:

$$I_{in} = \frac{sX(s)}{\phi} = \frac{\dot{x}}{\phi} \qquad 3.34$$

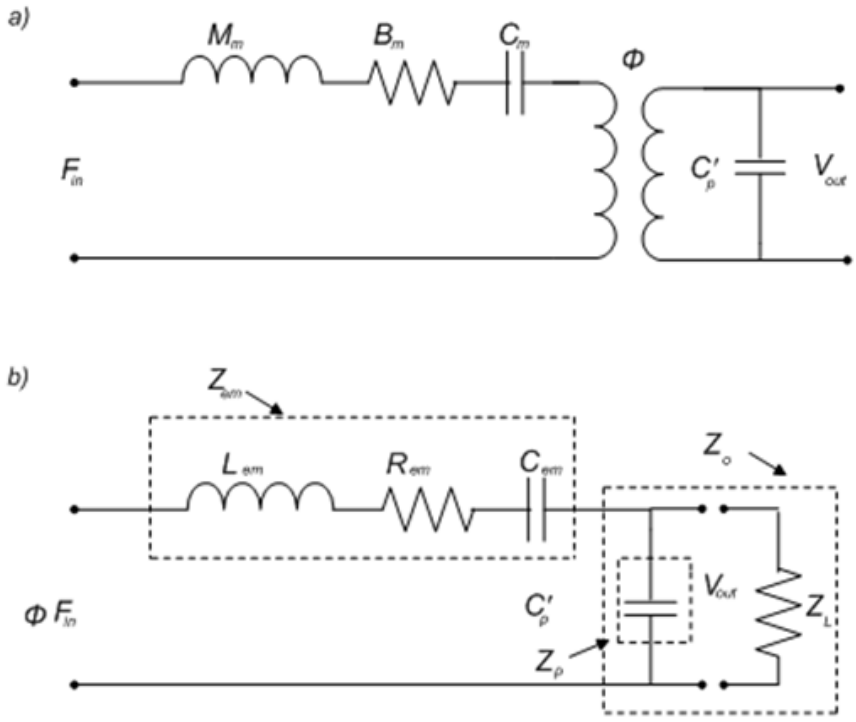

Figure 3.11 The circuit model of the piezoelectric structure

Using the equivalent electrical circuit, the output voltage can be expressed as following:

$$V_{out} = V_{in} \frac{|Z_o|}{|Z_{total}|} \qquad 3.35$$

The input voltage can be calculated using the following equation:

$$V_{in} = I_{in} Z_{total} \qquad 3.36$$

The output voltage is measured using a purely resistive load. The parallel impedance of the piezoelectric and the load is given by the following equation:

$$Z_o = \frac{R_L \cdot \frac{1}{j\omega C_p'}}{R_L + \frac{1}{j\omega C_p'}} = \frac{R_L}{\left(1 + R_L\, j\omega C_p'\right)} \tag{3.37}$$

Thus, by substituting equation 3.36 and equation 3.37 into equation 3.35, the output voltage on the piezoelectric element can be expressed in the frequency domain as a function of the mass velocity:

$$V_{out} = \frac{R_L}{\phi \cdot \left(1 + R_L\, j\omega C_p'\right)} sX(s) = \beta \cdot \dot{x} \tag{3.38}$$

β is the electrical damping generated by the piezoelectric material. Replacing the previous expression of the output voltage in equation 3.29, yields the following equation, where B_m is the total damping:

$$F_m = s^2 X(s) M_m + K_m X(s) + \underbrace{\left(B + \frac{R_L}{\phi^2 \left(1 + R_L\, j\omega C_p'\right)} \right)}_{B_m} sX(s) \tag{3.39}$$

Therefore, the equation of motion can be simply written as following:

$$F_m = M_m \ddot{x}_m + B_m \dot{x}_m + K_m x_m \tag{3.40}$$

On the other hand if the values of the equivalent circuit elements are known, the output voltage can be calculated using the following equation:

$$V_{out} = V_{in} \frac{\left|Z_1\right|}{\left|Z_{total}\right|} = \frac{\left|Z_1\right|}{\left|Z_{em} + Z_1\right|} = \frac{\left| \frac{Z_p Z_L}{Z_p + Z_L} \right|}{\left| Z_{em} + \frac{Z_p Z_L}{Z_p + Z_L} \right|} \tag{3.41}$$

where:

$$\begin{aligned} Z_{em} &= j\omega L_{em} + R_{em} + \frac{1}{j\omega C_{em}} \\ Z_L &= R_L \\ Z_p &= \frac{1}{j\omega C_p'} \end{aligned} \tag{3.42}$$

The output power is given as $V_{out,rms}^2 / R_L$ and the efficiency of the system, which is defined as the ratio of the average output power to the magnitude of the input power, is calculated using the following equation:

$$\eta = \frac{P_{out,rms} \cdot |Z_{total}|}{V_{in,rms}^2} \qquad 3.43$$

Property	Symbol	Units	PZT (5A)
Piezoelectric constant	h	V/m^2	21.5×10^8
Mechanical quality factor	Q_m	-	80
Relative permittivity	ε^T	-	1900
Charge constant	d_{33}	C/N	390×10^{-12}
Elastic constant	s_{33}^E	m/N^2	18×10^{-12}

Table 3.2 Physical and mechanical properties for PZT (5A) [68]

Parameter	Symbol	Units	Value
Capacitance	$C_p^{'}$	F	7×10^{-9}
Transformer ratio	ϕ	V/N	0.055
PZT layer stiffness	K_{PZT}	N/m	1.1×10^{10}
Mass	M_m	kg	10^{-3}
Damping	B	Ns/m	1.5
Stiffness	K_m	N/m	8.9×10^4

Table 3.3 Calculated value of the mechanical properties of pre-stressed beam

Table 3.2 shows some of the PZT (5A) physical and mechanical properties that are used to calculate the mechanical properties of the pre-stressed beam shown in Table 3.3. Equation 3.30 is used to calculate the total stiffness of the pre-stressed composite beam. The total stiffness of the beam changes with the value of the radius of curvature, mounting method, displacement ability, the location of the applied force and its value. Therefore, the stiffness will be measured under different values of harmonic applied force and presented in Section 3.4.4. If the applied force is less that the force value that causes the beam to be flat (36 N), the total movement of the structure is due to the beam deflection (δ'). For this case, increasing the mean value of the applied force causes the beam stiffness to be reduced. Increasing the mean force causes the curvature

(R^{-1}) to reduce. Due to that, the location of the neutral axis moves towards the centreline of the PZT layer causing a reduction in the value of the bending modulus as discussed in Section 3.2.4 and Section 3.2.6. As a result, the resonant frequency of the structure reduces and thus the stiffness.

If the mean applied force causes the beam to be flat, the total movement of the structure will be due to a deformation within the material. In this case, the beam is no longer simply supported as the bottom layer of the structure is in contact with the supported surface. According to equation 3.23 and equation 3.30, if the bottom layer of the stainless steel is clamped, the stiffness of the beam equals to 4.78×10^9 N/m. In this case, higher applied value of the mean force causes an increase in the stiffness of the structure. The total damping of the structure is obtained experimentally in Section 3.4.2 and presented in Table 3.3.

3.4 Performance of piezoelectric pre-stressed beam

In order to evaluate the model developed in Section 3.3, the resonant frequency of the composite beam is measured and compared to the value obtained using analytical calculation. The resonant frequency and the total damping of a simply supported structure under different boundary conditions are measured. Section 3.4.1 presents the method used to measure the structure's resonant frequency, while Section 3.4.2 outlines the method used for measuring the structure damping.

3.4.1 Resonant frequency and stiffness

In order to measure the resonant frequency of the composite pre-stressed beam, the beam is mounted on a shaker. The vibration of the shaker is controlled using a PC via LabVIEW software. The shaker is operated in sinusoidal vibration over a range of different frequencies close to the calculated resonant frequency of the beam (100 Hz - 10000 Hz). The value of the acceleration is maintained at constant level 50 m$\boldsymbol{g}$ (1$\boldsymbol{g}$ = 9.8 m/s^2). A spectrum analyser is used to plot the relationship between the measured output voltage of the beam and the frequency. The resonant frequency is the one that generates the maximum amplitude. The measured fundamental resonant frequency for the simply supported beam is approximately 1532 Hz. The calculated resonant frequency is around 6.5 % less than the measured one. The difference between theses two readings is due to the fact that the full beam length is used to calculate the resonant

frequency analytically. However, to measure the resonant frequency, one side of the beam is screwed to the shaker. This reduces the length of the beam by 1.5 mm. As the resonant frequency is inversely proportional to the length of the beam, the measured resonant frequency is higher than the calculated one. The stiffness of the curved composite beam can be found using equation 3.30. Using the measured resonant frequency, the stiffness of the beam is 9.26×10^4 N/m. The increase in the stiffness is expected as the length of the beam is reduced.

3.4.2 Damping

The total quality factor Q of the structure is determined experimentally by dividing the measured resonant frequency by the full width at half maximum of the output power as follows:

$$Q = \frac{f_o}{\Delta f} \tag{3.44}$$

The value of the quality factor determines the performance of the structure. The higher the value of Q, the lower the rate of energy dissipation relative to the oscillation frequency will become. The damping ratio of the structure is calculated using the following equation:

$$\xi = \frac{1}{2Q} \tag{3.45}$$

As can be seen the structure resonant frequency is inversely proportional to the damping ratio. The mechanical damping coefficient of the structure (B) is calculated using the following equation:

$$B = 2\xi\omega_o M_m \tag{3.46}$$

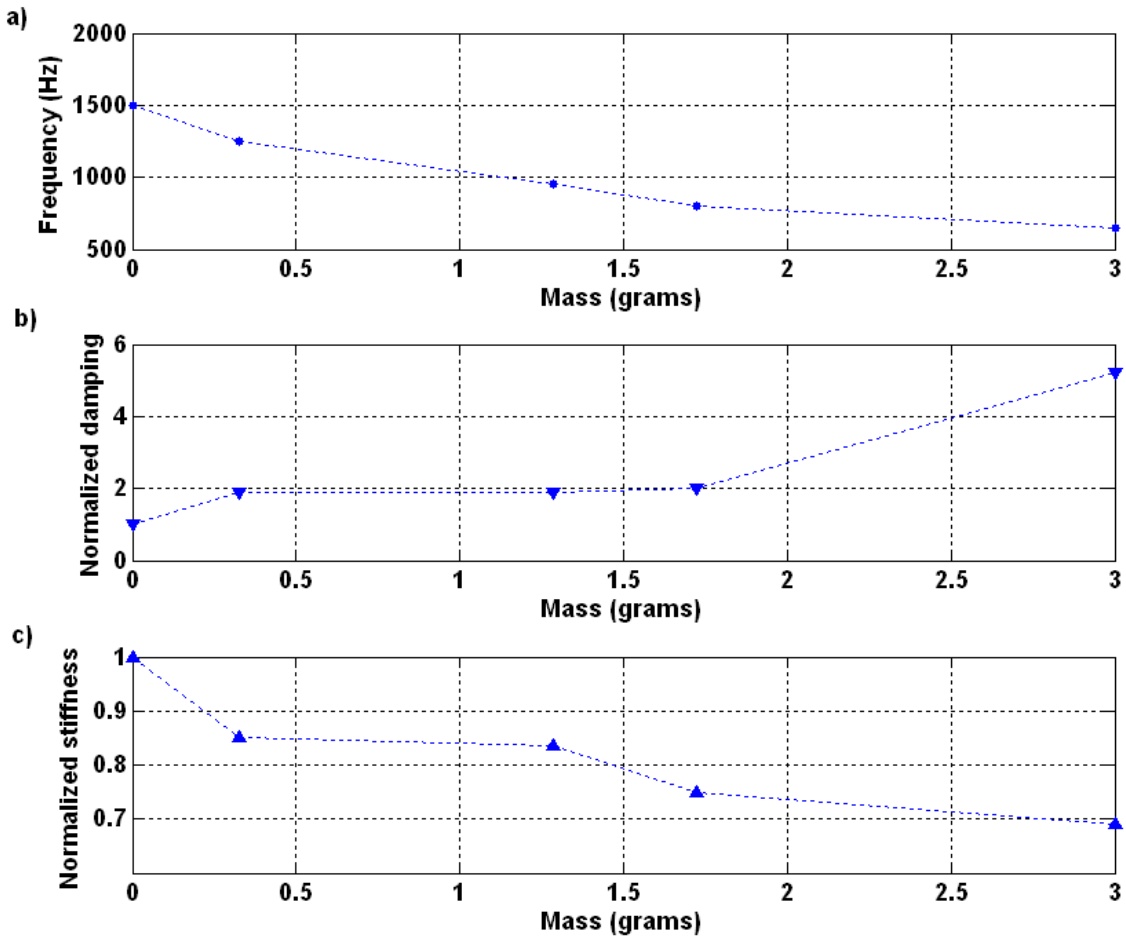

Figure 3.12 a) Frequency as a function of the attached mass, b) Normalized mechanical damping as a function of the attached mass, c) Normalized stiffness as a function of the attached mass

As stated in equation 3.39, the total damping of the pre-stressed beam is the sum of the mechanical and the electrical damping. The maximum output power is generated when the electrical damping match the mechanical damping. The electrical damping can be controlled by changing the value of the resistive load connected to the beam. According to equation 3.38 the maximum power is obtained when $R_L = \frac{1}{(\omega C_p')}$. The effect of attaching a proof mass at the middle of a simply supported curved composite beam on the damping ratio is investigated. Adding a mass lowers the resonant frequency of the curved beam as shown in equation 3.30. The attached mass reduces the value of the radius of curvature and thus reduces the resonant frequency of the structure. Moreover, the added mass induces more stress on the structure, which increases the mechanical damping. Figure 3.12 (a), Figure 3.12 (b) and Figure 3.12 (c) show the experimental results of the effect of the attached mass at the middle of Thunder™, model TH 10-R on the structure frequency, normalized mechanical

damping, and the normalized stiffness. As the mechanical damping of the structure increases due to the attached mass, the electrical damping presented in the load resistance gets higher. The experimental value of the damping ratio of the simply supported structure is approximately 0.12. This value reduces as the value of the attached mass increases.

As can be seen, the values of the structure stiffness, damping and resonant frequency depend on the materials parameters, dimensions of the structure and the method that the structure has been mounted. As the values of the piezoelectric material constants are measured using the impedance measurement which involves using a small excitation signal with high applied frequency (1 kHz). The values of these parameters depend on the electrical and mechanical boundary conditions. Moreover, the application by which the curved composite beam is used happens at low frequency and high amplitude. Therefore, it is more accurate to measure the stiffness and the damping. Figure 3.12 illustrated that the stiffness of the structure reduces and its damping increases as the compression force increases. If the applied compression force causes the curved beam to be flat, the beam will no longer be simply supported. In this case, the composite beam considered to be rigidly clamped at the bottom surface of the stainless steel layer. Section 3.4.3 presents the method by which the effect of the applied compressed force on both the damping and the stiffness is measured. For this experiment, a compression force value that is equal and higher than the one that causes the beam to be flat (36 N) is applied.

This can be determined by measuring the system response to a known input signal. After that equation 3.33 can be used to relate the equivalent electric parameters back to the physical mechanical parameters. Using the circuit model shown in Figure 3.11, the output voltage across the resistive load, under a sinusoidal input force, can be calculated using equation 3.41. In this equation, the unknown values of the four electrical elements (R_{em}, L_{em}, $C_{em,}$ C_p') and the transformer ratio (ϕ) can determined by applying non-linear least squares fit to the measured output voltage under known sinusoidal input force for various values of the load resistance.

3.4.3 Test setup

The experimental tests were obtained by subjecting the piezoelectric element (pre-stressed Thunder™ beam) to various cyclic mechanical loads using an ElectroPuls, E1000 fatigue test machine. This machine is controlled using software

provided with the test machine. The software is capable of applying various force or displacement waveforms to the piezoelectric element, which is fixed on the bottom head as shown in Figure 3.13. The applied forces are measured using a calibrated load cell. Moreover, both the force and the displacement waveforms are monitored using the software. In order to analyze the response of the piezoelectric pre-stressed beam, a fixed compression force equal to 35 N with a cyclical force is applied. A PC running a custom LabVIEW application is used to measure the output voltage. Under each input force waveform the average output voltage is measured across various load resistance ranging form 100 Ω to 5 kΩ. The mechanical characteristics of the pre-stressed beam are calculated using the piezoelectric model as explained in Section 3.3. Two different cyclic loads are applied; a 5 Hz sinusoidal waveform with amplitude changing from 10 N to 25 N and a 15 N waveform with frequency changing from 5 Hz to 25 Hz. The output voltage generated by the piezoelectric element were measured under different cyclic input forces and compared to the one predicted by the model in order to verify and test the model.

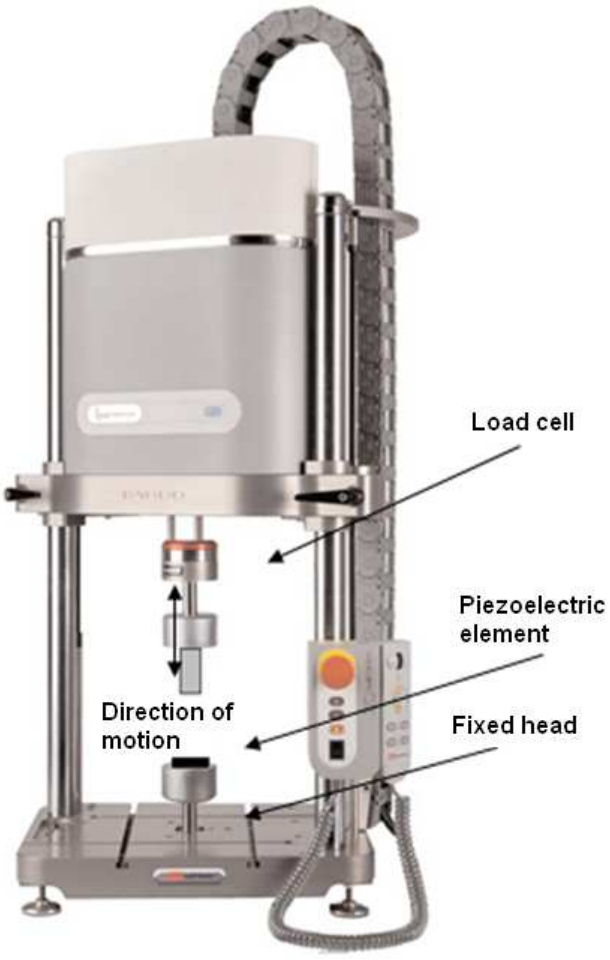

Figure 3.13 Layout of the experimental setup

3.4.4 Damping and stiffness of piezoelectric pre-stressed beam

As an example, Figure 3.14 shows the output voltage across various load resistances for a sinusoidal input force with a mean force of 35 N and peak to peak amplitude of 15 N and frequency of (25 Hz). The curve presents the model fit while the squares present the measure voltage across the load resistance. The average output power as a function of the resistive load is presented in Figure 3.15. It is found that, the values of the electromechanical model parameters change as the input force amplitude and frequency change. As the applied force causes the beam to be flat, different boundary conditions are applied. The measured stiffness is approximately 5.2×10^9 N/m.

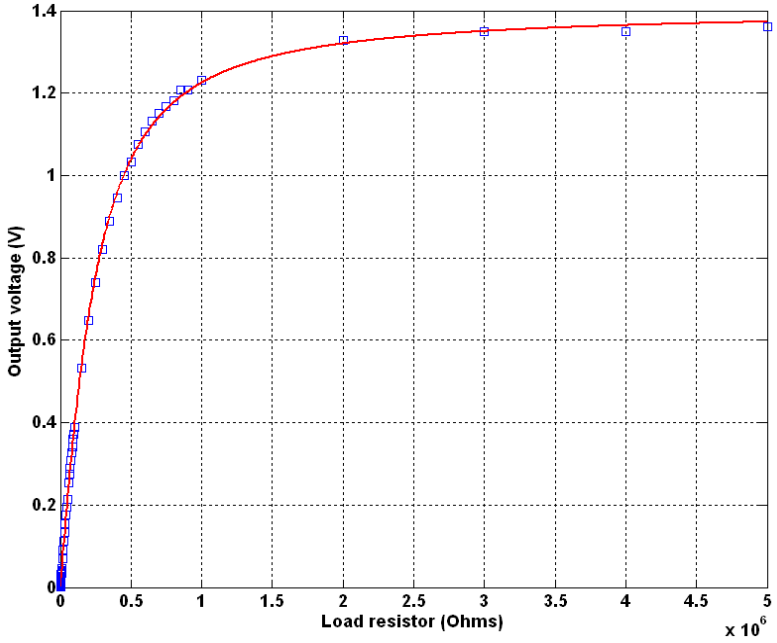

Figure 3.14 The voltage across the resistive load with the model fit

The effects of the amplitude and the frequency of the input force on the stiffness and the damping of the Thunder™ are presented in Figure 3.16 and Figure 3.17. A compression force of 35 N has been applied to the beam with an amplitude input force of 15 N. In this experiment the input frequency is increased from 5 to 25 Hz and the change of the beam damping (Figure 3.16 (a)) and stiffness (Figure 3.16 (b)) has been measured.

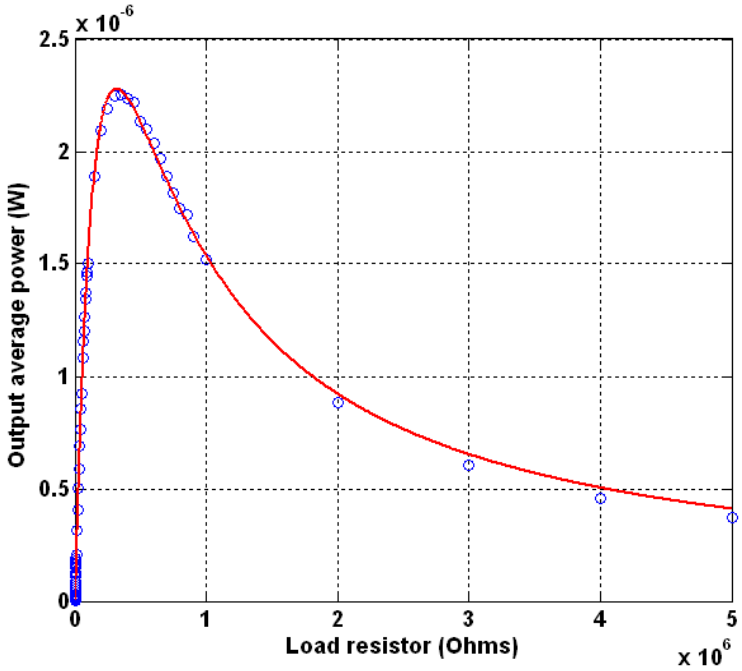

Figure 3.15 Experimental and model fit results of the output power as a function of the resistive load

As the amplitude of the input force is constant, increasing the frequency of the input force reduces the beam damping by 85 % and increases its stiffness by 55 % when the frequency changes from 5 to 25 Hz.

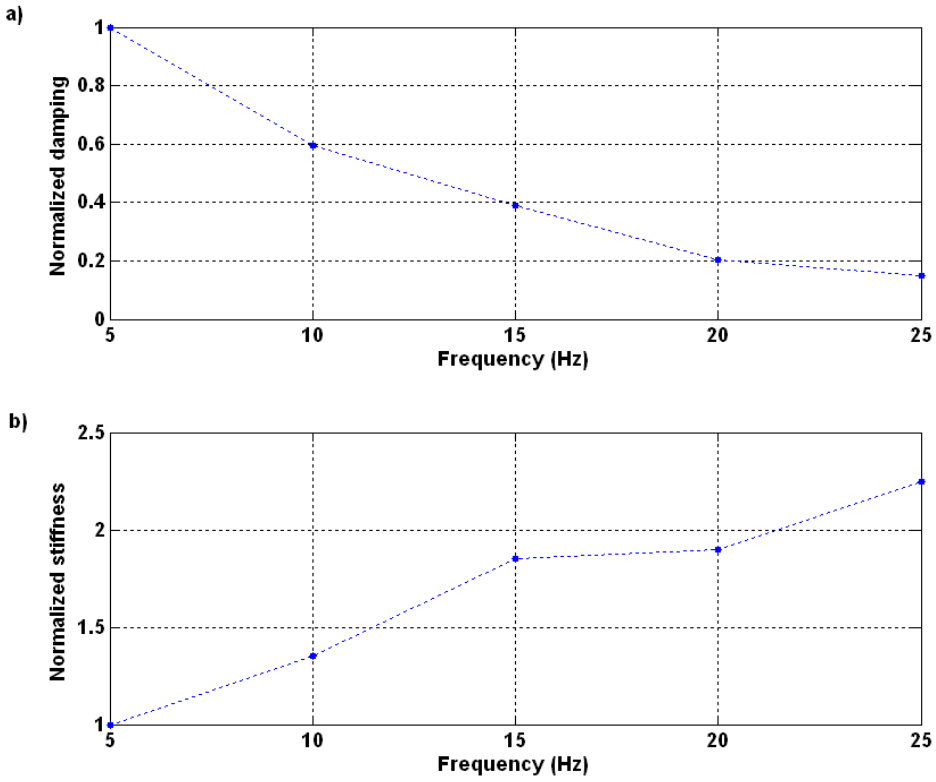

Figure 3.16 a) Normalized experimentally measured values of damping versus input frequency, b) normalized experimentally measured values of stiffness versus input frequency

In order to investigate the effect of the amplitude of the input force, a compression force of 45 N has been applied to the beam at a frequency of 5 Hz. The amplitude of the input force is increased from 10 to 25 N and the change of the beam damping (Figure 3.17 (a)) and stiffness (Figure 3.17 (b)) has been measured.

As can be seen, as the frequency of the input force is held constant, increasing the amplitude of the input force reduces the beam damping by 73 % and increases its stiffness by 11 % when the input force amplitude changes from 10 to 25 Hz. As more force is applied to the beam, this causes the beam curvature to reduce and thus increases the stiffness of the beam.

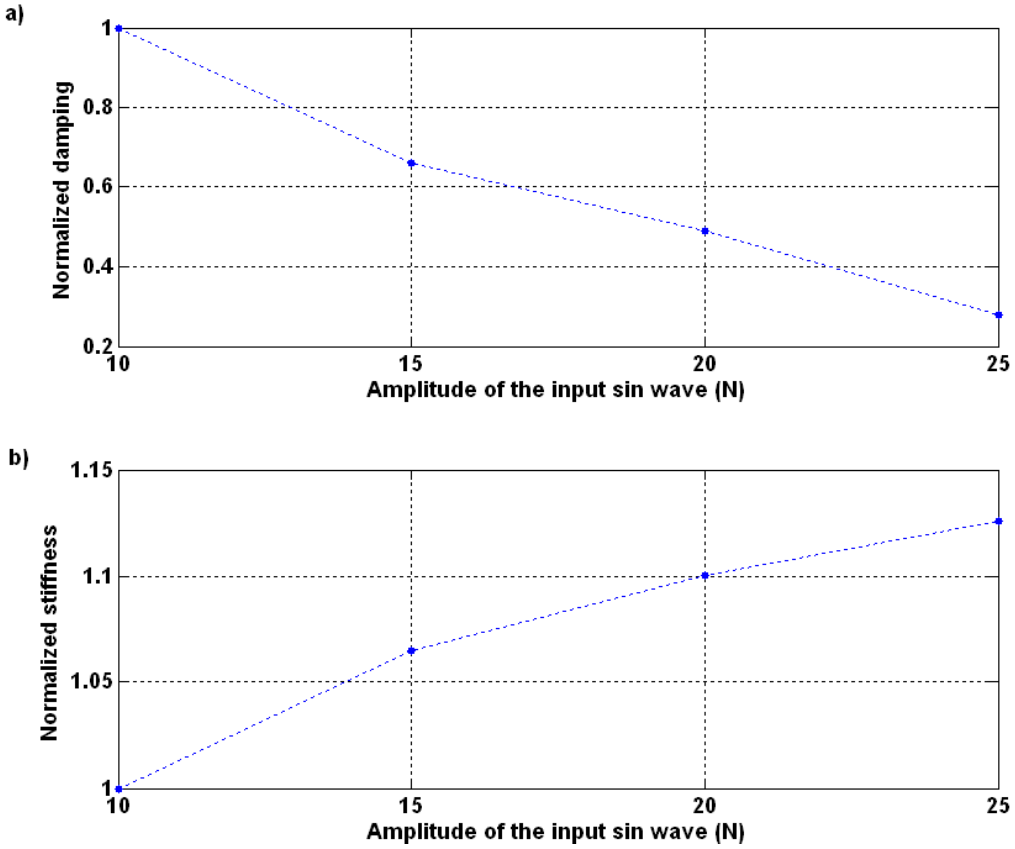

Figure 3.17 a) Normalized experimentally measured values of damping versus input force, b) normalized experimentally measured values of stiffness versus input force

3.4.5 Output power generated by piezoelectric pre-stressed beam

Figure 3.18 presents the average output power across various load resistance. Increasing the frequency causes the output power to increase.

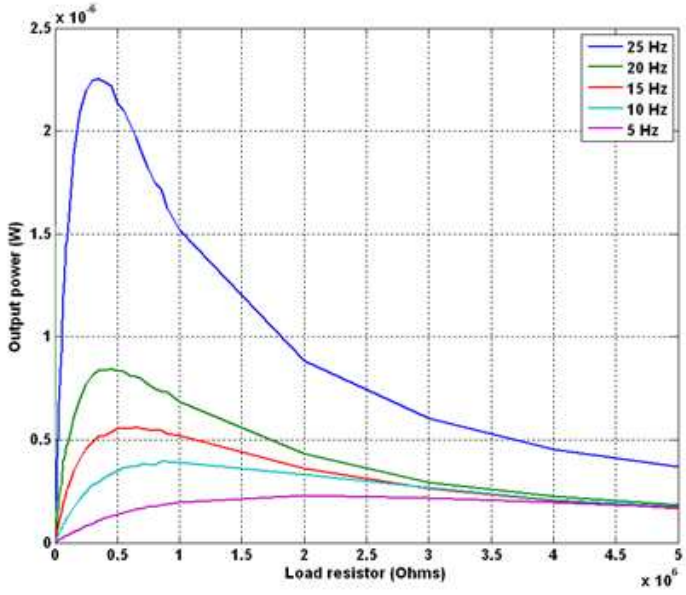

Figure 3.18 Output power as a function of resistive load at different values of the input frequency

Figure 3.19 shows the average output power across various load resistances. Increasing the amplitude of the input force causes the output power to increase. Comparing Figure 3.18 with Figure 3.19 illustrates that the output power depends not only on the amplitude and the frequency of the input force, but also on the main compression force. Changing the main compression force from 35 to 45 N, causes the output power to drop by more than an order of magnitude. In this situation, the beam was subjected to an input force with an amplitude of 15 N at frequency of 5 Hz. This can be explained as increasing the compression force leads the beam damping to increase by one order of magnitude causing the output power to drop.

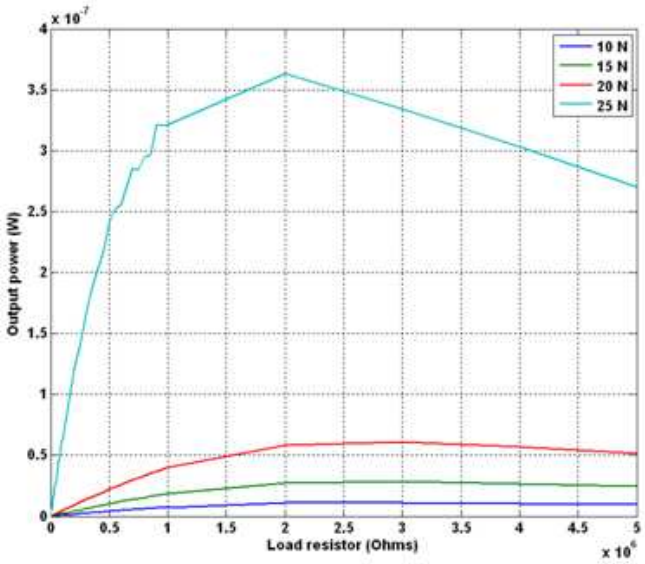

Figure 3.19 Output power as a function of resistive load at different values of input force

3.4.6 Efficiency

Using equation 3.43, the efficiency is calculated for a range of frequencies and load resistors using the parameters measured experimentally (Figure 3.20). The input force is sinusoidal with 15 N amplitude and compression force of 35 N. As can be seen, as the input signal frequency increases, the maximum efficiency occurs at lower values of the load resistor. This is due to the fact that the source impedance (Z_p) is inversely proportional to the input frequency. Moreover, the efficiencies tend toward higher values as the input frequency increases. Figure 3.21 shows the efficiency as a function of the load resistor at different values of the input force amplitude ranging from 10 N to 25 N with a constant compression force of 45 N. the input force frequency is hold constant at 5 Hz. As can be seen, the maximum efficiency can be obtained at a narrow range of load resistor at which the source and the load impedance match. As the input force amplitude increases from 10 to 20 N, the efficiency increases. However, any further increase in the amplitude of the input force causes the value of the efficiency to drop. This indicates that the increase in the force acts to increase the losses in the system rather than the output power. This will be explained in more detail in Section 4.5.3.2.

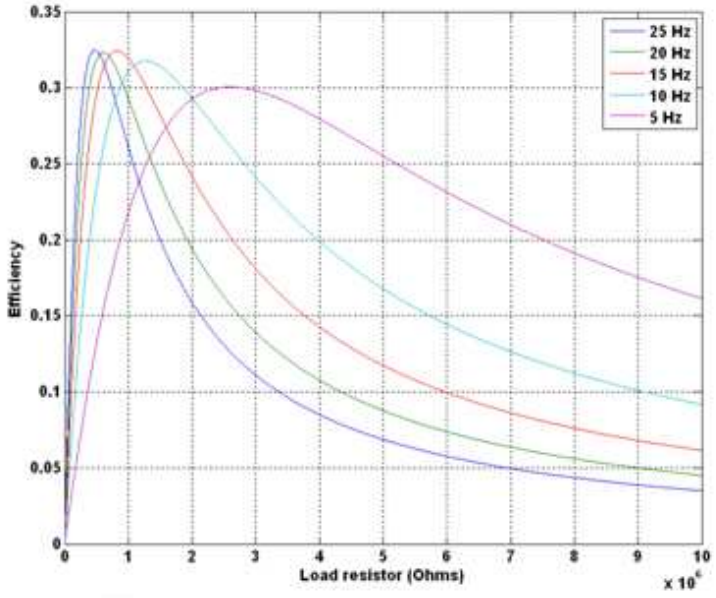

Figure 3.20 Efficiency as a function of resistive load at different values of the input frequency

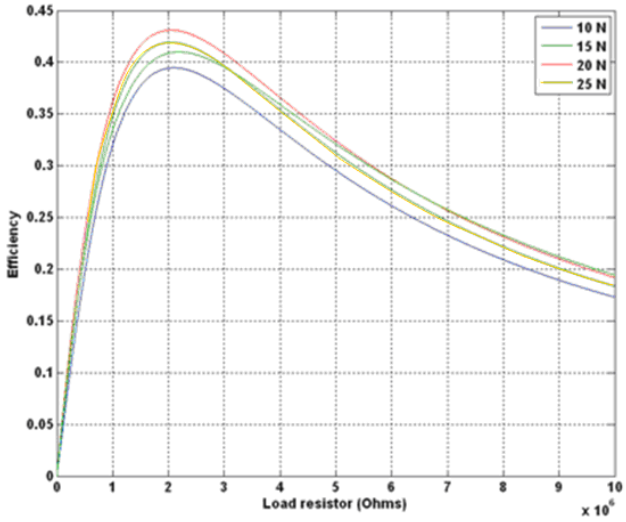

Figure 3.21 Efficiency as a function of resistive load at different values of input force

3.5 Conclusions

There are a many challenges in fabricating or buying an available commercial piezoelectric element for energy harvesting. The physical dimensions, shape, type of materials and the clamping method affect the behaviour of the piezoelectric structure and thus the amount of the generated output power. The configuration and the clamping method of the piezoelectric element depend on the environment by which the mechanical energy is converted into electrical one. The effect of the thermal stress on the curvature of the composite beam was analysed theoretically. The maximum deflection was found to be located in the middle of the beam. The effect of the curvature on the resonant frequency of the beam was investigated. It was found that the resonant frequency of the beam increased as the curvature value got higher. Thunder™ beam model TH-10R was analysed theoretically and tested in order to investigate the effect of the applied force on its behaviour. Theoretical results showed that the maximum applied load that caused the Thunder™ beam to be flat was 35.9 N. The calculated resonant frequency of the Thunder™ beam was found to be 1432 Hz, when it was simply supported and 578 Hz, when it was mounted as a cantilever. A general model of a piezoelectric harvester that can be used to predict the output power was presented in this chapter. The experimental tests carried out on the Thunder™ beam showed that the values of its stiffness and damping varies with the applied force due to the effect of the curvature. For a given input force, the stiffness and the damping of the

Thunder™ beam can be measured experimentally and then used in the model to predict the output power.

Chapter 4

Simulation of the impact based piezoelectric harvester

4.1 Introduction

This chapter presents the principle of using an impact based piezoelectric harvester to convert kinetic energy into electrical energy using a Thunder™ beam. In this method, the output power is generated due to impact between the piezoelectric element and the mass. The principle is explained in detail in Section 4.2. The main purpose of the harvester is to harvest energy from rotation. The forces that affect the piezoelectric harvester undergoing a rotational motion are analyzed. The behaviour of the harvester mounted at a particular distance from the centre of rotation is analysed.

The effect of mounting the piezoelectric harvester in different ways on a rotating wheel is discussed in Section 4.3. As the output power of the piezoelectric transducer depends on the amount of strain developed within the piezoelectric element, ANSYS software is used to simulate the effect of clamping of the Thunder™ beam on the developed strain in the piezoelectric structure for a given input force.

The Thunder™ beam is clamped in three different ways; rigidly supported at both ends, simply supported and as a cantilever (Figure 2.26). For a given input force, the effects of clamping on both the output voltage and the developed stress in the structure are analysed using FEM. The effect of the harvester size and dimensions on the output power when the Thunder™ beam is simply supported is investigated.

For this design, the output power is generated due to a direct impact between the piezoelectric beam and the mass. The harvester uses rotational forces as a source of

kinetic energy to produce electrical power. The effect of rotational forces on the behaviour of the harvester is addressed. In order to evaluate the device performance an analysis of the dynamics of the system is coupled to a model of the piezoelectric harvester. The effects of the impact force on the Thunder™ pre-stressed beam are examined analytically and numerically. The maximum applied stress that the structure can withstand and thus the maximum applied force that can be applied is determined.

4.2 Structure of the harvester and operating principle

A cross section of a proposed impact based piezoelectric harvester is shown in Figure 4.1. This device transforms the forces due to rotation into electrical energy. The harvester consists of a tube with a Thunder™ pre-stressed beam mounted at each end. The tube allows a small ball bearing to move freely, in response to forces acting on it and hence, impact on the transducers. The kinetic energy is converted into electrical power by the harvesters. The deflection of the piezoelectric transducer due to the impact of the ball bearing generates a current flowing into the resistive load which is connected to the transducer. Therefore, the motion of the ball bearing is damped and the power is dissipated into the load resistance.

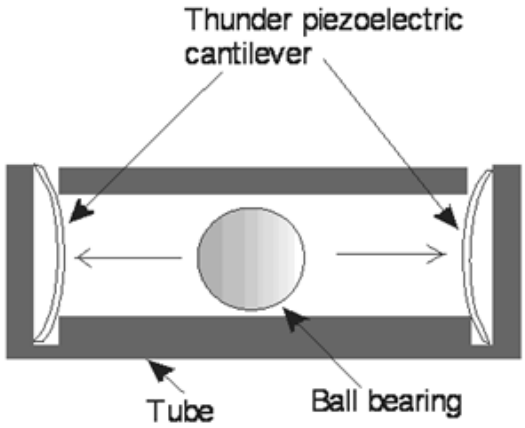

Figure 4.1 Cross section of the proposed piezoelectric harvester

The impact is produced due to the relative motion between the frame and the mass. In order to reduce the frictional force between the mass and the frame and to increase the life of the mass, a ball bearing is used. A ball bearing exhibits a low friction coefficient, i.e. 10^{-2} [74]. As the maximum power is generated when the applied force is in the same direction as the free movement of the mass, a straight tube is chosen. Moreover, the tube must be mounted in a way that the applied rotational forces are in the same direction as the mass movement. In this case, the rotational motion of

the wheel is converted into linear motion. The total resultant force on each pre-stressed beam is the sum of the rotational force and the impact force from the ball bearing. The model which explains the movement of the mass and the behaviour of the piezoelectric element under impact is explained in Section 4.5. The key parameters of the model are the value of the mass, the properties of the piezoelectric material, the internal displacement of the mass and the equivalent mechanical damping due to the power dissipation in the load resistor.

The type and the way that the piezoelectric beam is attached to the frame affects the amount of strain developed in the material, the mechanical stability and the structure sensitivity under the applied load as presented in Section 4.4.2.

4.3 Method of mounting the piezoelectric harvester

This section outlines different ways of mounting the piezoelectric harvester on a rotating wheel. The effect of rotational forces on the behaviour of the ball bearing and thus the output power is addressed. Tangential and centripetal forces act on the mass due to rotation. Another force that can affect the mass is the gravitational force. The effect of each force on the mass depends on the way that the harvester is mounted and its orientation. The considered orientation of the harvester is the one where the maximum applied rotational forces are in the same direction as the free movement of the mass. This maximizes the work done on the mass and hence generates more output power. In terms of the main acting rotational force on the mass, two methods of mounting the harvester on a rotating wheel are addressed. In the first method, the main acting force is the gravitational and tangential forces, whereas, in the second method the main acting force is the centripetal force. An analytical analysis about the dynamic behaviour of the harvester is explained when the main acting force is tangential and centripetal in Sections 4.3.1 and 4.3.2, respectively. The impact force from the ball bearing on the piezoelectric element depends on the mounting method.

4.3.1 Effect of gravitational force

In this method the harvester is mounted directly into a rotating wheel as shown in Figure 4.2. The acting forces on the mass are the tangential force and the components of both the centripetal force ($F_{ce(x)}$) and the gravity force that are acting in the direction of the free movement of the ball bearing. Under uniform circular motion the tangential

force acting on the mass is zero and thus the other two components (gravity and centripetal forces) are the main acting forces on the mass of the harvester. In order to know the behaviour of the ball bearing under rotation, the applied forces on the ball bearing are analyzed. Figure 4.2 shows the forces that affect the ball bearing under constant rotating speed, where the rotating direction is clockwise. The frame is mounted in a way that the direction of the centripetal force (F_{ce}) is perpendicular to the free movement of the ball bearing in the middle of the frame. For most applications, the rotor rotates under a constant rotating speed. Therefore, the analysis will be carried out under uniform circular motion.

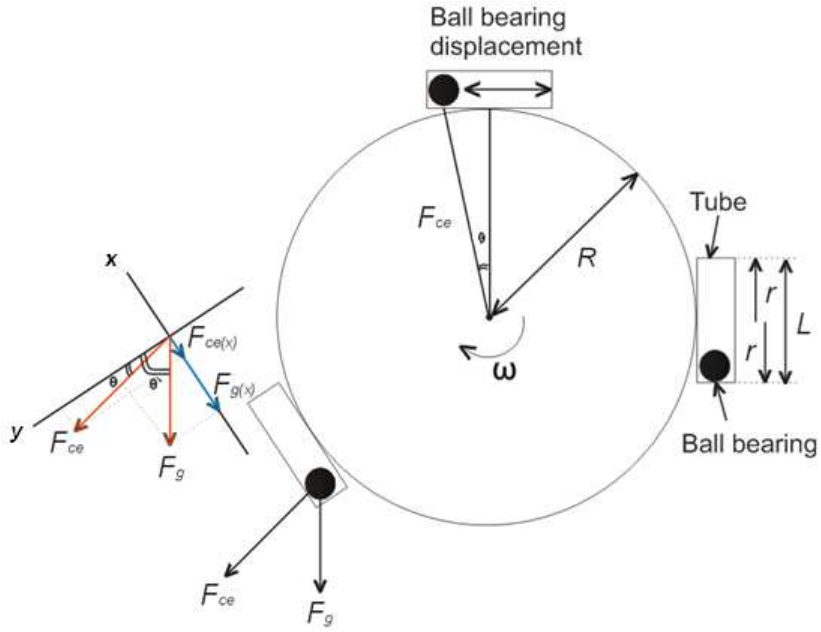

Figure 4.2 Applied force on the piezoelectric transducer under uniform circular motion

The component of the centripetal force affecting the movement of the mass is given by the following equation:

$$F_{ce(x)} = \frac{mv^2}{R}\sin\theta = m4\pi^2\omega_f^2 R\sin\theta \qquad 4.1$$

where θ is the angle between the direction of the centripetal force acting on the mass and the vector perpendicular to the free movement of the ball bearing. This angle can be obtained by the following equation:

$$\tan\theta = {}^{+}_{-}\frac{r}{R} \qquad \left\{\begin{matrix} 0 \geq |r| \geq L/2 \\ 0 \geq |\theta| \geq \theta_{\max} \end{matrix}\right\} \qquad 4.2$$

where L is the length of the frame and R is the distance between the frame and the centre of rotation. The component of the gravity force that affects the movement of the ball bearing can be given by the following equation:

$$F_{g(x)} = 9.8 \sin \theta' \qquad 4.3$$

where θ' is the angle between the direction of the gravity force and the vector perpendicular to the free movement of the ball bearing. Therefore, the total force acting on the ball bearing is the sum of the gravitational and the centripetal forces acting in the direction of the free movement of the ball bearing. When the gravity component is higher than the centripetal component, the ball bearing drops to one end of the frame. Therefore, the ball bearing collides with each side of the frame once during one cycle due to the effect of the gravity force. Increasing the rotating speed increases only the magnitude of $F_{ce(x)}$ as the magnitude of F_g is constant. The direction of $F_{ce(x)}$ always acts against the direction of F_g trying to keep the ball at one end of the frame. Therefore, increasing the value of $F_{ce(x)}$ reduces the amplitude of the total force acting on the ball bearing and thus the impact force produced by the bearing on the piezoelectric element. When the amplitude of the acting component of the centripetal force ($F_{ce(x)}$) is equal to or more than the maximum value of the gravitational force, the ball bearing will be pushed to one side of the frame.

$$4\pi^2 \omega_f^2 R \sin[\tan^{-1} \frac{r}{R}] \geq 9.8 \qquad 4.4$$

Thus the critical rotating speed by which the ball bearing sticks to one end of the frame is given by the following equation, where r equals to $L/2$:

$$\omega_{f(critical)} = \sqrt{\frac{9.8}{4\pi^2 R \sin[\tan^{-1} \frac{L}{2R}]}} \qquad 4.5$$

From equation 4.5 $\omega_{f(critical)}$ does not depend on the distance between the frame and the centre of the rotating object (R). This is because increasing R reduces θ, for a given frame length, but increases the magnitude of the component of the centripetal force that is acting on the ball bearing. Increasing the length of the frame, on the other hand, results in reducing the value of rotational speed required to hold the ball at one end of the frame.

Figure 4.3 shows the case where the distance between the beginning of the frame and the point where the direction of the centripetal force is perpendicular to the free movement of the ball bearing equals to ΔL.

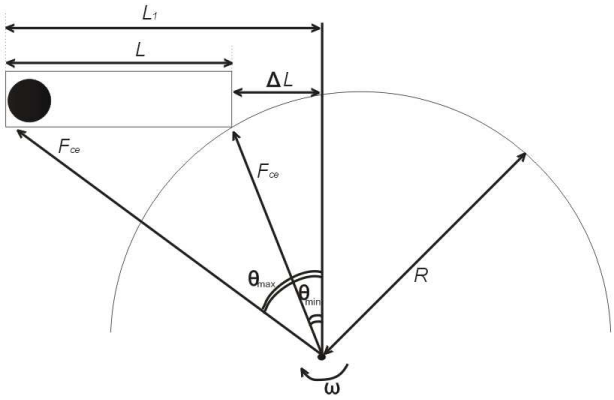

Figure 4.3 The direction and magnitude of $F_{ce(x)}$ at different points inside the frame

In this situation the maximum value of θ is given by equation 4.6, where L_1 is the distance between the vector of centripetal force acting perpendicular to the free movement of the ball bearing and the end of the frame:

$$\tan\theta = \pm\frac{r}{R} \qquad \left\{\begin{array}{l}\Delta L \geq |r| \geq L_1 \\ \theta_{\min} \geq |\theta| \geq \theta_{\max}\end{array}\right\} \qquad 4.6$$

In this situation, increasing the value of ΔL reduces the value of the critical rotating speed by which the ball bearing will stick to one end of the frame. In order to verify equation 4.4, a simulation using Working Model software is carried out. This software enables limited physical motions to be simulated. The results from equation 4.4 are compared to the simulation results. Figure 4.4 shows the simulation results when the mass displacement (L) is twice the mass diameter at a value of 2 cm.

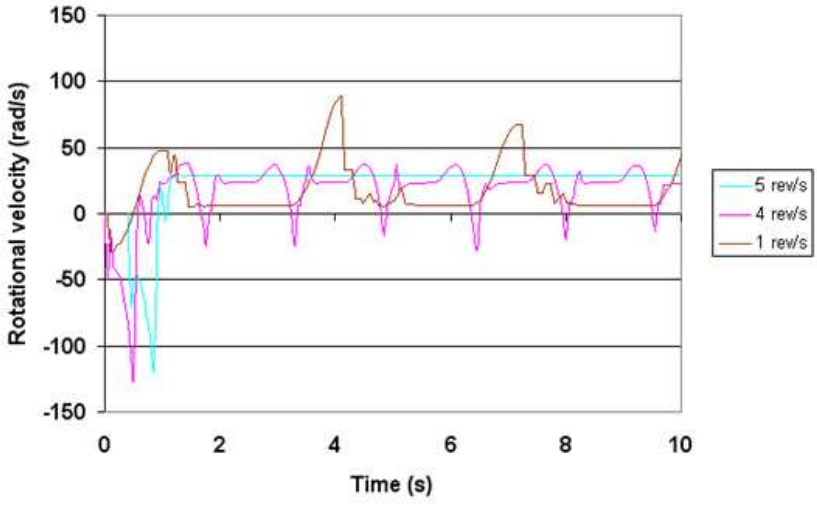

Figure 4.4 Simulation of the ball bearing movement under gravitational force (L = 2 cm).

The frame is mounted in a way that the direction of the centripetal force (F_{ce}) is perpendicular to the free movement of the ball bearing in the middle of the frame. The critical rotating speed by which the ball bearing sticks to one end of the frame is 5 rps. Therefore, mounting the harvester in this position is suitable for an application where the rotating speed is low. This allows the mass to move from one side of the frame to the other and to generate output power due to the relative motion between the mass and the frame. Under the same conditions equation 4.4 predicts that the critical rotating speed is 5 rps when r is replaced by $L/2$.

Figure 4.5 shows the simulation results when a ΔL with a value of 1 cm is introduced. The critical rotating speed is reduced to 3 rps. At this speed, the ball bearing sticks to one end of the frame. This creates no relative motion between the frame and the mass. Under the same conditions equation 4.4 predicts that the critical rotating speed is 3 rps when r is replaced by L_1. Under variable rotating speed, the tangential forces contribute to the movement of the ball bearing beside the other two components. The direction of this force always acts opposite to the direction of the gravity components. Therefore, the critical rotating speed will be reduced by $m\frac{dv}{dt}$, where v is the linear speed. This method of mounting the harvester on a rotating wheel will be referred to as GF, because the main acting force that causes the mass to move from one side to another is the Gravity Force.

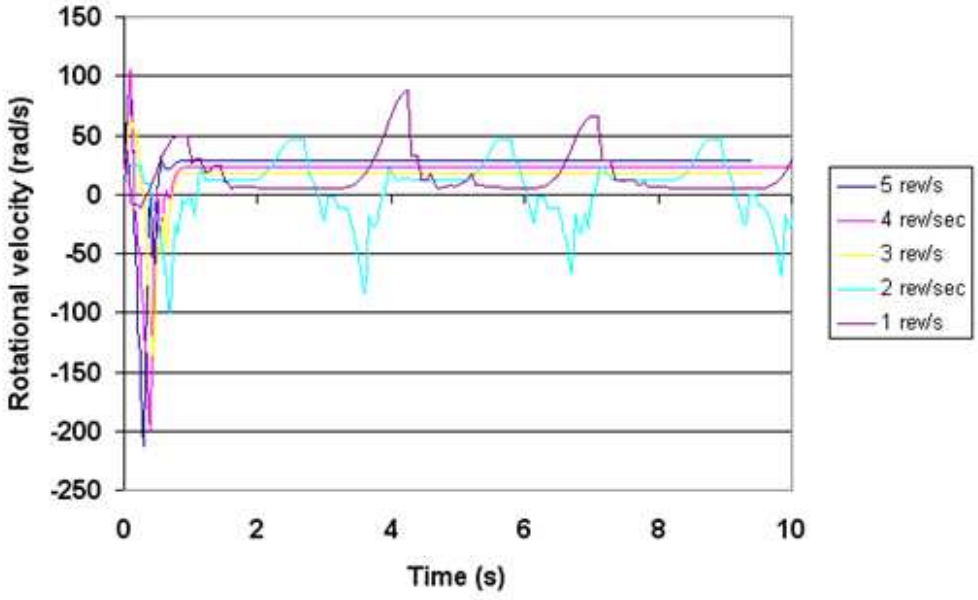

Figure 4.5 Simulation of the ball bearing movement under gravitational force (L = 2 cm and ΔL=*1 cm*).

4.3.2 Effect of centripetal force

Unlike the tangential force the centripetal force is always a result of rotational motion under uniform and non-uniform circular motion. Therefore, centripetal force can be used as the main acting force on the proposed harvester presented in Section 4.2. As previously mentioned, the maximum work is achieved when the direction of the applied force is in the same direction as the free movement of the mass. However, the direction of this force must be under constant change in order for the mass to move inside the tube. In order to achieve that, the tube must be kept in a horizontal position while rotating as shown in Figure 4.6. Unlike the GF method, this method requires a mechanical support to keep the harvester in a horizontal position while the wheel is rotating. This method of mounting the harvester on a rotating wheel is referred to it as CF because the main acting force that causes the mass to move from one side to another is the Centripetal Force.

As the extracted power from the piezoelectric elements depends on the applied forces, these forces should be calculated first. In this section the direction and the amplitude of the main acting rotating force are analyzed under uniform circular motion assuming that the harvester is kept in a horizontal position and the rotation is clockwise. In case the ball bearing is removed from the system, the force that affects the piezoelectric beams is the component of the centripetal force which is acting in the direction of the free movement of the piezoelectric beam. Therefore, the force that is acting on the piezoelectric beam located on the right side of the tube is given by equation 4.7, while the piezoelectric beam located on the left side will be subjected to force that can be calculated using equation 4.8. The methods by which these equations have been obtained are explained in Appendix A.

$$F_{ceR(x)} = m4\pi^2\omega_f^2 R_1 \sin\theta + m4\pi^2\omega_f^2 \frac{L}{2} \tag{4.7}$$

$$F_{ceL(x)} = m4\pi^2\omega_f^2 R_1 \sin\theta - m4\pi^2\omega_f^2 \frac{L}{2} \tag{4.8}$$

where R_1 is the distance between the centre of rotation and the point located in the middle of the frame. θ is the angle between the direction of the centripetal force acting on the object under study and the vector perpendicular to the free movement of that object, for example the piezoelectric beam. L is the length of the harvester, ω_f is the rotating frequency and m is the effective mass of the piezoelectric beam. The

magnitude of component of the centripetal force acting on both piezoelectric beams is proportional to the distance between the centre point of the frame and the centre of rotation. Moreover, this applied force is proportional to the square of the rotating speed.

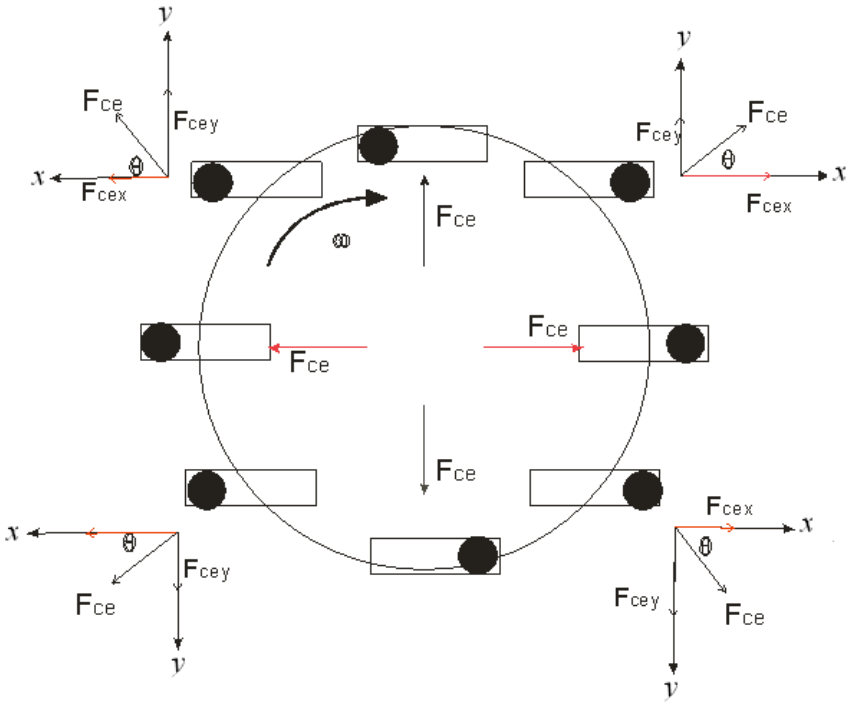

Figure 4.6 Applied force on the piezoelectric transducer under uniform circular motion

Equation 4.7 and equation 4.8 show that the effect of centripetal force on the piezoelectric harvester that is mounted on a rotating wheel in a horizontal position during rotation is a pure sinusoidal signal. This analytical study is carried out without using a mass. By introducing the ball bearing into the system the applied force on the piezoelectric transducer located at both ends of the frame will increase. This force is the sum of the centripetal force and the impact force from the ball bearing. The total force acting on the piezoelectric beams due to the impact is analyzed numerically in Section 4.5.3. However, a simple physical explanation of the movement of the ball bearing inside the tube can be analysed as following. The acting component of the centripetal force tries to move the ball bearing from one side of the tube to another and keeps it there until the direction of the centripetal forces changes. At this point the ball bearing will be released and forced to move to the other side of the tube. Therefore during one rotating cycle, the centripetal acceleration forces the mass to move from one side of the frame to another. Under non-uniform circular motion the acting component of the tangential force works in the same direction as the acting component of the centripetal force if the object is speeding up.

4.3.3 Comparison between the effect of gravitational force and the effect of centripetal force

Rotational motion is used to generate electrical energy using an impact based piezoelectric harvester. The way that the harvester is mounted on a rotating wheel affects both the behaviour of the mass and thus the output power. For the GF method, the main acting forces are the tangential force and the components of the centripetal force and the gravitational force acting in the same direction as the free movement of the mass. The tangential force is available only when the rotating speed is changing. In this method, the output power due to the gravitational force can only be generated due to impact at low rotating speed. This is due to the fact that when the rotating speed reaches a critical value the ball bearing stays at one end of the frame due to the effect of the centripetal force. Therefore, a different method of mounting the harvester on a rotating wheel is required when the centripetal acceleration is higher than the gravitational acceleration. Therefore, the centripetal force can be used as the main source of producing an impact force on the piezoelectric element. This method is called CF. In order to maximize the work done by this force the direction of the centripetal force must be in the same direction as the mass movement. However, if the direction of the centripetal force is held constant, the ball bearing will be pushed to one end of the frame and thus no relative movement between the mass and the frame can be achieved. Therefore, a mechanical mechanism is needed to keep the harvester in a horizontal position during the wheel rotation. In this case, the effect of the centripetal force on the harvester can be described as sinusoidal. Unlike CF method, the GF method can be fitted directly to the rotating wheel. The GF can be only used at low rotating speeds, while the other method can be used at any rotating speeds. The power level from a device which is mounted using CF method is predicted to be higher than the one which uses GF method. This is due to the fact that the output power depends on the applied force on the piezoelectric element. In the CF method the main acting force is the centripetal force while in the GF method the main acting force is the is the vector sum of the gravity force, the centripetal and the tangential forces. The last two forces try to reduce the effect of the gravity force. Therefore, the CF method will be used as the main way of generating power from rotation. The dynamic behaviour of the ball bearing when the generated mounted using the CF method is simulated. The simulation reveals that a multiple impact situation occurs between the mass and the piezoelectric pre-stressed beam. Then both of the mass and the beam behave as one body until the

centripetal acceleration changes its direction. At this point the mass will be ejected to the other end of the frame. In the next section, the estimated output power is calculated.

4.4 Computational analysis using ANSYS

Thunder™ pre-stressed beam is a complex structure. Therefore, the developed stress within the structure is analysed using finite element method (FEM). A model is created using ANSYS software as presented in Section 4.4.1. The effect of clamping the beam is analysed numerically under an impulse force. Simply supported, rigidly supported and a cantilever are the three configurations that are analysed. The aim of this analysis is to understand the effect of clamping on the stiffness of the structure as well as the amount of stress developed in the clamped area. The finite element method (FEM) is used to understand the developed stress in the structure after an impulse force is applied to the centre of the curved beam. In ordered to reveal the main developed stress in the structure, stresses in the axial, lateral directions and shear stress are analysed. The resonant frequency of Thunder pre-stressed beam is calculated numerically using FEM.

4.4.1 Pre-stressed beam model

The ANSYS software is used to simulate the behaviour of the pre-stressed beam under an impulse force. ANSYS uses the finite element method to simulate the physical behaviour of complex structures. This complexity can be due to the geometry of the device, its scale or governing equations. These structures can be analysed using finite element method (FEM), which is a numerical approach of deconstructing a complex system into very small pieces called elements. The software implements equations that govern the behaviour of these elements and tries to solve them. This creates a comprehensive explanation of the behaviour of the entire system. These results then can be presented in graphical form.

Numerical analyses of the behaviour of the Thunder™ beam using ANSYS is achieved by following certain steps. Firstly, the geometry of the structure is built and the material properties are defined. The model of the curved beam consists of two layers glued together, a PZT (5A) layer and a stainless steel layer. A thin layer of electrode is applied on both sides of the piezoelectric layer. The top layer is made of PZT (5A) followed by a layer of stainless steel each of which is 0.2 mm thickness. The

top layer has a length of 1.27 cm and the bottom layer has a length of 2.54 cm. both layers have the same width of 1 cm. The beam deflection is 0.6 mm. The properties of the materials used are presented in Table 3.1. Secondly, the structure is divided into elements by generating a mesh. The size of the element is achieved by dividing the thickness, length and the width of the structure by 8, 100 and 20, respectively. The element size is chosen to ensure numerical convergence.

After designing the curved beam, constraints such as boundary conditions and physical loads are applied to the structure. Finally, the solution domain is defined and the obtained results are presented. As a solution, a transient analysis is used to simulate the effect of the dynamic force (impact). An impulse load with a magnitude of 10 N and width of 3×10^{-5} m is applied along the *y* direction to the central point located at the surface of the piezoelectric layer (Figure 4.7).

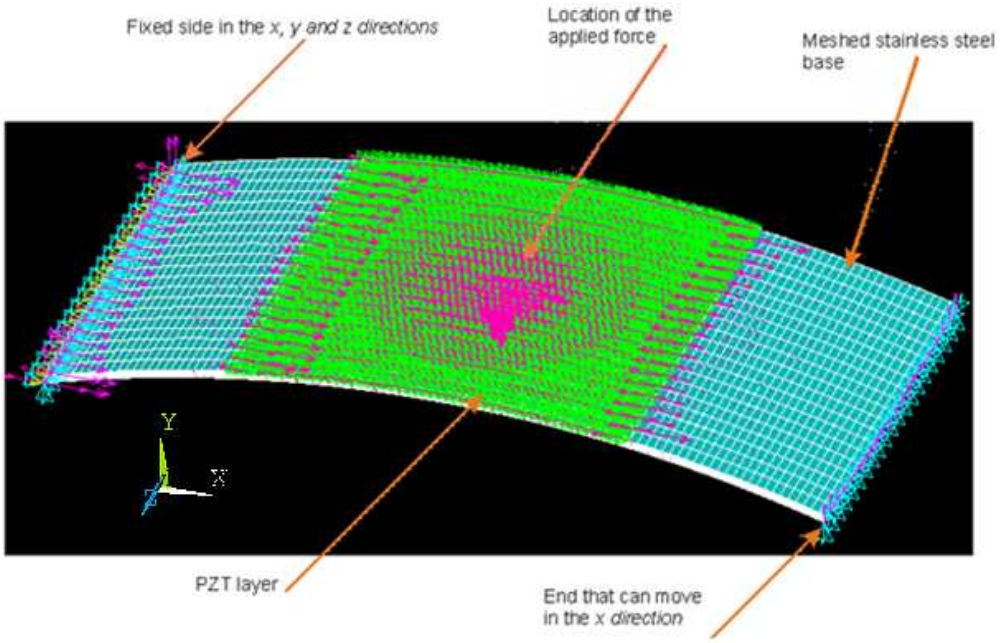

Figure 4.7 3-D finite element mesh of simply supported Thunder™ pre-stressed beam subjected to an impulse force.

This figure shows a 3-D image of a simply supported meshed curved beam. The magnitude of the force is chosen to be less than the required force that makes the beam flat (36 N) and the duration of the impulse is chosen to be lower than the inverse of the resonant frequency of the structure. This means the applied force is dynamic. Moreover, the duration of the impulse matches the one that is obtained experimentally in Chapter 5.

4.4.2 Analysis of clamped pre-stressed beam

For a given input force, the effect of the curved beam clamping on the output voltage and the developed stress within the clamped area are analysed. The pre-stressed beam is supported in three different ways; rigidly supported on both ends, rigidly supported on one end (cantilever) and simply supported. The numerical results for each boundary condition are obtained and compared with each other to choose the most suitable way of mounting the beam under impact force in terms of mechanical stability and the output power.

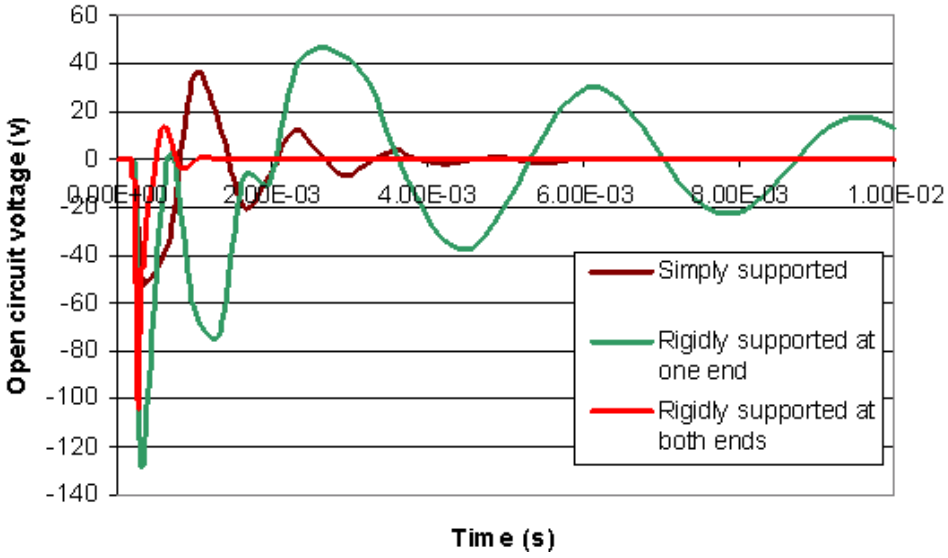

Figure 4.8 Simulated Thunder™ open circuit voltage over time under different boundary conditions.

The simulated open circuit voltage over time for the Thunder™ beam using the three different clamping methods is shown in Figure 4.8. As can be seen the maximum amount of energy can be extracted when the Thunder™ beam is rigidly supported at one end (cantilever), while the least amount of power can be obtained when the beam is rigidly supported at both ends. This is due to the fact that, when the beam is rigidly supported at both ends, the generated voltage is due to developing stress and strain in the impacted area. In this case the stiffness of the beam prevents the pre-stressed beam from vibrating. However, when the pre-stressed beam is rigidly supported at one end only, the output energy is generated from global deformation. In this case, the pre-stressed beam vibrates after the impact. The stiffness of a simply supported pre-stressed beam is somewhere in between the previous two cases and similarly the output energy. In this situation the generated output energy is due to local deformation and vibrations

that have been generated after the impact. Therefore, in order to extract the maximum output power, the Thunder™ beam must be rigidly mounted at one end. However, the way that the pre-stressed beam is mounted should not only provide the maximum output power, but also it should provide mechanical stability. As the beam deformation generates due to an impact force, knowing the generated stress in the clamped area is essential for mechanical stability. Under an input force, the developed tensile stress in the clamped area should be less than the tensile yield strength of stainless steel material. Moreover the developed shear stress due to the impact force should be lower than the value of the piezoelectric shear strength, because the piezoelectric material has the lowest value of shear strength in comparison with stainless steel and aluminium.

Figure 4.9 shows the stress developed in the clamped areas when the beam is mounted in three different ways; rigidly supported at both ends, simply supported and rigidly supported at one end. The rigidly supported beam on one end generates 7 times more stress in the clamped area than the simply supported beam. The rigidly supported beam on both ends generates 5 times more stress in the clamped area than the simply supported beam. This means the cantilever configuration is the least favourite method of clamping the curved beam under an impact force. As the piezoelectric material is only located in the middle of the pre-stressed beam. All the stresses and thus the strains generated in the clamped area do not contribute to the output power.

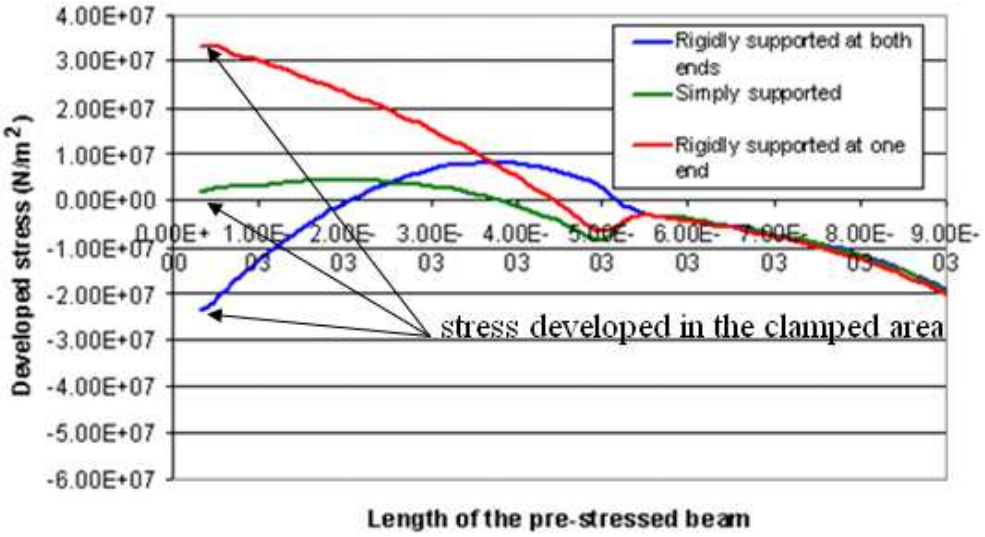

Figure 4.9 Simulated stress developed in the clamped area using different boundary conditions.

There is a trade off between the amount of power generated and the mechanical stability of the pre-stressed beam. The simply supported pre-stressed beam proves to generate modest amount of output voltage and the lowest amount of stress in the clamped area in comparison with the cantilever configuration and the rigidly supported

beam on both ends. Therefore, both the numerical analysis and the experiments are carried out using simply supported Thunder™ pre-stressed beam.

4.4.3 Modal analysis

Under impact force global deformation is generated across the whole structure of the simply supported beam due to existence of the curvature and the method of clamping. Therefore, output energy is generated due to the local effect of the impact force and the travelling of the transverse waves. Therefore, stresses and strain in the *x* and *y* direction are generated a well as a sheer stress in the *xy* direction all of which contributed towards the output energy. The vector sum of the displacement is given in Figure 4.10. As can be seen the curvature and the method of clamping gives the structure the ability to deform in the *x* and *y* direction and the maximum displacement is located in the middle of the beam.

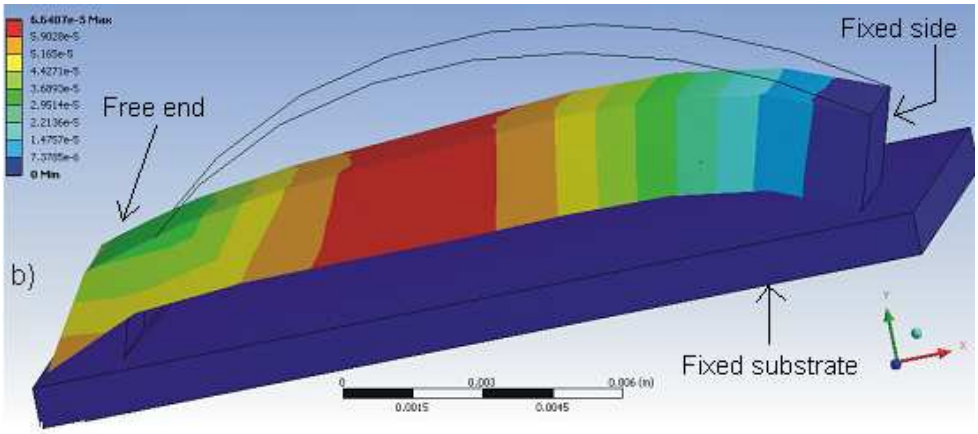

Figure 4.10 Simulated results of the vector sum of the Thunder™ beam displacement in meter.

Figure 4.11 shows the developed stress in the *y* direction across the length of the piezoelectric layer. The chosen nodes are the ones located at the centre line of the surface of the piezoelectric material. The developed stress are analysed across the thickness of the piezoelectric layer, where each nodal line is chosen at every 0.05 mm from the previous nodal line. Thus, the piezoelectric layer with a thickness of 0.2 mm has 5 nodal lines across its thickness. The stress is obtained when the applied force is at its maximum value.

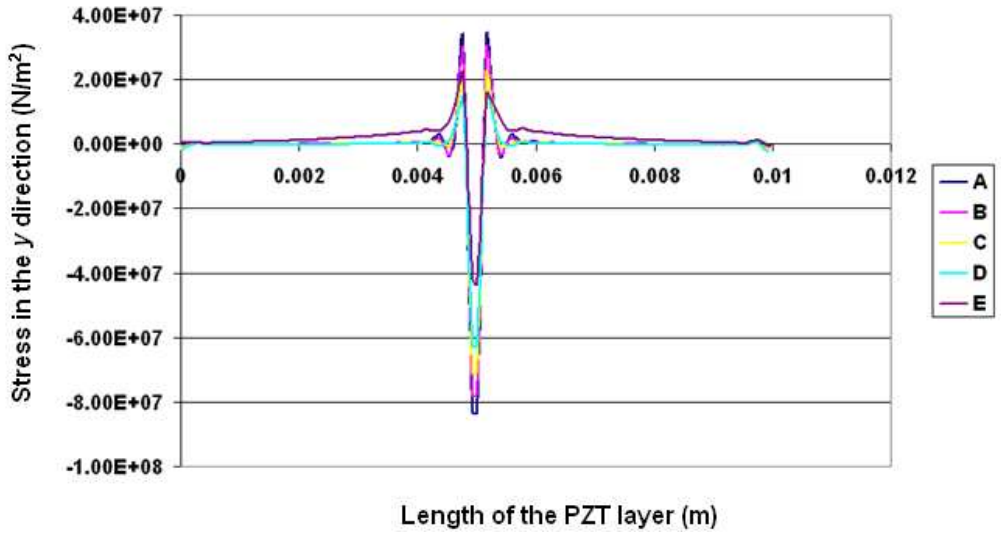

Figure 4.11 Simulated stress developed in the *y* direction across the length of the PZT layer at different nodal lines.

Figure 4.11 shows that the compressive stress reaches its maximum value around the area where the impulse is applied. This value of stress decreases rapidly outside this area. At both ends of the nodal line a stress in the *y* direction starts to form again due to the connection with the stainless steel layer. The letters A and E correspond to nodal lines located at the top and the bottom surfaces of the PZT layer, respectively. The letters B, C and D are corresponding to the nodal lines between the two surfaces of the material ranging from the top to the bottom layer. As can be seen, the peak of the stress in the contact area is at its maximum value at the top surface of the material and this value reduces across the thickness of the material. The bottom layer has the lowest peak value.

Using the same nodal lines, Figure 4.12 shows the developed stress in the *x* direction across the length of the piezoelectric layer. The stress magnitude in the contact area is approximately twice higher than the compressive stress developed in the same area. Along the nodal line, the maximum tensile stresses are developed in the contact area and these values reduce gradually until it reaches zero at the end of the nodal line. As the situation in the developed compression stress, the tensile stress is higher at the surface of the piezoelectric layer (*A*). This value reduces along the thickness of the piezoelectric material. At the bottom surface of the piezoelectric material, point *E*, there is extra stress developed at the end of the nodal line due to the connection with the stainless steel layer. Most of the mechanical input energy is converted into deformation in the piezoelectric material along the *x* (radial) and the *y* directions.

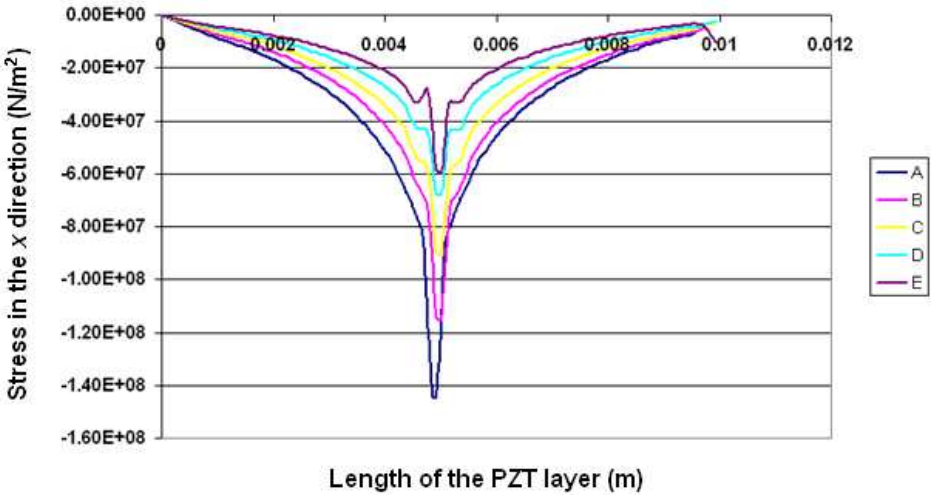

Figure 4.12 Simulated stress developed in the *x* direction across the length of the PZT layer at different nodal lines.

In the area where the force is applied both tensile and compressive stresses dominate. However, outside this area the tensile stress dominates, while the value of the compressive stress is negligible. The developed stress across the length of the stainless steel layer in the *y* and *x* directions are presented in Figure 4.13 and Figure 4.14, respectively.

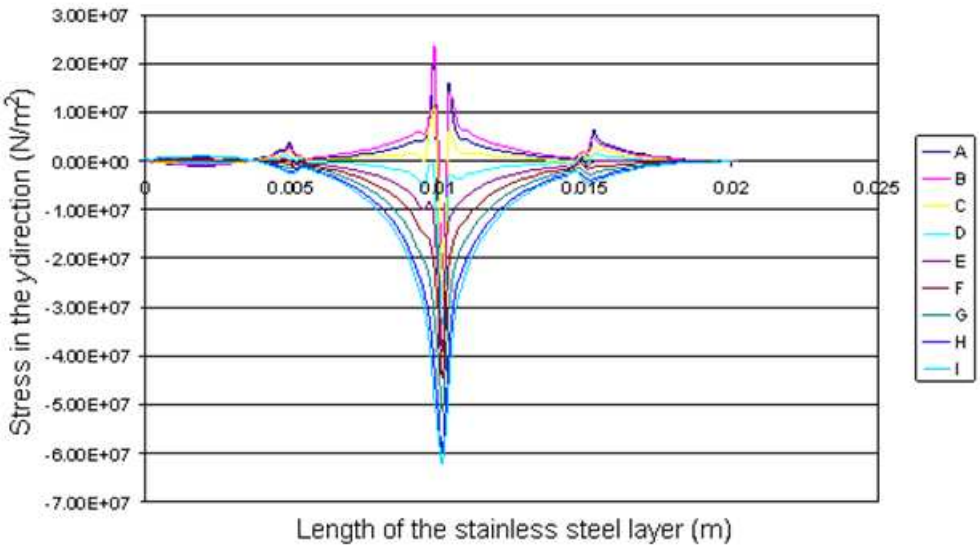

Figure 4.13 Simulated stress developed in the *y* direction across the length of the stainless steel layer at different nodal lines.

In order to determine the location of the neutral axis, nodal lines are chosen every 0.025 mm from the top surface along the thickness of the stainless steel material. Thus, this layer with a thickness of 0.2 mm has 9 nodal lines. The letters A and I correspond to the nodal lines located at the top and the bottom surfaces of the stainless steel layer, respectively. The top surface of the stainless steel layer is the one connected to the

piezoelectric material. The letters B, C, D, E, F, G and H correspond to the nodal lines that are located between the two surfaces of the stainless steel material ranging from the top to the bottom layer.

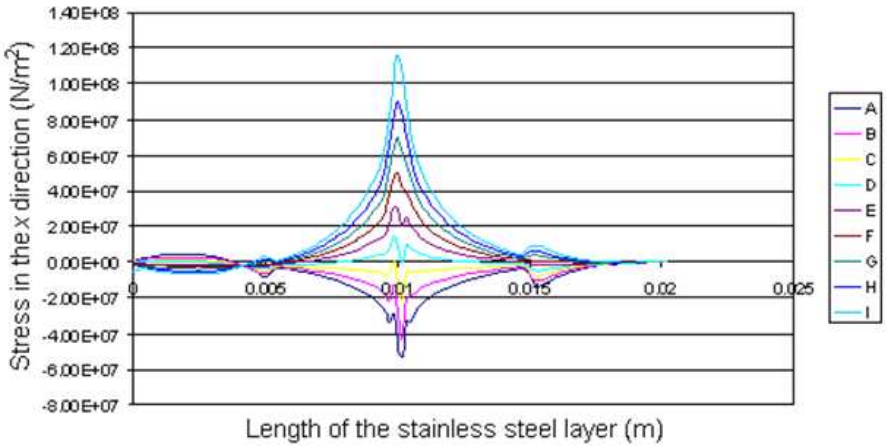

Figure 4.14 Simulated stress developed in the *x* direction across the length of the stainless steel layer at different nodal lines.

As it can be seen in Figure 4.14, the first three nodal lines from the top surface of the stainless steel layer are under compression. However, the rest are under tensile stress. Therefore, the simulated results show that the neutral axis is located approximately at a distance of 0.125 mm from the bottom of the stainless steel layer. This agrees with the predicted analytical results presented in Section 3.2.7 where the location of the neutral axis is found to be at a distance of 0.12388 m from the bottom of the stainless steel layer.

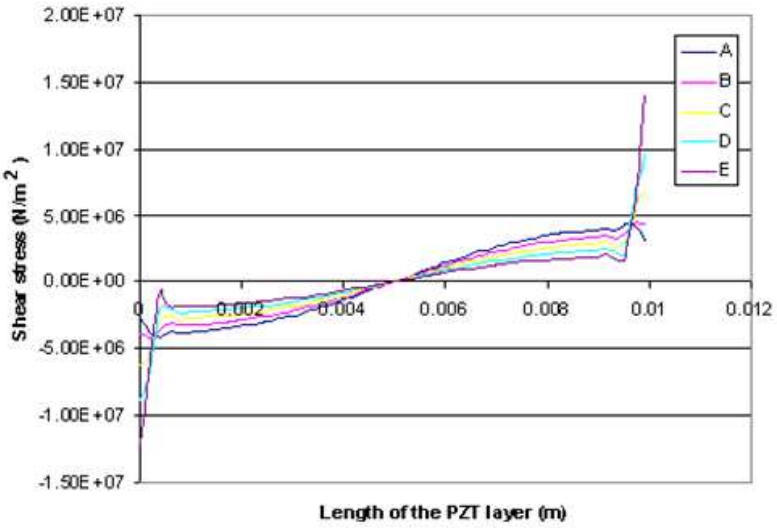

Figure 4.15 Developed shear stress across the thickness of the PZT layer at different nodal lines.

Figure 4.15 and Figure 4.16 present the developed shear stress across the thickness of the PZT and the stainless steel layers, respectively. These figures prove that the maximum shear stresses are developed at the edges of the PZT material, especially at the bottom surface of the PZT where it comes in contact with the stainless steel layer. If this stress exceeds the shear strength of the material, damage will appear at the edges of the PZT layer. There is no data available about the shear strength of the PZT material. Typically, the shear strength at yield for different materials equals half of the tensile strength at yield according to machinery's handbook [75]. This gives the PZT (5A) material a maximum shear strength of 10 MPa.

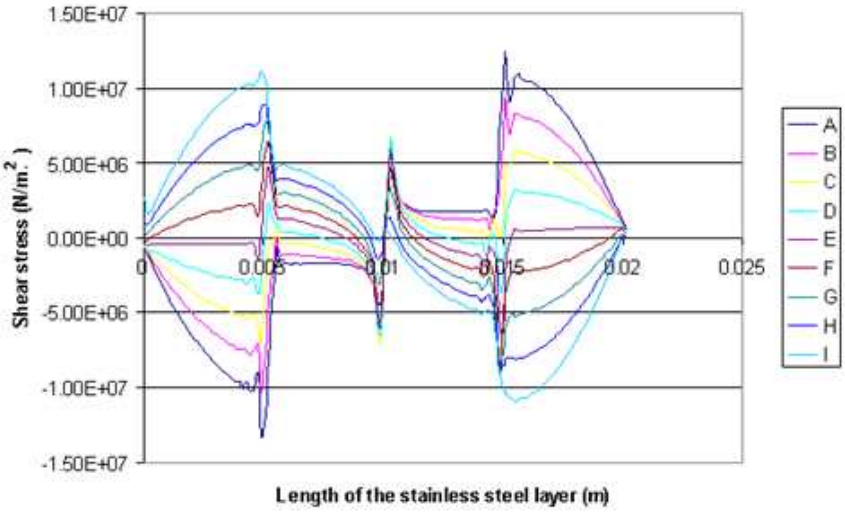

Figure 4.16 Developed shear stress across the thickness of the stainless steel layer at different nodal lines.

Figure 4.17 shows the shear stresses distributions for sections (X-X) 0.635 cm and (Y-Y) 5mm away from the centre of the beam where the force is applied.

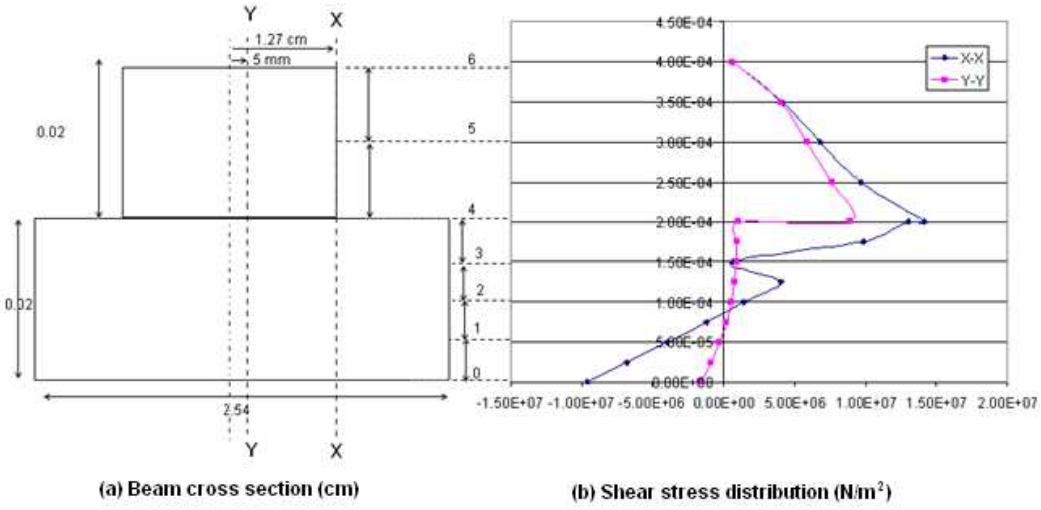

Figure 4.17 Simulated developed shear stress across the thickness of the Thunder™ beam.

The value of the shear stress increases in the *y* direction moving away from the surface of the piezoelectric material until it reaches its maximum value when the PZT layer comes in contact with the stainless steel layer. Theoretically, as explained in Section 3.2.7 the value of the shear stress on the bottom surface of the stainless steel should be negligible. However, Figure 4.17 shows that the shear stress developed at the bottom layer of the stainless steel material has a negative value and is not zero as expected using equation 3.21. This is due to the way that the pre-stressed beam is mounted. As the curved beam is simply supported, both ends of the bottom layer of the stainless steel are in contact with the substrate and thus are not free. Therefore, shear stress is expected at the bottom layer of the stainless steel. By moving away from both ends the shear stress reduces until it reaches zero at the centre of the bottom layer of the stainless material.

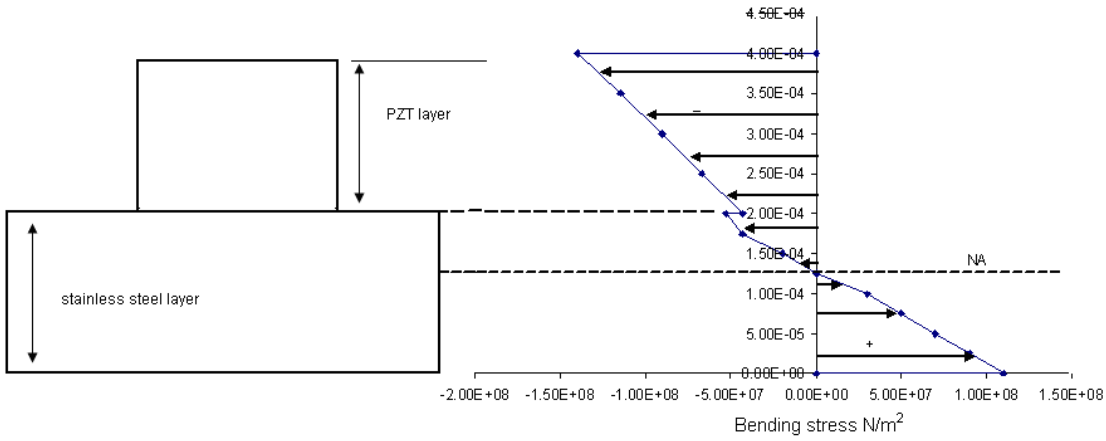

Figure 4.18 Developed bending stress across the thickness of the Thunder™ beam.

Figure 4.18 shows the bending stress developed in the pre-stressed beam. As expected this value of stress equals zero at *NA* and it increases when moving away from the *NA*. The maximum stress values are located on the surface of the pre-stressed beam. As can be seen, at the location where the two different materials are bonded together there is a different value of the bending stress. This is due to the fact that each layer has its own value of Young's modulus.

The simulated fundamental resonant frequency is found to be 1430 Hz. There is an agreement between the simulated value and the measured one (1432 Hz).

4.5 Theoretical analysis of pre-stressed piezoelectric beam under impact

4.5.1 Introduction

In this section, analytical and numerical calculations are carried out to analyse the effect of ball bearing impact on the surface of Thunder™ beam configuration. This study is aimed at calculating the applied impact force, the contact period and understanding the dynamic behaviour of the material and structure under impact.

The generated deformation in the piezoelectric material due to impact, and thus the value of the contact force, depends on the hardness of the colliding bodies, their structures as well as the relative velocity between them at the point of initial contact.

For modelling purposes, the area of contact between the two bodies can be considered as a short stiff spring with a large spring constant which is compressed during the period of contact. The contact duration depends on the material of the colliding bodies, the mechanical structure as well as on the effective mass of the colliding bodies. In other words, the period of contact depends on the compliance of the contact region. For example, if the same ball bearing generates an impact on two different structures of the same material, the contact period, the generated deformation and the applied force will vary.

During collision, the contact force induces a local deformation as well as a global one (vibration). The simply supported pre-stressed beam suffers from both local and global deformation. In addition to that, two types of wave propagation might be present in the pre-stressed beam; transverse wave propagation and axial wave propagation. Transverse wave propagation happens when at least one of the colliding bodies suffers bending due to the interface pressure in the contact zone. This bending reduces the interface pressure and prolongs the period contact. Bending is significant at points far from the contact zone, if the depth of the body is small in comparison with surface area. Axial wave propagation occurs when a boundary condition is applied at some distance from the impact point which reflects the radiating wave back to the source. The effect of the axial waves in case of a pre-stressed beam is negligible.

The stress developed in the structure due to the impulse force was analysed in Section 4.4.2 using ANSYS software. A developed model is used to analyze the impact effect of a ball bearing on the Thunder™ structure in Section 4.5.2. The model used to

analyse the behaviour of the piezoelectric harvester under the effect of the centripetal force is analysed in Section 4.5.3.

4.5.2 Analysis of pre-stressed piezoelectric beam under impact

The analytical analysis for the impact between the ball bearing and the piezoelectric structure is carried out using Newton's laws of motion and conservation of energy. In order to understand the change in velocity as a function of time during the contact period, the deformation of the colliding bodies can be lumped in an infinitesimal deformable particle. Therefore, impact theory can be applied. For this model a few assumptions are taken into account:

1. The impact is collinear. The collision is considered to be collinear if the initial relative velocity vector is parallel to the vector between the centre of mass of each body and its contact point. During contact there are equal but opposite compressive reaction forces which develop at the contact points.
2. The ball bearing is smooth and spherical. Therefore, only the component of the interaction impulse and the component of the initial relative velocity that are normal to the contact surface will be taken into the account. Moreover, tangential forces due to friction are considered to be negligible.
3. The two rigid bodies are separated by an infinitesimal deformable particle. This particle represents small local deformation of the contact region. The finite body forces such as gravity do not affect the velocity during the collision because these forces don’t work during small displacements that develop during an instantaneous collision. Therefore, during impact between rigid bodies, the only forces acting are the reaction forces at the contact zone.

In hard materials, where the value of the elastic modulus is high, only very small deformations are required to generate very large contact pressures [76]. In the contact area the colliding bodies are subjected to a large amount of stress that might exceed the yield point of the Thunder™ beam. The yield point is defined as the stress by which a material begins to deform plastically. Below this point, the material deforms and it returns to its original shape when the applied stress is removed. If the mean applied stress is greater than the yield one, an irreversible indentation starts to form underneath

the surface of the softer material. The plastically deforming region enlarges as the contact pressure increases. However, it remains underneath the contact surface as long as the mean applied stress is less than 2.8 times the yield stress [76]. At this point, a fully plastic region represented as irreversible indentation is created at the surface of the structure. Therefore, calculating the yield point is essential when designing the harvester as it puts limits on the applied load. The transition pressure (P_y), by which the deformation will be at yield, equals to 1.1 Y, where (Y) is the yield stress of the piezoelectric material [76]. This material is chosen due to the fact that piezoelectric material has a low yield value in comparison with yield value of the aluminium and stainless steel materials (Table 3.1). Therefore, the failure of the Thunder™ beam happens because of the breaking of the piezoelectric layer. If the mean applied pressure is 1.1 $Y < \bar{p} <$2.8 Y, then elastic-plastic indentation is formed underneath the contact surface. However, if the mean applied pressure ($\bar{p}$) is ≥2.8 У, then a full plastic irreversible indentation is formed on the contact surface. The material properties of the steel ball bearing and the Thunder™ beam are presented in Table 3.1. The value of the applied force (F_y) that causes a plastic indentation to start forming under the contact force can be calculating using equation 4.9 [76].

$$F_y = \pi P_y R^{*2} \left(\frac{3\pi P_y}{4Y^*} \right)^2 \qquad 4.9$$

where Y^*, R^* and m are the effective Young's modulus at contact, the effective radius of contact curvature and the effective mass, respectively. These values can be calculated using the following equations [76]:

$$Y^* = \frac{3K_m}{4\sqrt{R^*}} \qquad 4.10$$

$$R^* = [R_B^{-1} + R_{B'}^{-1}]^{-1} \qquad 4.11$$

$$m = \frac{MM'}{M + M'} \qquad 4.12$$

Where R_B and $R_{B'}$ are the radii of curvature for the Thunder™ beam and the ball bearing, respectively. The calculated values for the Thunder™ beam at yield are 22 MPa, and 63 N for the pressure (P) and the applied force (F). For this calculation, the ball bearing has a mass (M') of 3.5 × 10^{-3} kg, while the Thunder™ beam has a mass (M) of 10^{-3} kg. This mass of the ball bearing is chosen because it is used later in the

experiments. Therefore, the theoretical and experimental results can be compared to each other. The other parameters that are required to calculate the force at yield are presented in Table 4.1.

m	Y^*	R^*	$R_B^{'}$	R_B	K_m
0.77×10^{-3} kg	2.6×10^{8}	4.8×10^{-3} m	5×10^{-3} m	0.135 m	2.4×10^{7} $Nm^{-3/2}$

Table 4.1 Values of parameters at impact

The initial applied force due to the ball bearing impact must be calculated and compared to the value at yield in order to protect the Thunder™ beam from plastic deformation. The impact time and the amount of force and pressure generated due to impact are calculated in the following paragraph. The initial relative velocity (v_0) equals the initial velocity of the piezoelectric beam minus the initial velocity of the ball bearing by which the impact takes place. The velocity of the ball bearing at impact is calculated numerically using the first equation of the set of equations 4.31. The boundary conditions by which the simulation has been obtained is explained in Section 4.5.3.

4.5.3 Modelling of the piezoelectric harvester under impact

The optimized output power of the piezoelectric harvester has been studied in case of harmonic and steady-state analysis in the literature. However these studies do not explain the dynamic behaviour of the transient characteristics when the input energy is given by repeated impulses. The model that was developed by Renaud [77] calculates the output power at optimum load resistance from the piezoelectric element after impact. Experiments were performed on the impact based piezoelectric harvester to compare the experimental results with the numerical one developed in this section. The objective of this section is to develop a theoretical model that predicts the amount of power that the harvester can provide under the effect of the input forces. In order to do that, it is assumed that the Thunder™ beam has been given an initial velocity v_o and becomes unforced after impact. This behaviour can be observed if the duration of the impact is less than the period of the Thunder™ beam and the mass does not have any interaction with the transducer after the impact. Firstly, the effect of the rotational forces on the velocity of the ball bearing at impact must be calculated. This can be achieved by solving the first equation of the set of equations 4.31. The equation

indicates that the acting force on the ball bearing mass (M') is the inertial force due to the frame acceleration. The value of the initial velocity at impact (v_o) depends on the boundary conditions, radius at which the rotational force is applied and the rotational speed. The boundary conditions define both the position and the length of the tube. Figure 4.19 shows that the relationship between the initial impact velocity and the rotating speed is linear. For this simulation, the central point of the tube is positioned 0.06 m from the centre of rotation and the available displacement of the ball bearing is 0.02 m. Both the dimensions of the tube and its position are chosen to match the ones that are used in the experiments and thus the results can be compared with each other.

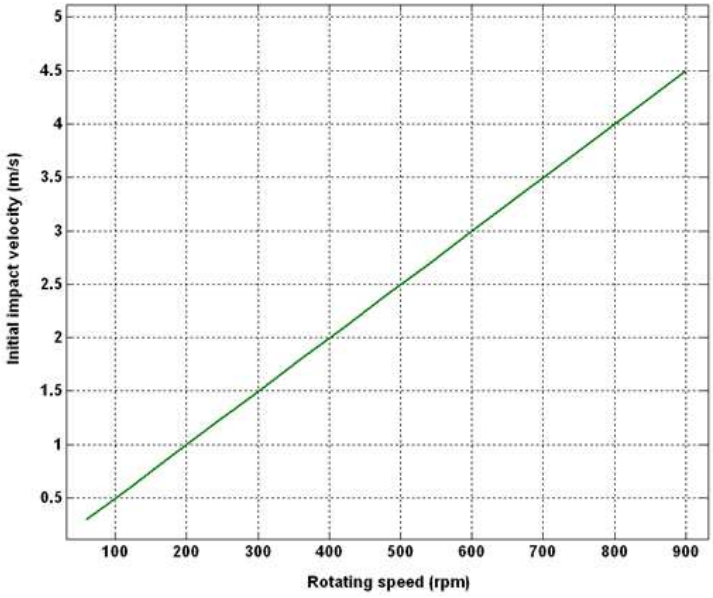

Figure 4.19 Initial impact velocity as a function of the rotating speed

The values of the velocity of the ball bearing at impact can be used to predict the amount of power that the Thunder™ can produce under impact. Therefore, in the next section an expression of the output voltage equation is developed.

4.5.3.1 Output power under impact force

The mechanical model of the piezoelectric element located at both ends of the tube can be presented with lumped elements as shown in Section 3.3. In this case the piezoelectric transducers have been replaced with mass, spring and damping mechanisms as shown in Figure 3.10. Applying Kirchhoff's law to the circuit presented in Figure 3.11(a) leads to the governing differential equations that describe the behaviour of the piezoelectric element in the frequency domain (equation 4.13). In this

equation all the initial variables are zero apart from the initial velocity (v_o), s is the Laplace variable and ψ is the inverse of the transformer ratio (ϕ).

$$\begin{aligned} 0 &= \left(s^2 X(s) - v_o\right) M_m + sBX(s) + K_m X(s) + \psi V(s) \\ 0 &= \psi s X(s) - C_p' s V(s) - \frac{V(s)}{R_L} \end{aligned} \qquad 4.13$$

By rearranging the previous set of equations, the Laplace transform of the voltage is given by the following equation:

$$V(s) = \frac{\psi s R m v_o}{m R_L C_p' s^3 + (m + B R_L C_p') s^2 + (B + K_m R_L C_p' + R_L \psi^2) s + K_m} \qquad 4.14$$

The expression of the output voltage in the time domain can be obtained by analysing the denominator of equation 4.14, which will be referred to as $D(s)$. The values of the piezoelectric beam's stiffness, damping, capacitance and the value of its transformer ratio presented in Chapter 3 indicate that the denominator has one real root and two complex conjugated ones. The denominator, which is given by equation 4.15, is a cubic equation in which its root can be found using Cardano's method [78].

$$D(s) = m R_L C_p' s^3 + (m + B R_L C_p') s^2 + (B + K_m R_L C_p' + R_L \psi^2) s + K_m \qquad 4.15$$

Therefore, the roots of the previous equation are given as follows:

$$\begin{aligned} s_1 &= \sqrt[3]{r + \sqrt{(q)^3 + (r)^2}} + \sqrt[3]{r - \sqrt{(q)^3 + (r)^2}} - \frac{a_2}{3a_3} \\ s_2 &= -\frac{\left(\sqrt[3]{r + \sqrt{(q)^3 + (r)^2}} + \sqrt[3]{r - \sqrt{(q)^3 + (r)^2}}\right)}{2} - \frac{a_2}{3a_3} \\ &\quad + \frac{\sqrt{3}\left(\sqrt[3]{r + \sqrt{(q)^3 + (r)^2}} - \sqrt[3]{r - \sqrt{(q)^3 + (r)^2}}\right)}{2} i \\ s_3 &= -\frac{\left(\sqrt[3]{r + \sqrt{(q)^3 + (r)^2}} + \sqrt[3]{r - \sqrt{(q)^3 + (r)^2}}\right)}{2} - \frac{a_2}{3a_3} \\ &\quad - \frac{\sqrt{3}\left(\sqrt[3]{r + \sqrt{(q)^3 + (r)^2}} - \sqrt[3]{r - \sqrt{(q)^3 + (r)^2}}\right)}{2} i \end{aligned} \qquad 4.16$$

Where the parameters of the cubic equation and the values of r and q are given by equation 4.17 and equation 4.18, respectively:

$$
\begin{aligned}
a_0 &= K_m \\
a_1 &= B + K_m R_L C_p' + R_L \psi^2 \\
a_2 &= m + B R_L C_p' \\
a_3 &= m R_L C_p'
\end{aligned}
\qquad 4.17
$$

$$
\begin{aligned}
r &= \frac{9 a_3 a_2 a_1 - 27 a_3^2 a_0 - 2 a_2^3}{54 a_3^3} \\
q &= \frac{3 a_3 a_1 - a_2^2}{9 a_3^2}
\end{aligned}
\qquad 4.18
$$

Therefore, equation 4.14 and equation 4.15 can be rewritten as following:

$$V(s) = \frac{\psi s R_L m v_o}{a_3 s^3 + a_2 s^2 + a_1 s + a_0} = \frac{\psi s R_L m v_o / a_3}{(s - s_1)(s - s_2)(s - s_3)} \qquad 4.19$$

Using partial fraction method, the previous equation can be written as follows:

$$V(s) = \frac{\psi s R_L m v_o / a_3}{(s - s_1)(s - s_2)(s - s_3)} = \frac{A}{(s - s_1)} + \frac{Cs + D}{(s - s_2)(s - s_2)} \qquad 4.20$$

Clearing the fraction leads to the following equation:

$$\psi s R m v_o / a_3 = A(s - s_2)(s - s_3) + (Cs + D)(s - s_1) \qquad 4.21$$

Substitution of s_1 for s leads to determining the value of the constant A, which is given by the following equation:

$$A = \frac{\psi s_1 v_o}{C_p'(s_1 - s_2)(s_1 - s_3)} \qquad 4.22$$

Substitution of 0 for s leads to determining the value of the constant D, which is given by the following equation:

$$D = \frac{\psi s_2 s_3 v_o}{C_p'(s_1 - s_2)(s_1 - s_3)} \qquad 4.23$$

Substitution of 1 for s leads to determining the value of the constant C, which is given by the following equation:

$$C = \frac{\psi v_o}{C_p'(1 - s_1)} - \frac{\psi s_1 v_o (1 - s_2)(1 - s_3)}{C_p'(s_1 - s_2)(s_1 - s_3)(1 - s_1)} - \frac{\psi s_2 s_3 v_o}{C_p'(s_1 - s_2)(s_1 - s_3)} \qquad 4.24$$

After determining the value of the constant *A*, *C* and *D*, inverse Laplace transform tables can be used to convert equation 4.20 into time domain as given by equation 4.25.

$$V(t) = Ae^{s_1 t} + e^{\mathrm{Re}(s_2)t}\left\{C\cos(\mathrm{Im}(s_2)t) + \frac{C\,\mathrm{Re}(s_2) + D}{\mathrm{Im}(s_2)}\sin(\mathrm{Im}(s_2)t)\right\} \qquad 4.25$$

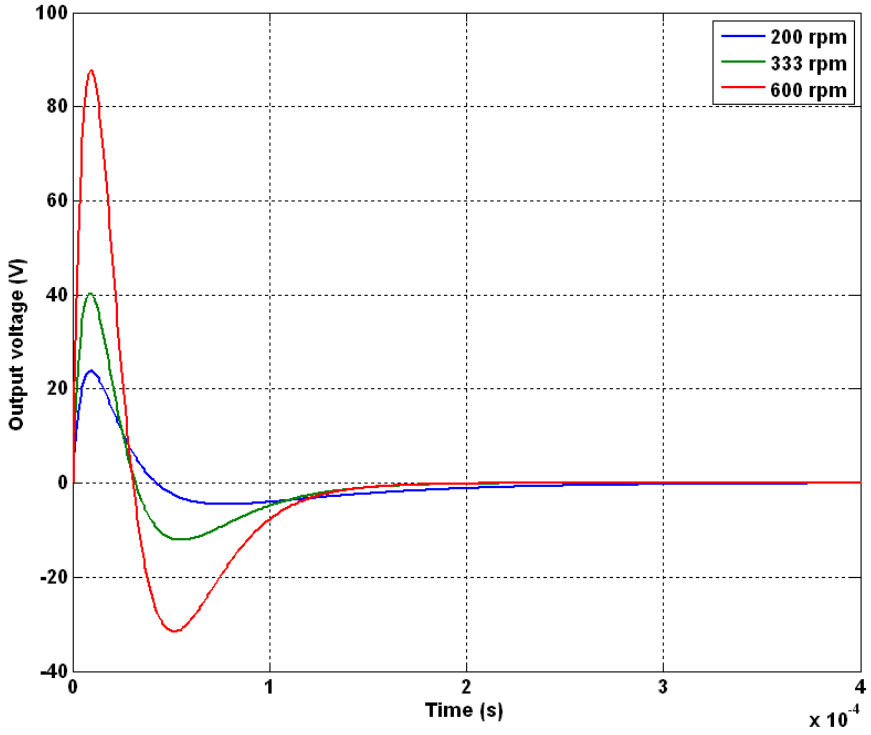

Figure 4.20 Output voltage of the piezoelectric transducer after impact as a function of time.

The average output power (*P*) dissipated into the load resistance is given by the following equation, where *V(t)* is the output voltage produced by the piezoelectric structure and *T* is the time interval between two impacts.

$$P = \frac{1}{R_L T}\int_0^T V(t)^2\,dt \qquad 4.26$$

In order to approach the maximum value of the output power, an optimum value of the load resistance should be used. The expression for the optimum load resistance is given and discussed in Section 3.4.2. The piezoelectric element produces a transient voltage pulse when it is mechanically compressed as shown in Figure 4.20. This figure presents the simulated results of the output voltage, at the optimum resistance, over time at different values of the rotating speed ranging from 200 rpm to 600 rpm. The average output power as a function of the load resistance is calculated and compared to the experimental results as presented in Figure 5.13. The parameters required to obtain

the output voltage are presented in Table 3.3. However, the values of the Thunder™ stiffness and damping at different applied force are measured experimentally as explained in Section 3.4.4.

4.5.3.2 Efficiency of the Thunder™ beam under impact

When the ball bearing comes in contact with the piezoelectric beam, some of the initial kinetic energy (T_0), which can be calculated using equation 4.27, is transformed into internal energy of deformation during the compression period [76].

$$T_0 = 0.5MV_0^2 + 0.5M'V_0'^2 \qquad 4.27$$

If the collision is elastic, this stored internal energy is the source of the normal force that drives the two bodies apart from each other. However, as the collision between the ball bearing and the piezoelectric beam is not elastic, a loss in the absorbed kinetic energy in the contact region during the compression and the restitution occurs. Figure 4.21 shows the energy dissipation in the system. The absorbed energy during compression phase equals T_0 - T_c, where T_c is the kinetic energy of the system at the transition between the compression and the restitution phases and it is given by the following equation:

$$T_c = T_0 - 0.5mv_0^2 \qquad 4.28$$

If 100 % efficiency of the piezoelectric transducer is assumed, the average output power per impulse can be defined as follows where T is the time interval between two impacts.

$$P = \frac{T_0 - T_c}{T} \qquad 4.29$$

However, in a real situation, depending on the piezoelectric element efficiency only a percentage of the stored mechanical energy is converted into electrical energy. The unrecovered energy equals to T_0 - T_f, where T_f is the kinetic energy at restitution and it is given by the following equation:

$$T_f = T_c + 0.5mv_f^2 \qquad 4.30$$

v_f is the relative velocity at separation. Only some of the initial kinetic energy of the impact is absorbed. Some of absorbed energy will be stored as strain energy. This energy is used to drive the contact points apart during the restitution phase. However,

some of the absorbed energy will be lost due to the conversion of some of the mechanical energy into electrical energy, plastic deformation, sound and heat.

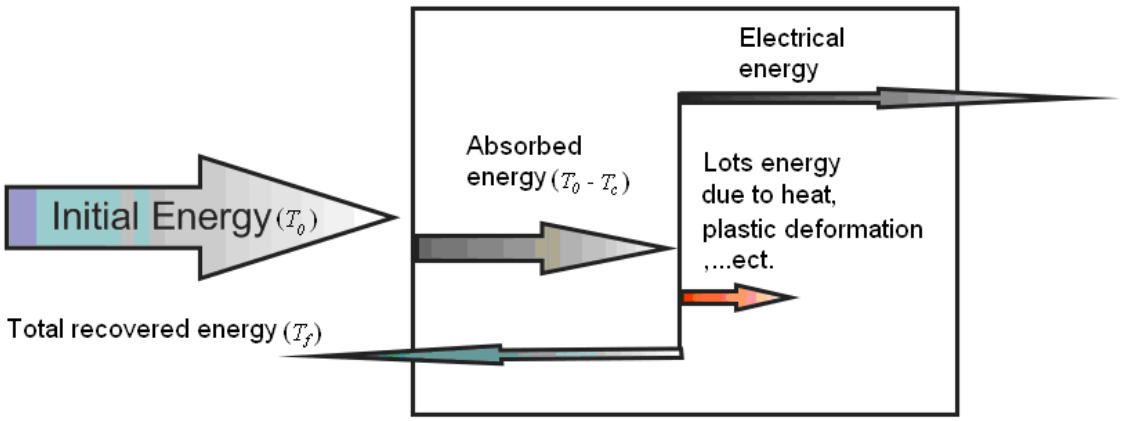

Figure 4.21 Energy dissipation in the system.

The efficiency of the system equals the input mechanical energy T_0 divided by the dissipated energy in the load resistance, which is calculated numerically using equation 4.26. The output voltage is obtained experimentally as will be presented in Section 5.5.4. The efficiency is plotted as a function of the load resistance as shown in Figure 4.22. This figure shows that the maximum efficiency is obtained when the load resistance is approximately 3 kΩ, 2 kΩ and 1 kΩ for 333 rpm, 600 rpm and 800 rpm, respectively. As the initial velocity of the ball bearing increases from 333 rpm to 800 rpm, the maximum efficiency decreases from 30 % to 12 %, respectively. The drop in the efficiency value is due to the increase in the loss generated by the impact such as sound and plastic deformation. It is found that large part of the energy is dissipated as a kinetic energy of the ball bearing after impact. The kinetic energy for the ball bearing after impact, at different rotating speed, is found to be approximately 61 % of the initial energy. Therefore, the effect of the rotating speed on the percentage of the recovered energy is negligible. However, the loss in energy (that did not turn into electricity) is found to be 9 %, 21 % and 27 % of the initial kinetic energy at 333 rpm, 600 rpm and 800 rpm, respectively. The percentage of the part of the absorbed energy that gets lost in the system increases with speed. This is due to the plastic deformation that starts to form within the piezoelectric element. The rotating speeds by which the plastic deformations start to from in the piezoelectric element are discussed in Section 4.5.5.

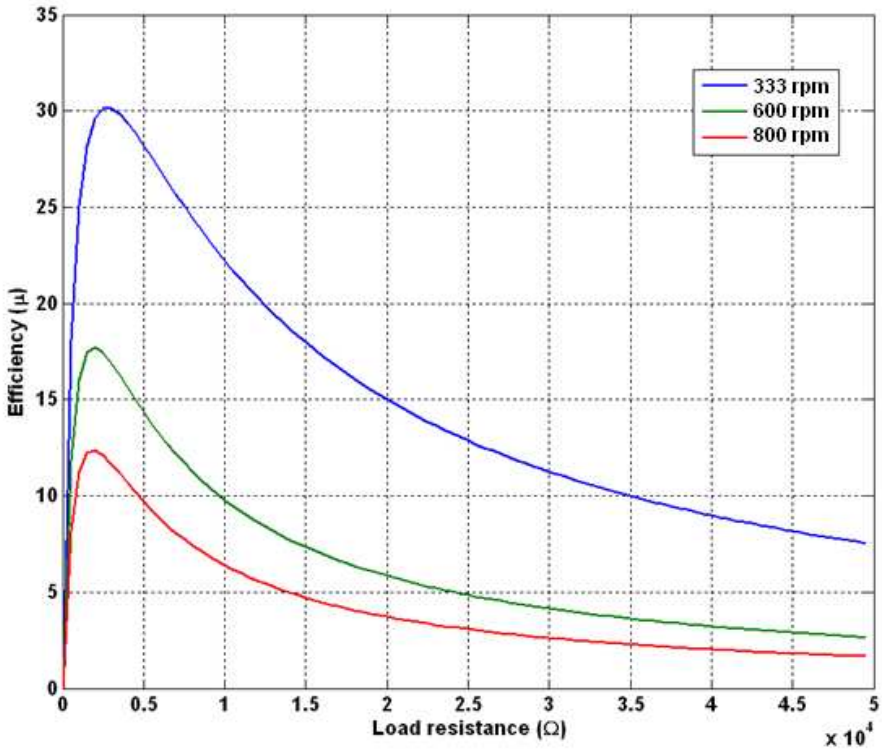

Figure 4.22 Percentage of the efficiency versus load resistance at 200, 333 and 600 rpm

During collisions, the contact time can be separated into two phases; compression and restitution. During the compression time, the kinetic energy of the relative motion between the colliding bodies is transformed into internal energy of deformation by the contact force. This force reduces the initial relative velocity (v_0) and increases the internal deformation energy of the deformable particle. By the end of the compression phase, the relative velocity is zero. However, during the restitution phase, some of the elastic energy stored during the compression phase is used to drive the two bodies apart. This energy is called the storage strain energy and it is the source that drives the two bodies apart. The compressed force in the normal direction creates a contact pressure that generates local deformation and a surface displacement. The deformation and thus the value of the contact force depend on the boundary conditions, hardness of the two bodies as well as the relative velocity between them at the point of initial contact.

Figure 4.23 shows the contact force resulting from an impact of a ball bearing on the Thunder™ beam as a function of time at different values of the rotating speed ranging from 200 rpm to 600 rpm. Increasing the initial velocity by which the ball bearing collides with the piezoelectric structure results in increasing the contact force in magnitude and reduces the contact period. By solving equation 4.13 numerically in the time domain using a Runge-Kutta method, the displacement of the Thunder™ beam is

obtained. The force between the two colliding bodies is given by the force in the spring. Therefore, the force, which is presented in Figure 4.23, is obtained by multiplying the Thunder™ beam displacement with the stiffness. As can be seen, the force reaches its maximum value at the end of a compression period as the displacement is at its maximum value at this point. During the restitution period the value of the displacement reduces and thus the amount of the generated force. The boundary conditions used for this simulation are presented in Section 4.5.3.

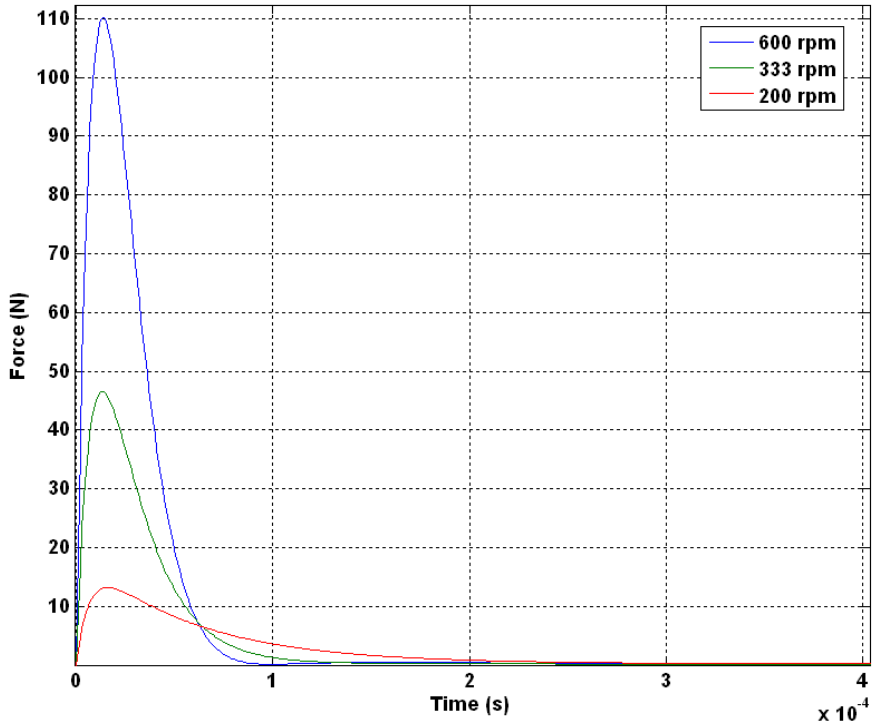

Figure 4.23 Generated force in the Thunder™ beam over time at different rotating speeds

4.5.4 Numerical modelling of the piezoelectric harvester under impact

The developed model assumes that the mass leaves the Thunder™ beam after creating an impact force. This means the beam will oscillate at its natural frequency after impact. However, in reality the ball bearing leaves the piezoelectric element when the direction of the applied acceleration changes.

The behaviour of the ball bearing when the impact based piezoelectric harvester is mounted using the CF method is analysed numerically in the next section. In order to understand the dynamic behaviour of the harvester when it is kept in a horizontal position, the equations of motion are solved numerically using a Runge-Kutta method.

$$\left\{\begin{array}{l} M\ddot{x} = 4\pi M'\omega_f^2 R\sin(\omega t) \\ M_m\ddot{y} + B_m\dot{y} + K_m y = 4\pi M\omega_f^2 R\sin(\omega t) \end{array}\right\} \quad 4.31$$

The first equation of the set of equations 4.31 shows that the acting force on the ball bearing mass (M') is the inertial force due to the frame acceleration. The second equation shows that the inertial force acting on the piezoelectric beam with (M_m) mass equals to the sum of the forces acting on the beam due to its acceleration, damping force due to electrical and mechanical damping (B_m) and elastic force due to the beam stiffness (K_m). x is the ball bearing position and y is the piezoelectric beam position. The dot superscript indicates the time derivative of the corresponding variable. This set of differential equations is solved until $x = \pm L/2$, where L is the length of the tube. At this point the equation of motion is given by equation 4.32, where the values of its initial conditions are passed from equation 4.31.

$$(m)\ddot{y} + B_m\dot{y} + k_m y = (m)4\pi\omega_f^2 R\sin(\omega t) \quad 4.32$$

m is the effective mass at impact. When the piezoelectric beam and the ball bearing are not in contact equation 4.31 will be used again. For this simulation a mass with 3.5 grams and 0.01 m diameter is used. The available displacement of the mass is 0.02 m. The distance between the centre of rotation and the centre of the tube is 0.06 m. All the results in this section are obtained when the harvester is kept in a horizontal position while rotating (CF method). The simulated dynamic behaviour of the ball bearing inside the tube is show in Figure 4.24. As the ball bearing accelerates due to the centripetal force, an impact occurs when the ball bearing reaches one end of the tube. Due to the impact, the ball bearing will be pushed away from this end of the tube. However, the centripetal acceleration forces the ball bearing to impact the same end of the tube. This creates a multiple impact situation. The ball bearing stays at the same end of the frame until the centripetal acceleration changes its direction. The arrows indicate that multiple impacts occur between the ball bearing and each side of the tube.

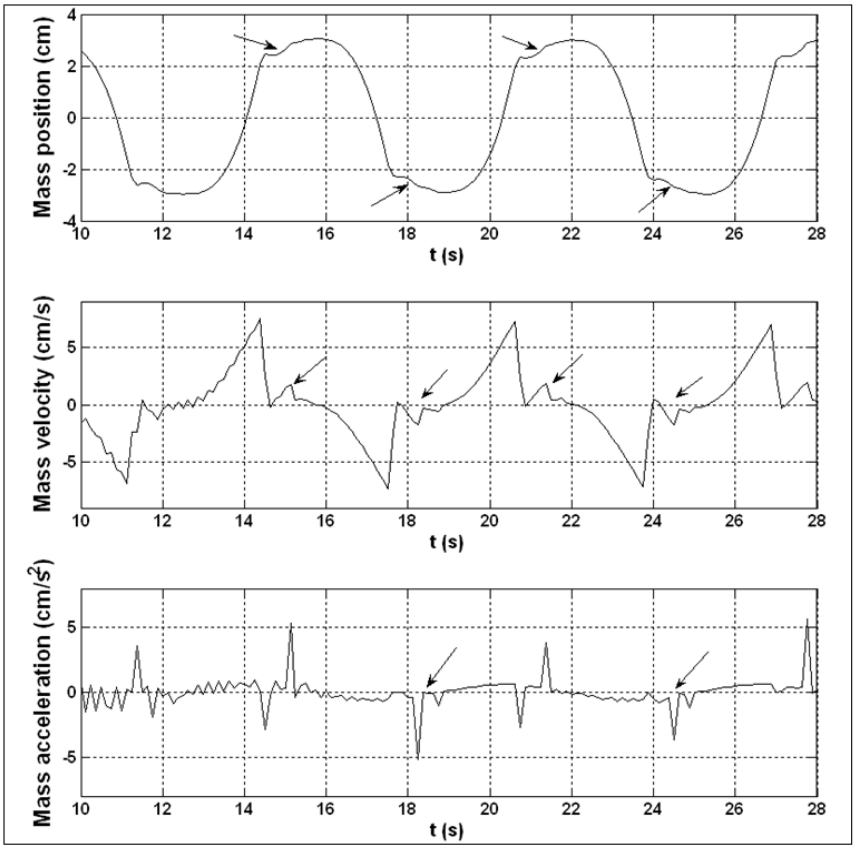

Figure 4.24 Dynamic behaviour of the ball bearing inside the harvester frame. The arrows show the multiple impact effect.

4.5.5 Optimization of the output power in geometries perspectives

The total volume of the impact based piezoelectric harvester consists of three main parts. The first one is the sum of the volumes of the two Thunder™ beams. The second part is the base that the Thunder™ beam is attached to and the last part is the volume of the tube between the two Thunder™ beams which ensures a free movement of the ball bearing due to the effect of the input force (Figure 4.25). The height and the width of the Thunder™ beam provide the minimum limit of the height (H = 0.026 m) and the width (W = 0.02 m) of the total volume of the harvester. This is due to the fact that the volume of the Thunder™ beams is fixed. Therefore, the optimum output power as a function of the harvester's volume can be only achieved by changing the length of the harvester (L) which depends on the mass of the ball bearing for a given maximum value of the rotating force. The only change in the total length of the harvester is achieved by changing the length of the tube located between the two Thunder™ beams as the value of the length (L_b) is constant. The value of L_b is 0.0016 m, which consists of the length of the base (0.001 m) and the height of the Thunder (0.0006 m). 19 %

from the bottom of the total height of the harvester (*H*) will be used to screw the harvester into the rotating wheel. The same percentage will be taken from the top of the harvester's height, so the ball bearing hits the middle of the Thunder™ beam. Therefore, a ball bearing located in the space between the top and the bottom layers has 61.5 % of the total height of the harvester. This means the maximum diameter of the ball bearing equals to 0.015 m. This generates a 0.0001 m difference between the diameter of the ball bearing and the diameter of the space that the ball bearing moves inside. This difference is made to reduce the amount of friction while the ball bearing moves inside the tube.

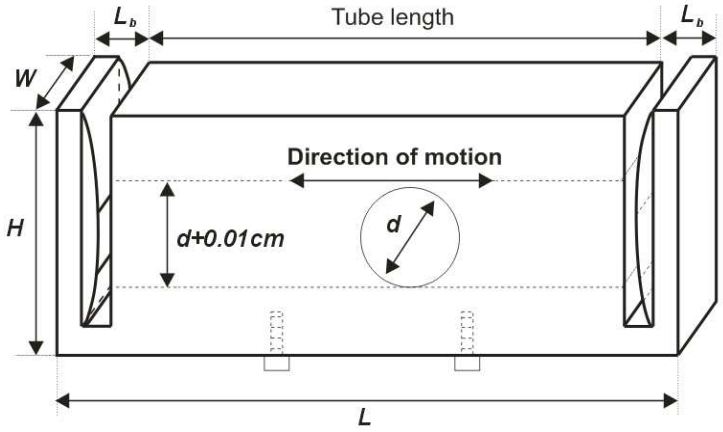

Figure 4.25 Total volume of the impact based piezoelectric harvester

The harvester is designed for a given value of the distance between the centre of rotation and the centre of the tube (*R*) as well as the maximum value of the rotational speed (*f*). For a given rotating speed and *R*, the generated force by the ball bearing depends on the value of its mass and the length of the frame. The maximum developed stress by the ball bearing in the Thunder™ beam must be equal to its yield value. This defines the amount of the initial energy that the Thunder™ can withstand before any plastic deformation occurs. The initial energy at impact (T_0) is directly proportional to the mass of the ball bearing (M') and to the squared value of the initial velocity of the ball bearing at impact (v_o), assuming that the velocity of the Thunder™ at impact is negligible compared to the ball bearing speed. Therefore, in order to achieve the maximum value of the input energy, the smaller the mass, the longer the tube will be. The criteria by which the harvester is designed for are: withstanding the maximum amount of input energy without breaking, occupying the minimum volume, having low value of mass and generating the maximum output power.

In order to achieve that, the values of the impacted force should be lower or equal the value at yield as calculated in Section 4.5.2. For the maximum value of *R* and *f*, the

procedure of optimizing the output power starts with using a mass with maximum available diameter (0.015 m). The value of its mass is calculated using the volume equation of a sphere and the density of the stainless steel. This value is used in equation 4.12 to calculate the effective mass at impact. Then equation 4.31 is solved numerically using a Runge-Kutta method in order to obtain the value of the impact force at different values of the frame length. The optimum length of the tube (L) is the one by which the value of the impact force is at yield when the rotational speed is at its maximum value. The impact force equals the stiffness of the Thunder™ beams times its displacement which is calculated numerically. The maximum output power is then calculated numerically as a function of rotating speed. The same procedure is repeated again for smaller ball bearing and thus lower value of the effective mass at impact. Finally, the relationship between the value of the output power and the dimensions of the ball bearing at the maximum value of the rotating speed (f), is obtained. From this relationship the optimum volume is the one that generates the maximum output power for a given rotation speed. Using the method explained in this section, the impact based piezoelectric harvester which its centre located at a distance of 0.06 m from the centre of rotation is optimized at maximum rotating speed of 15.55 Hz. This number is chosen because the maximum rotating speed for the wheel used in the experiment is 15.55 Hz. Figure 4.26 shows the relationship between the output power and the rotating speed at different values of the mass diameter.

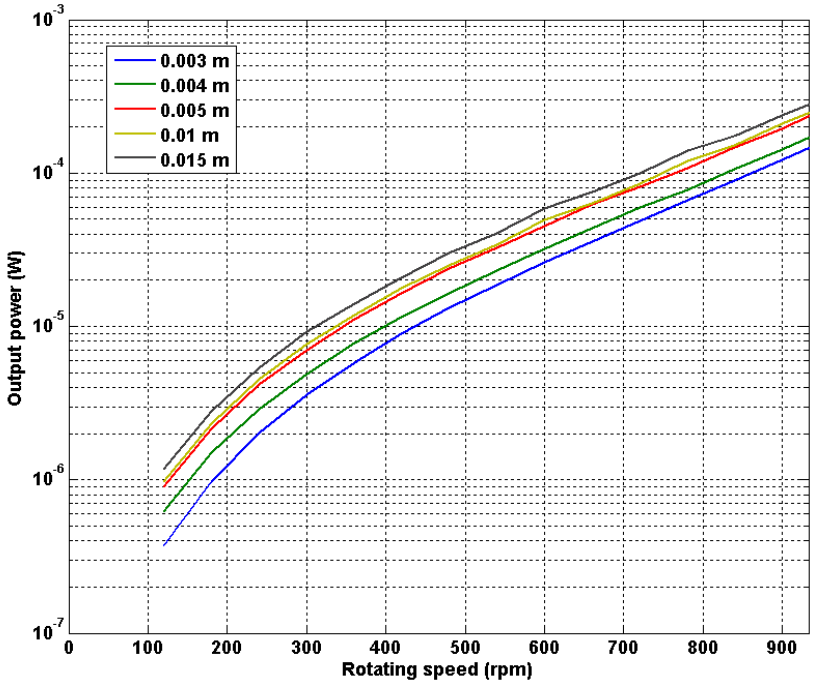

Figure 4.26 Output power versus the rotating speed using different size of the ball bearing.

The maximum output power is achieved when the mass diameter equals 0.015 m. For this mass value, the maximum available displacement for the ball bearing is found to be 0.00075 m. Therefore, the volume of the impact based piezoelectric harvester when R and f equal to 0.06 m and 15.55 Hz, respectively is 2.6 cm × 1.89 cm × 2 cm.

The relationship between the total volume of the generator and the mass diameter is shown in Figure 4.27.

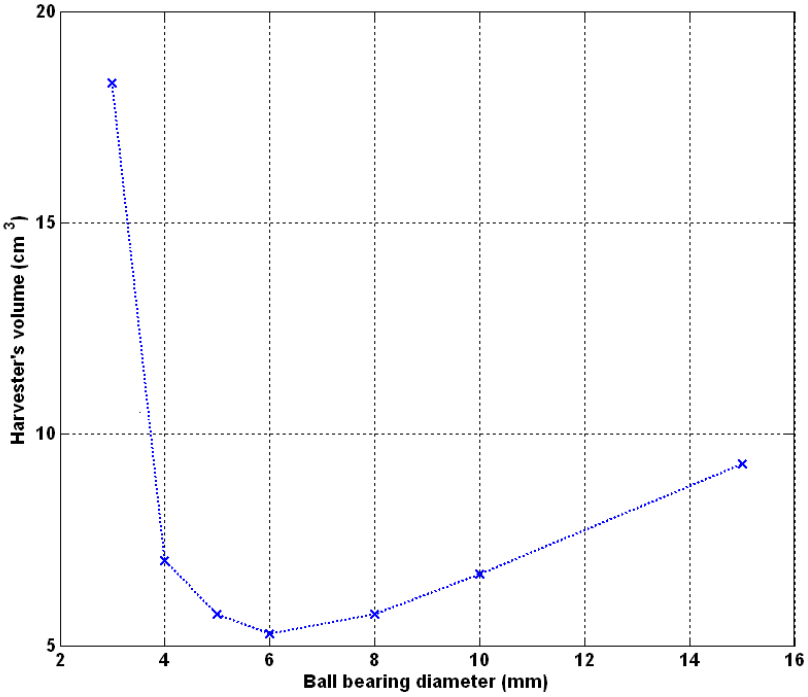

Figure 4.27 Total volume of the impact based piezoelectric harvester as a function of the ball bearing diameter

For a given value of the rotating speed, reducing the diameter of the mass from its maximum value (0.015 m) will result in reducing the total length of the tube and thus the total volume of the harvester. When the mass diameter is 0.006 m the harvester's volume is at its minimum value. After that any reduction in the mass diameter causes the harvester's volume to increase rapidly. Therefore, using a harvester with a mass diameter of 0.006 m instead of 0.015 m causes a reduction in the total volume of 43 % as well as a reduction in the output power by 17.8 %. The power density is at its maximum value when the diameter of the ball bearing is 0.006 m. The numerical calculations show that the output power is proportional to the cubic value of the rotating speed as shown in Figure 5.14.

4.6 Conclusion

This chapter detailed a method of extracting electrical power from rotational forces using an impact based piezoelectric harvester. Theoretically, it was proven that gravity force as well as both tangential and centripetal forces can provide electrical power by using an impact based piezoelectric harvester. The tangential forces are available only if the rotating speed is changing. Although the gravity and the centripetal forces can be considered as a permanent source of kinetic energy, their effect is limited by the way that the nonlinear harvester is fixed while the rotational motion is applied.

The harvester consisted of a tube, where a Thunder™ piezoelectric beam was placed at each end of the tube. A ball bearing was introduced to the tube. Due to the rotating forces the ball bearing moved from one side of the tube to the other creating an impact force on the piezoelectric beams. It was demonstrated that the amount of developed strain within the piezoelectric material depended on the way that the impact based piezoelectric harvester was mounted during rotation. For a given rotation speed, the power level from the piezoelectric harvester which had been mounted using the CF method was much higher than the one which used the GF method. This was due to the fact that the output power depends on the applied force on the piezoelectric transducer. In the CF method the main acting force that caused the mass to move from one side of the frame to the other was the centripetal force, where the effect of the gravity force and tangential force was negligible under constant rotating speed. However, under non-uniform circular motion the direction of the component of the tangential force was always in the same direction as the acting component of the centripetal force. In the GF method the main acting force that caused the mass to move from one side to the other was the gravitational force. Under non-uniform circular motion, the component of both the centripetal force and the tangential force (when the object is speeding up) acting on the ball bearing tried to keep the mass on one side of the tube. Therefore, in the GF method when the rotating speed reached a critical speed the ball bearing stuck at one end of the frame.

FEM was used to analyse the effect of clamping on the generated stress in the clamped area of the curved beam. The result showed that, under a given applied force, a simply supported curved beam generated the least amount of stress in the clamped area in comparison with rigidly supported on both ends and cantilever configurations. Therefore, the generated stress across the Thunder™ beam was analysed for an impulse force only when the beam was simply supported. The results from FEM showed that

stress in the axial, lateral directions as well as shear stress were generated in the structure due to the impulse force applied to the middle of the curved beam.

Analytical and numerical calculations were used to analyse the behaviour of the Thunder™ beam after impact and to calculate the maximum amount of stress that the device can withstand. Analytical calculations were obtained to analyse the impact force and the duration of impact and to calculate the value of the coefficient of restitution. The numerical calculations were used to understand the behaviour of the impact based piezoelectric harvester when it was mounted using the CF method. The model showed that a multiple impact was produced on each piezoelectric element. The model provided a method to predict the amount of power that can be generated due to the effect of the rotational forces. Moreover, the model showed the relationship between the output power and the dimensions of the harvester. The maximum output power was found to increase by increasing the length of the frame, the mass of the ball bearing, the rotating speed and the separation distance between the centre of the tube and the centre of rotation.

Chapter 5

An experimental investigation of the impact based piezoelectric harvester

5.1 Introduction

This chapter outlines the experimental techniques employed in this research and a description of how the test wheel and piezoelectric harvester are designed. A series of experiments are conducted to investigate the effect of rotating forces on the behaviour of the impact based piezoelectric harvester and to understand the effect of the impact force on the piezoelectric material for energy harvesting purposes. The experimental results are used to verify the model developed in Chapter 4. The piezoelectric harvester is tested under the effect of the gravity force when it is mounted using the GF method and it is tested under the effect of the centripetal force when it is mounted using the CF method. For the CF method, an extra mechanical structure is designed to keep the harvester in a horizontal position during rotation. This design is presented in Section 5.2.2. The strategy by which the experiments are carried out to investigate the effect of the rotational forces on the behaviour of the impact based piezoelectric harvester is presented in Section 5.3. Experimental tests are carried out to measure the effect of the harvester's parameters on the output power. These experimental results are compared to the ones obtained analytically.

5.2 Description of equipments

In order to analyse the performance of the piezoelectric harvester and verify the model developed in Chapter 4, a test wheel was designed for this purpose. The harvester was tested by mounting it on a wheel that was driven by a Motomate DC motor. The speed of the motor was controlled using Crouzet Logic Software. The piezoelectric harvester was attached to the wheel using a host. Details about the design of both the host and the wheel are described in Section 5.2.2, while the reason behind using Motomate DC motor is explained in Section 5.2.1.

5.2.1 DC motor

For this experiment a Motomate 80 watts-brushless motor with an integrated logic controller is used. This integrated motor, which had been manufactured by Crouzet Company, consisted of [79]:

- DC motor with available torque of 0.2 Nm, maximum speed of 3250 rpm and input voltage of 24 V.
- Programmable Logic Controller (PLC).
- Encoder with 2 channels which provided information regarding motor position and direction of rotation.
- Variable speed drive.

The Motomate integrated motor is simple to install, low-cost, and has the ability to control the movement, speed, acceleration, braking and the direction of rotation. Moreover, the integrated PLC allowed the user to use a simple programming language, Graphic Blocks, to program the motor and adjust it easily.

The principle of programming the Motomate can be broken down into 3 steps.

- Design a program on a PC using Crouzet Logic Software
- Compile the program
- Write to the Motomate

The purpose of the software is to increase the motor speed from a certain value to a maximum value over a certain time. The effect of the rotating speed on the impact based piezoelectric harvester is recorded by analysing the generated output power. The full graphic blocks diagram of the software has been given in Appendix B. The output of the software controls the status of the motor (On/Off), direction of rotation and its speed. The program is tested and simulated before programming the motor using

Crouzet Logic Software. Then it is compiled and written to the motor. The status of the motor (On/Off) can easily be controlled and its behaviour can be monitored by the Crouzet Logic Software.

5.2.2 Designing the rotating wheel

A rolling wheel offers a huge amount of kinetic energy especially at high speeds as presented in Section 8.3. A rotating disk was designed and then built in the Zepler workshop in ECS department in Southampton University. The aim of rotating disk was to mimic the rotating behaviour of a vehicle wheel for experimental purposes. The design simply consisted of Motomate motor (0.2 Nm 3250 rpm), a rotating disk, two metric pitch timing belt pulleys (30 T), where T represent teeth, (32 T) synchronous timing belt pulleys, (48 T) synchronous timing belt pulleys, two synchronous toothed belts (628, T2.5/230) and (707, T5/480) and a slip ring. The motor provided the required rotational movement to the disk. The piezoelectric transducer was fitted at the edge of the disk and the same mass was added opposite to the transducer in order to balance the disk while rotating.

The motor should provide enough torque to the spinning disk. Torque is the time-derivative of angular momentum and it can be given by the following equation:

$$\tau = \frac{dL}{dt} \qquad 5.1$$

The angular momentum L can be written in term of its mass moment of inertia (I_m) and its angular velocity (ω) as following:

$$L = I_m \omega \qquad 5.2$$

If (I_m) is constant then (τ) can be given by the following equation:

$$\tau = I_m \frac{d\omega}{dt} = I_m \alpha \qquad 5.3$$

Where α is the angular acceleration.

The mass moment of inertia (I_m) for a solid disk of radius (R), height (h) and mass (M) with added mass ($2m$) of a piezoelectric transducer and its balance weight can be given in the following equation:

$$I_m = \frac{1}{2} MR^2 + 2mR^2 \qquad 5.4$$

Angular acceleration is the rate of change of angular velocity over time. Therefore, the angular acceleration for a mass (m) located at a distance (R) of a rotating disk which was changing its linear velocity from v_1 to v_2 during certain period of time (t) can be given by the following equation:

$$\alpha = \frac{v_2 - v_1}{Rt} \tag{5.5}$$

Substituting equation 5.5 and equation 5.4 into equation 5.3 and rearranging terms yields to the following equation:

$$\tau = I_m \alpha = \frac{(0.5M + 2m)(v_2 - v_1)R}{t} \tag{5.6}$$

Aluminium with a density (ρ) of 2700 kg/m^3 was used to build a rotating disk with a mass (M). Equation 5.6 can be rewritten as follows:

$$\tau = \frac{(0.5\pi\rho R^2 h + 2m)(v_2 - v_1)R}{t} \tag{5.7}$$

Equation 5.7 allowed the disk height to be determined and gave the maximum torque that the motor can provide (0.2 Nm). Due to the design requirement the minimum thickness (h) of the disk should be 15 mm. The mass of piezoelectric transducer and its host can be up to 20 grams and thus the balanced weight is 20 grams. The maximum change in the linear velocity of the transducer under rotation is 13 m/s in 3 s. Therefore, the disk radius (R) was limited to 80 mm, if it was fitted directly to the motor. The length of the base, which carried the harvester, was 50 mm. This base was fitted on a pulley located 20 mm away from the disk edge. This required more torque from the motor. The torque from the motor was increased by fitting a synchronous timing belt pulley (32 T), where T represents the number of teeth, to the motor shaft. The rotation was then transferred using synchronous toothed belts to a bigger pulley with 48 teeth. The ratio between the two pulleys (1.5) increased the motor torque up to 0.3 Nm, but it reduced the maximum speed to 2166 rpm. Increasing the motor torque allowed an increase in the disk radius up to 100 mm. The pulley (48 T) was fitted into a shaft through a ball bearing. One end of the shaft was fixed rigidly while the rotating disk was fitted on the other end of the shaft. A metric pitch timing belt pulley (30 T) was fitted on the free end of the shaft, which went through the middle of the disk. Finally, a slip ring was added to the free end of the shaft. All mechanical components along the shaft were concentrically aligned. Another timing belt pulley (30 T) was

added to the disk 20 mm away from its edge. This pulley was used to hold the piezoelectric transducer through an L shaped aluminium base. A synchronous toothed belt was used to connect the two timing belt pulleys together. As the pulley in the middle of the disk was fixed (not rotating), the belt would force the other pulley, 20 mm away from the disk edge, to stay in a horizontal position while it was rotating. Therefore, everything mounted on this pulley will stay in the same position during the rotation. Removing the belt connecting these two pulleys means that the harvester will not be kept in a horizontal position and it will rotate with the wheel. A cross section of the mechanical design that was used to keep the piezoelectric transducer in a horizontal position is shown in Figure 5.1.

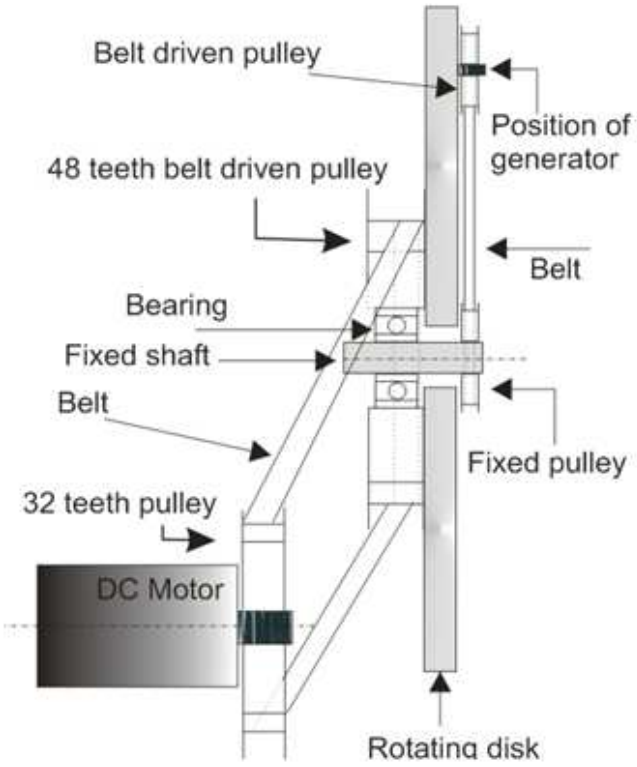

Figure 5.1 Cross section of the designed rotating wheel that allows the harvester to stay in a horizontal position while rotating.

Finally, the wires from the transducer electrodes were connected to the slip ring for measurement reading. Figure 5.2 shows the experimental set-up to extract energy from rotation.

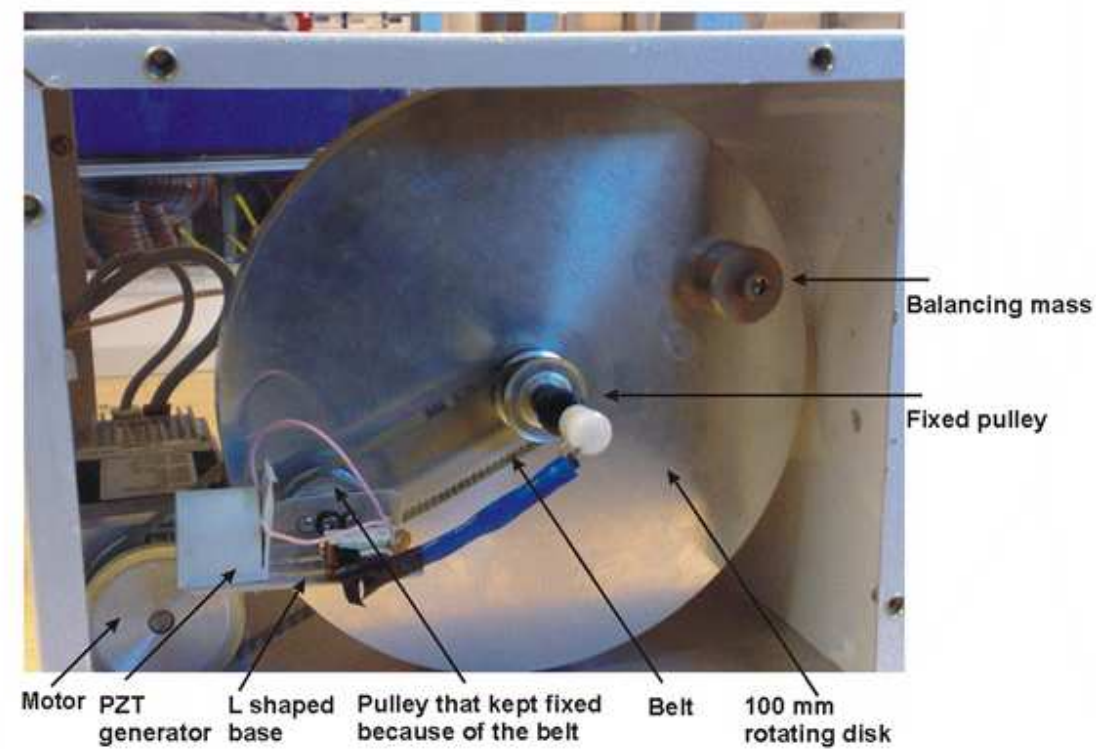

Figure 5.2 The testing wheel that has been used in the lab.

A photograph of the constituent parts of the impact based piezoelectric harvester including the tube, ball bearing and the Thunder™ piezoelectric pre-stressed beam is shown in Figure 5.3.

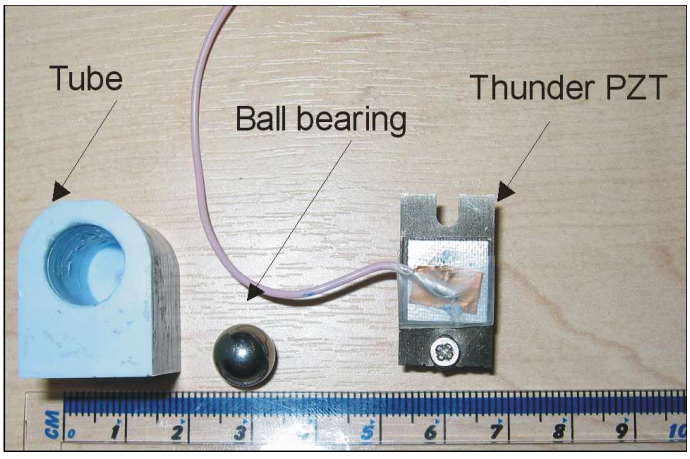

Figure 5.3 A photograph of the constituent parts of the piezoelectric harvester.

5.3 Experimental strategy

To determine the behaviour of the impact based piezoelectric harvester under rotation and to measure its average output power, both a rotating disk and a piezoelectric transducer host were designed as detailed in Section 5.2.2. The

experiment was carried out using a Thunder™ pre-stressed beam mentioned in Section 3.2.7 due to its mechanical stability. After the impact based piezoelectric harvester was assembled, the whole structure is attached to the host (Figure 5.2). The distance between the centre of the tube and the centre of rotation was 0.06 mm. Two series of experiments at different constant speeds ranging from 100 rpm to 800 rpm are performed to verify the theoretical prediction of the average output power and its dependency on the rotating speed.

For both experiments, the length of the frame was kept constant at a value of 0.015 m. A ball bearing with a diameter of 0.01 m and a mass of 0.0035 kg was used. The tube had a diameter of 0.011 m. The 1 mm difference in diameter between the ball bearing and tube was made to reduce the friction between them.

In the first experiment the belt that connects the central pulley to the one located at the edge of the rotating wheel was removed. Therefore, the position of the piezoelectric harvester will change and the GF method will be applied on the harvester. In this situation, the main acting force that causes the ball bearing to move from one side of the tube to the other is the gravity force. The behaviour of the transducer in terms of the generated output power due to the impact force was recorded. The effect of the rotational and gravity forces on the generated output power when the ball bearing is removed from the tube was recorded.

In the second experiment, the harvester was kept in a horizontal position during rotation. This was achieved by connecting the central pulley to the one located at the edge of the wheel using a belt (see Section 5.2.2). The reason behind mounting the transducer in this position was explained in Section 4.3.3. In this case, the main acting force that causes the ball bearing to move from one side of the tube to the other is the centripetal force. The effect of this force on the generated output power was recorded in the absence and the presence of the ball bearing.

After the relationship between the rotating speed and the output power was tested, the dependency of the output power on both the frame length and the ball bearing mass was examined. Firstly, the relationship between the frame length and the maximum average output power for a given mass is investigated. A 0.0035 kg ball bearing mass was used to generate an impact force on the piezoelectric elements under different rotating speed. Four different frame lengths with available mass displacements of 0.002, 0.005, 0.01 and 0.02 m were used. Secondly, the effect of the ball bearing mass on the maximum average output power was investigated under different rotating

speeds. Therefore, the 0.0035 kg ball bearing was replaced with a 0.0083 kg ball bearing. Frame lengths with available mass displacements of 0.002, 0.005, 0.01 and 0.015 m were used. The measurements of the open circuit voltage and the average output power were achieved using a mixed signal oscilloscope, a programmable resistance substituter and a resistance box as detailed in Section 5.4.2 and Section 5.4.3.

5.4 Measurement techniques

The method that was used to measure the capacitance of Thunder™ beam is presented in Section 5.4.1. Sections 5.4.2 and Section 5.4.3 present the methods that were used to measure the open circuit voltage and the average output power of the piezoelectric element under different conditions of the applied forces.

5.4.1 Capacitance of the piezoelectric curved beam

A Wayne Kerr Automatic LCR meter 4237 was used to measure the capacitance between the electrodes of the piezoelectric curved beam (Thunder™). The measured value was compared to the one is obtained analytically using equation 3.31. The analytical value of the capacitance is 7 nF, while the measured value of the Thunder™ beam is found to be 6 nF.

5.4.2 Open circuit voltage

The open circuit voltage is measured by connecting the electrodes of the piezoelectric beam to a mixed signal oscilloscope (300 MHz) from Agilent Technologies. The open circuit voltages were recorded when different types and amplitudes of the forces were applied on the piezoelectric element.

5.4.3 Output voltage and average output power

The Root Mean Square voltage (V_{rms}) was measured by connecting the electrodes of the piezoelectric element into a programmable resistance substituter from IET LABS, INC. National Instrument LabVIEW8 hardware and software tools were used to change the output resistance load (R) of the piezoelectric element from 1 Ω to 9 MΩ. At different values of the output resistance, LabVIEW software calculates the RMS

voltage of the output signal. The software uses equation 5.8 to calculate the value of V_{rms}, where n is the number of values of the output voltage at a specific resistance load. As discussed in Section 4.5.3.2 and Section 4.5.4 the width of the impulse due to the ball bearing impacting on the Thunder™ beam is in the range of 10^{-4} s. Therefore, the acquisition rate was chosen to be 50 MHz.

$$V_{rms} = \sqrt{\frac{V_1^2 + V_2^2 + ... + V_n^2}{n}} \qquad 5.8$$

The procedure for obtaining the RMS voltage is described as follows. Initially, a run was performed with programmable resistance substituter. This gave the zero value. Then the input of the programmable resistance substituter was connected to the electrodes of the piezoelectric element. A run was performed again and the values of RMS voltages at different output resistances were saved. The same procedure was repeated three times in order to obtain the average value of V_{rms}. The zero value was subtracted from the average voltage to obtain the real value of V_{rms}, which was used to calculate the average output power using the following equation:

$$p_{average} = \frac{V^2{}_{rms}}{R} \qquad 5.9$$

The same procedure was used in order to measure RMS voltage under different conditions of applied force. The optimum resistance was determined from a plot of $P_{average}$ against R. The optimum resistance was defined as the value of the output resistance by which the obtained output power was at its maximum value.

5.5 Experimental results and discussion

In this section, experiments are carried out to investigate the effect of using the GF and the CF method on the generated output power using Thunder™ beam. The measured results from the impact based piezoelectric harvester under impact are compared to the model that is developed in Chapter 4. Experimental results from the impact based piezoelectric harvester are obtained in two situations when the harvester is mounted using the GF and the CF methods. For both methods, the distance between the centre of rotation and the centre of the tube is 0.06 m, the available displacement of the ball bearing inside the tube is 0.02 m and the diameter of the ball bearing (d) is 0.01 m. In the GF method, the Thunder™ pre-stressed beams are rigidly supported while in

the CF method the Thunder™ beams are simply clamped. In order to investigate the effect of the gravity and the centripetal forces, the ball bearing is removed from the tube and the generated output voltage is recorded. These results are compared to the one obtained theoretically.

5.5.1 Power output generated due to the effect of the gravitational force

In this experiment the harvester is mounted using the GF method without using the ball bearing. The effect of the gravity force on the Thunder™ beam is measured and analysed. For this experiment, the motor accelerates from its initial value to its target value in 5 sec. When the motor reaches its target speed, it rotates at that speed for 7 min. This time is enough to measure the output voltage across different values of the load resistance ranging from 100 Ω until 1 MΩ. The motor changes its rotating speed from 0 rpm to 800 rpm with a step of 100 rpm, where data is collected. The readings of the open circuit voltage when the wheel rotates under constant angular velocities (200, 333, 600, 800 rpm) are presented in Figure 5.4. The output voltage is generated due to the rotational forces only. Increasing the constant velocity from 200 rpm to 800 rpm, results in an average increase in the open circuit voltage peak by 0.04 V. These results show little dependence on the rotating speed over the speed range measured.

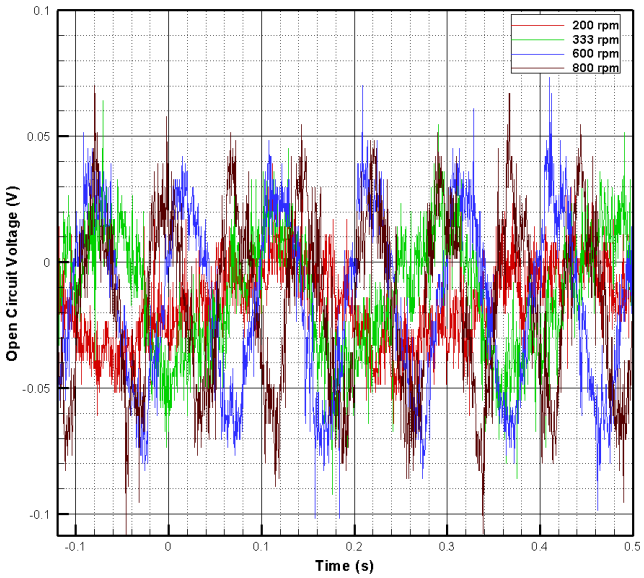

Figure 5.4 Open circuit voltage measurements using Thunder™ pre-stressed beam at different rotating speeds under gravitational force

The output average power over the speed ranged from 200 rpm to 600 rpm at optimum load resistance is approximately 3.64×10^{-11} W. This value increases up to 1.8×10^{-9} W at a rotating speed of 800 rpm.

5.5.2 Power output under impact force due to the effect of the gravitational force

In this experiment, the motor accelerates from its initial value to its target value in a time of 5 sec. The rotating speed increases from 0 to 300 rpm at a step of 15 rpm and every time the motor reaches its new target it will rotate at that speed for 7 min. For this experiment the available displacement of the ball bearing is 0.015 m. The frame is mounted in a way that the distance between the beginning of the frame and the point where the direction of the centripetal force is perpendicular to the free movement of the ball bearing (ΔL) is around 0.005 m. The radius of the rotating wheel is 0.06 m and the diameter of the ball bearing is 0.01 m. Therefore, the critical rotating speed by which the ball bearing sticks to one end of the frame can be calculated using equation 4.5 and it is equal to 3.6 rps.

Figure 5.5 and Figure 5.6 present the open circuit voltage of the impact based piezoelectric harvester. These results show that the output voltage peak increases by increasing the rotating speed and it reaches its maximum value of 5.6 V at a rotating speed of 133 rpm (Figure 5.5(b)). This speed corresponds to the maximum rotating speed that allows the ball bearing to move across the length of the tube during one cycle. Higher rotating speeds allow the ball bearing to generate an impact on only one side of the frame as the ball bearing can not move from one side of the frame to the other. By increasing the rotating speed even further the displacement of the ball bearing inside the frame reduces due to the effect of centripetal force. In this situation the ball bearing generates an impact force only on one side of the frame and this force reduces with increasing the rotating speed (Figure 5.5 (c)). This is due to the fact that increasing the rotating speed reduces the displacement of the ball bearing until the rotating speed reaches its critical value when the ball bearing sticks to one end of the frame. At this critical speed the component of the centripetal force becomes significant enough to prevent the ball bearing from moving away from one end of the frame. Figure 5.5 (d) shows that the peak output voltage drops to 0.55 V at a constant speed of 200 rpm due to the decrease of the displacement of the ball bearing. At a speed of 210 rpm the output power peak was 0.01 V and the ball bearing is completely attached to one end of the frame and its internal displacement is negligible. Beyond 210 rpm, one of the

Thunder™ pre-stressed beams and the ball bearing act as one body and the output voltage then increases slightly with the rotating speed.

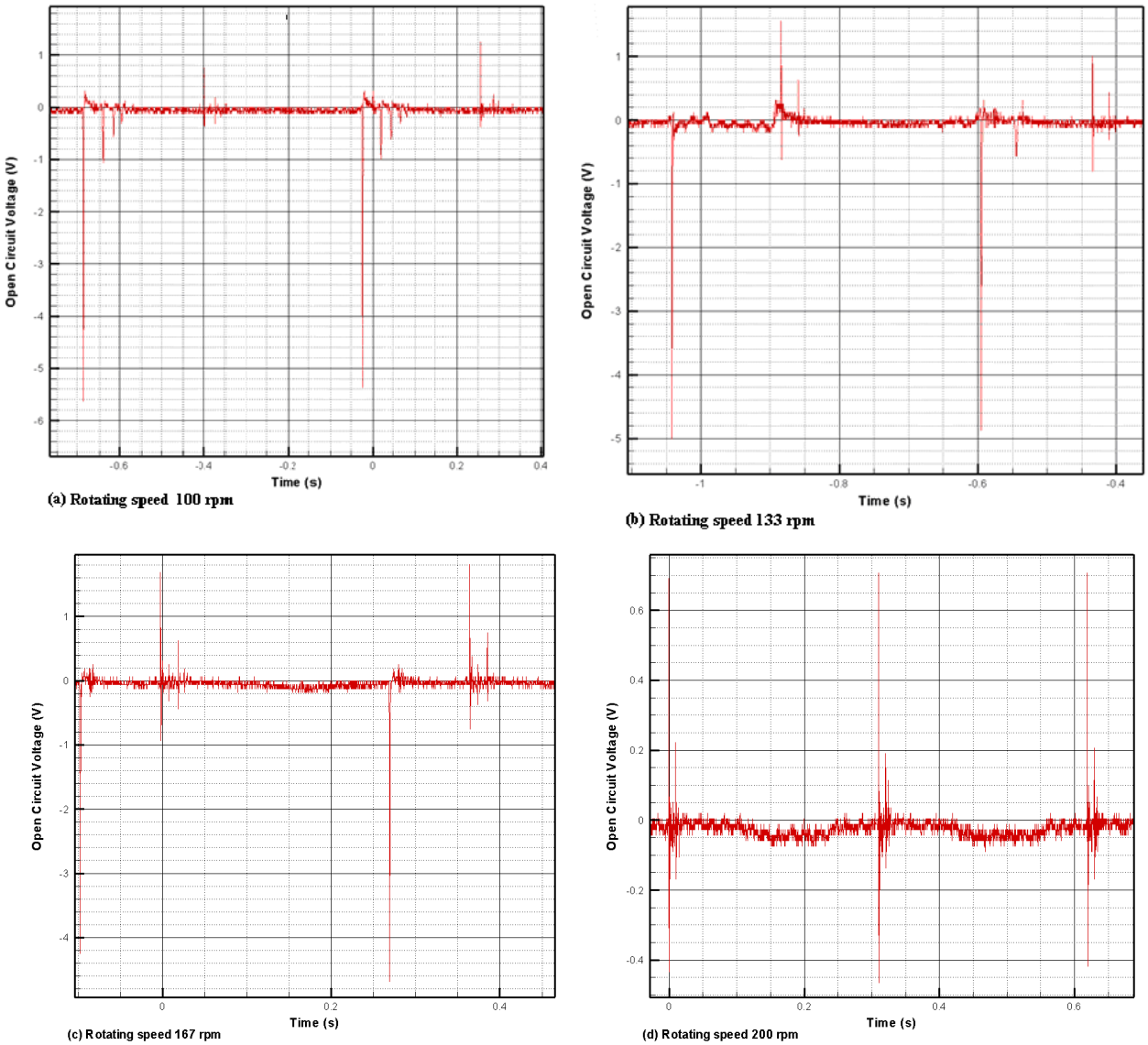

Figure 5.5 Open circuit voltage measurements using Thunder™ beam at up to 200 rpm under the effect of the impact force

In addition, the waveform of the open circuit voltage is similar to the one where no ball bearing is introduced to the system as shown in Figure 5.6. However, the peak value is slightly higher at around 0.01 V at 330 rpm. It is predicted theoretically that the ball bearing sticks to one end of the tube when the rotating speed reaches 3.6 rps using the GF method. The experimental result agrees with the analytical one. The numerical model, presented in Section 4.5.4, that describes the behaviour of the mass predicts that a multiple impact situation occurs after the mass and the pre-stressed beam are in contact with each other. This can be demonstrated in Figure 5.5 where after each peak

due to the direct collision between the mass and the piezoelectric material there are a few peaks with lower amplitude.

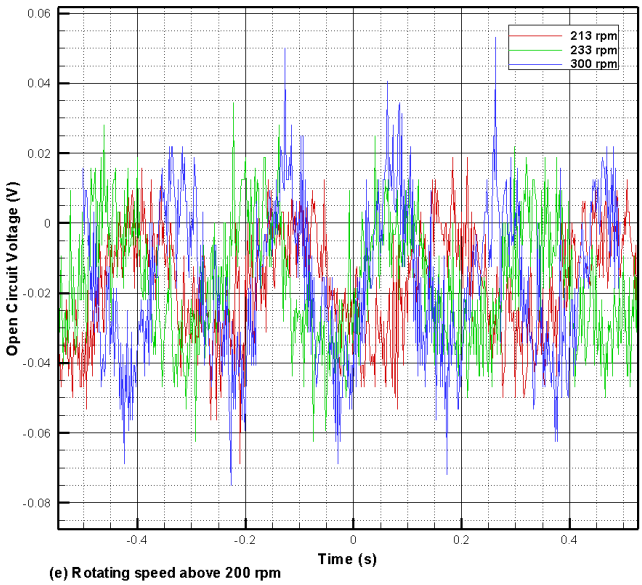

Figure 5.6 Open circuit voltage measurements using Thunder™ pre-stressed beam at rotating speed between 213 and 300 rpm under gravitational and impact forces

In order to investigate the relationship between the output power and the load resistance, the root mean square voltage at each value of the load resistance is measured and the output power is calculated as has been illustrated in Section 5.4.3. Figure 5.7 shows the effect of increasing the rotating speed on the average output power when the harvester is mounted using the GF method. The output power is measured across the optimum load resistance. The value of the load resistance changes with the rotating speeds. The different values of the of the load resistance are given at the end of this section.

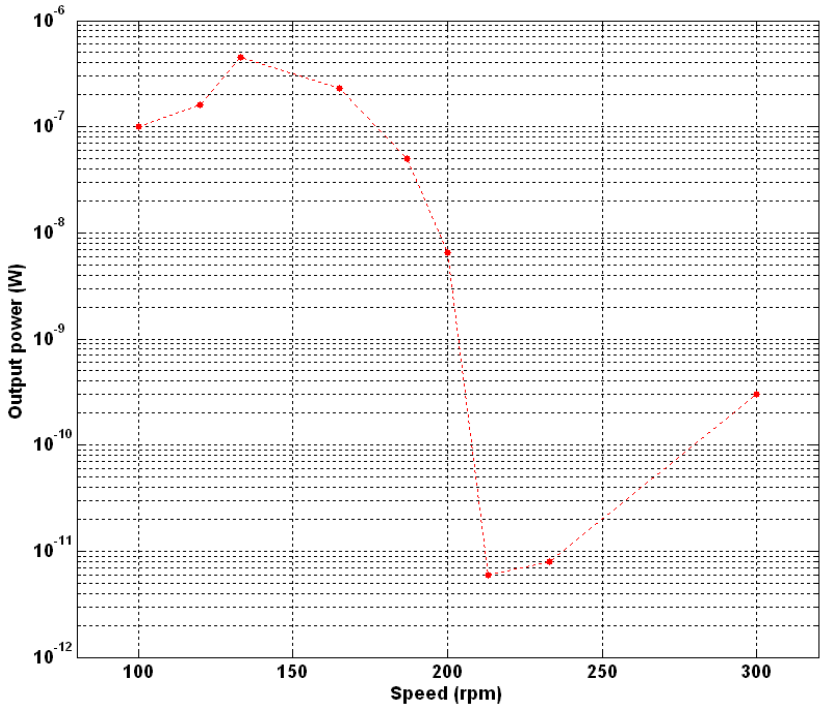

Figure 5.7 Output power as a function of rotating speed using Thunder™ pre-stressed beam under gravity and impact forces

These results are obtained experimentally. This graph can be divided into 3 main regions. In the first region, the power increases slightly from 10^{-7} W to 4×10^{-7} W when the rotating speed increases from 100 rpm to 133 rpm respectively. In this region the internal displacement of the ball bearing equals the whole length of the frame. Therefore, increasing the rotating speed in this region results in an increase in the ball bearing momentum acceleration by which it hits each end of the frame and hence the applied force. In the second region, increasing the speed from 133 rpm to 200 rpm reduces the output power dramatically to 5×10^{-9} W. This is due to the effect of the component of the centripetal force acting in the direction of the free movement of the ball bearing. The value of this force increases by increasing the rotating speed.

The higher the applied speed the less available internal displacement the ball bearing has. At a speed of 210 rpm the average output power will reach its minimum value of 6×10^{-11} W. This speed defines the beginning of region three where the ball bearing is completely attached to one end of the frame and its internal displacement is negligible. In this region, the ball bearing and one of the piezoelectric pre-stressed beam begin to behave as one entity. Therefore increasing the rotating speed will result in a slight increase in the average output power due to the applied force from rotation. Figure 5.8 shows the average output power versus the load resistance in region one.

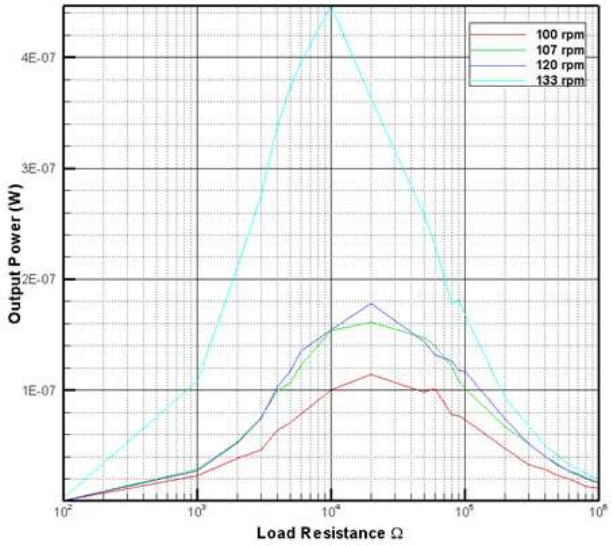

Figure 5.8 Output power as a function of load resistance at rotating speeds up to 133 rpm using impact based piezoelectric harvester mounted using the GF method

The average output power increases by increasing the load resistance until it reaches its maximum value at the optimum load resistance. After that any increase in the load resistance results in a reduction in the output power. Moreover, increasing the rotating speed, results in an increase in the output power due to the increase in the impact force. The optimum output load resistance slightly reduces from 20 kΩ to 10 kΩ by increasing the rotating speed from 100 rpm to 133 rpm. Figure 5.9 shows the effect of increasing the load resistance on the average output power at different values of rotating speed in region two.

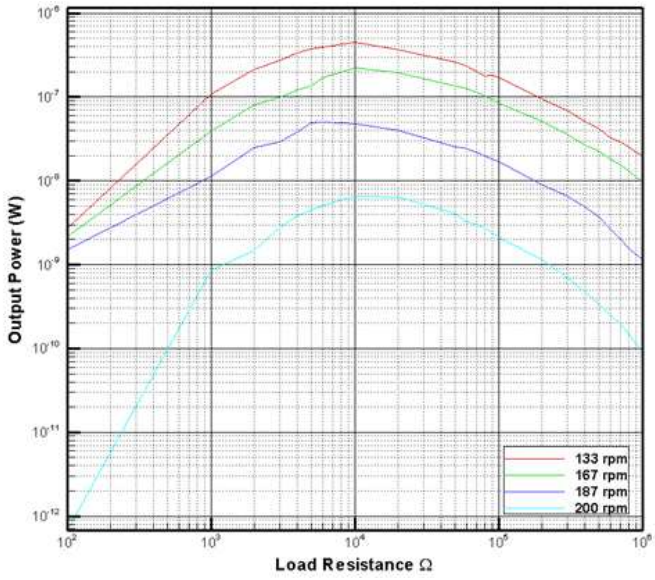

Figure 5.9 Output power as a function of external resistance at a rotating speed between 133 and 200 rpm using Thunder™ piezoelectric pre-stressed beam under centripetal and impact forces output

In this region, increasing the speed reduces the output power dramatically. However, the load resistance is fixed at one value of 10 kΩ in this region. Any further increase in the rotating speed beyond 210 rpm results in a slight increase in the output power and a major increase in the value of the optimum resistance. The optimum load resistance at a rotating speed of 210 rpm is approximately 200 kΩ. The reason behind the changes in the value of the optimum load resistance is explained in the last paragraph of Section 5.6.

5.5.3 Power output generated due to the effect of the centripetal force

The motor accelerates from its initial value to its final one in 5 sec. When the motor reaches its target speed, it rotates at that speed for 7 min, which is enough time to measure the changes in the output power across various values of the load resistance. The load resistance varies from 10 Ω to 1 MΩ at a step of 1 kΩ, where the output power is calculated. After reaching 100 kΩ, the step increases up to 10 kΩ. The changes in the output voltage across the load resistance are recorded at 200 rpm, 333 rpm, 600 rpm and 800 rpm. In this experiment, the harvester is mounted using the CF method without the use of the ball bearing.

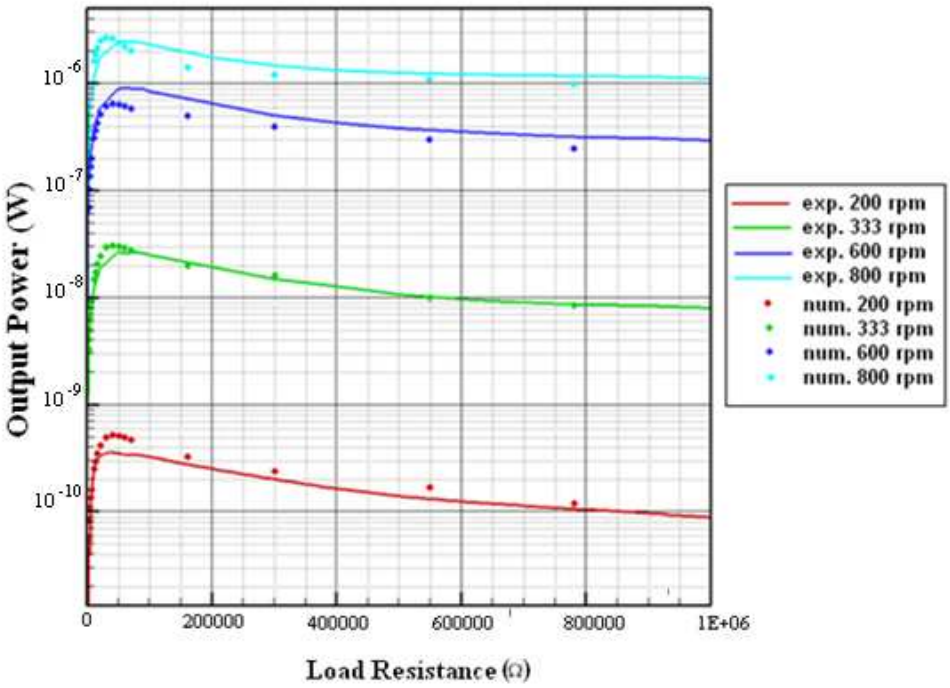

Figure 5.10 Output power as a function of external resistance with different operational frequencies using Thunder™ pre-stressed beam under centripetal force, solid lines present the experimental (exp.) results and the symbols present the numerical (num.) data

The ball bearing is taken from the tube in order to measure the effect of the centripetal force on the output power generated from the Thunder™ beam. Figure 5.10 shows the average output power versus the load resistance. It is found that the maximum output power is achieved when the load resistance is at its optimum value. The optimum load resistance is found to be 60 kΩ over the speed range. Increasing the rotating speed, results in an increase in the output average power due to the increase in the applied centripetal force. The output averaged power at 200, 333, 600 and 800 rpm are 3.5×10^{-10}, 2.7×10^{-8}, 9×10^{-7} and 2.5×10^{-6} W respectively. Figure 5.10 shows that the resistance corresponding to the peak power between the experimental and the numerical results is displaced by 50 %. The difference in the amplitude peaks between the experimental and the numerical results reach up to 20 %.

5.5.4 Power output under impact force due to the effect of the centripetal force

In this experiment, the impact based piezoelectric harvester is mounted using the CF method. The main source of the output voltage is the impact generated by the ball bearing within the tube due to the effect of the centripetal force. The changes in the output voltage across the load resistance are recorded at 200 rpm, 333 rpm, 600 rpm and 800 rpm. The values of the load resistance ranged from 100 Ω to 1 MΩ at a step of 1 kΩ, where the output power is calculated. After reaching 100 kΩ, the step increases to up to 10 kΩ. Both experimental and theoretical results prove that the amount of power generated by mounting the impact based piezoelectric harvester using the CF method is higher than the one generated by the GF method for a given rotating speed. The main source of energy in the impact based piezoelectric harvester is the impact generated by the ball bearing. The numerical model that describes the behaviour of the mass predicts that a multiple impact situation occurs after the mass and the pre-stressed beam are in contact with each other. Therefore, after each peak due to the direct collision between the mass and the piezoelectric material there are a few peaks with lower amplitude. After that the mass sticks to the beam until the frame acceleration changes its direction. This experiment is carried out to verify the developed model. Figure 5.11 shows the output open circuit voltage produced by one of the pre-stressed beam at a rotating speed of 800 rpm.

The main output voltage peak generated by a direct contact between the piezoelectric beam and the mass is followed by a few peaks with lower amplitude. This agrees with the model where multiple impacts are predicted (4.5.4). In Figure 5.11 the

long peak is formed when the piezoelectric element is directly compressed by the ball bearing. This is followed with shorter amplitudes generated by the multiple impacts. Another long peak appears again after one cycle. Figure 5.11 shows that there is a peak after half a cycle, which is formed due to the impact between the ball bearing and the other side of the tube.

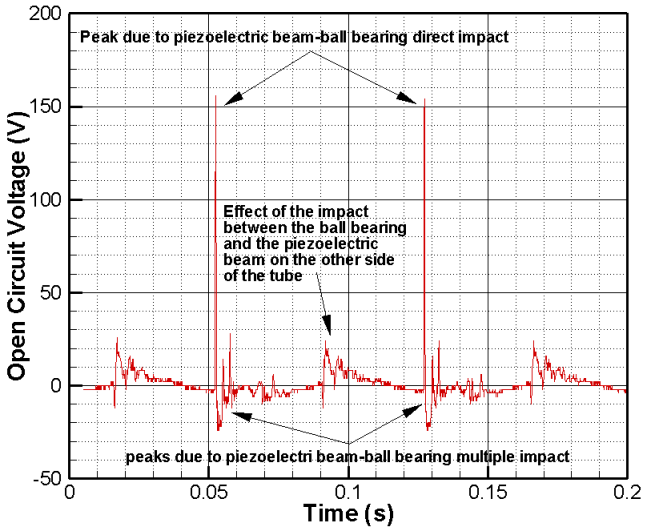

Figure 5.11 The open circuit voltage at a rotating speed of 800 rpm

This impact creates a vibration that can transfer through the tube and causes output power to be generated from the piezoelectric located on the other side of the tube. The experimental results that show the effect of rotating speed on the open circuit voltage of the pre-stressed beam when subjected to impact force are presented in Figure 5.12.

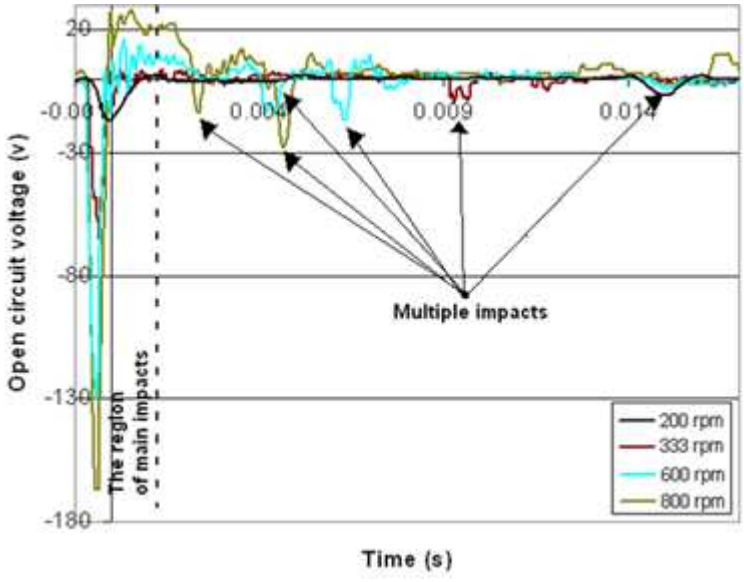

Figure 5.12 Open circuit voltage measurements using Thunder™ pre-stressed beam at different rotating speeds under centripetal and impact forces

As can be seen, multiple peaks occur after the direct collision between the mass and the piezoelectric pre-stressed beam due to multiple impacts between them. Although increasing the speed increases the amplitude and the frequency of the waveform, it slightly reduces the width of the pulses. Figure 5.13 shows the average output power introduced by one of the Thunder™ pre-stressed beam versus the load resistance.

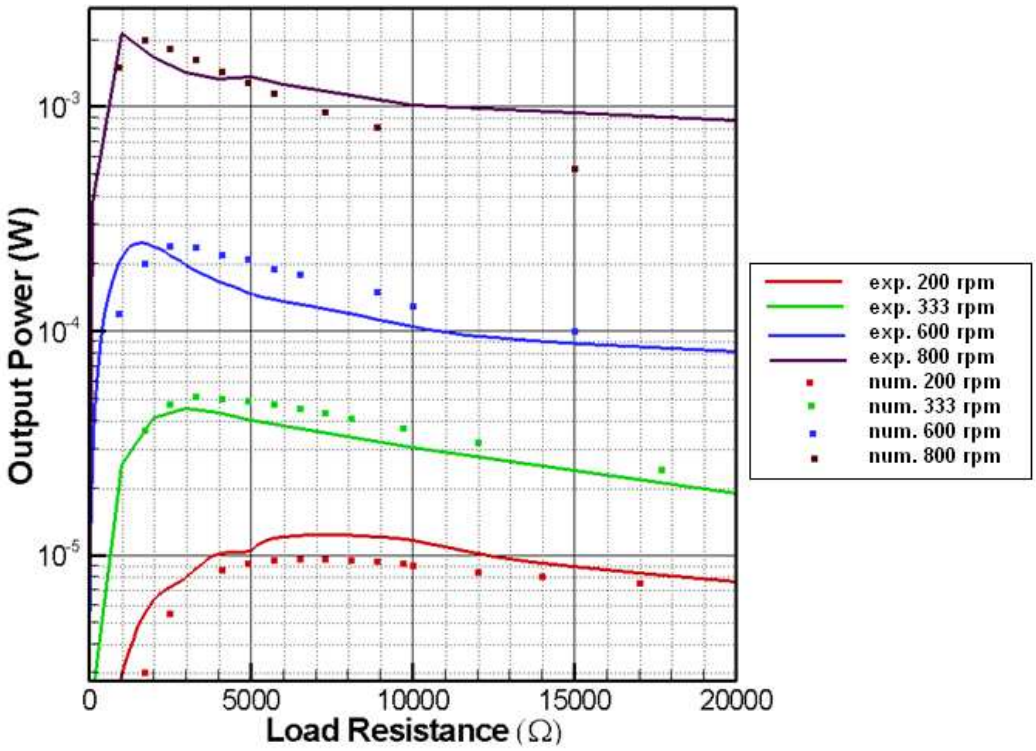

Figure 5.13 Output power as a function of external resistance at different rotating speeds using Thunder™ piezoelectric pre-stressed beam under centripetal and impact forces, solid lines present the experimental (exp.) results and the symbols present the numerical (num.) data

Figure 5.13 shows that the resistance corresponding to the peak power between the experimental and the numerical results is displaced by up to 50 %. The difference in the amplitude peaks between the experimental and the numerical results reach up to 20 %. The experimental results outline the effects of using the ball bearing on the average output power. A maximum average power of 2 mW, occurs at a rotating speed of 800 rpm. As can be seen, reducing the rotating speed resulted in a reduction in the average output power. The slight shift in the maximum value of the output power indicates a decrease in the optimum load resistance of the transducer when the rotating speed increases. This is due to reduction in the mechanical damping of the Thunder™ and an increase in its stiffness.

The output averaged power produced by each transducer at 200, 333, 600 and 800 rpm are 1.2×10^{-5}, 4×10^{-5}, 2.4×10^{-4} and 2×10^{-3} W at an optimum resistance of 6 k Ω, 3 k Ω, 2 k Ω and 1 k Ω respectively. Comparing the value of the optimum resistance of the simply supported Thunder™ beam with and without the use of the ball bearing in the tube shows that introducing the ball bearing to the system results in a reduction in the mechanical damping of the transducer. Therefore, the electrical damping presented by the optimum load resistance is reduced by one order of magnitude.

5.6 Effect of the harvester's parameters on the average output power

Two series of experiments at different rotating speeds, ranging from 10 rpm to 900 rpm are performed to verify the theoretical prediction of the average output power and its dependency on both the frame length and the ball bearing mass. The first experiment investigates the relationship between the frame length and the maximum average output power for a given mass at different rotating speeds. The second experiment investigates the effect of the ball bearing mass on the maximum average output power. The second experiment is performed at different rotating speeds and for a given frame length.

In the first experiment, a 0.0035 kg ball bearing mass is used to generate an impact force on the piezoelectric element. Four different frame lengths with available mass displacements of 0, 0.005, 0.01 and 0.02 m are used. The voltage drop across the optimum resistance of the Thunder™ beam for each frame length is measured and recorded at different rotating speeds. Figure 5.14 presents the effect of rotating speed (f) on the maximum average output power (P) at different frame lengths using 0.0035 kg ball bearing.

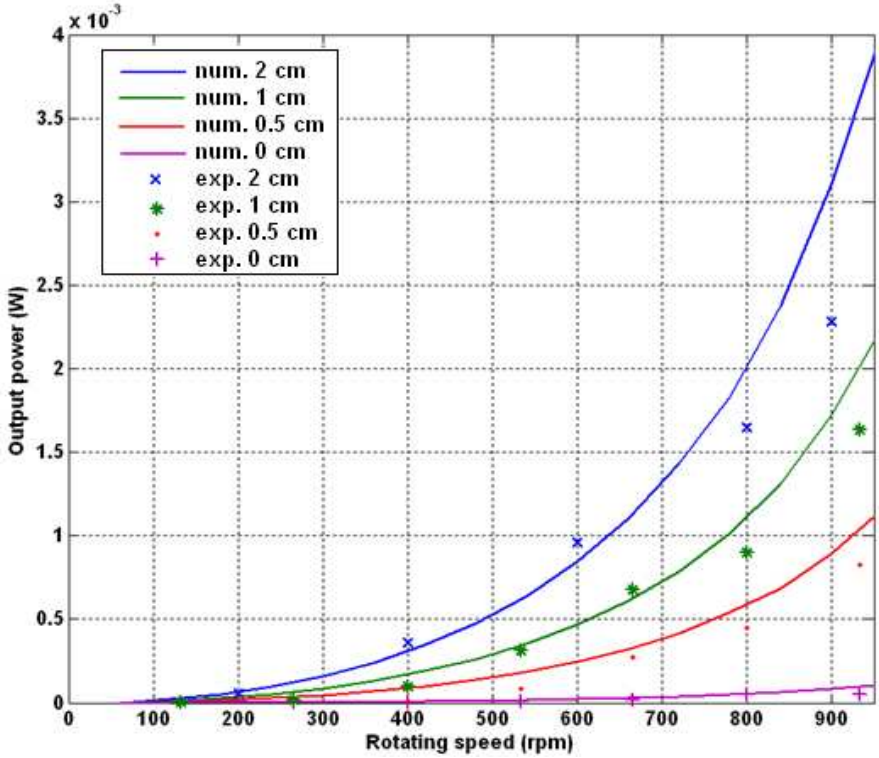

Figure 5.14 Rotating speed versus maximum average output power using 3.5 grams ball bearing at different frame length, solid line is the numerical (num.) results and the symbols are experimental (exp.) data

Theoretically, it is found that the average output power is proportional to the cubic value of the rotating speed $P \propto f^3$. Practically, this relationship is valid if the rotating speed does not exceed the value at which the piezoelectric beam will be at yield. If the rotating speed exceeds the recommended value, the generated output power will be less than the one predicted theoretically due to plastic deformations. Both the theoretical and experimental results agree that the harvester with a ball bearing produces more average output power than the same harvester without the use of a ball bearing. Both results agree that increasing the rotating speed results in an increase in the average output power. The effect of increasing the available mass displacement on the maximum output average power at different rotating speeds using 0.0035 kg ball bearing is illustrated in Figure 5.15.

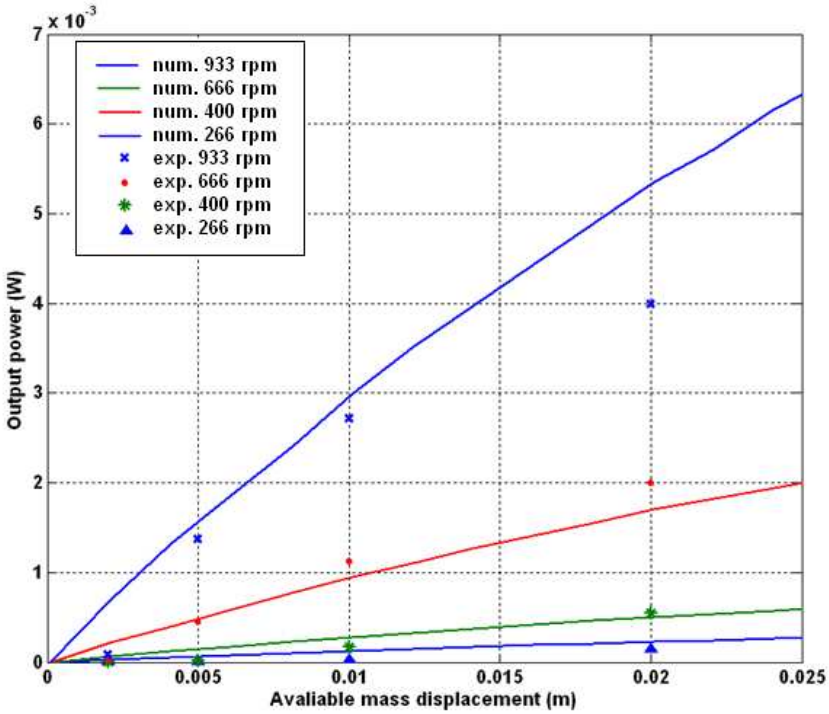

Figure 5.15 Average output power versus mass displacement using 0.0035 kg mass at different rotating speed, solid line is the numerical (num.) results and the symbols are experimental (exp.) data

For a given value of the mass and the length of the tube the numerical method that was presented in Section 4.5.5 is used to calculate the maximum rotating speed that causes the Thunder™ beam to be at yield. Numerical calculations show that when the available displacements of the mass change as follow 0.02 m, 0.01 m, 0.005 m and 0 m, the maximum rotating speeds that put the piezoelectric element at yield change as follow 510 rpm, 560 rpm, 660 rpm, and 1080 rpm, respectively. This is calculated when R and M' equal to 0.06 m and 0.0035 kg, respectively. As the percentage of the absorbed energy from the impact is approximately constant increasing the rotating speed beyond its maximum value causes the loss in the system to increase due to the formation of the plastic deformation within the piezoelectric material. This phenomenon is explained in Section 4.5.3.2. Figure 5.14 and Figure 5.15 show that when the rotational speeds exceed their maximum value for a given length of the tube, the experimental results are lower than the one predicted numerically. This is due to the fact that the model does not take into the account the plastic deformation and the extra losses caused by it.

For the second experiment two ball bearings with a mass of 0.035 and 0.083 kg are used to measure the effect of increasing the mass on the average output power. Figure 5.16 shows the effect of increasing the rotating speeds on the average output

power using the two ball bearings. This figure compares the numerical results with the one obtained experimentally, where a good agreement between the two results are obtained.

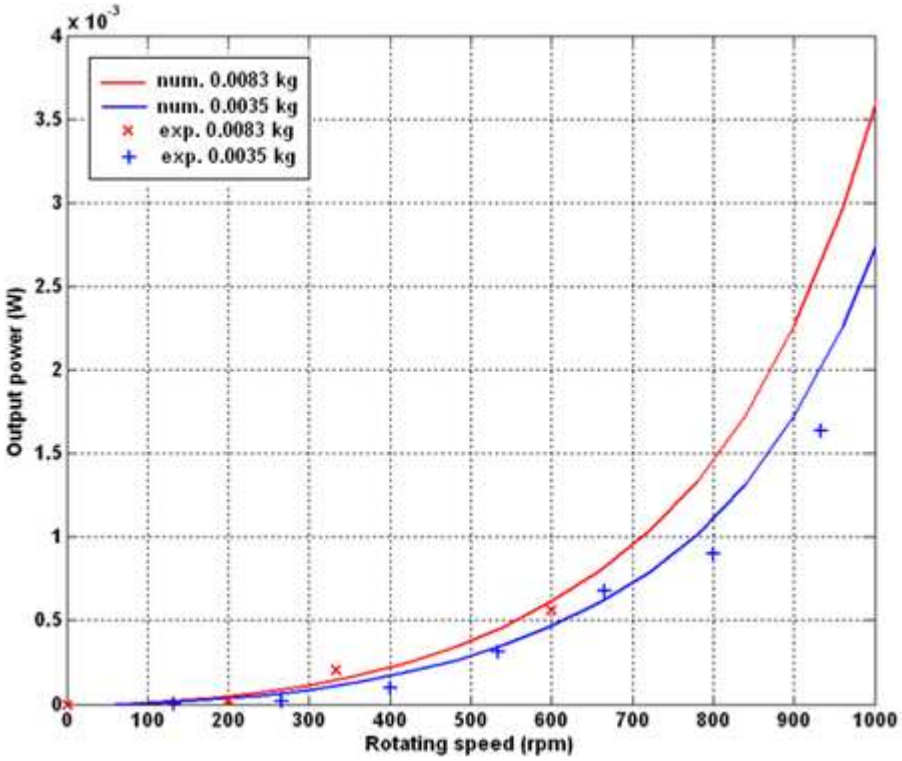

Figure 5.16 Speed versus maximum average output power using 0.0035 and 0.0083 kg ball bearing with a mass available displacement of 0.01 m.

The experimental results show that the value of the optimum load resistance for the simply supported Thunder™ pre-stressed beam drops from 60 kΩ to 6 kΩ when the ball bearing is adding to the tube. Moreover, the value of the optimum load resistance shows a slight dependence on the rotating speed over the range of measurement. Increasing the rotating speed from 200 rpm to 800 rpm results in reducing the load resistance from 6 kΩ to 1 kΩ, respectively. Therefore, the greater the rotating speeds, the lower the optimum load resistance will be. This indicates that the increase in the applied force on the Thunder™ pre-stressed beam due to the mass impact changes the equivalent constant of the piezoelectric beam and thus the resonant frequency of the harvester. This agrees with the results presented in Section 3.4.4 as increasing the applied force causes the stiffness of the piezoelectric element to increase and the damping to reduce. This reduction in the stiffness causes the resonant frequency of the Thunder™ beam to increase, thus reducing the value of the load resistance.

Some simulations and experimental results carried out by Umeda [56] show that the impact force from the ball bearing results in a reduction in the resonant frequency

of the curved beam and thus increases the output optimum load resistance. However, these results are in contrast to the experimental results that are obtained in this project as introducing the ball bearing results in lower load resistance. The reason behind this contradiction is that the Umeda uses an unstressed beam, whose stiffness is constant. Therefore the effect of the ball bearing impact causes the effective mass of the impacted piezoelectric element to increase. This results in a lower resonant frequency of the piezoelectric element and thus an increase in the load resistance. However, Thunder™ beam is a pre-stressed device of which stiffness changes depends on the value of the impact force. Both the stiffness and the damping are measured experimentally using the curve fitting method explained in Section 3.4.4. These values are used in the numerical model in order to predict the amount of power generated and the value of the optimum resistance.

If the rotating forces are the only forces acting on the piezoelectric transducer (no ball bearing is added to the tube) the optimum load resistance shows no dependency on the rotating speed. In this case the value of the load resistance depends on the method of mounting the Thunder™ beam. For simply supported and rigidly supported methods, the optimum load resistance is found to be 60 kΩ and 200 kΩ, respectively. Introducing the ball bearing to the system causes the optimum load resistance to drop by an order of a magnitude in both cases. Any further increase in the impact force causes the extra reduction in the value of the optimum load resistance due to the reasons explained previously in this section.

5.7 Conclusions

The developed model that was used to predict the amount of power generated from rotational forces using an impact based piezoelectric harvester was verified in this chapter. In order to test the performance of the piezoelectric harvester, a testing wheel which was driven by a motor was designed. The harvester was attached to the edge of the wheel through a host. A Thunder™ pre-stressed beam was used in this experiment to generate power from a rotating wheel using GF and CF methods.

In the GF method the harvester was mounted at the edge of a rotating wheel and left to rotate with the wheel. This method was considered because the way that the harvester was mounted was simple and it did not need any complicated mechanical support to hold the harvester in place.

When the ball bearing was not introduced into the tube, any increase in the rotating speed resulted in an increase in the output voltage and thus the output power. The maximum average output power at a speed of 800 rpm was 1.8×10^{-9} W. In this case the harvester optimum load resistance was found to be 200 kΩ. By introducing the ball bearing into the tube, the average output power improved by increasing the rotating speed to reach a value of 4×10^{-7} W at 133 rpm. Any further increase in the rotating speed, resulted in a reduction in the output power. This was due to the effect of the centripetal acceleration component that worked against the gravitational force. The average output power kept reducing until it reached its minimum value of 5×10^{-9} W at 210 rpm. At this point the ball bearing stuck at one end of the frame. Any further increase in the rotating speed resulted in a slight increase in the output power. The optimum load resistance was approximately 20 kΩ when the rotating speed was less than 100 rpm. This value dropped to 10 kΩ at a rotating speed above 100 rpm. By increasing the rotating speed beyond 133 rpm, the optimum load resistance started to increase and it reached the value of 200 kΩ at 210 rpm.

The effect of increasing the rotating speed on the output power of a piezoelectric transducer, which was kept in a horizontal position (CF), was analyzed in this chapter. It was found that increasing the rotating speed resulted in an increase in the output power. The generated average power from each pre-stressed beam was 2.5×10^{-6} W at 800 rpm. These results were obtained using the optimum resistance, which was 60 kΩ. In this case, the piezoelectric transducer was converting the available energy from the centripetal force into useful electrical power.

Adding a ball bearing to the system meant that the force acting on the piezoelectric harvester was the sum of the centripetal force and the impact force generated by the ball bearing. A pulse was generated every time the ball bearing hit the transducer. The frequency, amplitude and the width of the generated pulse depended on the rotating speed. For each Thunder™ pre-stressed beam, the average output power at 800 rpm was 2×10^{-3} W. However, the optimum load resistance dropped by an order of magnitude when the ball bearing was introduced to the system to a value of 6 kΩ at 200 rpm. Any further increase in the rotating speed reduced the optimum load resistance to 1 kΩ at 800 rpm. From the experimental results, increasing the rotating speed resulted in an increase in the average output power. Both experimental and theoretical results agreed that the relationship between rotating speed and the average output power was cubic. Finally, the average output power was directly proportional to

the mass of the ball bearing. In summary the theoretical analysis and the simulation results showed that using CF method to mount the piezoelectric harvester at the edge of a rotating wheel generated more output power that using GF method with or without using a mass.

Chapter 6

Simulation of the non-contact based piezoelectric harvester

6.1 Introduction

This chapter presents a method to extract electrical power from curved composite beam that contains a piezoelectric material (Thunder™, model TH 10-R) using magnetic forces. The principle of this method is presented in Section 6.2. Numerical and analytical methods of calculating the magnetic force between two magnets is presented in Section 6.3. The magnetic forces developed between two magnets under a wide range of sinusoidal input forces with different values of amplitude and frequency are analysed numerically. The effect of the separation distance between the magnets on their magnetic force and behaviour is analysed numerically. Theoretical analysis of the developed piezoelectric harvester is presented and verified with the simulated results. The effect of the load matching and efficiency are explored. Moreover, the effect of the physical dimensions of the magnets, tube length and the value of the input force on the generated output power is illustrated. Finally, an overview of the design is presented in section 6.8.

6.2 Structure of the harvester and operating principle

The principle of using magnetic forces to generate power from piezoelectric material is discussed in detail in this section.

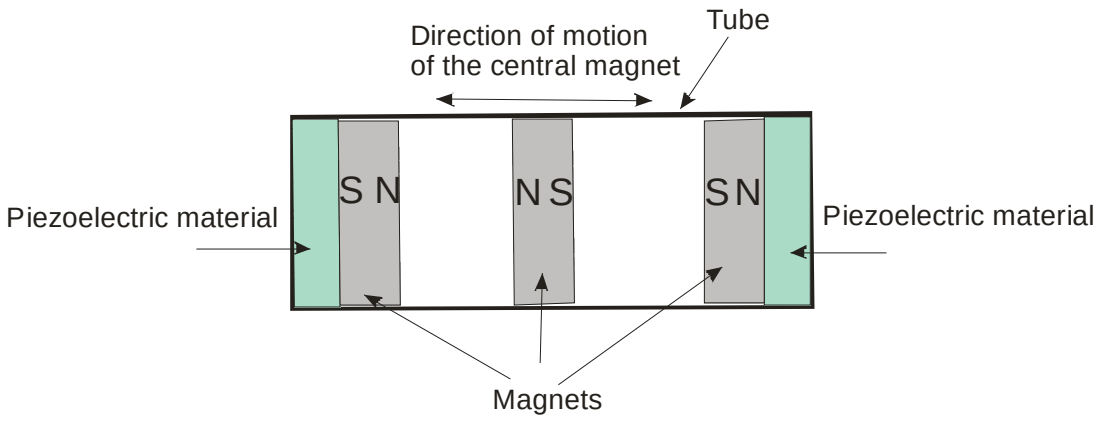

Figure 6.1 A schematic diagram of the magnetic levitation system

A schematic diagram of the system is shown in Figure 6.1. The device uses two outer magnets that are mechanically attached to a piezoelectric element using an adhesive material. A central magnet is placed axially in line between the two outer magnets. The magnetic poles are oriented to repel the central magnet and thus suspending the central magnet with restoring force. Due to applied acceleration forces, the central magnet moves within the given space between the outer magnets. The displacement depends on the applied force as well as the restoring force as explained in Section 6.6. As the distance between each of the outer magnets and the central one changes, the axial load on the piezoelectric material changes. Thus an output power will be generated. For further analysis, Thunder™, model TH 10-R, is used as a source of converting mechanical energy into electrical one. All the calculated and measured parameters that are presented in Chapter 3 will be used to investigate the behaviour of the harvester under a sinusoidal input force.

6.3 Calculation of magnetic force

Assuming two cuboidal magnets each of which has a central point o and o' as shown in Figure 6.2. The magnet with central point o has magnetization of J and dimensions of 2*a*, 2*b*, and 2*c*. The magnet with central point o' has magnetization of J' and dimensions of 2*A*, 2*B*, and 2*C*. The poles of both magnets are in the z-axis direction. These magnets are separated (centre to centre) by α, β and γ in the x, y and z direction, respectively.

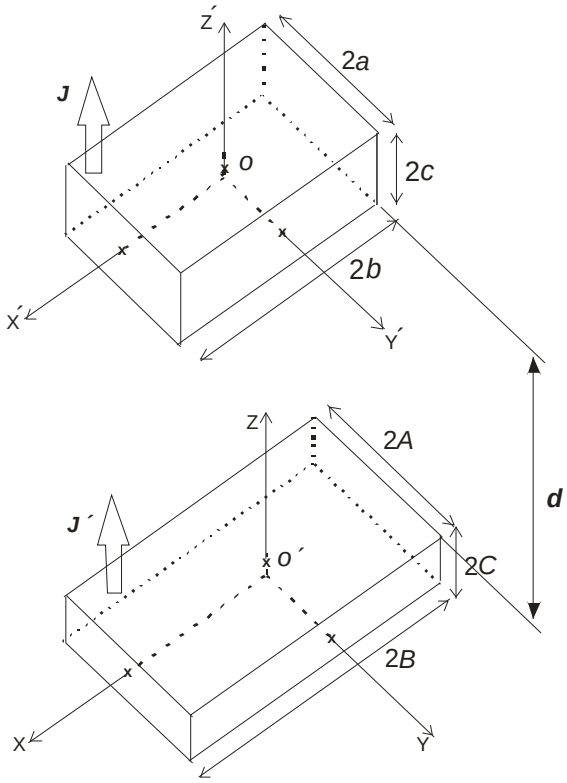

Figure 6.2 Magnet configuration

The magnetic force between two cuboidal magnets can be calculated analytically using the following equation [80].

$$F = \frac{J \cdot J'}{4\pi\mu_0} \sum_{i=0}^{1}\sum_{j=0}^{1}\sum_{k=0}^{1}\sum_{l=0}^{1}\sum_{p=0}^{1}\sum_{q=0}^{1}(-1)^{i+j+k+l+p+q}\phi(u_{ij}, v_{kl}, w_{pq}, r) \tag{6.1}$$

For F_x

$$\phi_x = 0.5(v_{ij}^2 - w_{pq}^2)\cdot\ln(r-u_{ij}) + u_{ij}v_{kl}\cdot\ln(r-v_{kl}) + v_{kl}w_{pq}\cdot\tan^{-1}\frac{u_{ij}v_{kl}}{rw_{pq}} + 0.5ru_{ij} \tag{6.2}$$

For F_y

$$\phi_y = 0.5(u_{ij}^2 - w_{pq}^2)\cdot\ln(r-v_{kl}) + u_{ij}v_{kl}\cdot\ln(r-u_{ij}) + u_{ij}w_{pq}\cdot\tan^{-1}\frac{u_{ij}v_{kl}}{rw_{pq}} + 0.5rv_{kl} \tag{6.3}$$

For F_z

$$\phi_z = -u_{ij}\cdot w_{pq}\cdot\ln(r-u_{ij}) - v_{kl}w_{pq}\cdot\ln(r-v_{kl}) + u_{ij}v_{kl}\cdot\tan^{-1}\frac{u_{ij}v_{kl}}{rw_{pq}} - r\cdot w_{pq} \tag{6.4}$$

Where

$$u_{ij} = \alpha + (-1)^j A - (-1)^i a$$
$$v_{kl} = \beta + (-1)^l B - (-1)^k b$$
$$w_{pq} = \gamma + (-1)^q C - (-1)^p c$$
$$r = \sqrt{u_{ij}^2 + v_{kl}^2 + w_{pq}^2}$$

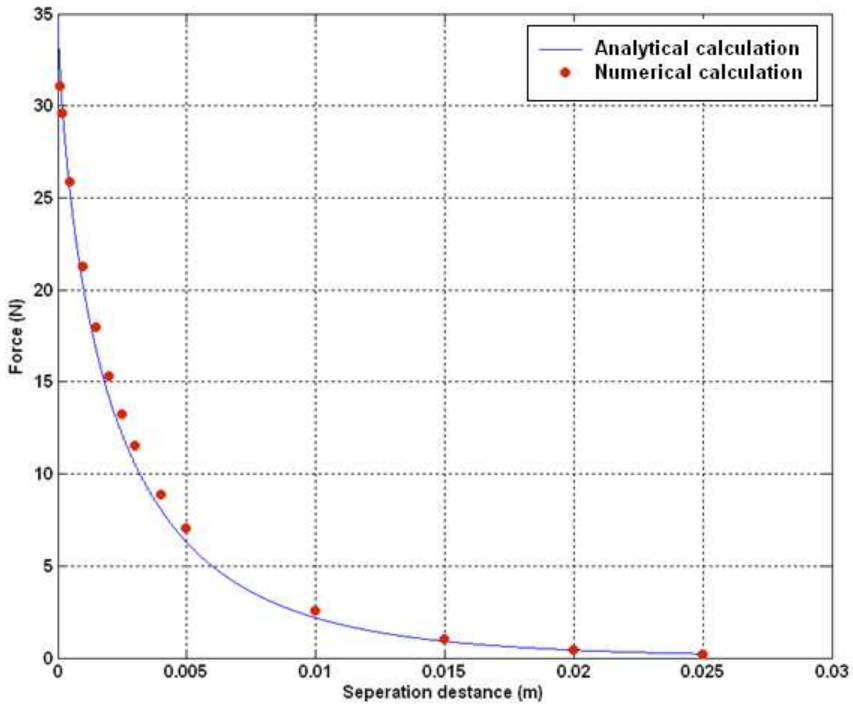

Figure 6.3 Calculation of the axial magnetic force as a function of a separation distance between the two magnets

If the two magnets share the same central line where the area of the first magnet $2a \times 2b$ overlaps perfectly with the face of the other magnet $2A \times 2B$, the value of the two forces F_x and F_y will be negligible. Therefore, the only force that acts between the magnets is F_z. In this case, α and β equals zero and $\gamma = d + (C + c)$, where d is the air gap between the two magnets in the z direction. The two magnets that are used in the preliminary test are made of Neodymium Iron Boron (NdFeB). Each magnet has the dimensions of $2a = 2A = 2b = 2B = 13$ mm and $2c = 2C = 4$ mm. The magnetization of the used magnet is 1.22 T. The relationship between the magnetic force and the separation distance in the z direction only, where α and β equals zero, is shown in Figure 6.3. In this figure the force generated between the two magnets is calculated numerically using 3-D Maxwell software [81] and compared to the analytical one using equations 6.1. Maxwell is electromagnetic field simulation software that can be used to model electromagnetic fields. The software is based on the finite element method (FEM) that allows the calculation of static, harmonic electromagnetic and electrical

fields. For this application, Maxwell is used to calculate the magnetic forces developed between two magnets. As can be seen, there is an agreement between the analytical results and the finite-element solution. Therefore, for further analysis only analytical model based on solving equation 6.1 is used.

6.4 Analytical analysis of the geometry effects on the forces between magnets

The benefit of using a magnetic force in the application presented in Section 6.2 is that forces are applied on the piezoelectric element without the need for physical contact. In order to design a harvester that uses magnets, the effect of magnet geometry and shape on the magnetic forces must be analyzed. Both the size and the aspect ratio, the ratio of the axial dimension to the lateral dimension ($2c/2a$), are important parameters that must be taken into account during the process of designing the harvester. This helps to optimize the size of the magnets and thus the size of the piezoelectric harvester. Equation 6.1 is used over a range of magnet sizes and geometries to explore scaling laws and other geometrical effects. For this investigation, two identical cuboidal magnets are used with a magnetization of 1.22 T. These magnets are placed axially in line with each other. Section 6.4.3 illustrates the effect of the magnetic shape on the generated magnetic forces. In this section two magnets are used, i.e. cuboidal and an equivalent sized cylindrical magnets.

6.4.1 Effect of volume on the magnetic forces

Figure 6.4 shows the effect of reducing the magnet volume on the contact force. This force is defined as the attraction or repulsive force with zero axial and lateral gaps between the two magnets. Figure 6.4 shows the relationship between the magnetic forces generated between two magnets and their volumes. These data are obtained analytically. In order to investigate this effect, the volume of the magnet varied from 0.0625×10^{-6} m^3 to 4×10^{-6} m^3 at a base of 0.3×10^{-6} m^3 and the aspect ratio is held constant at 0.5. This range of volume is used because the size of the used Thunder™ beam requires a magnet with a volume located within this range. Using equation 6.1, the magnetic contact force is found to be directly proportional to $V^{2/3}$, where V is the volume of the magnet.

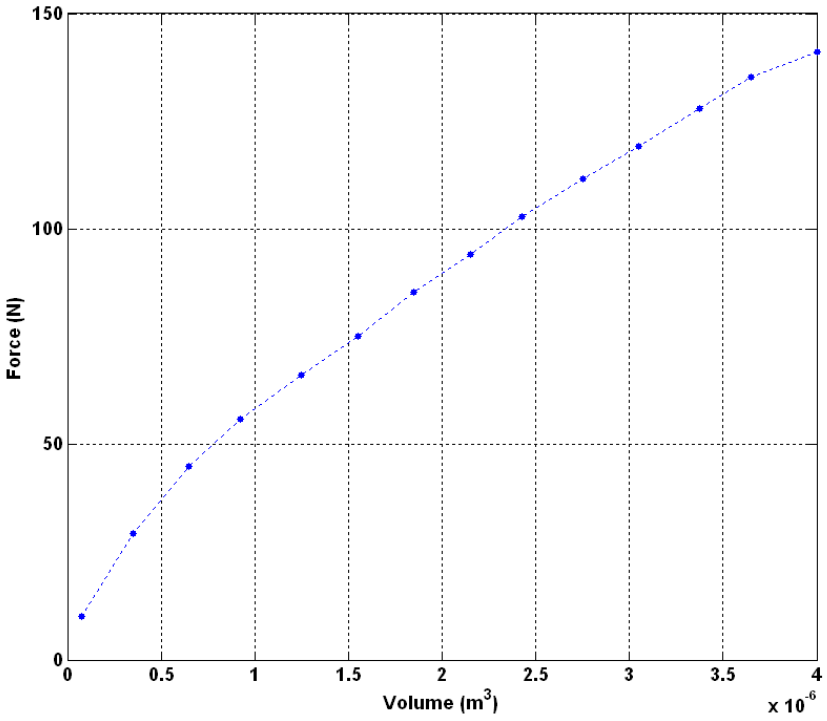

Figure 6.4 Effect of magnet volume on the contact force

6.4.2 Effect of aspect ratio on the magnetic forces

In order to investigate the effect of aspect ratio on the contact force, the magnets volume is held constant while the forces generated at different values of aspect ratio are calculated using equation 6.1. Figure 6.5 shows the effect of aspect ratio on the magnetic contact force for three volumes 0.0625×10^{-6} m^3, 0.5×10^{-6} m^3 and 4×10^{-6} m^3. These volumes are used because the magnet dimensions are suitable to be used with the Thunder™ beam. For a given volume, the maximum magnetic force can be achieved when the aspect ratio is approximately 0.4. Outside this range the values of the forces drop. Therefore, in order to maximize the magnetic force, the magnet must be designed to have an aspect ratio between 0.3 and 0.6. This is due to the effect of the magnetic field generated by the magnets [82]. Therefore, increasing the aspect ratio changes the shape of the magnet from plate into a rod causing a faster decay in the value of the magnetic force.

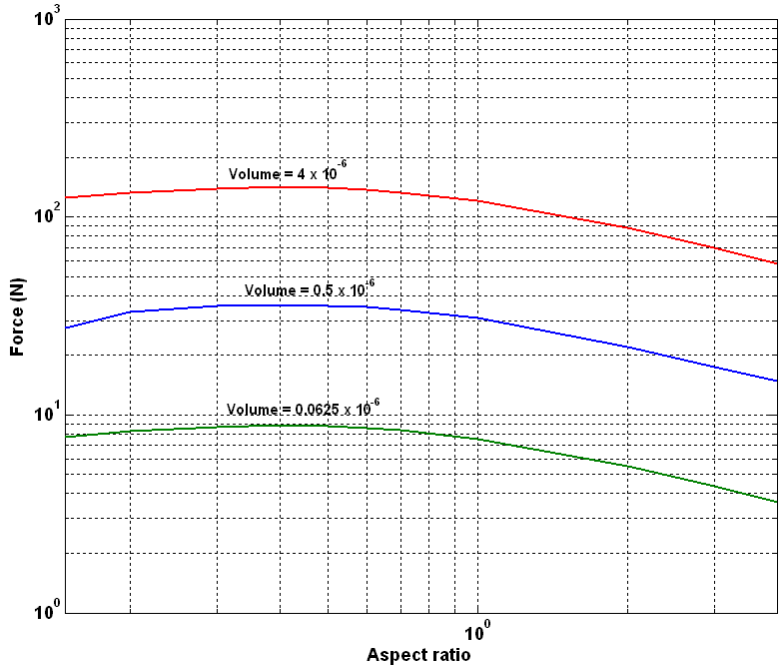

Figure 6.5 Effect of AR on the contact force between two magnets

Figure 6.6 shows the changes in the magnetic force as a result of increasing the separation distance between the two magnets at different aspect ratio. For this investigation the volume of the magnets is held constant at 0.5×10^{-6} m^3. Figure 6.6 shows a comparison between the analytical and the FEM calculation. These results are in a good agreement.

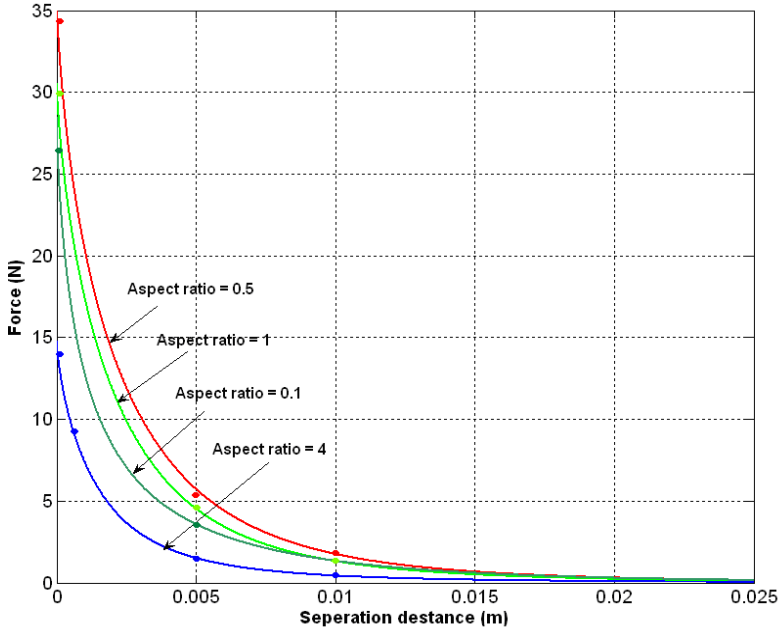

Figure 6.6 Axial forces versus the separation distance at different values of AR

Figure 6.7 shows the variation of the normalized axial force (F) by the contact force (F_o) with the increase in the normalized axial gap (d) by the magnet thickness

(2*c*). Four curves are shown for magnets with the same volume (0.5×10^{-6} m^3) at different aspect ratio 0.1, 0.5, 1 and 4. It is clear from Figure 6.7 that the axial force decreases rapidly when the aspect ratio is greater than unity compared to the magnets that have aspect ratio less than unity. Therefore, for the design that is proposed in Section 6.2, where the magnet has a large displacement, it will be preferable to use a magnet with low aspect ratio.

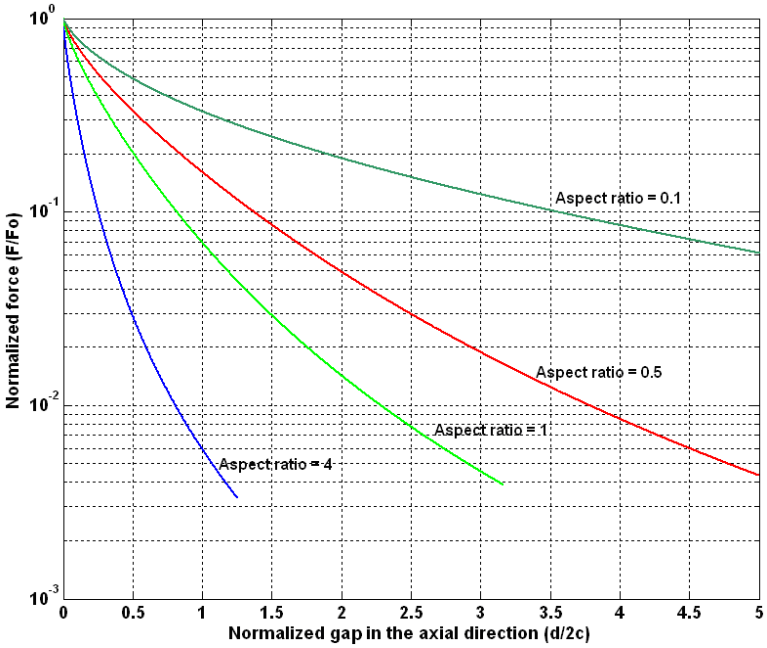

Figure 6.7 Normalized axial force (F/F_o) versus normalized axial displacement ($d/2c$)

If the magnet has a very high aspect ratio ($2c/2a$ >>1), the magnetic force is directly proportional to the $2a \times 2a$ as shown in Figure 6.8.

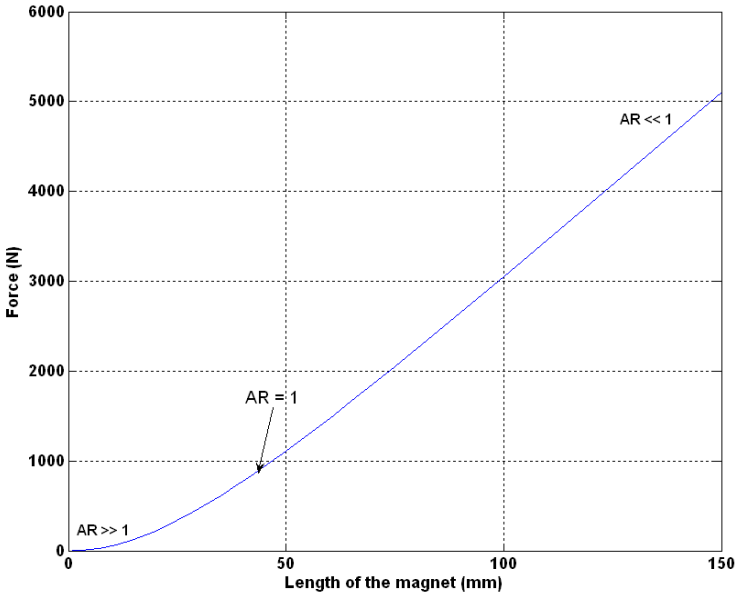

Figure 6.8 Effect of increasing the length of the magnet on the output force

Increasing the axial dimension (2*c*) has negligible effect on the generated magnetic force as presented in Figure 6.9.

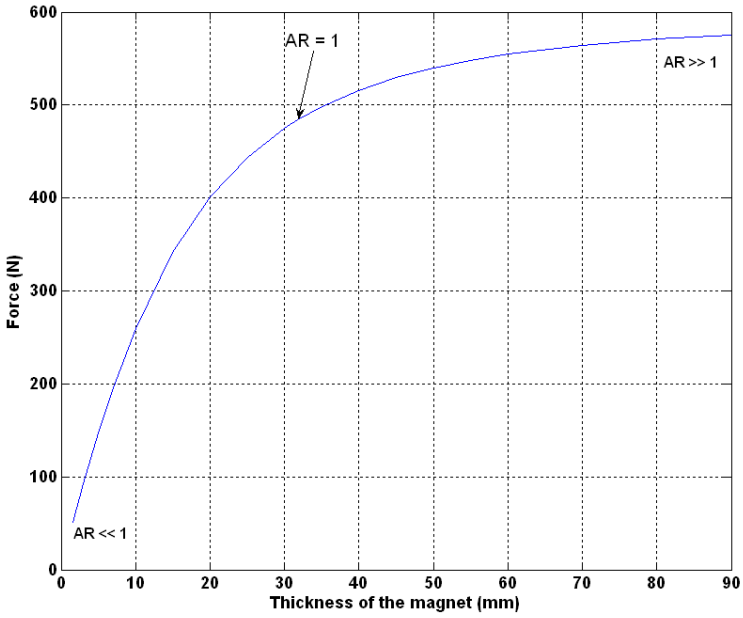

Figure 6.9 Effect of increasing the thickness of the magnet on the output force

If the magnet has low aspect ratio ($2c/2a$ <<1), the magnetic force is directly proportional to the $2a \times 2c$ as shown in Figure 6.8 and Figure 6.9. The magnetic force at contact increases by increasing the size of the smallest area of the magnet. In order to investigate the effect of increasing the length (2*a*) of the magnet, the initial dimensions of the magnet are 1 mm × 1 mm × 40 mm. The length and the width of the magnet increase from 1 mm to 150 mm with a step of 2mm. Therefore, the aspect ratio reduces from 40 to 0.266. The dimension of the magnet is chosen by which the initial aspect ratio (AR) >> 1 and the total volume of the magnet is 1600 mm^3.

In order to investigate the effect of increasing the thickness (2*c*) of the magnet, a magnet with a volume equals to 1600 mm^3 is used in the simulation. Therefore, the initial dimensions of the magnet are 31.7, 31.7, 1.58 mm. The thickness of the magnet increases from 1.58 mm to 90 mm with a step of 2mm. Therefore, the aspect ratio increases from 0.05 to 2.83. The dimensions of the magnet are chosen by which the initial aspect ratio (AR) << 1.

6.4.3 Effect of the magnet shape

In order to investigate the effect of the magnet shape on the magnetic forces, a comparison between cuboidal and an equivalent sized cylindrical magnets is carried

out. Assuming that both cylindrical magnets are sharing the same central line and the separation distance changes only in the axial direction, the magnetic force between them can be calculated analytically using the following equation [83].

$$F_z = 2\pi K_d R^2 \sum_{i,j=-1}^{1} i \cdot j \cdot A_{11}^0(\varsigma + i\tau_1 + j\tau_2, 1, 1) \qquad 6.5$$

R is the radius of the cylindrical magnet and $\tau_{1,2}$ is the aspect ratio of the two magnets, which equals the thickness of the magnet divided by its diameter. The magnetic energy constant (K_d) is given by the following equation, where μ_o is the permittivity of the vacuum and M is the magnetization:

$$K_d = 0.5\mu_o M^2 \qquad 6.6$$

These magnets are separated (centre to centre) by ς in the z direction and the function $A_{11}^0(\varsigma + i\tau_1 + j\tau_2, 1, 1)$ is given by the following equation [83]:

$$A_{11}^0(\varsigma + i\tau_1 + j\tau_2, 1, 1) = \frac{\varsigma + i\tau_1 + j\tau_2}{\pi K_1} E\left(K_1^2\right) - \frac{\left(2 + 0.5(\varsigma + i\tau_1 + j\tau_2)^2\right) K_1(\varsigma + i\tau_1 + j\tau_2)}{2\pi} K(K_1^2) + \frac{1}{2} \qquad 6.7$$

where (K_1^2) is given by the following equation:

$$K_1^2 = \frac{4}{4 + (\varsigma + i\tau_1 + j\tau_2)^2} \qquad 6.8$$

K and E are the complete elliptic integrals of the first and the second kind, respectively and they are given as follows:

$$K\left(K_1^2\right) = \frac{\pi}{2} \sum_{n=0}^{\infty} \left[\frac{(2n-1)!!}{(2n)!!} \right]^2 \left(K_1^2\right)^{2n} \qquad 6.9$$

$$E\left(K_1^2\right) = \frac{\pi}{2} \sum_{n=0}^{\infty} \left[\frac{(2n-1)!!}{(2n)!!} \right]^2 \frac{\left(K_1^2\right)^{2n}}{1-2n} \qquad 6.10$$

Figure 6.10 demonstrates that the contact force generated by a cuboidal magnet is around 20 % more than an equivalent sized cylindrical magnet.

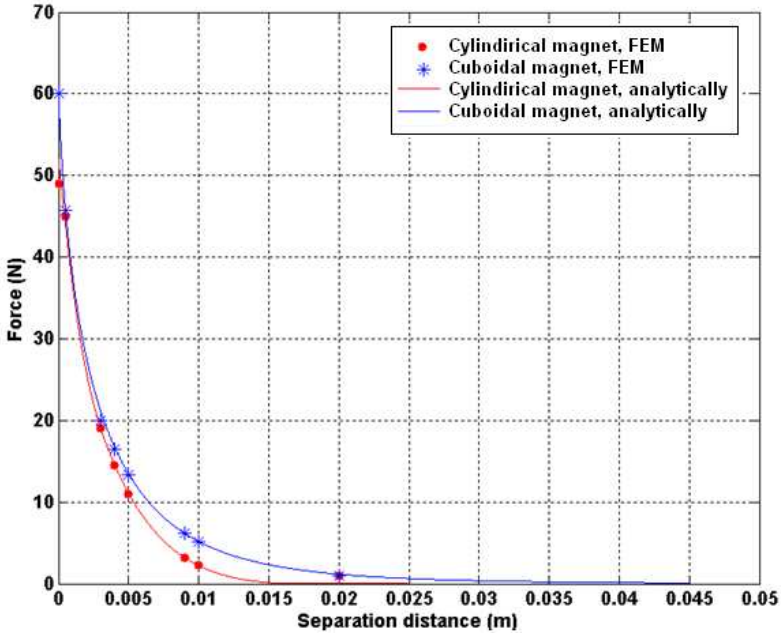

Figure 6.10 Axial force versus separation distance for cuboidal and cylindrical magnets

6.5 Length of the tube and the magnet size

In this section an analytical calculation is used to optimize the dimensions of the magnet and the tube and thus the size of the harvester. Assuming F_{max} is the maximum force that the middle magnet is facing under rotation. This value is calculated at the maximum rotating speed which corresponds to a linear speed of 100 mph. Therefore, the contact force between the middle magnet and the two outer magnets must equal F_{max}. In this case, the middle magnet travels in the axial direction between the outer magnets and no contact occurs between them if the rotating speed is less than 100 mph. Under higher rotating speed, the applied force on the middle magnet will exceed the contact force and thus an impact force occurs between the middle and the outer magnets. The applied force, which the harvester is designed for, should not exceed its maximum value because the impact force causes damage to the harvester.

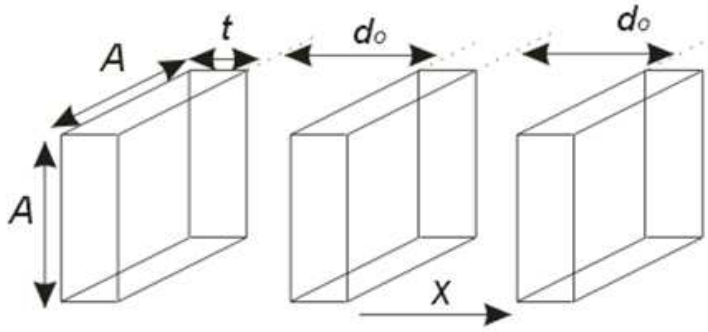

Figure 6.11 Distances and dimensions between the magnets in the levitation system

By knowing the contact force, the dimensions of the magnet can be determined using the equation presented in Section 6.3. Figure 6.11 shows the dimensions of the three identical magnets and the air gaps between them. The total volume of this configuration equals the volumes of the magnets added to the volume of the two air gaps. As was explained in Section 6.4.2, the maximum magnetic force can be achieved when the aspect ratio of the magnet is 0.5. Therefore, the thickness of the magnet (t) equals half of the length of the magnet (A/2).

$$V = 3A^2t + 2A^2d_o = \frac{3}{2}A^3 + 2A^2d_o \qquad 6.11$$

Where d_o is the axial distance between the middle and each of the outer magnet. By assuming d_o equals $\alpha \cdot t$, the total volume of the configuration can be given by the following equation:

$$V = \frac{3}{2}A^3 + \alpha A^3 \qquad 6.12$$

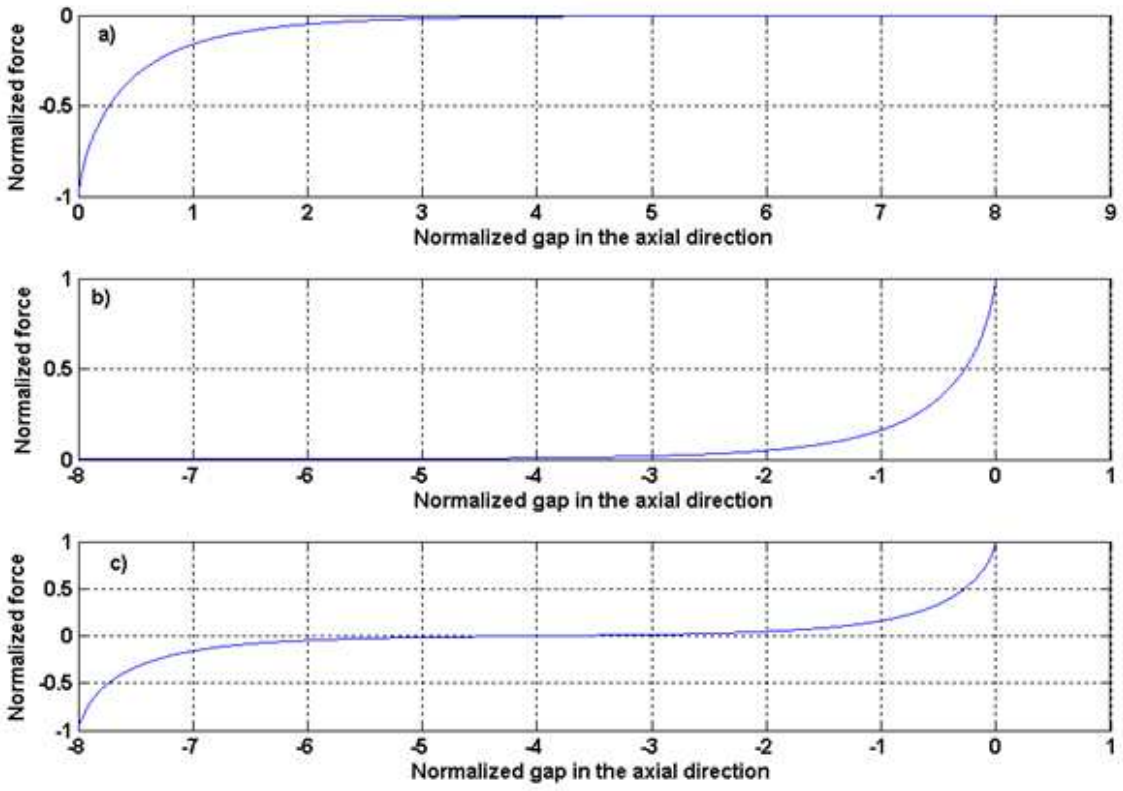

Figure 6.12 Normalized forces that the outer magnets are facing as a function of the normalized axial gap graph (a) and (b). Normalized forces that the middle magnet is facing as a function of the normalized axial gap (c)

Figure 6.12 shows the variation of the normalized axial force (F/F_o) with the normalized axial gap (d_o/t). Figure 6.12 (a) and Figure 6.12 (b) show the relationship

between the normalized forces with the normalized gaps for the outer magnets, while Figure 6.12 (c) shows this relationship for the middle magnet. These figures are generated using MATLAB and the equations presented in Section 6.3. It has been assumed that if the applied force on the magnet is in the same direction as the motion that is shown in Figure 6.11, the force will be positive and vice versa.

In Figure 6.12, the maximum force that the outer magnets faces is when the magnet is in contact with the middle magnet. This value reduces gradually by increasing the axial gap between the outer magnet and the middle one. The maximum gap between the outer magnet and the middle one is $2d_o$. The analytical calculation shows that the magnetic force between the middle and the outer magnet is approximately 0.09 % of the contact force when the the total axial gap between them is $8t$. Therefore, it is assumed that at this distace the contact force between the middle and the outer magnet is negligible. In order to optimize the dimensions of the configuration presented in Figure 6.11, the effect of reducing the axial gap will be investigated. Figure 6.13 (a) shows the effect of reducing the total axial gap on the outer magnet.

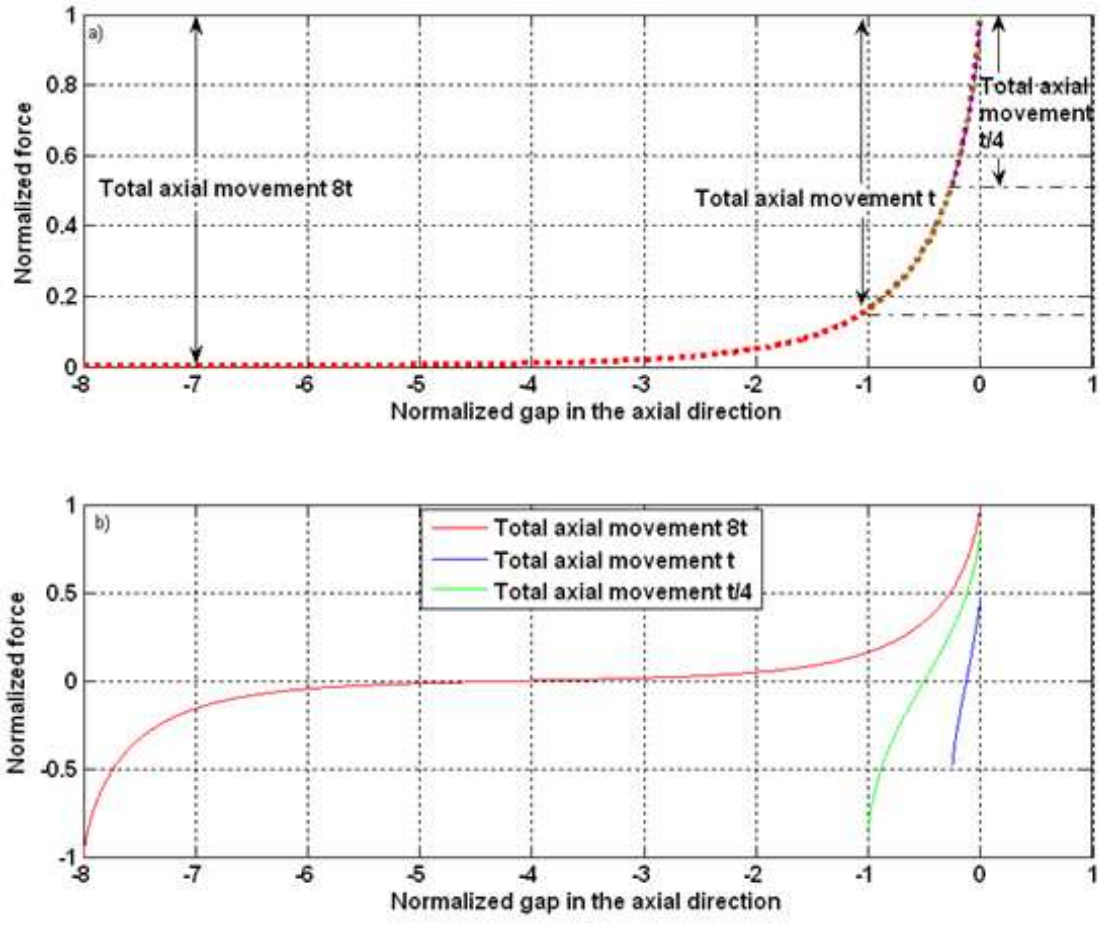

Figure 6.13 Normalized force as a function of the Normalized axial gap at different values of $2d_o$ on the outer magnets, graph a) and on the middle magnet, graph b)

When the axial distance between the outer and the middle magnet is zero, the axial force between the two magnets reaches its maximum value which is reffered to as the contact force (F_o). If the total avaliable axial gap equals to more than 8*t*, the forces between the magnets are small enough. Therefore, these forces can be considered to be negligible. Thus, when the middle magnet travels all of the avaliable distance, the maximum force applied on the outer magnet is 100 %. However, if the total distance is reduced to *t* and 0.25*t*, the maximum force between the two magnets at that distance will be 83.86 % and 48 % of the contact force, respectively. Therefore, reducing the axial gap results in reducing the total force applied on the outer magnets. In case of having an total axial gap of *t* and 0.25*t*, the total loss in the magnetic force is 16.14 % and 48 %, respectively.

Figure 6.13 (b) shows the effect of reducing the total axial gap on the middle magnet. The total magnetic force that the middle magnet is facing, when it is located half way batween the outer magnets, is zero. Moving away from the centre, the applied force on the magnet starts to increase until it reaches its maximum value when the magnet is in contact with the outer one. The relationship between the total axial distance and the force required to bring the outer and the middle magnet in contact with each other is explained in Section 6.6. For a given magnet volume, reducing the axial gap results in increasing the required force that brings the middle magnet in contact with the outer one.

6.6 Numerical analysis of the magnet behaviour

As shown in Figure 6.1, the device consists of a magnetic levitation system. To describe the behaviour of the middle magnet under external forces, two reference frames are taking into the account. The first one is used to describe the motion of the frame and thus the two outer magnets as they are attached to the frame. This equation is described as $z = R\cos(\omega t)$, where R is the motion amplitude and ω is the angular frequency. The second reference frame describes the motion of the middle magnet (x). The relative displacement between the outer and the middle magnet is y. The magnetic levitation system will be mounted at the edge of a rotating wheel and mounted using the CF method. The reason for this is explained in Section 4.3.3. Therefore, the centripetal force in the x direction is the driving force that causes the middle magnet to

move. The governing differential equation that will be used to describe the behaviour of the system is given by the following equation:

$$\ddot{y} + \left(\frac{c}{m}\right)\dot{y} + \frac{1}{m}F_{total} = \omega^2(R + y)\cos(\omega \cdot t) \qquad 6.13$$

Where, m, c and F_{total} are the mass of the middle magnet, damping coefficient, total force generated by the two outer magnets. R is the distance between the wheel centre and the middle point of the tube and ω is the rotating angular frequency of the wheel. The total force from the outer magnets acting on the middle one can be calculated using equation 6.1. The time integration of the ordinary differential equation, equation 6.13, is performed using a fourth-order Runge-Kutta method. The resonant frequency of the magnetic levitation system can be calculated using the undamped and unforced oscillation as presented in the following equation, where the dot is the derivative with respect to time:

$$\ddot{y} + \frac{1}{m}F_{total} = 0 \qquad 6.14$$

This equation is solved numerically using fourth-order Runge-Kutta method. At equilibrium, the middle magnet is located at the middle of the tube at $x = 0$. Initial displacement is applied, where $x = 0.5 \cdot d_o$ .The axial gap (d_o) between the magnets is changed and the relation between the normalized gap (d_o/t) and the resonant frequency is plotted in Figure 6.14. Changing the magnet axial gap alters the stiffness of the system and thus the resonant frequency. This behaviour is reported in the literature [84].

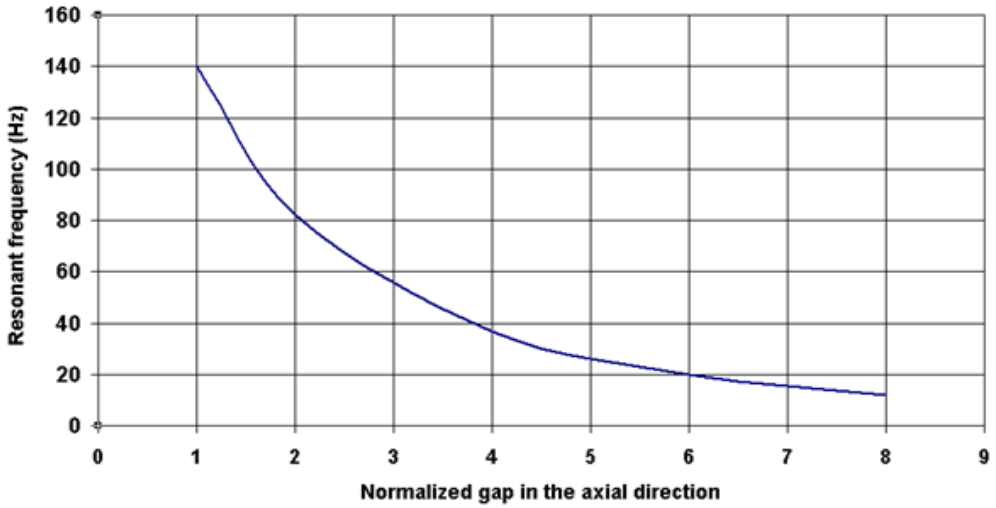

Figure 6.14 Change in the resonant frequency as function of the normalized gap (d_o/t)

As the initial axial gap reduces, the stiffness increases. This is due to the fact that the effect of both the magnetic field and the flux density increases as the distance between the magnets reduces. Figure 6.15 shows that any change in the initial displacement (x) causes the resonant frequency of the system to change. This is due to the nonlinear behaviour of the levitation system. This figure presents the relationship between the normalized initial distance in the axial direction (x/d_o) and the normalized resonant frequency ($f_{o(x)}/f_{o(do)}$) at different axial gap, where $0.1d_o < |x| \le d_o$.

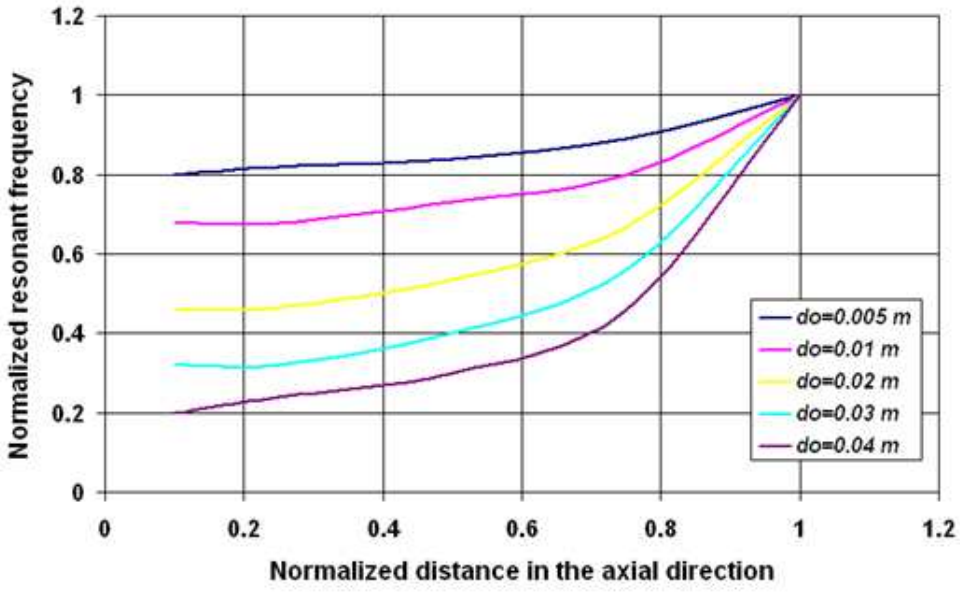

Figure 6.15 Normalized resonant frequency ($f_{o(x)}/f_{o(do)}$) as function of the normalized initial distance (x/d_o) at different values of the axial gap d_o, numerical results.

Both Figure 6.14 and Figure 6.15 reveal three important effects:

- Increasing the axial gap between the outer and the middle magnet causes the resonant frequency of the system to drop.
- For a fixed axial gap, increasing the initial displacement of the middle magnet causes the resonant frequency of the system to increase.
- When the normalized gap (d_o/t) is unity, the normalized frequency increases only by 20 % when x increases from $0.1d_o$ to d_o. However, when the normalized gap equals to 8, the normalized frequency increases by 80 % when x increases from 0.1 d_o to d_o. This means for wider range of excitation frequency a longer axial gap is more preferable.

The numerical solution for equation 6.14 is shown in Figure 6.16, where the three magnets have the same dimensions of 15, 15, 5 mm and the initial displacement is 0.02 m. Figure 6.16 (a) and Figure 6.16 (b) show the displacement and the applied force on the middle magnet, respectively.

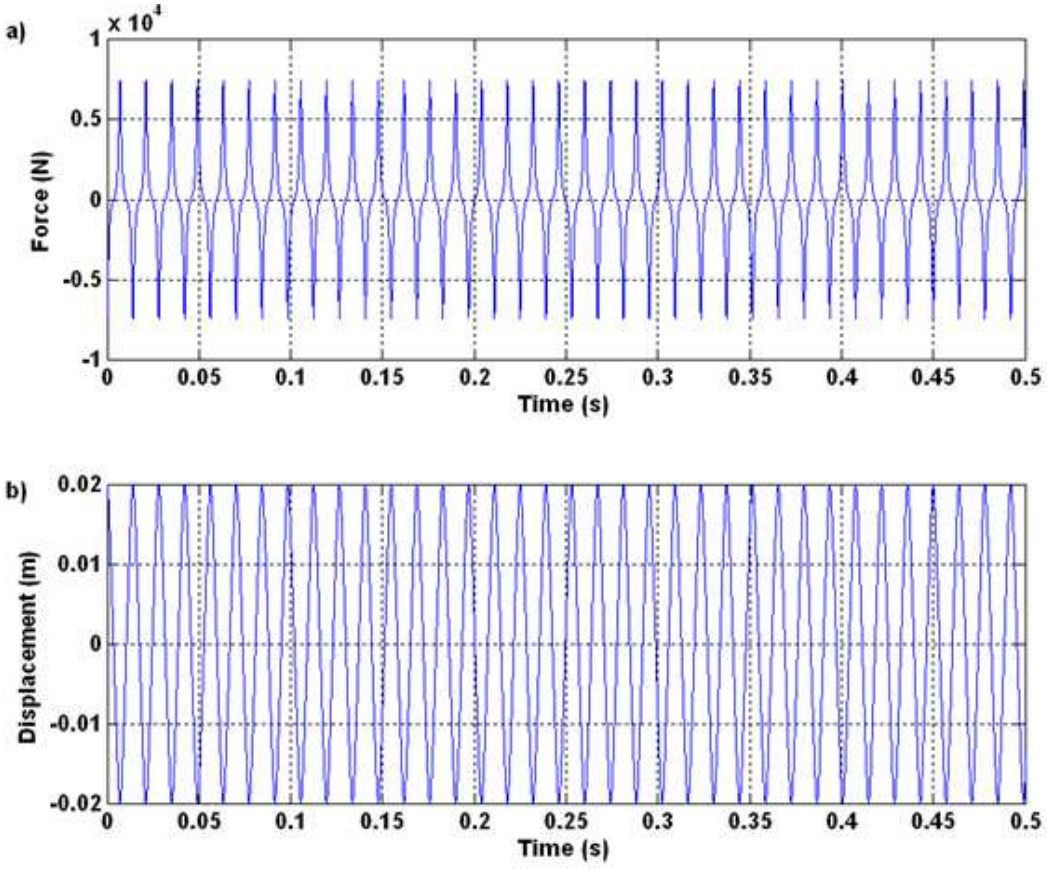

Figure 6.16 Numerical solution of equation 6.14

However, in real applications the system behaves differently due to the mechanical damping (*c*), which represents the energy loss due to friction. The damping force is proportional to the velocity of the middle magnet mass and the damping coefficient which is given by equation 3.46. The damping coefficient is directly proportional to the resonant frequency of the system. Therefore, its value changes with the applied excitation frequency. As the excitation frequency increases, the distance between the outer magnet and the middle one reduces causing the system resonant frequency and thus the damping coefficient to increase. This effect can be seen in Figure 6.17.

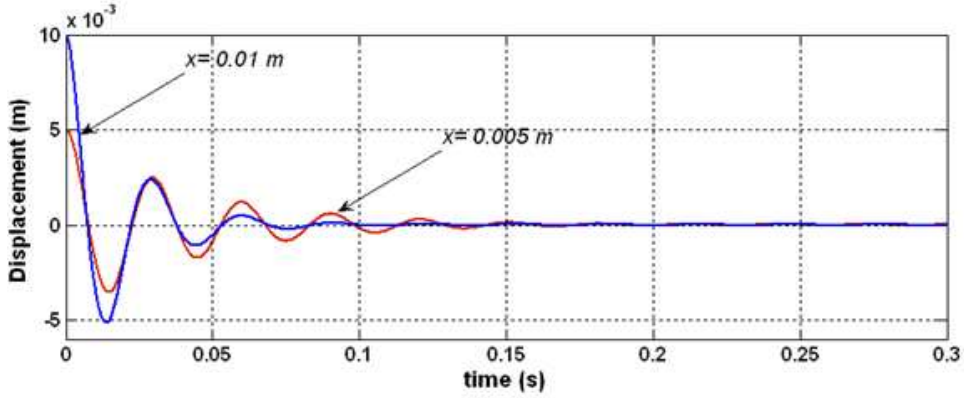

Figure 6.17 Numerical calculation of equation 6.13 when damping is introduced

By taking the non-linearity into account and its effect on the damping, the solution of equation 6.13 can be shown in Figure 6.18, where *R* equals 0.06 m.

Figure 6.18 (a) shows the non-linearity in the system where it presents the relationship between the displacement of the middle magnet and the force, where over 40 cycles are obtained. Figure 6.18 (b) and Figure 6.18 (c) present the changing of force over time and the displacement of the magnet over time, respectively. These figures present the numerical solution after the waveforms are converged. The maximum rotating speed that the system withstands before the middle magnet hits the outer magnets is 22.6 rps.

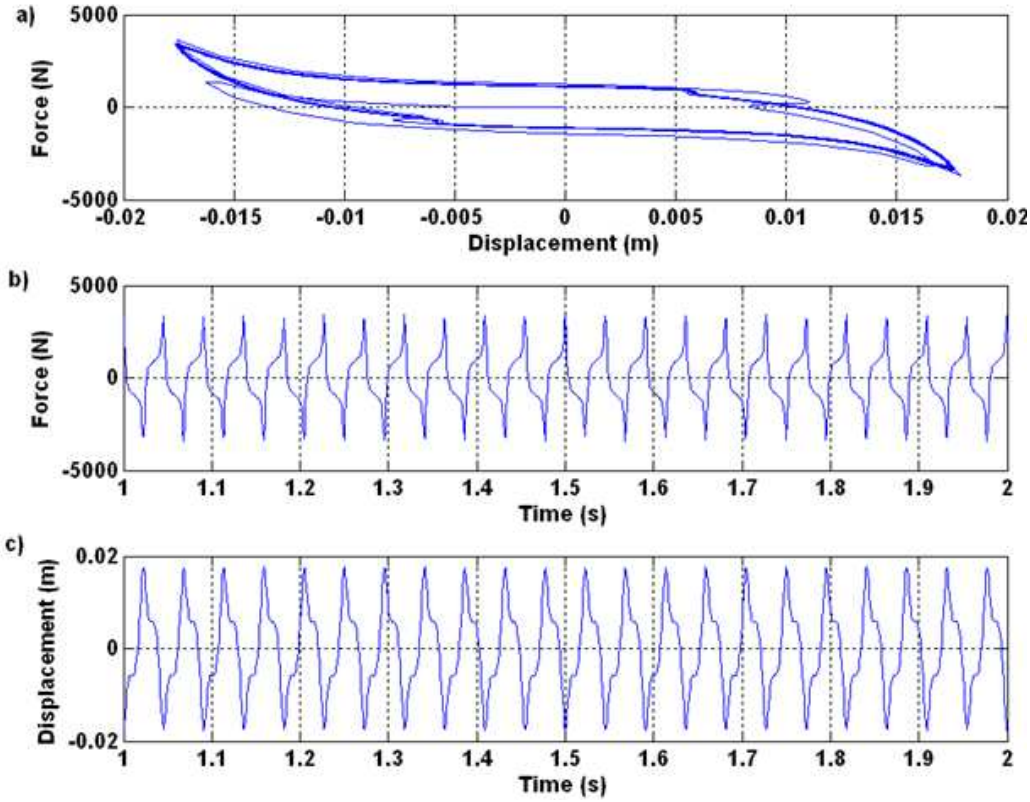

Figure 6.18 Numerical calculation of equation 6.13

Figure 6.19 illustrates the effect of the axial gap between the outer magnet and the middle magnet (d_o) on the applied force on the outer magnet under different values of the input frequency. At a certain input frequency, more force is applied to the outer magnet when d_o is 8 times the width of the magnet (0.005 m) than when d_o has the same width as the magnet. This is due to the increase in the magnet stiffness as the axial gap reduces. This causes a reduction in the magnet displacement and velocity. Moreover, as the stiffness of the magnetic levitation system increases with the decrease in the axial gap, the required frequency to bring the middle and the outer magnet in contact with each other, when d_o has the same width as the magnet, is 38 % lower than the one when d_o is 8 times the width of the magnet. As the axial gap reduces, the maximum force applied on the outer magnet at contact drops. Figure 6.19 shows that, when d_o has the same width as the magnet, the maximum force at contact effecting the outer magnet is 10 % lower than the one when d_o is 8 times more than the magnet width.

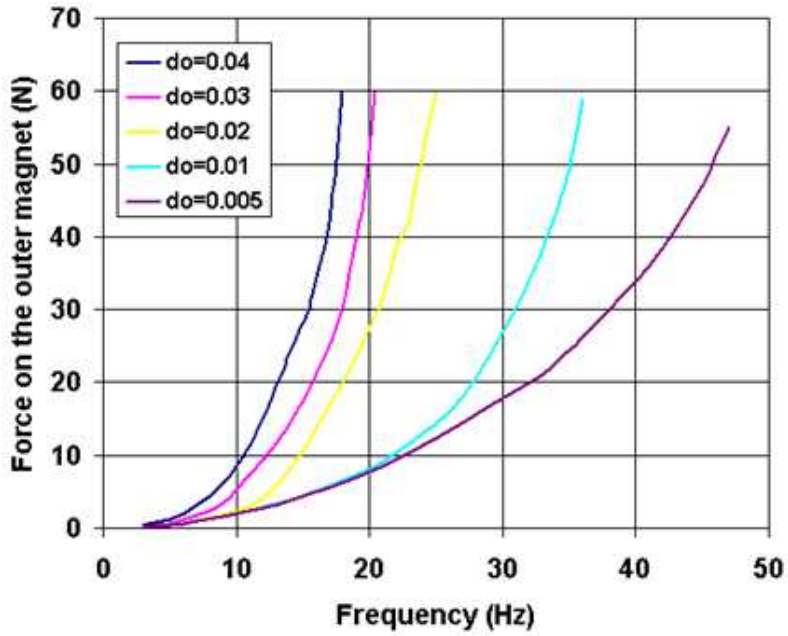

Figure 6.19 Axial force versus the input frequency at different values of d_o

6.7 Governing equations and energy harvesting model

The aim of this section is to analyse the model used for the piezoelectric harvester. A diagram of the complete energy harvesting device is presented in Section 6.8. The device consists of magnetic levitation system with Thunder™ pre-stressed beam as a source of converting mechanical energy into electrical. Equation 3.38 shows

that the output voltage depends on the velocity of the Thunder™ beam. Therefore, equation 3.40 is solved numerically using a fourth-order Runge-Kutta method to calculate the velocity of the beam at different harmonic input excitation, where M_m, B_m, K_m are experimentally measured as explained in Section 7.3. When the device is mounted at a distance *R* from the centre of a rotating wheel using the CF method, the applied force (F_m) is the sum of two forces. The first one is the one generated due to the centripetal force and its peak values equal to $4\pi^2 f^2 RM_m$. The second force is applied by the middle magnet on the outer magnets and thus the piezoelectric elements. The numerical solution (velocity) is fed into equation 3.38 which produces the output voltage and thus the output power over time. The changes in the average output power with respect to the load resistance at different values of the rotating speed is presented Section 7.4.2. In this section the numerical results are compared to the experimental one. Analysis of the effect of the rotating speed and the value of d_o on the average output power is also presented in Section 7.4.2.

6.8 Overview of the design

The principle of this harvester is presented in Section 6.2. The piezoelectric harvester is using Thunder™ beam, model TH 10-R, as the main source to convert the kinetic energy into electrical energy due to its high mechanical stability. The magnetic levitation system is used to apply force on the piezoelectric elements. Figure 6.20 shows the different parts that form the non-contact based piezoelectric harvester. Figure 6.20 (a) shows the base that is screwed on each end of the tube. The Thunder™ beam is screwed into each of the bases. A cuboidal magnet made of NdFeB material is attached to the curved piezoelectric beam using an adhesive. Magnets made of NdFeB are commercially available and provide a high energy density. The outer magnets are positioned to repel the middle magnet. The tube, presented in Figure 6.20 (b), is attached to the source that provides the excitation force. Therefore, the middle magnet moves with respect to the outer magnets within the given space in an axial direction. The moving distance depends on the applied force as well as the initial axial gap. As the middle magnet moves away from its equilibrium position, force will be applied on the outer magnets and thus the piezoelectric elements generate an output power. The tube, the bases on both ends of the tube by which the Thunder™ beams are screwed into and the carrier that the middle magnet is attached into are made of plastic. This

material is used because it is commercially available, cheap, light and easy to manufacture. The tube is made of transparent plastic with holes placed alongside the tube and used to vary the initial axial gap by repositioning the outer magnets Figure 6.20 (b).

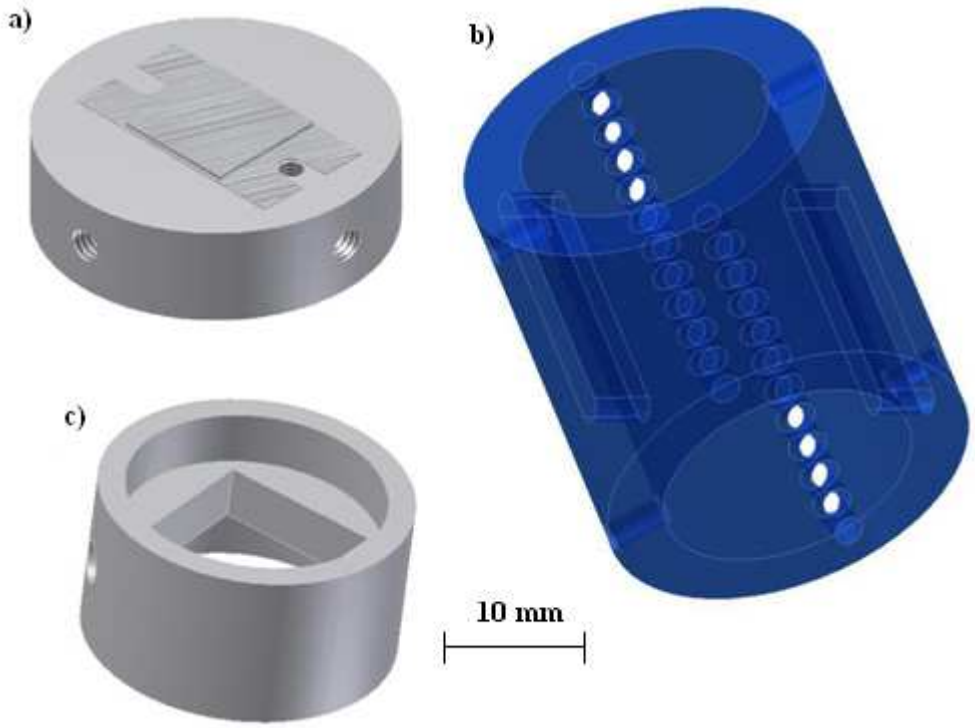

Figure 6.20 Different parts of the non-contact piezoelectric harvester. a) the base that carries the Thunder™ beam and the outer magnet, b) the tube, c) the middle magnet carrier

For numerical and experimental results, the magnet will be chosen to have an aspect ratio in the range of 0.3-0.6. For a given volume, the maximum magnetic force is achieved when the aspect ratio is within this range (Section 6.4.2). The magnet shape is chosen to be cuboidal instead of cylindrical. This is based on the numerical results which show that for a given volume and aspect ratio, the cuboidal magnet provides 20 % more magnetic force than the cylindrical magnet. The shape of the tube is round to reduce the amount of friction. The tube diameter is limited by the length of the Thunder™ beam. Therefore, if the length or the diameter of the middle magnet is less than the diameter of the tube, the magnet will flip and stick to one of the outer magnet. In order to solve this problem, a carrier shown in Figure 6.20 (c) is designed such that the magnet will fit tightly into it. This carrier moves in an axial direction between the outer magnets carrying the middle magnet. The carrier consists of two parts. The first part is a middle cylinder where the magnet fits tight in. The thickness of this part is approximately 40 % lower than the thickness of the magnet. This thickness allows the

middle magnet to stick outside both ends of the plastic cylinder and face the outer magnets. The other part of the plastic carrier is a ring that is bonded to the outside diameter of the first part. The length of the ring must be designed to be $> A/\sin 45$, where A is the separation distance between the carrier and the tube. If the length of the ring is lower than this value the carrier will flip and the middle magnet will stick to one of the outer magnets. The two plastic bases, to which the Thunder™ beams are attached, are screwed into the tube. As mentioned the minimum value of the tube diameter is restricted to the length of the Thunder™ beam. However, the tube length and the size of the magnets can be changed to fit the amplitude of the input excitation force.

The total size of the harvester is determined by the length of the tube and the dimensions of the magnets. Section 6.5 presents the method to obtain the size of the magnets. The applied force between the outer and the middle magnets equals the maximum force that the middle magnet is facing due to the excitation force. Therefore, the size of the magnets is designed at the maximum applied force. In this case, the middle magnet travels all the axial distance between the outer magnets without creating any physical contact with them. In this initial design, the total distance that the middle magnet is travelling between the outer magnets is eight times the thickness of the magnet as explained in Section 6.6. The design after that can be optimised in respect to the required volume. Smaller volumes can be achieved by reducing the length of the tube. This increases the stiffness of the harvester which allows the size of the magnet to be reduced (Section 6.6). This results in a reduction in the applied force on the outer magnet and thus the piezoelectric element causing the output power to be reduced. Another fact should be taken into the account while designing the harvester is that the applied force should not be beyond 63 N. Higher values of the applied force induces extra stress within the structure, thus reducing the reliability of the device over time. Introducing the magnetic levitation system to the Thunder™ beam adds additional stiffness to the piezoelectric beam measured in Section 3.3. Therefore, the total effective stiffness of the piezoelectric beam is given by the following equation:

$$K_{eff} = K_m + K_{mag} \tag{6.15}$$

The magnetic stiffness (K_{mag}) acts as a variable spring whose stiffness depends on the initial axial gap as well as the change in the magnetic force over the separation distance.

6.9 Conclusions

In this chapter, a non-contact based piezoelectric harvester using magnetic forces was presented. The design of the harvester was optimized using numerical analysis. In this design, the applied force on the piezoelectric element was produced by a magnetic levitation system without the need for direct physical contact. The magnetic force between two cuboidal magnets was calculated numerically and verified using a finite element methodology (Maxwell 3D). These results showed good agreement.

An analytical method was used to analyse the forces between permanent magnets of various geometries. The impact of the magnet size and shape was studied and the results became a guideline that was used to design the piezoelectric harvester. For a given volume of cuboidal magnet, the maximum force was achieved when the aspect ratio was in the range between 0.3 and 0.6. The magnetic contact force was found to drop faster when the aspect ratio was higher than one. Moreover, at high aspect ratio, the magnetic force decreased faster in value as the distance between the two permanent magnets increased. Therefore, it was preferable to have a magnet with a low aspect ratio if a long axial gap was required. For a given value of a volume and aspect ratio, the cuboidal magnet generated 20 % higher contact force than the cylindrical magnet.

Numerical calculations showed that the resonant frequency of the levitation system depended on the axial gap between the outer magnet and the middle one. Increasing the axial gap caused the system stiffness to reduce and thus the resonant frequency. The investigation of the effect of the applied harmonic force on the resonant frequency of the levitation system revealed that the system was nonlinear. Therefore, for a given axial gap an increase in the input excitation caused the resonant frequency to drop. For a given input force on a piezoelectric harvester that used a magnetic levitation system, the output power is predicted to increase as the axial gap got longer. As the axial gap increased, the stiffness of the system reduced allowing the middle magnet to travel a longer distance. This applied more force on the outer magnet and thus the piezoelectric element attached to it causing an increase in the output power. The effect of the axial gap on the output power of the harvester will be discussed in Chapter 7.

Chapter 7

An experimental investigation of the non-contact piezoelectric harvester

7.1 Introduction

This chapter presents the experimental strategies that were carried out to verify the model developed in Chapter 6. The principle of the non-contact piezoelectric harvester is presented in Section 6.2. Section 7.2 presents the test setup that is used to measure the magnetic force between two cubical magnets. Section 7.3 presents the test setup that is carried out to examine the behaviour of the non-contact piezoelectric harvester. The experimental results are presented and compared to the analytical one in Section 7.4. In this section the damping and the stiffness of the harvester are analysed. This section presents the effect of the rotating speed and the load resistance on the output power. The experimental results of the output power are compared to the one obtained numerically. The numerical and experimental results provide a guidance to optimize the harvester which is used to harvest energy from rotational forces using magnetic forces.

7.2 Test setup for measuring the magnetic forces

Figure 3.13 shows the apparatus used to measure the relationship between the magnetic force and the magnetic spacing between two magnets in the *z* direction. In

this experiment, the two magnets share the same central line where the area of the first magnet overlaps perfectly with the face of the other magnet. The magnets are oriented to repel each other. The schematic diagram in Figure 7.1 shows that one of the magnets is connected to the bottom head, which is fixed, while the other one is placed on the top head, which has the ability to move up and down in the *z* direction. The top head is connected to a load cell. Moreover, the movement of the top head is controlled using Console software provided with the test machine. As the magnet attached to the top head moves down, the applied forces between the two magnets are measured using the calibrated load cell. Figure 7.3 shows a series of experimental measurements of the force plotted as a function of the separation distance between the two magnets. The dimensions of the magnets used are 14 mm × 14 mm × 5 mm.

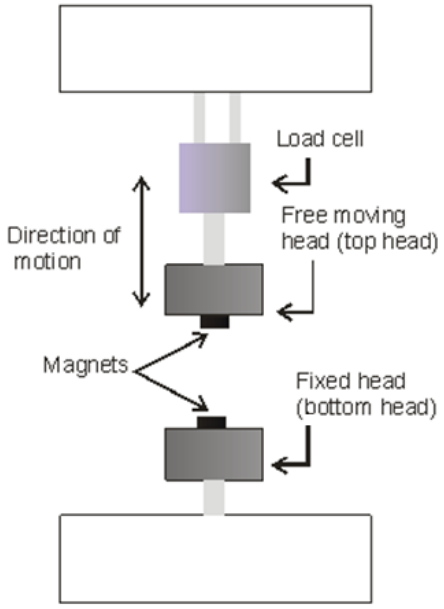

Figure 7.1 Schematic diagram of part of the experimental instrument that used to calculate the axial magnetic force

7.3 Test setup for the non-contact piezoelectric harvester

To determine the behaviour of the non-contact piezoelectric harvester under rotation and to measure its average output power, the final design presented in Section 6.8 is mounted on the host of the rotating wheel designed in Section 5.2.2. A Thunder™ pre-stressed beam is used as a source to convert the kinetic energy into electrical energy due to its mechanical stability. After the non-contact piezoelectric harvester is assembled, the whole structure is screwed to the host as shown in Figure 7.2. The distance between the Thunder™ beam where power is extracted and the centre

of rotation is 0.075 m. An experiment at different constant rotating speeds ranging from 66.6 rpm to 266.6 rpm is performed to verify the theoretical prediction of the average output power and its dependency on the rotating speed. For this experiment, the initial axial gap between the outer and the middle magnet (d_o) is kept constant at a value of 0.012 m. This gap value is the maximum that can be achieved experimentally due to the size of the testing wheel. Any further increase in the tube length causes a direct contact between the centre of the testing wheel and the tube when the latter is mounted using the CF method. Both outer magnets and the middle one have the same dimensions of 0.015 m length, 0.015 m width and 0.005 m thickness. The mass of the each of the magnets in the experiment is 0.0083 kg. The tube had a diameter of 0.028 m. The 0.001 m difference in diameter between the middle magnet carrier and tube is made to reduce the friction between them. The same experiment is repeated at different values of d_o ranging from 0.009 to 0.003 m in order to investigate the effect of the initial gap on the output power for a given rotating speed. The relationship between the output power and both the rotating speed and the d_o is recorded. Moreover, the output power as a function of the load resistance is recorded at different values of d_o. For this experiment, the load resistance varies from 100 Ω to 6 MΩ.

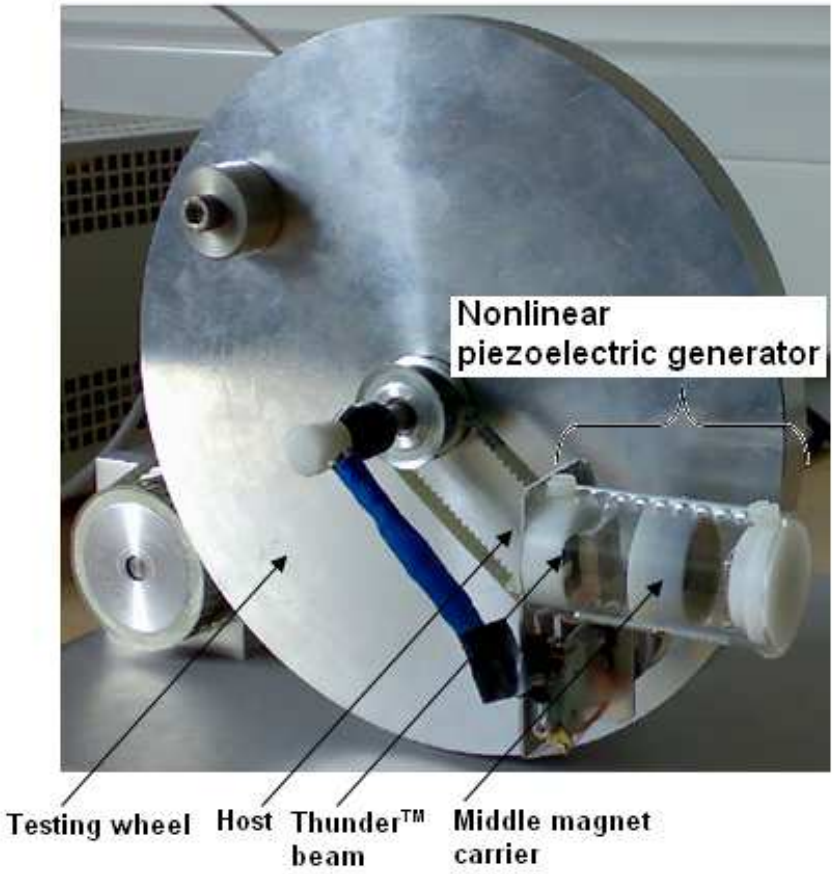

Figure 7.2 The non-contact harvester mounted on the testing wheel

Another experiment is carried out to investigate the dependency of the levitation system resonant frequency on the travelling distance of the middle magnet as well as the initial distance between the outer and the middle magnet. The method by which the resonant frequency and the damping of the system are measured is introduced in this section. The method can be explained as follows, the middle magnet is moved to one end of the tube away from its equilibrium position at a step of 0.002 m. After that the middle magnet is released from that position and the attenuation plot of the system is recorded at each step and used to calculate both the damping ratio and the resonant frequency of the system using a curve fitting method. The generated curve can be expressed as equation 7.1. The same method is used under different values of the initial gap (d_o) ranging from 0.012 m to 0.003 m.

$$z(t) = \frac{A}{m\omega_o\sqrt{1-\xi^2}} e^{-\xi\omega_o t} \sin\left(\omega_o\sqrt{1-\xi^2}\,t\right) \tag{7.1}$$

For both experiments, the harvester is mounted using the CF method where the centripetal force is the main source that forces the middle magnet to move from one end of the tube to the other end. Moreover, the same magnets are used in both experiments. The experimental results are limited to relatively low rotating frequency 4.4 rps. This is due to the limitation of the practical experimental measurements.

7.4 Experiment results and discussion

In this section experimental results are compared to numerical ones obtained in the previous chapter. In Section 7.4.1 the forces between two cuboidal magnets are presented as a function of the separation distance. Section 7.4.2 presents the experimental and the numerical results of the relationship between the resonant frequency of the levitation system and the initial axial distance between the outer and the middle magnet. Moreover, the experimental results that present the resonant frequency of the levitation system as a function of the moving distance of the middle magnet are shown in Section 7.4.2. Section 7.4.3 presents the output power of the non-contact harvester as a function of the rotating speed at different values of the initial axial gap between the outer and the middle magnet.

7.4.1 Magnetic forces

The resulting force-displacement graph is compared to the results generated by the analytical calculations in Figure 7.3. The force is measured with an accuracy of ±0.15 N and the displacement is measured with an accuracy of ±0.005 mm. The minimum distance between the two magnets, by which the force has been measured is 0.1 mm. This is due to the fact that the two magnet surfaces are not 100 % parallel to each other. Reducing the distance to less than 0.1 mm, will cause part of the magnet surfaces to come in contact with each other and thus gives an incorrect force reading.

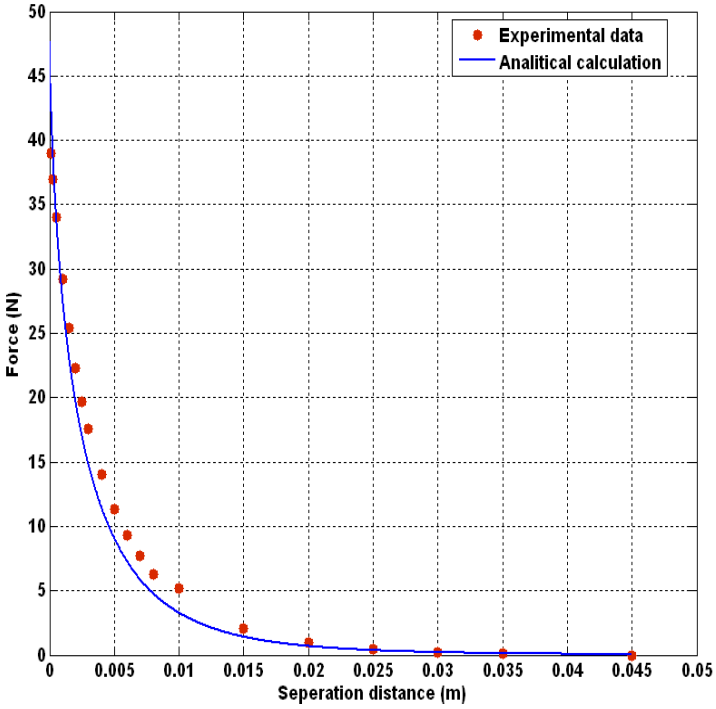

Figure 7.3 Comparison between the experimental and calculated results between the magnetic force and the distance between the two magnets

7.4.2 Resonant frequency and damping

The damping and the resonant frequency of the non-contact piezoelectric harvester that uses magnetic levitation system to extract power from centripetal forces are measured using the methods explained in Section 7.3 and Section 3.4.4. The measurement carried out at different values of the rotating speed, ranging from 66.6 rpm to 333.33 rpm, as well as at different values of the axial gap, ranging from 0.012 m to 0.003 m. These values are used in the numerical model presented in Section 6.7 to predict the output power. Both the rotating speed and the value of the axial gap affect

the damping and the stiffness of the magnetic levitation system as presented in Chapter 6. This affects the amount of force applied on the Thunder™ beam and thus the values of its stiffness and damping. For a given axial gap (d_o), the method presented in Section 7.3 is used to investigate the effect of the moving distance of the middle magnet on the total stiffness and damping of the non-contact harvester. Figure 7.4 shows the relationship between the normalized distance in the axial direction (x/d_o) and the normalized resonant frequency ($f_{o(x)}/f_{o(do)}$) at different values of the axial gaps, where $0.27d_o \le |x| \le d_o$. The experimental results agree with those obtained numerically as illustrated in Section 6.6. As can be seen, for a given initial axial gap, increasing the moving distance of the middle magnet causes the stiffness of the system to increase. The damping of the system reduces as the middle magnet moves closed to the outer magnets. When the normalized axial distance increased from 0.3 to 1, the damping reduced by 50 %, 65 % 71 % and 3 % at an initial axial gap of 0.012 m, 0.009 m, 0.007 m and 0.003 m, respectively.

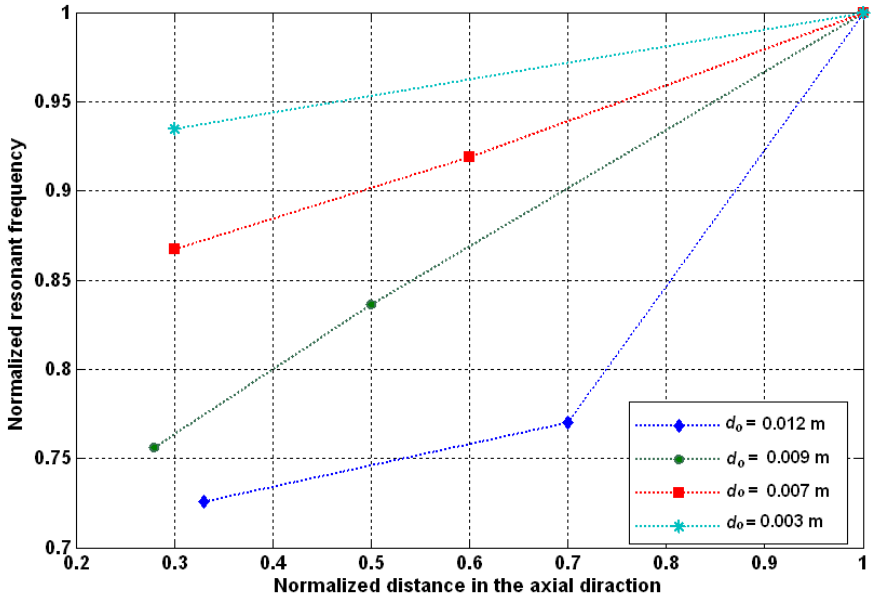

Figure 7.4 Normalized resonant frequency ($f_{o(x)}/f_{o(do)}$) as function of the normalized distance (x/d_o) at different values of the axial gap d_o, experimental results.

For a given rotating speed, the method presented in Section 3.4.4 is used to investigate the effect of the value of the initial axial gap (d_o) on the total stiffness and damping of the non-contact harvester. Figure 7.5 shows the effect of the initial axial gap (d_o) on the effective stiffness of the harvester. For a given rotating speed, the experimental results show that, as the axial gap increases, the effective stiffness of the harvester reduces until it reaches its minimum value at d_o equals to 0.005 m. After that

any increase in the initial axial gap causes the harvester's effective stiffness to increase. This is due to the fact that the effective stiffness of the non-contact harvester is affected by the stiffness of the magnetic levitation system as well as the stiffness of the Thunder™ beam. As the initial axial gap reduces from 0.012 m to 0.005 m, the stiffness of the levitation system increases; however, the stiffness of the Thunder™ beam reduces due to the reduction in the value of the beam's curvature as explained and presented in Figure 3.12 (c). Therefore, the effective stiffness of the harvester reduces as the reduction in the Thunder™ beam stiffness is higher than the increase in the stiffness of the levitation system. Increasing the initial axial gap beyond this point (0.005 m) causes the Thunder™ beam to be flat. In this case, increasing both the rotating speed as well as the initial axial gap leads to an increase in the Thunder™ beam stiffness (Figure 3.17 (b)) and the stiffness of the magnetic levitation system. This causes the effective stiffness of the harvester to increase again as the initial axial gap increases. Therefore, the maximum power is expected to be generated when the effective stiffness of the harvester is at its minimum value. Both the damping and the stiffness of the harvester is recorded and used in the theoretical model to estimate the amount of the output power at different rotating speeds and initial axial gaps.

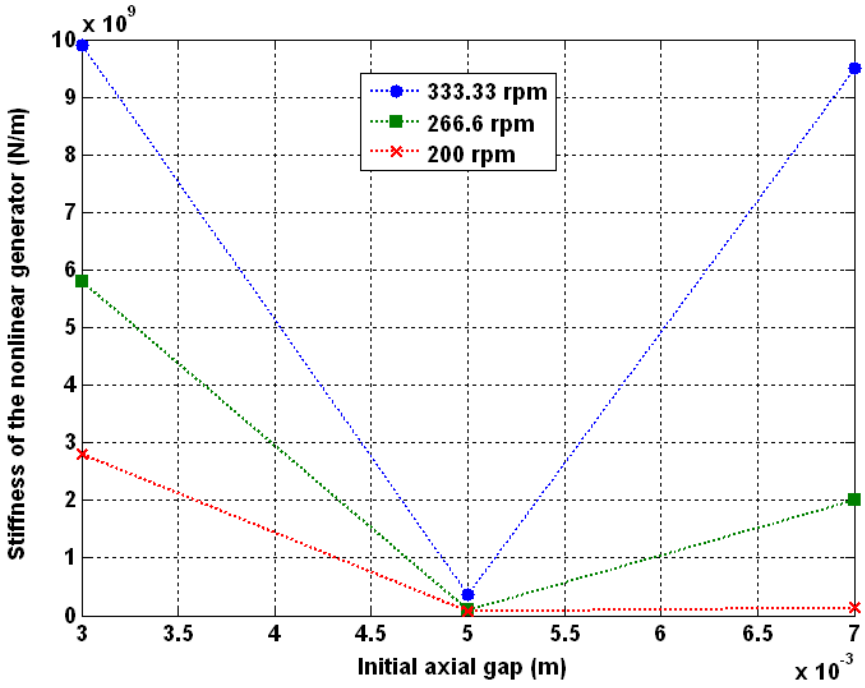

Figure 7.5 Stiffness of the non-contact harvester as a function of the initial axial gap at three different rotating speeds 333.3 rpm, 266.6 rpm and 200 rpm.

7.4.3 Output power

Figure 7.6 shows the average output power produced by one of the Thunder™ pre-stressed beams versus the load resistance. The maximum rotating speed by which the experimental results are obtained is 266.6 rpm. This figure shows a good agreement between the experimental and numerical results. The experimental results show the effect of using the levitation system on the average output power. Increasing the rotating speed resulted in an increase in the average output power. The maximum output power is obtained when the value of the load resistance equals 250 kΩ. The maximum measured values of the averaged output power produced by Thunder™ beam at 66, 133, 266 and 333 rpm are 1.9×10^{-9}, 1.3×10^{-8}, 1.4×10^{-6} and 3.5×10^{-6} W, respectively at the optimum load resistance. Figure 7.6 presents the expected output power when the rotating speed is as high as 333.3 rpm. The initial axial gap by which both the numerical and the experimental results are obtained is 0.005 m.

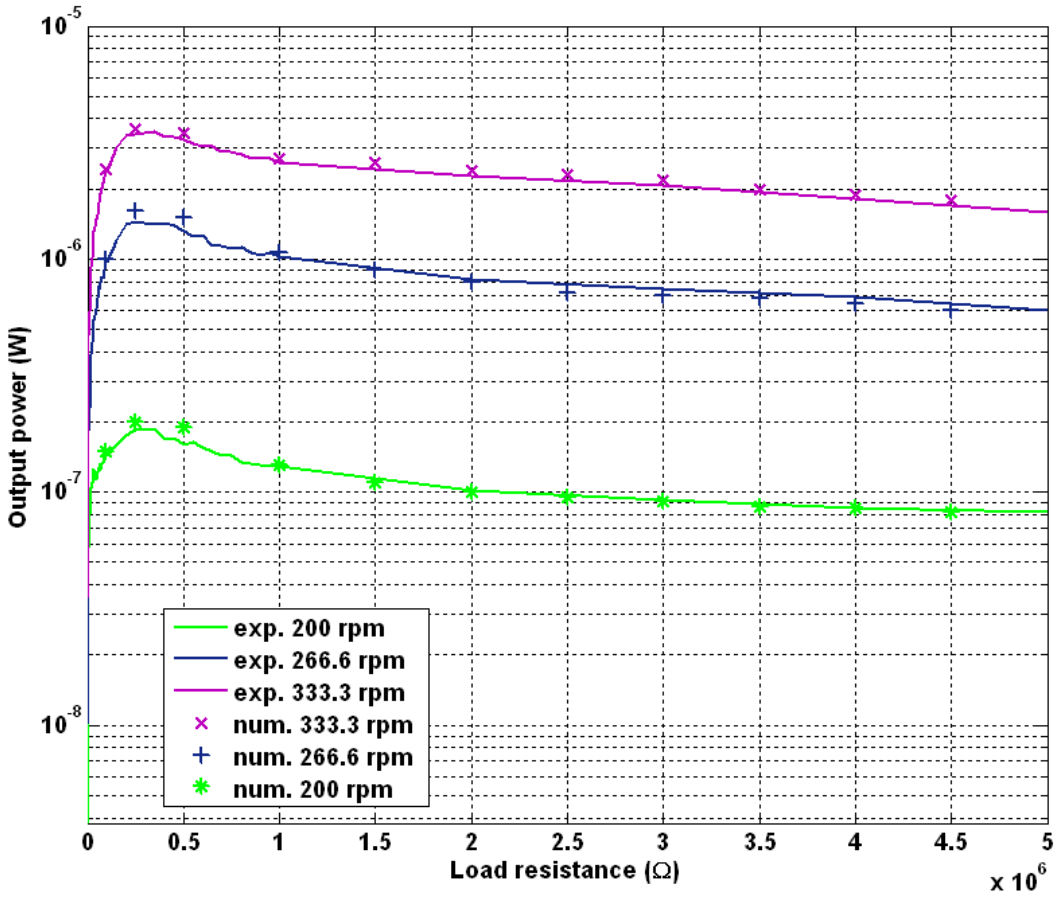

Figure 7.6 Output power as a function of external resistance at different rotating speeds using the non-contact piezoelectric harvester which is mounted using the CF method, solid lines present the experimental results (exp.) and the symbols present the numerical data (num.)

The voltage drop across the optimum resistance of the Thunder™ beam for each value of d_o is measured and recorded at different rotating speeds. Figure 7.7 presents the effect of rotating speed (f) on the maximum average output power (P) across the optimum load resistance at different value of the axial gap (d_o). For a given axial gap, the average output power increases with an increase in the rotating speed. For a given axial gap (d_o), increasing the rotating speed forces the middle magnet to move closer to the outer magnets. This induces an extra force on the piezoelectric element and thus generates more output power. However, for a given rotating speed, the average output power increases as the axial gap increases until it reaches a certain value and then starts to drop. This is due to the fact that the total stiffness of the harvester depends on the value of the axial gap. The change in the total stiffness of the non-contact harvester will be examined in more detail in the next section.

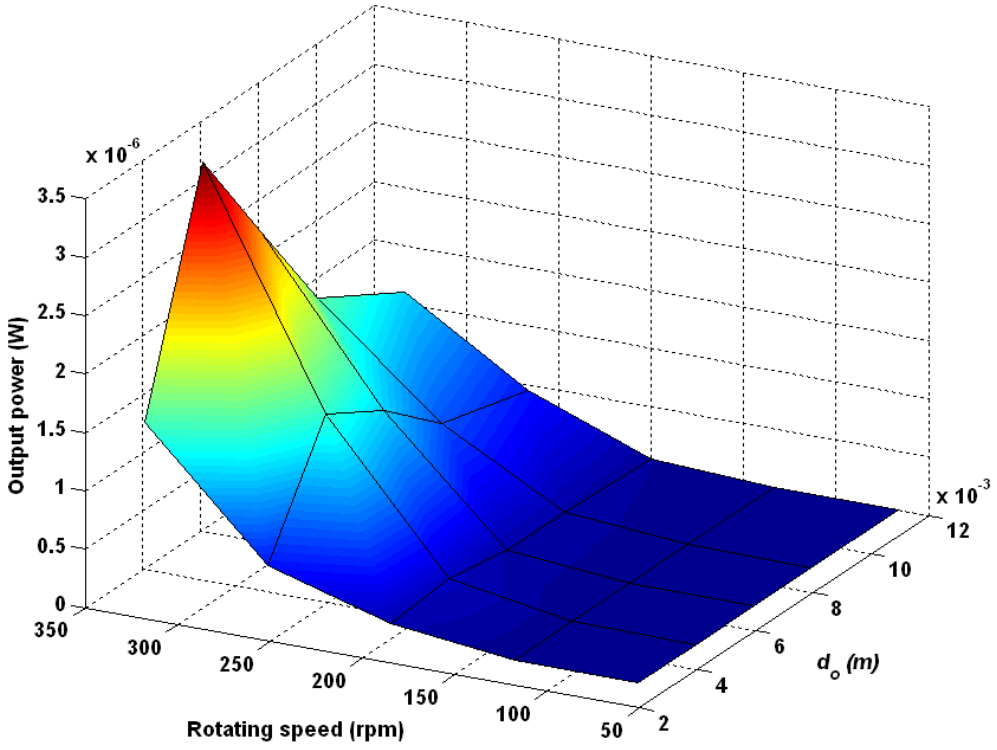

Figure 7.7 Numerical calculation of the output power as a function of the input frequency and d_o

7.4.4 Optimization of the output power in geometries perspectives

The total volume of the non-contact harvester consists of two main parts. The first one has a fixed volume and its value equals the sum of the two volumes of the bases, the volumes of the 3 magnets and the volumes of the two Thunder™ beams. The

two bases, each of which is located at one end of the tube, are used to hold the Thunder™ beams and the two outer magnets. The second part is the volume of the tube provided between the two outer magnets. This space ensures a free movement of the middle magnet carrier caused by the effect of the input force (Figure 7.8).

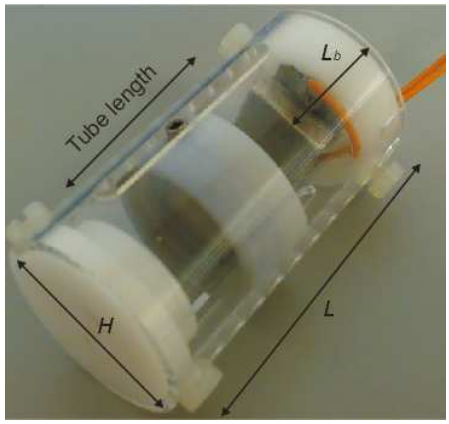

Figure 7.8 Total volume of the non-contact harvester

The height and the width of the Thunder™ beam put limitations on the minimum volume of the whole harvester. This means the minimum height of the harvester equals the height of the Thunder™ beam which is H = 0.026 m. The same thing is applied to the width of the harvester as the width of the Thunder™ beam equals W = 0.02 m. This is due to the fact that the volume of the Thunder™ beams is fixed. Therefore, the optimum output power as a function of the harvester's volume can be only achieved by changing the length of the tube located between the two Thunder™ beams. The value of L_b is 0.0106 m, which consists of the thickness of the base (0.005 m), the height of the Thunder (0.0006 m) and the thickness of the magnet (0.005 m). The bases are screwed to the tube and one of them is used to screw the harvester onto the rotating wheel. The carrier of the middle magnet ensures that the three magnets share the same central line and they are oriented to repel each other. The tube has a cylindrical shape. Therefore both bases and the middle carrier have a disk shape all of which have a diameter equal to the length of the Thunder™. Therefore, for this configuration, the maximum length and width that can be used for the middle magnet are 0.015 m. The thickness of the magnet is kept within the recommended range of the aspect ratio as discussed in Section 6.4.2 and its value equals 0.005 m. A 0.0001 m difference between the diameter of the middle magnet carrier and the inner diameter of the tube is kept to reduce the amount of friction between them.

The harvester is designed for a given value of the distance between the centre of rotation and the centre of the tube (R) as well as the maximum value of the rotational

speed (*f*). For a given rotating speed and *R*, the force generated by the magnetic levitation system on the each Thunder™ beam depends on the size of the magnets and the length of the tube. The maximum applied force on the Thunder™ beam must be equal to its yield value (Section 4.5.2). The criteria by which the harvester is designed for are: withstanding the maximum amount of input energy without breaking, occupying the minimum volume, having a low value of mass and generating the maximum output power. The optimum volume of the non-contact harvester is the one that generates the maximum output power for a given rotating speed. The harvester must be designed to withstand the applied force at the maximum rotating speed (*f*). At this rotating speed, the stiffness of the harvester should allow the middle magnet to achieve the maximum displacement inside the tube without creating any physical contact with the two outer magnets. The procedure of optimizing the size of the harvester starts with using a magnet with a volume equals to 0.015 m × 0.015 m × 0.005 m. Then equation 6.1 is applied in order to obtain the value of the applied force due to the use of the magnetic levitation system on the Thunder™ beam at different values of the tube length. The applied magnetic force is then used in equation 3.40, which is solved numerically using a Runge-Kutta method. The same procedure is carried out at different values of the tube length, where the relationship between the output power and the tube length is obtained (Figure 7.7). Figure 7.9 show the output power at the optimum load resistance (200 kΩ) as a function of the rotating speed at different values of d_o. These data are obtained experimentally.

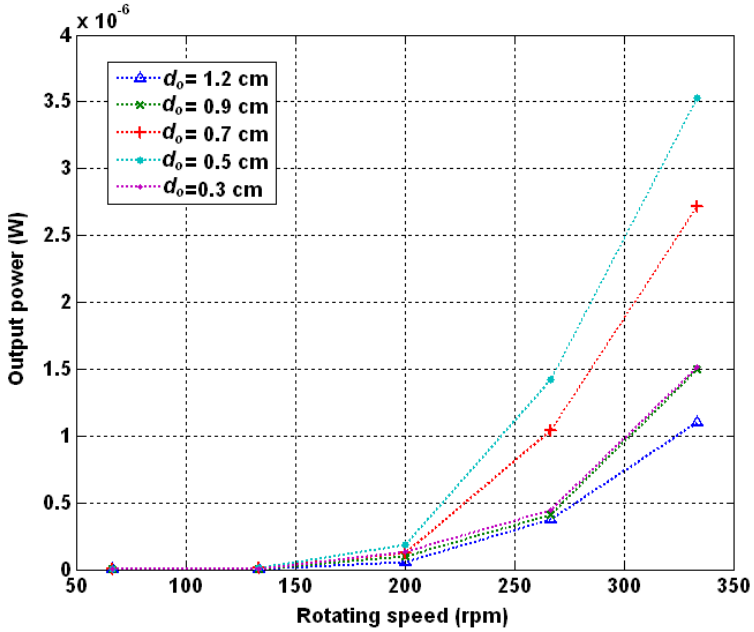

Figure 7.9 Output power versus the rotating speed at different values of d_o

As is can be seen the maximum output power is achieved when the initial axial gap (d_o) equals 0.005 m. This means that the maximum available displacement for the middle magnet is 0.01 m. The maximum rotating speed that can be applied to this harvester is 25 Hz. This rotating speed is calculated theoretically when the harvester is mounted at a distance of 0.072 m from the centre of rotation. Any further increase in the rotating speed causes the middle and the outer magnet to come in contact with each other. Therefore, the volume of the non-contact harvester when R and the maximum value of f equal to 0.072 m and 25 Hz, respectively is 4.9×10^{-4} m^2 $\times$ 0.0362 m. In order to compare the impact based piezoelectric harvester with this harvester, the theoretical calculation showed that magnets with dimensions equal to 7 m$\times$7 m$\times$3.5 m can be used when the maximum rotating speed is 15.55 Hz. Moreover, the model predicted that the maximum power is generated when the initial axial gap equals to 0.0003 m. Therefore, the maximum volume of the harvester is 4.9×10^{-4} m^2 $\times$ 0.021 m.

7.5 Conclusions

The developed model that was used to predict the amount of power generated from rotational forces using the non-contact piezoelectric harvester was verified in this chapter. The performance of the harvester was tested and analysed. The harvester was attached to the testing wheel using the CF method through the host that kept it in a horizontal position during rotation. The distance between the Thunder™ pre-stressed beam, where the output power was collected, and the centre of rotation was 0.072 m. The magnetic force between the two cuboidal magnets that were used in the experiment was measured at different values of the axial gap between them. In this experiment, the two magnets shared the same central line and they were oriented to repel each other. The experimental results agreed with the numerical one. The behaviour of the non-contact harvester was tested under different values of the rotating speeds ranging from 1.1 rps to 5.5 rps as well as different values of the tube length. This included measuring the damping and the stiffness of the system and recording the generated output power. The values of the stiffness and the damping for a given tube length and a rotating speed were used in the theoretical model to predict the output power of the non-contact harvester. The experimental results revealed that the maximum power was generated when the initial axial gap between the middle and the outer magnet was at its optimum value which was approximately 0.005 m. For a given rotating speed, the effective

stiffness of the non-contact harvester reached its minimum value at that distance. If the distance was below this value, the magnetic force caused the Thunder™ beam to be flat and thus increasing its stiffness. Increasing the distance beyond 0.005 m reduced the initial applied force by the magnet on the Thunder™ beam and thus increased the value of its curvature. This increased the stiffness of the piezoelectric beam.

Chapter 8

Comparative study of the two piezoelectric harvesters

8.1 Introduction

This chapter is divided into two main sections. Section 8.2 outlines the differences between the impact based piezoelectric harvester and the non-contact one based on the amount of generated power for a given rotating speed. Both the limitations and the advantages of each method are highlighted and compared to each other. In Section 8.3 the possibility of using the two different types of piezoelectric harvesters inside a vehicle wheel is presented. The maximum rotating speed of the vehicle wheel is calculated and used to modify the dimensions of the piezoelectric harvesters located at the rim of the vehicle wheel. As the two harvesters extract power from the centripetal force, some modification on the vehicle wheel is needed to allow the harvesters to be mounted using the CF method. The predicted amount of power from the vehicle wheel is calculated from both harvesters.

8.2 Comparison between the impact based and the non-contact piezoelectric harvesters

In this research both harvesters extract power from the centripetal acceleration by mounting them using the CF method. In this method the harvesters are kept in a horizontal position during rotation. In order for this method to be implemented, the rotating object must be modified mechanically. Both harvesters are easy to assemble

and mount on the rotating object. Both the theoretical and the experimental results show that a harvester that uses Thunder™ beam on its own generates less power than the one that uses a ball bearing as a mass or magnetic levitation system. The harvester that uses only Thunder™ beam to extract power from rotation when it is mounted using the CF method generates an output power ranging from 3.5×10^{-10} W to 7×10^{-8} W when the rotating speed changes from 200 rpm to 400 rpm.

In the impact based piezoelectric harvester, the ball bearing causes an impact on the Thunder™ beam due to the effect of the centripetal force and thus power will be extracted. The output power in this harvester is proportional to the square value of the available displacement of the ball bearing inside the tube and it has a cubic relationship with the rotating speed. However, the maximum speed should not exceed the critical value at which the applied force on the piezoelectric element is at its yield value. In order to compare the two piezoelectric harvesters in terms of the generated output power, the minimum volume provided due to the size of the Thunder™ beam is used. This volume determines the diameter of the ball bearing (0.015 m) in case of the impact based harvester and the magnet size (0.015 m $\times$ 0.015 m $\times$ 0.005 m) in the case of the non-contact harvester. The experimental results of the output power of the two harvesters are compared whilst maintaining the length of the tube at 0.01 m. The generated output power from the impact based harvester ranges from 10^{-5} W to 2×10^{-4} W when the rotating speed changes from 200 rpm to 400 rpm. For the same rotating speeds, the output power of the non-contact harvester ranged from 1.3×10^{-8} W to 6×10^{-6} W. For the non-contact harvester, the maximum applied rotating speed before the middle and the outer magnets come in contact with each other is 1500 rpm. For the impact based harvester, the maximum applied rotating speed is 540 rpm. Beyond this speed, the impact force will exceed its yield value causing damage to the Thunder™ beam. Both the size of the ball bearing and the length of the tube can be modified in order for the harvester to withstand the maximum rotating speed. One of the disadvantages of the impact based harvester is that there is no mechanical mechanism to protect the piezoelectric element from the impact force generated when the rotating speed exceeded the one that the harvester is designed at. This means this harvester is more suitable for applications where the rotating speed does not exceed its maximum value. Another disadvantage of the impact based harvester is the noise generated due to the physical contact between the mass and the piezoelectric elements. The non-contact piezoelectric harvester does not suffer from noise because there are no physical contact

between the middle and the outer magnet. Moreover, this harvester has a mechanical stop mechanism to prevent any contact between the magnets. This is introduced by the ring of the middle magnet carrier. When the maximum rotating speed, by which the harvester is designed at, is applied the ring will come into contact with the bases that carry the Thunder™ beam and thus protect the piezoelectric beam from direct impact. The same thing happens when the rotating speed exceeds its maximum value. However, for a given rotating speed, the non-contact harvester produces less power than the impact based harvester.

8.3 Harvesting energy from the tyre environment

The size of the vehicle wheel depends on the vehicle type and brand. The dimension of the tyre and the rim are printed on the tyre as following (X)/(Y)/R (Z) where X, Y and Z refer to the width of the tyre in mm, the height of the tyre as a percentage of the width and the rim diameter in inches respectively. The rim size can vary from 13 inches to 27 inches and more. For example, a vehicle tyre with 175/50R13 means:

- The width of the tyre is 175 mm
- The tyre height is 50 % of 175 mm = 87.5 mm
- The rim diameter is 13 inches = 33 cm. Therefore, the rolling radius for the vehicle is: 33/2 + 8.75 = 25.25 cm.

For this vehicle the value of the rotating speed in hertz (*f*) is 0.28 of the vehicle linear velocity given in mph. A range of national speed limits are set for general use across the UK. These speed limits vary according to the type of the road and location. The maximum national speed limit on the motorway is 70 mph (19.6 rps). Practically, the maximum speed can be exceeded, especially on the motorway, up to 90 mph (25 rps) or more. Therefore, the harvester should be able to generate enough power at low speed and withstand the applied forces at high speeds.

This research proves the concept of generating power from rotating objects. Prototypes of both an impact based harvester and a non-contact piezoelectric harvester are produced and tested in the laboratory. The method by which the harvesters are kept in a horizontal position due to rotation is demonstrated in this work. As the harvesters are kept in a horizontal position, the centripetal acceleration becomes the main cause of generating power. In this method, the higher the rotating speed, the more power can be

extracted from both types of harvesters. To date, the performance of the harvesters that have been presented in the literature and designed to harvest energy from the tyres is limited at high speed. This is due to the effect of the centripetal force. The limitation of keeping the harvester in a horizontal position during rotation is that a mechanical support is needed. To implement this method on a vehicle wheel requires a mechanical modification to be applied to the wheel. One way that the manufacturer can consider as a method of mounting the harvesters on the tyre is the model presented in this work.

If the impact based harvester with a ball bearing diameter equals to 0.015 m and a tube length equals to zero is mounted at the edge of the vehicle wheel rim (175/50R13) using the CF method, the maximum rotating speed that can be applied is 14.5 rps. This means the linear speed of this vehicle is 51.7 mph. It is found theoretically that an impact based harvester with a mass diameter of 0.0045 m and tube length of zero has the ability to withstand a maximum linear speed of 70 mph. The output power of this harvester ranged from 3 μW to 150 μW when the speed changed from 30 mph to 70 mph. If the non-contact piezoelectric harvester with a magnet dimensions equal to 0.015 m × 0.015 m × 0.005 m and tube length equals to 0.01 m is mounted at the edge of the vehicle wheel rim (175/50R13) using the CF method, the maximum rotating speed that brings the outer and the middle magnets together will be 16 rps. This happens at a linear speed of 57 mph. For a non-contact harvester with magnet dimensions of 0.025 m × 0.025 m × 0.012 m and a tube length of 0.045 m, the vehicle linear speed by which the contact force starts to form between the outer and the middle magnet equals to 70 mph. Theoretically, the output power of this harvester ranged from 3.56×10^{-5} W to 14 mW when the linear speed changed from 30 mph to 70 mph. For this configuration, when the middle and one of the outer magnets come in contact with each other at a rotating speed of 70 mph, the applied force on the piezoelectric beam is more than 3 times its value at yield. This problem can be solved by reducing the length of the tube which allows a further reduction in the size of the magnets. In this case, magnets with dimensions equal to 0.015 m × 0.015 m × 0.005 m can be used with an initial axial gap of 0.004 m. Therefore, the piezoelectric device will be at yield when the middle magnet comes in contact with one of the outer magnets; however, the output power at 70 mph has been reduced to a few tens of microwatts.

8.4 Conclusions

In conclusion, the impact based harvester generated more output power than the non-contact harvester for a given rotating speed. The non-contact harvester had an advantage over the impact based harvester in terms of a direct physical contact was not needed to apply force on the piezoelectric element. In the non-contact harvester, the mechanical stopping mechanism protected the piezoelectric elements from an impact force when the rotating speed exceeded its maximum value for which the harvester was designed.

Chapter 9

Conclusions and future work

9.1 Summary of achievement

In Section 1.1 the aims of the research were presented. The main focus of this work was directed towards designing suitable piezoelectric harvester that uses Thunder™ pre-stressed beam for the application of harvesting energy from the rotational forces in general and the centripetal force in particular. This was achieved and the following areas were investigated in detail:

- Demonstrating the possibility of harvesting electrical energy form the centripetal force.
- Designing an impact based piezoelectric harvester as well as non-contact piezoelectric harvester both of which use Thunder™ beam as a source of converting kinetic energy into electrical one.
- Modelling of Thunder™ beam and measuring its characteristics under impact force.
- Modelling of Thunder™ beam and measuring its characteristics under magnetic force.
- Testing both the impact based piezoelectric harvester and the non-contact piezoelectric harvester and optimizing their dimensions for the maximum amount of power at the maximum value of the applied rotating force.

The main results and conclusions were summarized in the following sections.

9.2 Summary of work

This research, which focused on designing piezoelectric harvesters that uses Thunder™ pre-stressed beam to harvest energy from centripetal force, was divided into four main parts. In the first part, the concept of generating power from centripetal force, when the harvester was mounted at a certain distance from the centre of rotation was investigated. In the second part, the behaviour of the Thunder™ pre-stressed beam under compression force and impact force was analysed. In the third part, both impact based piezoelectric harvester and non-contact piezoelectric harvester were designed and modelled under the effect of the centripetal force. In the fourth part, the performance of the developed harvesters was tested and their dimensions were optimized.

9.2.1 Using rotational forces to generate output power

The literature review, which was presented in Chapter 2, introduced three different transduction mechanisms that have commonly been used to convert kinetic energy into electrical energy, such as electrostatic, electromagnetic and piezoelectric. A variety of studies regarding these mechanisms were analysed and summarized. The theory behind rotation based harvesters was presented. In this project, rotation was considered to be the main source for harvesting energy. An impact based piezoelectric harvester was used to extract the energy provided by rotational forces and convert it into electrical power. A piezoelectric transducer was chosen over both electromagnetic and electrostatic harvesters because these technologies require two part designs making these technologies more complex and expensive in comparison with the piezoelectric technology. It has been proven in the literature that if the input acceleration is higher that the mass displacement of the harvester, a non-resonant system is an alternative method to convert mechanical input to electrical input. Therefore, an impact based piezoelectric harvester was used in this thesis to extract power from rotation. A rotating object provides two rotating forces, i.e. tangential and centripetal when the wheel is rotating in non-uniform circular motion, and only centripetal force under uniform circular motion. Due to these forces the developed stress and strain in the piezoelectric material can be converted into useful energy. However, there is more applied force available by the centripetal acceleration than the tangential acceleration on an object located on a rotating object. Therefore, this force was chosen to be the main source of the generated electrical energy in this project. Moreover, the centripetal force is

proportional to the distance between the centre of rotation and the object. Therefore, the piezoelectric transducer must be mounted as far as possible from the centre of rotation to generate the maximum amount of power. In addition this force is proportional to the square of the rotating speed. This present work introduced a new method to generate power from rotating objects using a piezoelectric harvester. It involved using centripetal force to generate an impact or compression force on the piezoelectric structure. Thunder™ pre-stressed piezoelectric beams were used because they provided higher mechanical stability and output power compared to unstressed beams with the same volume. The harvester was designed to be mounted at a certain distance from the centre of rotation. Chapter 2 presented some attempts that were carried out to generate power from rotation using electromagnetic harvesters. These harvesters were attached to the centre of the rotating object. However, when these harvesters were mounted at a certain distance from the centre of rotation, the output power reduced due to the effect of the centripetal force. Rolling vehicle tyres is one of the applications that can be used to harvest energy from rotation and it was used as the main application in this project. Several papers described the importance of checking vehicle tyre pressure and outlined different methods to measure it. There is not only an economic benefit from keeping the tyre at the correct air pressure, i.e. increasing the lifetime of the tyre and reducing the fuel consumption, but there is also a safety issue. TPMS is one of different techniques that have been used to inform the driver with the pressure reading in the vehicles tyres. In this technique, the sensors implemented inside the vehicle tyre send the reading directly to the driver using RF signals. Current TPMS sensors are powered by 3 V lithium batteries. In order to increase the lifetime of the wireless sensors, batteries can be replaced by energy harvesters. The harvester is fitted on the vehicle rim, which has the advantage to be mounted directly to the TPMS. All methods which were presented in Chapter 2 and used to generate power from a vehicle wheel depended on generating power from the contact zone between the tyre and the road. The maximum output power that was measured using this method was 80 μW at 80 km/h. These harvesters were mounted at the inner side of the tyre. In this project, centripetal force was used to generate an output power. This means that the vehicle wheel can generate electrical energy without the need for a contact zone. The developed harvesters in this project were designed to be mounted at the rim of the vehicle wheel.

9.2.2 Modelling of pre-stressed piezoelectric beam

This part of the research focused on analysing the performance of the Thunder™ pre-stressed piezoelectric beam when it is used as the main source to extract power from two types of harvesters; impulse based piezoelectric harvester and non-contact piezoelectric harvester. The Thunder™ beam consists of different materials each of which has its own thermal expansion coefficient. This causes a curvature to appear during the manufacturing of the Thunder™ beam. Due to that, the maximum deflection was found to be in the middle of the Thunder™ beam and the dome height was found to be 0.6 mm. Thus, the maximum applied load that causes the beam to be flat was 35.9 N. Finite element analysis using ANSYS was used to demonstrate the effect of the clamping method on the amount of stress developed in the clam area as well as the amount of the output power. It was found that maximum power was generated when the beam was mounted as a cantilever followed by a simply supported structure which was followed by a rigidly supported on both ends. For a given input force, the maximum developed stress in the clamped area was found to be when the beam was mounted as a cantilever followed by a rigidly supported on both ends which were followed by a simply supported structure. As the way that the pre-stressed beam was mounted affects the output power, Thunder™ pre-stressed beam was simply supported in both impact based and non-contact harvesters. The mechanical damping and the stiffness of the pre-stressed beam varied due to the applied force and thus its resonant frequency and the electrical damping (optimum load resistance). Therefore, both the stiffness and damping of the Thunder™ structure were measured and used in the general model of the piezoelectric harvester to predict the output power for a given input force and load resistance.

9.2.3 Generating electrical power from impact based piezoelectric harvester

This part of the thesis focused on designing, building, modelling, testing and optimizing an impact based piezoelectric harvester that used a Thunder™ pre-stressed beam as the main conversion source from mechanical to electrical energy. For harvesting energy from vibration, piezoelectric beams have been designed in the literature such that their resonant frequency matches the resonant system of the surrounding environment to maximize the output power. For a rotating object application, the centripetal acceleration corresponding to the rotation is greater than the

available mass displacement. Therefore designing an efficient resonant piezoelectric harvester is not sufficient. An alternative solution to this problem was achieved by using the centripetal force to generate an impact force on the piezoelectric elements. The impact based harvester that was designed in this project consisted of a ball bearing moving freely inside a tube and two piezoelectric pre-stressed beams each of which was located at one end of the tube to transform the impact energy into electric energy. The deflection of the piezoelectric element due to the impact of the mass generated a current flowing into the resistive load connected to the piezoelectric pre-stressed beams. In this case, the motion of the mass was damped and the power was dissipated into the load.

9.2.3.1 Modelling of the pre-stressed piezoelectric beam under impact

In Chapter 4, the model of the impact based piezoelectric harvester was discussed in detail. In order to convert the rotational energy into electrical energy, two different methods were used to mount the impact based piezoelectric harvester on a rotating object. The first method was using gravitational force as the main force that caused the ball bearing to move from one side of the tube to the other side (GF). In the second method, the centripetal force was the acting force that caused the mass to move from one side of the tube to the other (CF). The theoretical analysis showed that using the GF method was limited. This was due to the fact that, the ball bearing stuck to one end of the tube when the rotating speed reached its critical value (3 rps) due to the effect of the centripetal force. The critical rotating speed was found to be inversely proportional to the square root of the length of the tube. In addition this speed did not depend on the distance between the centre of rotation and the harvester. In the CF, the harvester was kept in a horizontal position during rotation. Therefore, the effect of the centripetal force on both the piezoelectric element and the ball bearing was considered to be sinusoidal. The theoretical analysis predicted that, for a given rotating speed, the power level from the piezoelectric harvester which had been mounted using the CF method was much higher than the one which used the GF method. Moreover, in the CF method, the output power had a cubic relationship with the rotating speed. Therefore, this way of mounting the harvester was used as the only method to design, model and test both the impact based harvester and the non-contact piezoelectric harvester. The key parameters of the model were the value of the mass, internal displacement of the mass and the value of the load resistor. It was found that the output power was directly proportional to the mass of the ball bearing. The results, from finite element analysis

using the ANSYS software, showed that stress in the axial, lateral directions as well as shear stress were generated in the Thunder™ structure due to the impulse force applied to the middle of the curved beam. This simulated result showed that the maximum stresses in the axial and lateral directions were developed in the middle of the pre-stressed beam due to the impact force. However, the maximum shear stress was generated when the piezoelectric material came in contact with the stainless steel substrate. Analytical calculations showed that the maximum impact force that the piezoelectric structure can tolerate before a plastic deformation started to form underneath the surface of the structure was 63 N. The developed model of the impact based piezoelectric harvester (Chapter 4) was used to calculate the speed at which the ball bearing hit the piezoelectric structure due to the effect of the rotating speed. By knowing the velocity at impact both the applied force and the generated output power were calculated numerically. The numerical model was used to analyse the collision between the ball bearing and the piezoelectric structure, clarify the relationship between the input mechanical impact and the electric output power and simulate the behaviour of the piezoelectric pre-stressed beam after impact. It had been shown theoretically that only some of the initial kinetic energy of the impact was absorbed. The percentage of the absorbed energy was calculated at different rotating speeds. Some of this energy was stored as strain energy. This energy was used to drive the contact points apart during the restitution phase. However, some of the absorbed energy was lost due to converting some of the mechanical energy into electrical energy, plastic deformation, sound and heat.

9.2.3.2 Evaluation, optimization and performance of the impact based piezoelectric harvester

The prototype of the impact based piezoelectric harvester was tested to compare the experimental results to those obtained theoretically. In order to carry out the experiment, the rotating disk was designed. The Crozet motor was used to drive the rotating wheel and the Crozet software was used to control the speed of the motor. The maximum rotating speed that the wheel can achieve was 24 rps. The resonant frequency of the Thunder™ pre-stressed beam was measured along with its optimum load resistance at different values of the impact force obtained at different rotating speed. The results from the model were compared to the experimental results to analyse the characteristics of the harvester and verify the accuracy of the model. Both experimental and numerical simulation results agreed that multiple impacts occur

between the mass and the piezoelectric beams located at each side of the tube. Experimental results showed that the impact based harvester produced an average output power in the range of 15 μW to 2 mW when the rotating speed changed from 200 rpm to 800 rpm. These experimental results were obtained when the harvester was mounted using the CF method. Using the GF method, the experimental results showed that the ball bearing stuck to one end of the tube when the rotating speed reached a value of 3 rps.

9.2.4 Generating electrical power from non-contact piezoelectric harvester

This part of the thesis focused on designing, building, modelling, testing and optimizing a non-contact piezoelectric harvester that used Thunder™ pre-stressed beam as the main conversion source from mechanical to electrical energy. In this harvester, a magnetic levitation system was used to initiate compression force on the piezoelectric elements due to the effect of the centripetal force. The two outer magnets, which were attached to the piezoelectric structures, each of which located at one end of the tube, were oriented to repel the central magnet and thus suspending the central magnet with restoring force. Due to the effect of the centripetal force, the central magnet moved within the given space between the outer magnets. The moving distance depended on the applied force as well as the restoring force. The change in the distance between each of the outer magnets and the central one led to a change in the axial load on the piezoelectric structure. This caused an output power to be dissipated into the load resistance.

9.2.4.1 Modelling of the pre-stressed piezoelectric beam under magnetic forces

In Chapter 6, the non-contact piezoelectric model was developed and used to analyse the behaviour of the harvester when it was mounted on a rotating object using the CF method. The magnetic force between the two magnets was calculated numerically and verified using the FEM method. These results showed a good agreement. The design of the harvester was optimized using numerical analysis. An analytical method was used to analyse the forces between permanent magnets of various geometries. The effect of the magnet size and shape was studied and the results become a guideline that was used to design and optimize the non-contact piezoelectric harvester. For a given value of the magnet volume and its aspect ratio, the cuboidal

magnet generated 20 % higher contact force than the cylindrical magnet. Moreover, for a given volume of the cuboidal magnets, the maximum force was achieved when the aspect ratio was in the range between 0.3 and 0.6. At a high aspect ratio, greater than unity, the value of the magnetic force dropped quickly as the distance between the two permanent magnets increased. Therefore, it was preferable to use magnets with low aspect ratio if a long axial gap was required. The results from the developed model of the non-contact harvester showed that the resonant frequency of the levitation system depended on the axial gap between the outer magnet and the middle one. Increasing the axial gap caused the system stiffness to reduce and thus the resonant frequency. The behaviour of this system was nonlinear. Therefore, for a given axial gap, an increase in the rotating speed caused the resonant frequency to drop. For a given value of the rotating speed, the output power of the non-contact harvester increased, as the axial gap got longer. This can be explained as follows: as the axial gap increased, the stiffness of the system reduced allowing the middle magnet to travel longer distance. This applied more force on the outer magnet and thus the piezoelectric element attached to it causing an increase in the output power.

9.2.4.2 Evaluation, optimization and performance of the non-contact piezoelectric harvester

The prototype of the non-contact based piezoelectric harvester was used and tested in Chapter 7 to compare the experimental results to the one obtained theoretically. The forces generated between two cuboidal magnets were measured at different separation distances. A good agreement between the experimental measurement and the analytical calculation was obtained. The initial gap between the outer and the middle magnets was adjusted in order to investigate the effect this gap had on the output power and the value of the optimum load resistance. This was obtained for a given rotating speed. Moreover, for a given axial gap, the effect of the rotating speed on the output power was investigated and the value of the optimum load resistance was measured. Both the stiffness and the damping of the Thunder™ piezoelectric beam were measured at different rotating speed for a given axial gap. In addition, for a given rotating speed the stiffness and the damping of the Thunder™ was measured at different values of the axial gap.

9.3 Future work

The research objectives that were presented in Section 1.1 were achieved in this thesis. This section discusses briefly some other potential areas of work that could be done as future work. Some of these potential research areas are as follows:

9.3.1 Testing the performance of the piezoelectric harvesters when it is connected to the TPMS inside the vehicle tyre

The output power from the piezoelectric harvesters needs to be managed and stored before it is connected to any sensors including TPMS. Connecting the harvesters presented in Section 8.3 to the TPMS mounted on the rim of the vehicle wheel can be done as a future work. The performance of the harvester can be tested and analysed. The effect of the temperature on the performance of the piezoelectric harvesters can be investigated [85]. This is due to the fact that for this application, the piezoelectric harvesters must survive a change in the temperature inside the tyre environment ranging from -20 to 200 ^{o}C. Mechanical stability and the lifetime of the piezoelectric harvester are other issues that need to be investigated [86]. Applying dynamic compressive stress at a high temperature, results in further reduction in the performance of the piezoelectric beam. The temperature inside the tyre is fixed as well as the number of stress cycles due to driving time and speed. Therefore, the only factor that can be reduced in order to increase the lifetime of the beam in case of using the impact based harvester is the amplitude of the applied dynamic stress. This can be achieved by increasing the contact area between the mass and the piezoelectric beam. However, using a different shape than a ball bearing increases the friction between the mass and the frame. Other methods could involve coating the piezoelectric beam with a protective rubbery layer to reduce the effect of the physical contact between the ball bearing and the piezoelectric beam.

Appendix A Analysing centripetal acceleration

In this appendix, the effect of the centripetal force on a piezoelectric transducer mounted at different point of the frame is analyzed. The effect of centripetal force at 3 different points in the frame will be illustrated. The first point is the middle of the frame, where the generator is screwed to the rotating wheel, and the other two points are the both ends of the frame. Only the component of the centripetal force which is acting in the direction of the free movement of the ball bearing is taken into account.

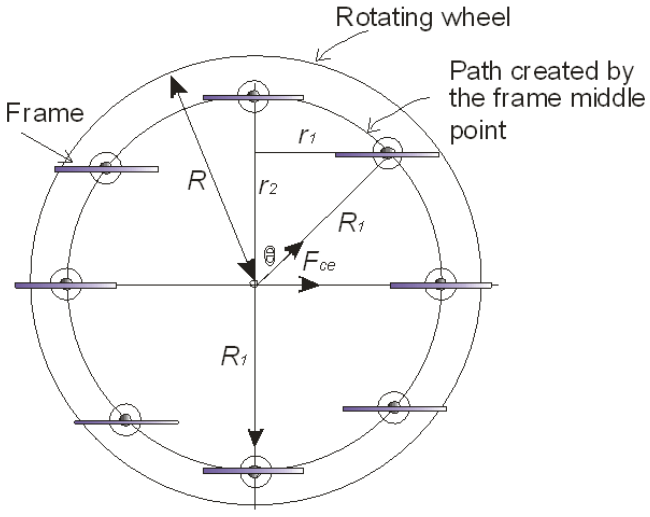

Figure A.1 Path created by middle of the frame

Firstly, the effect of $F_{ce(x)}$ on the middle of the frame will be analyzed. At this point the direction of the centripetal force is perpendicular to the free movement direction. Figure A.1 shows the path that this point creates when it has been kept in a horizontal position around the centre of rotation. The following equation presents the magnitude of the applied force that an object located on this point is subjected to:

$$F_{ce(x)} = \frac{mv^2}{R_1}\sin\theta = m4\pi^2\omega_f^2 R_1 \sin\theta \qquad \text{A.1}$$

where R_1 is the distance between the centre of rotation and the point located in the middle of the frame. The magnitude of R_1 is constant while the point is rotating. θ is the angle between the direction of the centripetal force and the vector perpendicular to the free movement of the ball bearing. This angle can be obtained by the following equation:

$$\tan\theta = \frac{r_1}{r_2} \qquad \left\{\begin{array}{l} 0 \geq |r_1| \geq R_1 \\ 0 \geq |r_2| \geq R_1 \\ 0 \geq |\theta| \geq n2\pi \end{array}\right\} n = 1,2,3... \qquad \text{A.2}$$

Equation A.1 shows that the magnitude of $F_{ce(x)}$ is proportional to the distance between the centre point of the frame and the centre of rotation. Moreover, this applied force is proportional to the square of the rotating speed. Figure A.2 shows the path that a point located at the left end side of the frame traces when it has been kept in a horizontal position around the centre of rotation. The path is a circular one. However, its centre has been shifted to the left by half the length of the frame. Therefore, the distance between the centre of rotation and each point on the path (r) varies during rotation from its minimum value of R_1 - $L/2$ to its maximum value of R_1 + $L/2$.

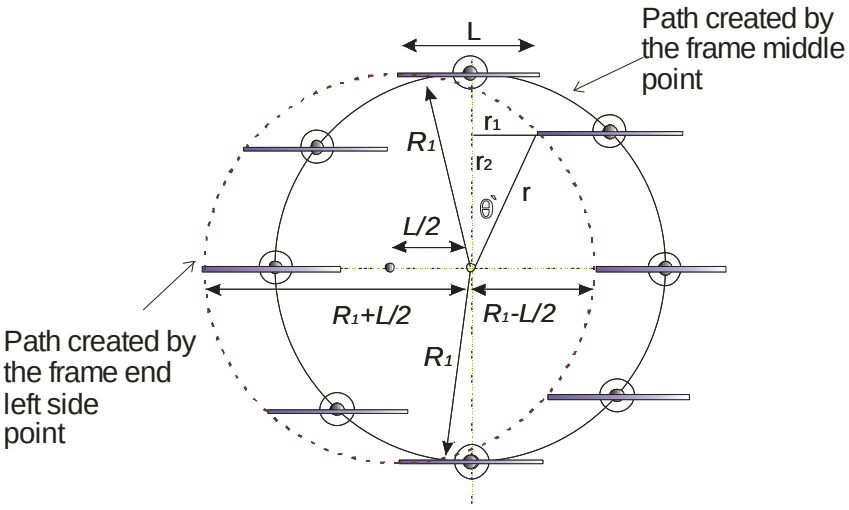

Figure A.2 Path created by the left end of the frame

The following equation presents the magnitude of the applied force that an object located on a left side hand of the centre of the frame at a distance of $L/2$ would be subjected to:

$$F_{ceL(x)} = \frac{mv^2}{r}\sin\theta' = m4\pi^2\omega_f^2 r\sin\theta' \qquad \text{A.3}$$

where r is the distance between the centre of rotation and the object. θ' is the angle between the direction of the centripetal force and the vector perpendicular to the free movement of the ball bearing. This angle can be obtained by the following equation:

$$\tan\theta' = \frac{r_1 + L/2}{r_2} \qquad \left.\begin{cases} 0 \geq |r_1| \geq R_1 \\ 0 \geq |r_2| \geq R_1 \\ 0 \geq |\theta'| \geq n2\pi \end{cases}\right\} n = 1,2,3... \qquad \text{A.4}$$

In order to find the relationship between $F_{ceL(x)}$ and $F_{ce(x)}$ equation A.3 will be rewritten in terms of R_1 and θ as follows:

$$\left.\begin{aligned} \sin\theta &= -\left(\frac{r_1}{R_1}\right) \\ \sin\theta' &= -\left(\frac{r_1 + L/2}{r}\right) \end{aligned}\right\} \qquad \text{A.5}$$

From the previous set of equations (A.5), the value of r can be achieved using the following equating:

$$r = \frac{R_1\sin\theta - L/2}{\sin\theta'} \qquad \text{A.6}$$

Substitute equation A.6 in equation A.3 gives the following equation:

$$F_{ceL(x)} = m4\pi^2\omega_f^2 R_1\sin\theta - m4\pi^2\omega_f^2\frac{L}{2} \qquad \text{A.7}$$

Using the same method presented previously, the magnitude of the applied force on an object located at a distance equals to $L/2$ from the centre of the frame is presented in equation A.8.

$$F_{ceR(x)} = m4\pi^2\omega_f^2 R_1\sin\theta + m4\pi^2\omega_f^2\frac{L}{2} \qquad \text{A.8}$$

Appendix B Crouzet software

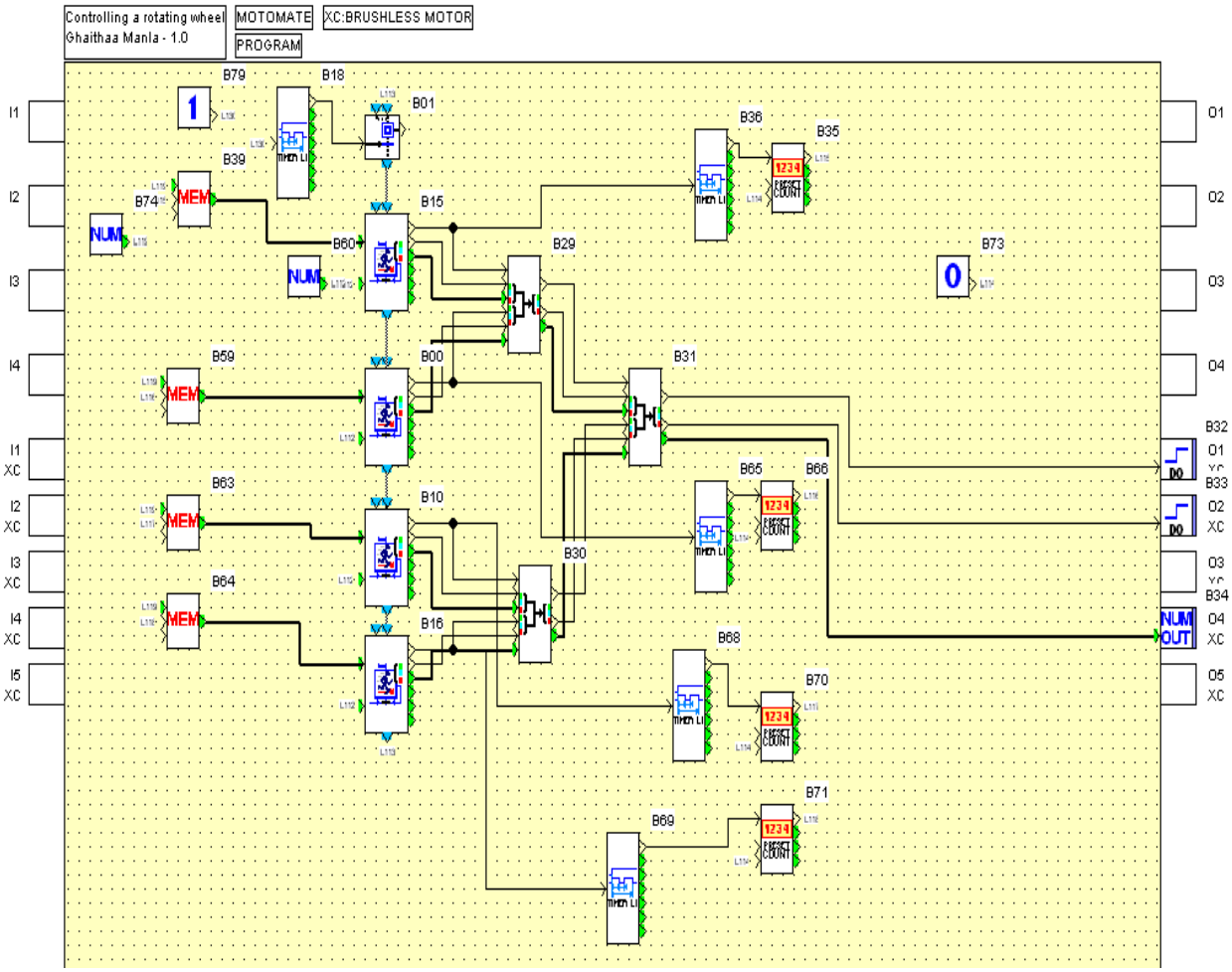

References

[1] Chait A. The EoPlex approach to powering wireless tire pressure sensors, http://www.eoplex.com/images/eoplex_whitepaper_tire.pdf. 2008.

[2] Périsse J. A study of radial vibrations of a rolling tyre for tyre-road noise characterisation. 2001. *Mechanical Systems and Signal Processing*. 16 (6): pp. 1043-58.

[3] Morreale P. Wireless sensor network application in urban telehealth. 2007. *Computer Society, IEEE 21st International Conference on Advanced Information Network and Applications Workshops*. pp. 1-5.

[4] Ye W., Heidemann J., Estrin D. An energy-efficient MAC protocol for wireless sensor networks. 2002. *Twenty-First Annual Joint Conference of the IEEE Computer and Communications Societies*. pp. 1567-76.

[5] Roundy S, Wright P, Rabaey J. Energy scavenging for wireless sensor network. Kluwer academic publisher; 2003.

[6] Beeby S. P., Tudor M. J., White N. M. Energy harvesting vibration sources for microsystems applications. 2006. *Measurement Science and Technology*. 17: pp. 179-95.

[7] Mitcheson P. D., Green T. C., Yeatman E. M., Holmes A. S. Architectures for vibration-driven micropower generators. 2004. *Microelectromechanical Systems*. 13 (3): pp. 429-40.

[8] Mitcheson P. D., Miao P., Stark B. H., Yeatman E. M., Holmes A. S., Green T. C. MEMS electrostatic micropower generator for low frequency application. 2004. *Science Direct*. 115: pp. 523-9.

[9] Amirtharajah R., Chandrakasan A. P. Self-Powered Signal Processing Using Vibration-Based Power Generation. 1998. *IEEE Journal of Solid State Circuits*. 33 (5): pp. 687-95.

[10] Beeby S. P., Torah R. N., Tudor M. J., Glynne-Jones P., O'Donnell T., Saha C. R., Roy S. A micro electromagnetic generator for vibration energy harvesting. 2007. *Micromechanics and Microengineering*. 17: pp. 1257-65.

[11] Glynne-Jones P., Tudor M. J., Beeby S. P., White N. M. An electromagnetic, vibration-powered generator for intelligent sensor systems. 2004. *Sensors and Actuators A: Physical*. 110: pp. 344-9.

[12] Yeatman E. M. Energy harvesting from motion using rotating and gyroscopic proof mass. 2008. *Mechanical Engineering science*. 222 (1): pp. 27-36.

[13] Spreemann D., Manoli Y., Folkmer B., Mintenbeck D. Non-resonant vibration conversion. 2006. *Micromechanics and Microengineering*. 16: pp. 169-73.

[14] Toh T. T., Mitcheson P. D., Holmes A. S., Yeatman E. M. A continuously rotating harvester with maximum power point tracking. 2008. *Micromechanics and Microengineering*. 18: pp. 1-7.

[15] Holmes A. S., Hong G., Pullen K. R. Axial-flux permanent magnet machines for micropower generation. 2005. *Microelectromechanical Systems*. 14 (1): pp. 54-62.

[16] Roundy S., Wright P. K., Pister K. S. J. Micro-electrostatic vibration-to-electricity converters. 2002. *ASME International Mechanical Engineering Congress & Exposition New Orleans, Louisiana*. pp. 17-22.

[17] Meninger S., Mur-Miranda J. O., Amirtharajah R., Chandrakasan A. P., Lang J. H. Vibration-to-electric energy conversion. 2001. *IEEE Transaction on Very Large Scale Integration (VLSI) Systems*. 9 (1): pp. 64-76.

[18] Despesse G, Jager T, Chaillout J, Leger J, Vassilev A, Basrour S. Fabrication and characterisation of high damping electrostatic micro devices for vibration energy scavenging. 2005.

[19] Tashiro R., Kabei N., Katayama K., Tsuboi F., Tsuchiya K. Development of a electrostatic generator for a cardiac pacemaker that harnesses the ventricular wall motion. 2002. *Journal of Artificial Organs*. 5: pp. 239-45.

[20] Mitcheson P. D., Miao P., Stark B. H., Yeatman E. M., Holmes A. S., Green T. C. MEMS electrostatic micropower generator for low frequency operation. 2004. *Sensors and Actuators A: Physical*. 115 (2-3): pp. 523-9.

[21] Yeatman E. M. Energy scavenging for wireless sensor nodes. 2007. *2nd International Workshop on Advances in Sensors and Interface, IWASI*. pp. 1-4.

[22] Mitcheson P. D., Green T. C., Yeatman E. M. Power processing circuits for MEMS inertial energy scavengers. 2006. *Design, Test, Integration and Packaging of MEMS/MOEMS Symposium*. pp. 332-7.

[23] James E. P., Tudor M. J., Beeby S. P., Harris N. R., Glynne-Jones P., Ross J. N., White N. M. An investigation of self-powered systems for condition monitoring applications. 2004. *Sensors and Actuators A: Physical*. 110 (1-3): pp. 171-6.

[24] Mitcheson P. D., Yeatman E. M., Rao G. K., Holmes A. S., Green T. C. Energy Harvesting From Human and Machine Motion for Wireless Electronic Devices. 2008. *Proceedings of the IEEE*. 96 (9): pp. 1457-86.

[25] Roundy S., Wright P., Rabaey J. A study of low level vibrations as a power source for wireless sensor nodes. 2003. *Computer Communications*. 26: pp. 1131-44.

[26] Li L., Wang F., Zhou Q. A watch in developments of intelligent tire inspection and monitoring. 2005. *IEEE International Conference on Vehicular Electronics and Safety*. pp. 333-8.

[27] www.freetpms.com/the-cost.html. 2006.

[28] www.rospa.co.uk/roadsafety/info/tyre_pressure_mon.pdf. 2007.

[29] www.autoexpress.co.uk/products/products/66830/tyre_pressure_gauges.html. 2007.

[30] www.tyresave.co.uk/smartire.html. 2007.

[31] www.schraderelectronics.com/HomePage.aspx. 2007.

[32] Roundy S., Wright P. A piezoelectric vibration based generator for wireless electronics. 2004. *Smart Materials and Structures*. 13: pp. 1131-42.

[33] Arms S. W., Townsend C. P., Churchill D. L., Galbreath J. H., Mundell S. W. Power management for energy harvesting wireless sensors. 2005. *SPIE Int'1 International Symposium on Smart Structure and Materials*. 5763: pp. 267-75.

[34] Allison D., Sharp R. On the low frequency in-plane forced vibrations of pneumatic tyre/wheel/suspension assemblies. 1997. *International Journal of Vehicle Mechanics and Mobility*. 27 (81): pp. 151-62.

[35] Löhndorf M., Kvisterøy T., Westby E., Halvorsen E. Evaluation of energy harvesting concept for tyre pressure monitoring systems. 2008. *Eurosensers*. pp. 1-4.

[36] Keck M. A new approach of a piezoelectric vibration-based power generator to supply next generation tire sensor systems. 2007. *IEEE Sensors Conference*. pp. 1299-302.

[37] Bao Z. H., Yao Y. Y., Zhu J. S., Wang Y. N. Study on ferroelectric and dielectric properties of niobium doped Bi4Ti3O12 ceramics and thin films prepared by PLD method. 2002. *Materials Letters*. pp. 861-6.

[38] Morgan Electroceramics Technical Publications. Effect of high static stress on the piezoelectric properties of transducer materials, www.morganelectroceramics.com/techpub1.html. 2009.

[39] Sodano H., Anton S. A review of power harvesting using piezoelectric materials (2003-2006). 2008. *Smart Materials and Structures*. 16: pp. 1-21.

[40] Lee C., Joo J., Han S., Koh K. Multifunctional transducer using poly (vinylidene fluoride) active layer and highly conducting poly (3,4-ethylenedioxythiophene) electrode: Actuator and generator. 2004. *Applied Physics Letters*. 85: pp. 1841-3.

[41] Kim H. W., Batar A., Priya S., Uchino K., Markley D., Newnham R. E., Hofmann H. F. Energy harvesting using a piezoelectric "cymbal" transducer in dynamic environment. 2004. *Applied Physics*. 43: pp. 6178-83.

[42] Roundy S. Energy harvesting for tire pressure monitoring systems: design consideration. 2008. *PowerMEMS*. pp. 1-6.

[43] Pearce D. H., Button T. W. Alternative processing routes for RAINBOW-type piezoelectric devices. 1998. *Proceedings of the Eleventh IEEE International Symposium on Application of Ferroelectrics*. pp. 547-9.

[44] Yang G., Liu S. F., Ren W., Mukherjee B. K. Uniaxial stress dependence of the piezoelectric properties of lead zirconate titanate ceramics. 2000. *Proceedings of the 12th IEEE International Symposium on Aplication of Ferroelectrcs*. 1: pp. 431-4.

[45] Juuti J. Pre-stressed piezoelectric actuator for micro and fine mechanical applications 2006.

[46] Application Notes, Face International Corporation, http://216.71.30.251/Face%20International/appnotes.pdf. 2007.

[47] Mossi K, Bishop R. *characterization of different types of high performance THUNDER^{TM} actuators*. 2000.

[48] Mossi K., Ounaies Z., Smith R., Ball B. Pre-stressed curved actuators: characterization and modelling of their piezoelectric behaviour. 2003. *Smart Materials and Structures*. 5053: pp. 423-35.

[49] Baker J., Roundy S., Wright P. Alternative geometries for increasing power density in vibration energy scavenging for wireless sensor networks. 2005. *Energy Conversion Engineering Conference*. pp. 5005-617.

[50] Yang J., Zhou H., Hu Y., Jiang Q. Performance of piezoelectric harvester in thickness-stretch mode of a plate. 2005. *IEEE Transaction on Ultrasonics, Ferroelectrics and Frequency control*. 52 (10): pp. 1872-6.

[51] Glynne-Jones P., Beeby S., White N. A novel thick-film piezoelectric micro-generator. 2001. *Smart Materials and Structures*. 10: pp. 850-2.

[52] Gurav S. P., Kasyap A., Sheplak M., Cattafesta L., Haftka R. T., Goosen J. F., Van F. Uncertainty-based design optimization of a micro piezoelectric composed energy reclamation device. 2004. *Multidisciplinary Analysis and Optimization Conference*. pp. 3599-70.

[53] Ng T. H., Liao W. H. Feasibility study of a self-powered piezoelectric sensor. 2004. *Smart Structure and Materials Conference*. 5389: pp. 377-88.

[54] Kim H. W., Priya S., Uchino K., Newnham R. E. Piezoelectric energy harvesting under high pre-stressed cyclic vibrations. 2005. *Journal of Electroceramics*. pp. 27-34.

[55] Dogheche K., Cavallier B., Delobelle P., Hirsinger L., Cattan E., Remiens D. Bi-stable micro-machined piezoelectric transducer for mechanical to electrical energy transformation. 2006. *Integrated Ferroelectrics*. 80: pp. 305-15.

[56] Umeda M., Nakamura K., Ueha S. Analysis of the transformation of mechanical impact energy to electric energy using piezoelectric vibrator. 1996. *Japanese Journal of Applied Physics*. 35: pp. 3267-73.

[57] Umeda M., Nakamura K., Ueha S. Energy storage characteristics of a piezo-generator using impact induced vibration. 1997. *Applied Physics*. 36: pp. 3146-51.

[58] Renaud M., Sterken T., Fiorini P., Puers R., Baert K., Hoof C. Scavenging energy from human body: design of a piezoelectric transducer. 2005. *The 13th International Conference on Solid-State Sensors, Actuators and Microsystems*. 1: pp. 784-7.

[59] Renaud M., Fiorini P., Hoof C. Optimization of a piezoelectric unimorph for shock and impact energy harvesting. 2007. *Smart Materials and Structures*. 16: pp. 1125-35.

[60] Keawboonchuay C., Engel T. G. Design, modeling, and implementation of a 30-kW piezoelectric pulse generator. 2002. *Transactions on Plasma Science, IEEE*. 30 (2): pp. 679-86.

[61] Keawboonchuay C., Engel T. G. Maximum power generation in a piezoelectric pulse generator. 2003. *Transactions on Plasma Science, IEEE*. 31 (1): pp. 123-8.

[62] Keawboonchuay C., Engel T. Electrical power generation characteristics of piezoelectric generator under quasi-static and dynamic stress conditions. 2003. *Transaction on ultrasonic, ferroelectrics, and frequency control, IEEE*. 50: pp. 1377-82.

[63] Cavallier B., Berthelot P., Nouira H., Foltête E., Hirsinger L., Ballandras S. Energy harvesting using vibrating structures excited by shock. 2005. *Ultrasonics Symposium, IEEE*. pp. 943-6.

[64] Kymissis J., Kendall C., Paradiso J., Gershenfeld N. Parasitic power harvesting in shoes. 1998. *Second International Conference,wearable Computing, IEEE*. pp. 132-9.

[65] Hearn EJ. Mechanics of materials. Oxford: Butterworth-Heinemann; 1997.

[66] Strong WJ. Dynamics models for structural plasticity. London:Spring-Verlag; 2003.

[67] http://faceinternational.com/. 2006.

[68] http://www.ctscorp.com/components/pzt/downloads/PZT_5Aand5H.pdf. 2006.

[69] http://ntrs.nasa.gov/archive/nasa/casi.ntrs.nasa.gov/19980236888_1998380452.pdf. 2007.

[70] http://www.euro-inox.org/pdf/auto/StructuralAutomotiveApp_EN.pdf. 2006.

[71] Minazara E., Vasic D., Costa F., Poulin G. Piezoelectric diaphragm for vibration energy harvesting. 2006. *Ultrasonics*. 44 (Supplement 1): pp. e699-e703.

[72] Richerd D., Anderson J., Bahr F., Richerds F. Efficiency of energy conversion for devices containing a piezoelectric component. 2004. *Micromechanics and Microengineering*. 14: pp. 717-21.

[73] Platt S. R., Farritor S., Haider H. On low-frequency electric power generation with PZT ceramics. 2005. *IEEE/ASME Transactions on Mechatronics*. 10 (2): pp. 240-52.

[74] Eschmann P, Weigand K, Brändlein J. Ball and roller bearings: theory, design and application. Wiley; 1999.

[75] Oberg E. Machinery's handbook. New York:Industrial Press; 1992.

[76] Strong WJ. Impact mechanics. University of Cambridge press; 2004.

[77] Renaud M., Fiorini P., Hoof C. Optimization of a piezoelectric unimorph for shock and impact energy harvesting. 2007. *Smart Materials and Structures*. 16: pp. 1125-35.

[78] Jean-Pierre T. Galois' theory of algebraic equations. World Scientific Publishing Co. Pte. Ltd.; 2001.

[79] www.crouzet.com. 2007.

[80] Akoun G., Yonnet J. P. 3D analytical calculation of the forces exerted between two cuboidal magnets. 1984. *IEEE Trasactions on Magnetics*. 20 (5): pp. 1962-4.

[81] Geng S. M., Schwarze G. E., Niedra J. M. A 3-D magnetic analysis of a linear alternator for a Stirling power system. 2000. *Energy Conversion Engineering Conference and Exhibit, 2000 (IECEC) 35th Intersociety*. 1: pp. 232-7.

[82] Agashe J. S., Arnold D. P. A study of scaling and geometry effects on the forces between cuboidal and cylindrical magnets using analytical forces solution. 2009. *Applied Physics*. 41 (10): pp. 1-9.

[83] Vokoun D., Beleggia M., Heller L., Sittner P. Magnetostatic interactions and forces between cylindrical permanent magnets. 2009. *Journal of Magnetism and Magnetic Materials*. 321 (22): pp. 3758-63.

[84] Mann B. P., Sims N. D. Energy harvesting from the nonlinear oscillations of magnetic levitation. 2009. *Journal of Sound and Vibration*. 319 (1-2): pp. 515-30.

[85] Morgan Electroceramics Technical Publications. Important properties of Morgan Electro Ceramics piezoelectric ceramics (PZT-a, PZT-5A, PZT-5H, PZT-8), www.morganelectroceramics.com/techpub1.html. 2008.

[86] Glynne-Jones P., Beeby S. P., White N. M. A method to determine the ageing rate of thick-film PZT layers. 2001. *Measurement Science and Technology*. 12 (6): pp. 663-70.